



Polish Maritime Research

Special Issue S2 (98) 2018
Vol. 25

ADDRESS OF PUBLISHER
& EDITOR'S OFFICE:

GDANSK UNIVERSITY
OF TECHNOLOGY

Faculty of Ocean Engineering
& Ship Technology
G. Narutowicza 11/12
80-233 Gdańsk, POLAND

EDITORIAL STAFF:

Wiesław Tarełko
| Editor in Chief
Janusz Kozak
| Deputy Editors-in-Chief
Wojciech Litwin
| Deputy Editors-in-Chief

Price:
single issue: 25 PLN

Prices for abroad
single issue:
- in Europe EURO 15
- overseas USD 20

WEB:
pg.edu.pl/pmr

e-mail : pmr@pg.edu.pl

ISSN 1233-2585

Computing Science and Mechanical Engineering in Marine Engineering

CONTENS

- 4 **Bolin Jiang, Bo Liang, Shanshan Wu**
FEASIBILITY STUDY ON THE SUBMERGED FLOATING TUNNEL IN QIONGZHOU STRAIT, CHINA
- 12 **Weixuan Hu, Yixiong He**
THE AUTOMATIC COLLISION AVOIDING PLAN RESEARCH OF GIVEN WAY VESSEL IN CROSSING SITUATION
- 17 **Zeng Xiangming, Zhang Huawu**
EXPERIMENTAL STUDY OF THE AERODYNAMICS OF SAIL IN NATURAL WIND
- 23 **He Zheng, Sun Xiao-yu, Gu Xuan**
THE INFLUENCE OF SHIP ROLLING MOTION ON TAKE-OFF AERODYNAMIC CHARACTERISTICS OF AIRCRAFT
- 30 **Teng XianBin, Zhang JunDong**
MARINE FOUR-STROKE DIESEL ENGINE CRANKSHAFT MAIN BEARING OIL FILM LUBRICATION CHARACTERISTIC ANALYSIS
- 35 **Hui-bing Gan, Bo Lv**
RESEARCH ON DRUM WATER LEVEL CONTROL OF MARINE AUXILIARY BOILER BASED ON ADRC
- 42 **Wenfeng Wu, Yubin Yang, Jianwei Zhang, Jinshu Lu**
STUDY ON STRIKING SHIP WITH LOADING IMPACT ON THE PERFORMANCE OF THE DOUBLE HULL OIL TANKER COLLISION
- 49 **Jun Du, Yan Zhang, Zeliang Cai**
SIMULATION AND EXPERIMENTAL STUDY OF SCR INJECTION SYSTEM
- 56 **Kaiye Hu, Yong Ding, Hongwei Wang**
HIGH-SPEED CATAMARAN'S LONGITUDINAL MOTION ATTENUATION WITH ACTIVE HYDROFOILS
- 62 **Jianguang Zhao, Jingjing Fan**
A SHIP NETWORK DYNAMIC ROUTING ALGORITHM BASED ON VECTOR NETWORK
- 69 **Chunxian Gao, Hui Liu**
PASSIVE LOCALIZATION FOR MIXED-FIELD MOVING SOURCES
- 75 **Fu Qiang, Zhang Benying, Zhao Yuanyuan, Zhu Rongsheng, Liu Gang, Li Mengyuan**
THE CAVITATION NUCLEI TRANSIENT CHARACTERISTICS OF LENNARD-JONES FLUID IN CAVITATION INCEPTION

ADDRESS OF PUBLISHER
& EDITOR'S OFFICE:

GDANSK UNIVERSITY
OF TECHNOLOGY

Faculty of Ocean Engineering
& Ship Technology
G. Narutowicza 11/12
80-233 Gdańsk, POLAND

- 85 **DONG Liang-xiong, SHI Yi-ran, WANG Shao-hua**
RESEARCH ON RUB-IMPACT LOADS RESPONSE OF SHIP SHAFTING
- 92 **Ying Zhu, Liang Geng**
*RESEARCH ON SDG FAULT DIAGNOSIS OF OCEAN SHIPPING BOILER SYSTEM
BASED ON FUZZY GRANULAR COMPUTING UNDER DATA FUSION*
- 98 **Hu Zhang, Lei Zhao, Quan Liu, Jingjing Luo, Qin Wei, Zude Zhou,
Yongzhi Qu**
*AN IMPROVED FEATURE EXTRACTION METHOD FOR ROLLING BEARING
FAULT DIAGNOSIS BASED ON MEMD AND PE*
- 107 **Qing Fang, Zeping Tong, Liang Ren, Ao Liu**
*RESEARCH ON THE MARITIME LOGISTICS PRICING MODEL OF RISK-AVERSE
RETAILER-DOMINATED DUAL-CHANNEL SUPPLY CHAIN*
- 117 **Min Zhang, Shidong Fan, Hanhua Zhua, Sen Han**
*NUMERICAL SIMULATION OF SOLID-FLUID 2-PHASE-FLOW OF CUTTING
SYSTEM FOR CUTTER SUCTION DREDGERS*
- 125 **Wang Biao, Tang Jiansheng, Yu Fujian, Zhu Zhiyu**
*IDENTIFICATION OF SONAR DETECTION SIGNAL BASED ON FRACTIONAL
FOURIER TRANSFORM*
- 132 **Yang Shuai, Liu Wenbai, Liu Hongwei**
*QUANTITATIVE ANALYSIS OF THE RELATIONSHIP BETWEEN SHEAR
STRENGTH AND FRACTAL DIMENSION OF SOLIDIFIED DREDGER FILL WITH
DIFFERENT FLY ASH CONTENT UNDER MONOTONIC SHEAR*
- 139 **Zhendong Ji, Zhihong Zhao, Jianhua Wang, Zhipeng Lv**
*A FLEXIBLE CONTROL STRATEGY FOR SHORE-TO-SHIP POWER SYSTEM IN
TERMS OF GRID-CONNECTED AND OFF-GRID SWITCH*
- 149 **Zhenwei Zhou, Jiaming Wu**
*LOW TO MIDDLE VIBRO-ACOUSTIC NOISE PREDICTION IN SHIP CABIN BY
USING PLATE-CAVITY COUPLING MODEL*
- 158 **Bi-Rong Ding, Yuan-long Chen, Ji Zhou, Pei-xuan Chen**
*RESEARCH ON KEY PROCESS TECHNOLOGY FOR PROFILE ELECTROLYTIC
FINISHING OF LARGE MARINE PROPELLER IMPELLER*
- 164 **Xiao Shen**
*RESEARCH ON OPTIMIZATION MODEL OF MARINE INDUSTRY STRATEGIC
ADJUSTMENT UNDER COMPLEX MARITIME CONDITIONS BASED ON ANT
COLONY ALGORITHM*
- 170 **Xiaofeng Han, Yan Li, Guodong Liu**
*STUDY ON THE OPTIMIZATION AND PERFORMANCE OF TDMA ALLOCATION
ALGORITHM IN SHIPS' AD HOC NETWORKS*
- 176 **Yaqi Shi, Wei Luo**
*APPLICATION OF SOLAR PHOTOVOLTAIC POWER GENERATION SYSTEM IN
MARITIME VESSELS AND DEVELOPMENT OF MARITIME TOURISM*

Editorial

POLISH MARITIME RESEARCH is a scientific journal of worldwide circulation. The journal appears as a quarterly four times a year. The first issue of it was published in September 1994. Its main aim is to present original, innovative scientific ideas and Research & Development achievements in the field of :

Engineering, Computing & Technology, Mechanical Engineering,

which could find applications in the broad domain of maritime economy. Hence there are published papers which concern methods of the designing, manufacturing and operating processes of such technical objects and devices as : ships, port equipment, ocean engineering units, underwater vehicles and equipment as well as harbour facilities, with accounting for marine environment protection.

The Editors of POLISH MARITIME RESEARCH make also efforts to present problems dealing with education of engineers and scientific and teaching personnel. As a rule, the basic papers are supplemented by information on conferences , important scientific events as well as cooperation in carrying out international scientific research projects.

Scientific Board

Chairman : Prof. JERZY GIRTLER - Gdansk University of Technology, Poland

Vice-chairman : Prof. MIROSLAW L. WYSZYNSKI - University of Birmingham, United Kingdom

Dr POUL ANDERSEN
Technical University of Denmark,
Denmark

Dr MEHMET ATLAR
University of Newcastle
United Kingdom

Prof. GORAN BARK
Chalmers University of Technology
Sweden

Prof. MUSTAFA BAYHAN
Süleyman Demirel University
Turkey

Prof. VINCENZO CRUPI
University of Messina
Italy

Prof. MAREK DZIDA
Gdansk University of Technology
Poland

Prof. ODD M. FALTINSEN
Norwegian University of Science
and Technology
Norway

Prof. PATRICK V. FARRELL
University of Wisconsin Madison
WI
USA

Prof. HASSAN GHASSEMI
Amirkabir University of Technology
Iran

Prof. STANISLAW GUCMA
Maritime University of Szczecin
Poland

Prof. ANTONI ISKRA
Poznan University of Technology
Poland

Prof. JAN KICINSKI
Institute of Fluid-Flow Machinery
Polish Academy of Sciences
Poland

Prof. ZBIGNIEW KORCZEWSKI
Gdansk University of Technology
Poland

Prof. NICOS LADOMMATOS
University College London
United Kingdom

Prof. JOZEF LISOWSKI
Gdynia Maritime University
Poland

Prof. JERZY MATUSIAK
Helsinki University of Technology
Finland

Prof. JERZY MERKISZ
Poznan University of Technology
Poland

Prof. EUGEN NEGRUS
University of Bucharest
Romania

Prof. VALERI NIEKRASOV
Admiral Makarov National
University of Shipbuilding
Ukraine

Prof. YASUHIKO OHTA
Nagoya Institute of Technology
Japan

Dr YOSHIO SATO
National Traffic Safety
and Environment Laboratory
Japan

Prof. KLAUS SCHIER
University of Applied Sciences
Germany

Prof. FREDERICK STERN
University of Iowa
IA
USA

Prof. ILCEV DIMOV STOJCE
Durban University of Technology
South Africa

Prof. JOZEF SZALA
UTP University of Science
and Technology
Poland

Prof. TADEUSZ SZELANGIEWICZ
Maritime University of Szczecin
Poland

Prof. BORIS TIKHOMIROV
Saint Petersburg State Marine
Technical University
Russian Federation

Prof. DRACOS VASSALOS
University of Glasgow
and Strathclyde
United Kingdom

FEASIBILITY STUDY ON THE SUBMERGED FLOATING TUNNEL IN QIONGZHOU STRAIT, CHINA

Bolin Jiang^{1,2}

Bo Liang²

Shanshan Wu³

¹ Chongqing Vocational Institute of Engineering, Chongqing, China

² College of Civil Engineering, Chongqing Jiaotong University, Chongqing, China

³ Chongqing Vocational College of Public Transportation, Chongqing, China

ABSTRACT

Abstract: Currently, one of the challenging tasks for Chinese engineering community is to construct a water-way crossing of Qiongzhou Strait in the south of China. This project has also gained significant attention from researchers in academia. The study presented herein is centered on providing a feasible solution for accomplishing the above mentioned task. Initially, different alternatives as the best location, judged on the basis of the environmental constraints, are studied. Then the comparison between various structural solutions such as suspension bridge, submarine tunnel and SFT is presented. Among these solutions, SFT appears to be a very suitable alternative for Qiongzhou Strait waterway crossing due to distinctive advantages, like shorter distance, lower cost, less impact on environment and navigation, etc. Based on the appropriate conception for cross sections, support systems, materials, joints and connection schemes, a numerical model is developed by means of the FEM software ANSYS/Fluent. It is then analyzed under the influence of different environmental loading conditions, varying the wave heights and lengths, current velocities and water depths, which are typical in Qiongzhou Strait. The numerical results reveal that the proposed SFT solution performs safely even under extreme weather conditions.

Keywords: Submerged Floating Tunnel, Qiongzhou Strait, waterway crossing, design features, numerical analysis

INTRODUCTION

In the last two decades, several proposals for waterway crossing have been carried out in China due to the demand of traffic and development of civil engineering technology. For example, crossings of Bohai Strait, Taiwan Strait, and Qiongzhou Strait are frequently discussed at present. On the other hand, the successful experiences of such waterway projects as Hangzhou Bay Bridge, Qingdao Jiaozhou Bay Submarine Tunnel, Xiamen Xiang'an Submarine Tunnel, and Hong Kong-Zhuhai-Macau Bridge have greatly increased the enthusiasm and confidence to make true the dreams.

Qiongzhou Strait is located in the south of China, between Leizhou Peninsula and Hainan Island. Since 1980s, the local government started to investigate the feasibility for a Qiongzhou

Strait waterway crossing, and relevant research about this topic still keeps going even up to now. Tan et al. (2001) investigated the feasibility to construct an undersea tunnel by means of the shield method for Qiongzhou Strait waterway crossing. Mai et al. (2003) analyzed the feasibility SFT in the Qiongzhou Strait in view of the environmental conditions, design schemes, construction, and cost. Li et al. (2009) studied the feasibility to design a cable-stayed submerged floating tunnel in the Qiongzhou Strait. Yan et al. (2015) provided several proposals for SFT schemes in Qiongzhou Strait. Wu et al. (2016) studied on the significant aspects for type selection of SFT in the Qiongzhou Strait.

In this article, the environmental conditions of Qiongzhou Strait are introduced firstly, including the alternatives of locations and solutions for crossing. Analyzed next are the

characteristics of bridge, submarine tunnel, and submerged floating tunnel (SFT) solutions. According to the comparisons, the central line and SFT are selected for location and solution of the Qiongzhou Strait waterway crossing respectively. Furthermore, several proposals for SFT basic aspects are made, and numerical analyses based on Qiongzhou Strait conditions are investigated, so as to verify the feasibility and stability of the proposed SFT.

GENERAL CONDITIONS OF QIONGZHOU STRAIT

GEOLOGICAL AND WEATHER CONDITION

The Qiongzhou Strait is one of the largest three straits in China. Its geological and weather conditions can be summarized briefly as following.

The length is about 80 kilometers from east to west, and the width ranges from 18 to 35.5 kilometers (29.5 km on average) from north to south. Its seabed is generally wide and deep, with the water depth ranging from 80 meters to 120 meters along the central axis. In addition, scraps with a maximum height of 70 meters and a maximum slope angle of 22°–24° are located on the south and north shores.

Fractures are the major geological structure. The submarine strata are mainly sedimentary shaped in the Tertiary and Quaternary Periods. The upper layer is filled with sludge, sandy clay or silt, and thick-bedded clay and silty sand are distributed on bottom layer with thickness of hundreds meters.

According to statistics, about ten ruinous earthquakes have occurred in this area, nine of which are over 6.0 in magnitude. The most serious earthquake occurred in the year of 1605 with a magnitude of 7.5. All of them are shallow earthquakes with the majority depth of focus ranging from 5 to 20 kilometers. Besides, there is no records about volcano in this area.

The average annual temperature is 24°C. From May to October is the rainy season, and the average annual precipitation is more than 1500 ml. From May to November is the typhoon season of the Qiongzhou Strait, especially in September.

ALTERNATIVES OF LOCATION AND SOLUTION

Alternatives of location

According to careful investigations and evaluations, several proposals of locations for waterway crossing in Qiongzhou Strait are put forward by some researchers. In general, they can fall into three lines: the east line, the central line, and the west line, as shown in Figure 1.

The East Line. The location is characterized by the complex topography, large water depth, and high risk of earthquakes. Because the connection point of this line on Hainan Island is far away from Haikou, the capital city of Hainan Province, it is inconsistent with the development plans of this city. It would bring more disadvantages than advantages to the city and even the province if constructed as proposed.

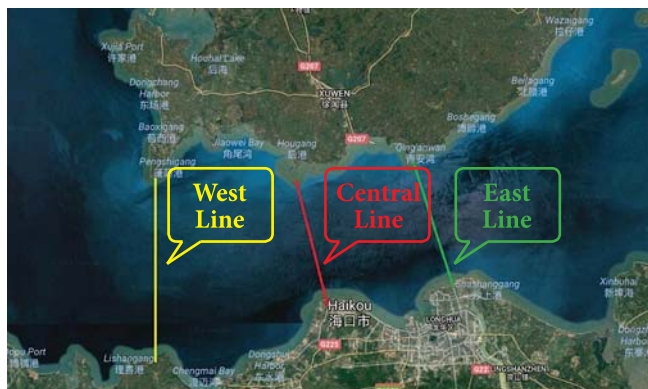


Fig. 1. Proposed lines for Qiongzhou Strait crossing

The Central Line. Straight line with a short waterway crossing distance, connected conveniently with the existing highways and railways at both shores. The main advantages of this line include low investment for both the main and lead projects, shorter travel time, and low operation cost. Therefore, it can well meet the requirements of the city planning. One fact should not be denied, however, which is the maximum water depth of 88 meters in this location.

The West Line. Compared with the other lines, its seabed is more flat, as the maximum water depth is only 55 meters, but the distance of waterway crossing is larger. It is farther away from the existing highways and railways at both shores, so the investment for the main project and lead projects will increase. In addition, this line has to avoid crossing the nature reserve in this area, which may cause more obstacles in construction.

Among the three lines, the central line is the most appropriate location for the waterway crossing due to its shorter distance and better geological conditions compared with the others. Therefore the central line is selected in this article, and the studies hereafter are based on this location.

Alternatives of solution

On the central line location, some solutions for crossing are proposed. In general, they can be summarized as in Figure 2.

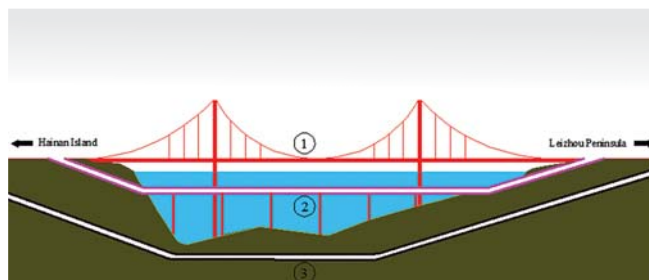


Fig. 2. Alternatives of solution: 1) Suspension bridge; 2) Submerged Floating Tunnel; 3) Submarine tunnel

Of all types of bridges, suspension bridge is the longest in span. Thus a suspension bridge is a good solution of all bridge alternatives, especially in dealing with long-distance waterways. A Submerged Floating Tunnel (SFT) is an innovative underwater structure, applied for waterway crossing in particular case of long distances. Submarine tunnels include immersed tunnels

and subsea tunnels, both of which have been applied for many waterway projects. For all the advanced technical and sufficient experiences, a submarine tunnel is not suitable for seabed of bad geological conditions.

COMPARISONS AMONG SOLUTIONS

BRIDGE

Advantages

Advanced technology of design and construction

The hydrological, meteorological, geological and navigational conditions of the Qiongzhou Strait are complicated, and therefore it is difficult to construct a bridge in the large-depth zone. At present, the longest span of suspension bridges is found in the Akashi Bridge, whose main span reaches 1,991 meters. China has rich experience in construction of long-span bridges, such as the Zhoushan Xihoumen Bridge (1,650 meters, 2009), the Runyang Yangtze River Bridge (1,490 meters, 2005), and the Jiangyin Yangtze River Bridge (1,385 meters, 1999). In the central line location aforementioned, it is feasible to construct a multiple spans bridge with a single span of over 1,000 meters. Although the construction of piles is very difficult, the problems can be solved by means of updated construction technology.

Better traffic conditions

Compared with tunnels, it is undoubtedly much better in lighting, ventilation, vision, comfort and so on when the vehicles are running on the bridge.

Easier and more economical maintenance

After operation for public transportation, the bridge requires less expense on lighting and ventilation compared with tunnels. In addition, the bridge is easier for maintenance service.

Disadvantages

Higher expense of construction

The central line is around 20 km in length. If the bridge is designed with single spans for about 1,000 meters, it will need about 20 piles and foundations. The average water depth is over 50 meters, so it is more difficult to construct the piers and foundations in these areas, and the cost is high. On the other hand, the height of the main tower of the bridge will increase as the length of single span extends.

The critical length of spans can be estimated under different materials of cables. If only the self-weight of cables is taken into account, the relationship between the critical length of span (L_c) and the height of the main tower (h) is obtained as in Figure 3.

HSS: High strength steel (Density: 7850 kg/m³; Elastic modules: 1000 MPa)

LSS: Low strength steel (Density: 7850 kg/m³; Elastic modules: 300 MPa)

FRP: Fiber reinforced polymer (Density: 1800 kg/m³; Elastic modules: 290 MPa)

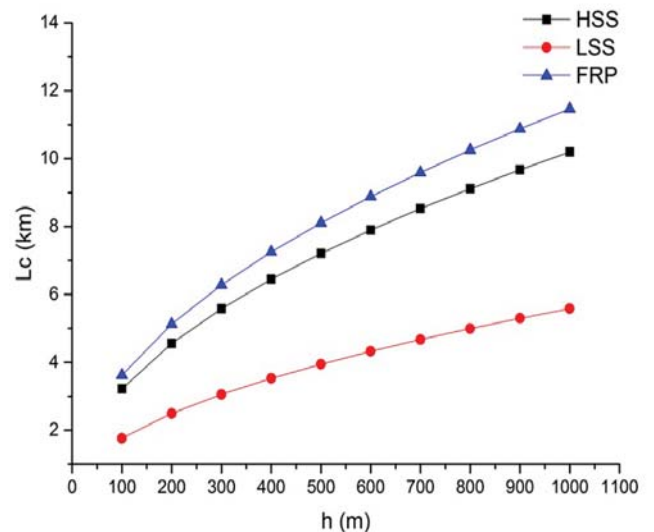


Fig. 3. Relationship between height of tower and critical length

Figure 3 shows that if HSS is selected for the cable material, when the single span reaches 5,000 meters, the height of the main tower will exceed 1,000 meters. In this case, the tower will become the tallest of its type in the world. For this reason, the design and construction of the foundation would be very complicated, but the current technology and economy can hardly support such a height.

Affected by weather

The Qiongzhou Strait is located in a tropical area which is subject to the tropical monsoon climate. Every year, the period from May to November is typhoon season. Every year, in particular, there are more than 5 days in September when the wind force is stronger than Level 8. Besides, there are more than 24 days with dense fog on average every year. Because the bridge is directly exposed to the natural environment, the traffic condition is affected largely by weather conditions. In case of strong wind, heavy fog, or other inclement weather conditions, the safety of vehicles would be reduced inevitably, or what's worse, the traffic will be interrupted due to serious weather conditions.

Impact on surroundings and navigation

The Qiongzhou Strait is a busy sea crossing. If the bridge proposal is accepted, the piers of the bridge will have impact on the navigation of ships. In addition, the height from the deck to the water surface will limit big ships from crossing the strait. Moreover, the tall main tower resulting from the long-span bridge will affect flights.

Security during war time

The bridge project will be the most effective and convenient in connecting China Mainland and the Hainan Island when open to the public. Hence the security of this kind of huge projects should be considered at the beginning phase of design. If war should happen one day, this bridge would be destroyed soon by the enemy. Moreover, it is also an easy target of terrorist attacks even during peace time.

SUBMARINE TUNNEL

Advantages

Advanced technology of design and construction

Over the past years, the world has seen great improvements in the technology of submarine tunnel design and construction. Several submarine tunnels have been completed in the past decades, such as the Seikan Tunnel (Japan, 1988) and the Channel Tunnel (Great Britain–France, 1994). In China, researchers have also obtained experiences from some subsea tunnel projects, such as the Xiamen Xiang'an Subsea Tunnel (2010) and the Qingdao Jiaozhou Bay Tunnel (2011). At present, the Hong Kong-Zhuhai-Macao Bridge is under construction in China, it will be completed in December, 2017. More construction experiences could be gained. Therefore, it is feasible in view of design and construction, according to the experiences from home and abroad.

Guarantee of crossing

The submarine tunnel can provide all-weather services, as the weather has slight influence on vehicles crossing.

Less impact on the environment

Compared with a bridge, a submarine tunnel has far less impact on the environment due to its location.

Disadvantages

Large buried depth and long distance

On the middle line, the maximum water depth is around 85 meters. According to the construction experiences of existing submarine tunnels, the buried depth of such a submarine tunnel in this location will be over 100 meters. In order to meet the slope requirement, the submarine tunnel should be extended to land with a long distance. It is estimated that the minimum distance of the submarine tunnel will reach 30 kilometers, and for certain the cost of construction will increase.

High requirements for geological conditions

A submarine tunnel needs to meet higher requirements for geological conditions. Due to some uncertain factors that could exist in the formation, it will result in large investment, high risks and a long construction period. In Japan, the Seikan Tunnel costs 24 years to complete the construction, during which there were 4 big accidents of landslides and water gushing. The most serious water gushing accident occurred in the Hokkaido side parallel heading in May 6, 1976, when the water inflow hit 70 m²/min. It consumed 5 months to bypass the water gushing area.

The Qiongzhou Strait consists of several groups of fractures: the East-West fracture, the North-East fracture, and the North-West fracture. Due to the net-structural frameworks fractures, landslide and water gushing accidents will almost inevitably occur during the construction and operation.

Higher expense of maintenance

During operation, the cost on lighting, ventilation and other maintenance aspects will be higher than those of a bridge.

Larger losses under disasters

As previously mentioned, the Qiongzhou Strait is located in a seismic region, so the subsea tunnel would suffer catastrophic damages in case of an earthquake. Once a disaster happens, the water will flow into the subsea tunnel from some partial failures

due to high water pressure. As a consequence, the tunnel could never be repaired. According to records, this region had thirty-one earthquakes of above magnitude 4.75 from year of 1400 to 1995, including nine earthquakes of above magnitude 6.0. In 1605, an earthquake of the highest magnitude (7.5) occurred in Qiongzhou. Two magnitude-6.1 earthquakes occurred in the Northern Gulf in December 1994 and January 1995, respectively. All these indicate that the southeast coastal area tends to enter a period of active earthquakes.

SUBMERGED FLOATING TUNNEL (SFT)

Advantages

Shorter distance

From the above figures, it is clear that the distance of the submerged floating tunnel is the shortest, for it does not need to consider the slope.

Less influence on surroundings and navigation

The underwater SFT has less influence on the surroundings. Besides, the gap between the SFT and the water surface can guarantee the security of navigation.

Lower cost

The unit cost of the SFT is constant, whereas the cost of the suspension bridge and the submarine tunnel will increase rapidly as the span increases.

Stronger resistance and easier escape

Compared with a bridge or a submarine tunnel, SFT has better performance in resisting earthquakes. Because the foundations of a bridge or a submarine tunnel are under the seabed, they will suffer big influence when an earthquake occurs undersea. In contrast, an escape route could be designed as an extra structure of the SFT, from where passengers can escape in a short time when an accident happens.

Disadvantages

Construction of foundation

The cables will need a foundation, and the requirement of such a foundation is strict and important.

Less experience on construction

So far, no SFT project has been constructed due to many reasons. In this case, the lack of relevant construction experience is a big challenge.

PROPOSALS FOR SFT IN QIONGZHOU STRAIT

GENERAL ASPECTS

Compared with a bridge or a submarine tunnel, SFT is the most suitable solution for the Qiongzhou Strait waterway crossing due to its distinctive advantages, such as shorter distance, lower cost, less impact on environment and navigation, etc.

The Qiongzhou Strait is a busy shipping way. In order to satisfy the requirement of navigation space for big vessels and reduce the impact from the water surface wave, the clearance

depth between the water surface and the submerged floating tunnel is proposed to be 30m. (Xiang et al. 2017).

Based on the geological condition of the central line and the requirements mentioned above, the longitudinal profile for the proposed SFT is shown in Figure 4.

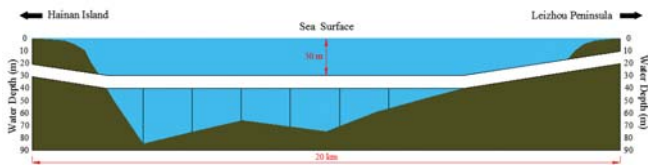


Fig. 4. Longitudinal profile of proposed SFT on central line

CROSS-SECTION

First of all, the cross-section of the proposed SFT should be confirmed. In this paper, only the type of motorway traffic is considered. Compared with other cross-sections, circular or elliptical cross-section has a better performance in the aspects of hydrodynamic behavior, space utility, fabricate convenience, etc. In addition, considering the workability and durability of fabrication and erection, the circular cross-section is confirmed eventually.

According to the clearance space requirements for traffic lanes in the Code for Design of Road Tunnel (JTG D70-2004, in Chinese), we combine the above-mentioned considerations and propose the following circular cross-section with dimension (external diameter: 14.0 m, internal diameter: 12.0 m) as illustrated in Figure 5.

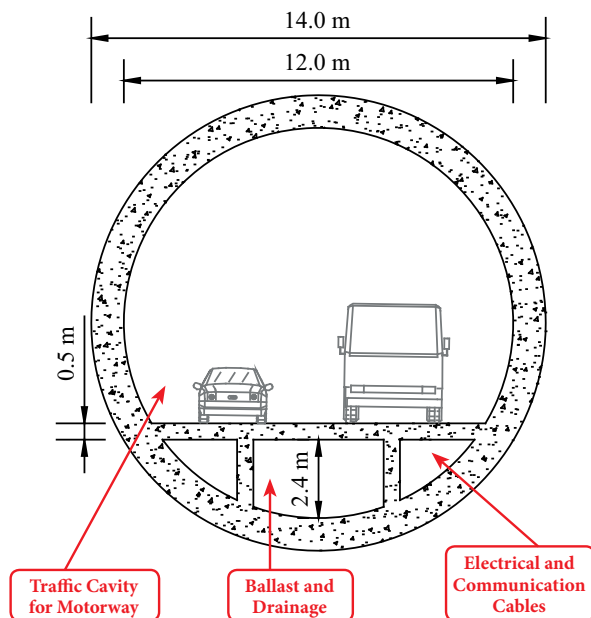


Fig. 5. Schedule of circular cross-section (Unit:m)

SUPPORT SYSTEM

Among all the support systems of the SFT, obviously free and pontoons support is not suitable for the long distance and busy navigation in the Qiongzhou Strait. In addition, with the

various fractures distributed on the seabed, column support is also not appropriate solution yet. Based on the geological condition of the Qiongzhou Strait, cables support is a more reasonable alternative for the proposed SFT, which is more popular in design of most SFT prototypes nowadays.

In order to control the displacement induced by the environmental loads, either in the horizontal or vertical direction, the inclined configuration of four cables into a group is proposed as in Figure 6.

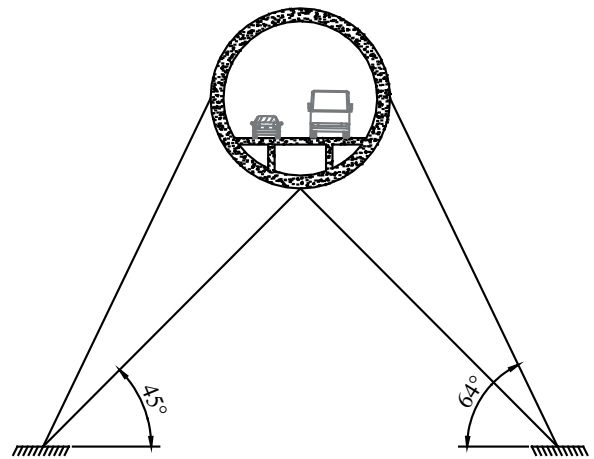


Fig. 6. Proposed inclined configuration of cables

MATERIALS

The appropriate selection of materials is one important decision for any projects, the design and execution of the SFT in particular. On the other hand, the marine structures have distinctive requirements for the materials.

Reinforced concrete is used widely in maritime structures and particularly recommended when a large structural weight is required to stabilize the structure. It can be used to contribute to the structural strength and stiffness, as well as to provide the weight needed to counteract the tunnel buoyancy. Bring references from Immersed Tunnel, reinforced concrete can be proposed for tube material of SFT, but the SFT structure must be guaranteed to have the excellent capacity of water-proof via concrete itself and coating material.

Besides, steel strands are proposed for the material of cables. The cables will be subjected to tremendous and reduplicated tension forces, and steel strands can provide high strength and high resistance to corrosion and fatigue.

JOINTS AND CONNECTIONS

Like an immersed tunnel, the SFT construction process includes the fabrication and installation of modules. In this process, the inter-module joints and the shore connections will play a significant role in the whole SFT structure.

In general, the inter-module joints either of a flexible or rigid type, must satisfy the requirements of tightness, durability and workability. The shore connections should allow different types of displacements, such as longitudinal,

vertical, horizontal, or tensional displacements, which depends on design (Panduro, 2013).

The SFT is to be suspended in the water and can be subjected to significant displacements and rotations in the longitudinal bending planes. In this case, rigid inter-module joints are more suitable than flexible ones. In addition, the axial displacements are allowable at the terminal joints due to thermal variations and triaxial rotations (Martire, 2010). Therefore, rigid joints are proposed for the inter-module joints of the Qiongzhou Strait SFT.

The connection between the SFT and the shore requires appropriate interface elements to couple the flexible water tunnel with the much more rigid tunnel bored underground. This connection should be able to restrain tube movements, without any unsustainable increase in stresses. Furthermore, the joints must be watertight. In particular, the Qiongzhou Strait is located on the seismic area, so the risk of submarine landslides needs additional attention.

Moreover, the longitudinal gradients of the underwater tunnel should be taken into account. Because the SFT should keep straight on the longitudinal direction, the longitudinal gradients cannot be ignored. The length of the bored tunnel is closely related to the cost of the entire project, so it should be implemented by appropriate gradients. From the regulations of longitudinal gradients specified in different codes as shown in Table 1 (Zhang et al. 2013), the longitudinal gradients of a bored tunnel are proposed to range from 0.3% to 3%. The aim of the variable gradients is to connect the two smoothly and reduce the entire length.

Tab. 1. Regulations of tunnel longitudinal gradients specified in different codes (Zhang et al. 2013)

Codes	Tunnel longitudinal gradients
P.R China (MOT. JTG D70-2004 Code for design of road tunnel)	0.3%–3%, maximum 4% depends on traffic conditions
European Union (DIRECTIVE 2004/54/EC)	Normal is less than 5%, it needs assistant measures between 3% and 5%.
United States (FHWA Road Tunnel)	Recommended less than 3%–4%
Great Britain (Design code for Road and Bridge)	Depends on traffic and ventilation requirements, should be less than 6%
Norway (NPRA Motorway Tunnel)	Maximum gradient depends on traffic, normal between 6%–8%
Sweden (VV Tunnel 2004)	Normal less than 5%, it can be increased in short distance permitted by experts
Netherlands (SATO)	Design speed 90 km/h, less than 4%; design speed 120 km/h, less than 3%.

NUMERICAL ANALYSES

On the basis of the aforementioned design aspects, the numerical model scheme is created as in Figure 7, with some basic parameters selected from Table 2.

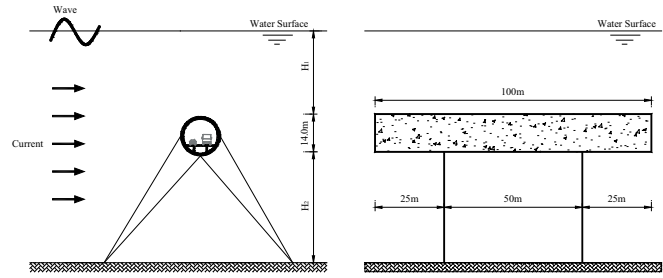


Fig. 7. Geometry of numerical model

Tab. 1. Regulations of tunnel longitudinal gradients specified in different codes (Zhang et al. 2013)

Parameters	Values	Units
Density of tunnel	2500	Kg/m ³
Elastic modulus of tunnel	32x10 ³	MPa
Density of cable	7850	Kg/m ³
Elastic modulus of cable	201x10 ³	MPa
Diameter of cable	0.3	m
Density of Fluid	1028	Kg/m ³

The numerical model is implemented by means of the FEM software ANSYS/Fluent, in which process the Airy wave and RNG $k - \epsilon$ viscous mode are applied for simulating the wave and turbulence, respectively. Only displacement and rotation along direction Z are restrained at both ends of the tube. Spherical hinges have been assumed at both ends of the cables. In order to reproduce the full turbulent phenomenon in the water volume, the distance from the inlet upstream side has been assumed equal to 3D (D width of the polygonal section = 32.3 meters). Likewise, a distance of 10D has been set so as to fully reproduce the wake turbulence that takes place downstream the tunnel. The width along direction Z is set to 100 meters, and so is the length of tube. The depth of the entire fluid volume varies depending on the location of the proposed SFT. The hexahedron elements are applied for meshing the fluid and tube.

Concerning traffic loads, only motorway traffic loads are considered in this numerical model. According to the Chinese code (MOT. JTG D70-2004 Code for design of road tunnels), the traffic loads are defined as distributed loads of 10.1 kN/m².

To investigate the variable loading conditions subjected to the SFT, different cases are adopted:

- 1) Different water depths. In Figure 7, H_1 is fixed as 30 meters, while H_2 is changed for 40 meters, 30 meters, and 20 meters according to different geological conditions of the seabed;
- 2) Different wave loads. According to the monitoring data in the Qiongzhou Strait, the extreme wave loads are selected. The extreme wave conditions include:
 - Return period of 20 years: Wave height 7.0 meters, Wave length 115.11 meters.
 - Return period of 25 years: Wave height 7.3 meters, Wave length 119.45 meters.
 - Return period of 100 years: Wave height 8.6 meters, Wave length 137.38 meters.

3) Different current velocities.

1.0 m/s, 2.0 m/s, 4.0 m/s

Displacement responses (U_x and U_y) of the SFT structure are investigated based on the aforementioned parameters and cases. The results are presented in Figures 8–10.

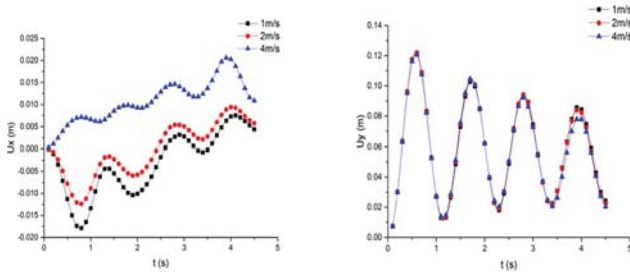


Fig. 8. Displacement response under different current velocities ($H_2:40$ m, Wave height: 7.0 m)

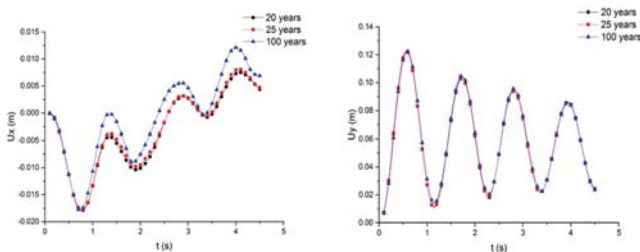


Fig. 9. Displacement responses under different waves ($H_2:40$ m, current velocity: 1.0 m/s)

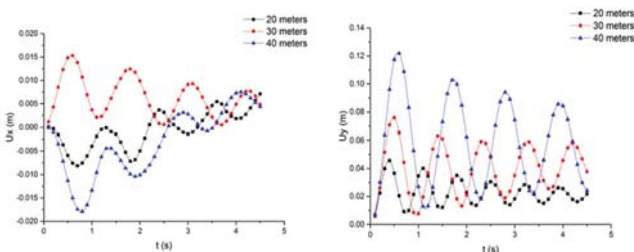


Fig. 10. Displacement responses under different water depths H_2 (wave height: 7.0, current velocity: 1.0 m/s)

According to Figure 8 and 9, the maximum amplitude of displacement responses (U_x and U_y) enlarge as the current velocity and wave height increase. In Figure 10, it shows that the SFT structure is more stable while the H_2 depth decrease. However, the displacement responses are slight and acceptable relative to the size of structure. In general, the results prove the proposed SFT structure is safe even under extreme weather conditions.

CONCLUSIVE REMARKS

This article presents the preliminary feasibility studies on a Submerged Floating Tunnel (SFT) for the Qiongzhou Strait waterway crossing.

According to the comparisons with a suspension bridge and a submarine tunnel, the SFT is selected as a better solution due to its distinctive advantages, such as shorter distance, lower cost,

less impact on the environment and navigation, etc. The central line in the Qiongzhou Strait is proposed as an appropriate location because of its geological and weather conditions.

Concerning the main aspects of the SFT design, the circular cross-section, the inclined cable support system, the concrete and steel strand materials, the rigid inter-module joints and special shore connections are investigated for the proposed SFT in the Qiongzhou Strait.

In addition, different simulated cases based on the Qiongzhou Strait conditions are calculated by means of the numerical software ANSYS/Fluent. The numerical results reveal that the SFT dynamic responses are still acceptable under ordinary and even extreme weather conditions.

In conclusion, the feasibility studies on the SFT aim to render the Qiongzhou Strait waterway crossing into reality. If the SFT technology is adopted in the Qiongzhou Strait, it will be a revolutionary event of civil engineering in the world, and will also be considered the realization of a common dream of all SFT researchers.

ACKNOWLEDGEMENT

The research was financially supported by Ministry of Transport of the People's Republic of China (Grant No. 2013 318 740 050), Chongqing Vocational Institute of Engineering (Science and technology project: KJB201813), Chongqing Education Commission (Science and technology project of 2018: Research on the dynamic response of Submerged Floating Tunnel under traffic loads.)

REFERENCES

1. Tan Z., Wang M., Yang X. 2001. Construction technology of undersea tunnel and the feasibility of Qiongzhou strait tunnel. *Journal of Jiaozuo Institute of Technology (Natural Science)*, 20(4):286–291.
2. Mai J., Guan B. 2003. A feasibility study on Qiongzhou Strait Submerged Floating Tunnel. *Journal of Railway Engineering Society*, 80 (4): 93–96.
3. Li B., Yang J., Xiong J. 2009. Feasibility study on rope bridge style of submerged floating tunnel in Qiongzhou Strait. *China Water Transport*, 9(10): 253–255.
4. Wu S., Chen X., Li Q., Cao G. 2016. Research on Type Selection of Submerged Floating Tunnel of Qiongzhou Strait. *Procedia Engineering*, 166: 307–316.
5. Yan H., Yang G., Yu J. 2015. The Lectotype Study on the Submerged Floating Tunnel. *Construction Technology*, 44(7): 113–116.
6. Mazzolani F. M., Landolfo R., Faggiano B., Esposto M., Perotti F., Barbella G. 2008. Structural analyses of Submerged Floating Tunnel prototype in Qiandao Lake (PR of China). *Advances in Structural Engineering*, 11(4): 923–938.

7. Panduro J. 2013. Submerged Floating Tunnel: a solution proposal for the problems of communication and development of the Baja California peninsula in the northwest of Mexico. Master Degree Thesis in Civil Engineering, National Autonomous University of Mexico, Mexico.
8. Martire G. 2010. The development of Submerged Floating Tunnels as an innovative solution for waterway crossings, PhD Thesis in Construction Engineering, University of Naples "Federico II", Tutors: Prof. F.M. Mazzolani, B. Faggiano, Italy.
9. Xiang Y., Chen Z., Yang Y. 2017. Research development of method and simulation for analyzing dynamic response of submerged floating tunnel. *China Journal of Highway and Transport*, 30(1): 69–76.
10. Zhang Z., Hu J., Liu H., Xu G. 2013. Study of the Maximum Longitudinal Gradient of Underwater Highway Tunnels. *Modern Tunneling Technology*, 50(4): 8–14.

CONTACT WITH THE AUTHOR

Bolin Jiang

e-mail: jiangbolin_stamp@163.com

Chongqing Vocational Institute of Engineering
Chongqing 402260, P.R.

College of Civil Engineering
Chongqing Jiaotong University
Chongqing 400074, P.R.

CHINA

Bo Liang

College of Civil Engineering
Chongqing Jiaotong University
Chongqing 400074, P.R.

CHINA

Shanshan Wu

Chongqing Vocational College of Public Transportation
Chongqing 402247, P.R.

CHINA

THE AUTOMATIC COLLISION AVOIDING PLAN RESEARCH OF GIVEN WAY VESSEL IN CROSSING SITUATION

Weixuan Hu, M. D.

Yixiong He, Ph. D.

School of Navigation, Wuhan University of Technology, Wuhan, Hubei, China

Logistics Institute, Wuhan Technical College of Communications, Wuhan, Hubei, China

ABSTRACT

This paper aims to the computing model of quantitative elements in crossing situation based on the separating of different states about vessel's meeting to study the automatic collision-avoiding plan of given way vessel in crossing situation. Following results are proved by simulations: The accuracy of hydrodynamic model is enough for studying and application for automatic collision-avoiding; computing model of quantitative elements by method of bisection is rapidly and reliably convergent during computing. The whole meeting process can be separated to several stages according to the quantitative elements in crossing situation. Different initial collision avoiding measures of given-way vessel in different stages produced as per rules and ordinary practice of seaman.

Keywords: Ship domain; Hydrodynamic model; Crossing situation; Quantitative element in meeting situation; Automatic collision- avoiding

INTRODUCTION

In most traditional automatic collision-avoiding studies, when an automatic collision-avoiding plan or an expert collision-avoiding system is being decided, such an automatic action plan is selected based on such factors as relative bearing and speed of the approaching vessel [1–3], and in some studies, the collision risk index, together with the automatic collision-avoiding plan, is worked out by applying missile guidance, robotic collision-avoiding principle, and so on. Due to insufficient considerations of the impacts of the approaching vessel's course and the current vessel's maneuverability on the collision-avoiding plan as well as the differences in collision-avoiding plans at different meeting stages, the automatic collision-avoiding plans deviate from the collision-avoiding rules and ordinary practice of seamen and largely limited when applied in sailing practice.

According to the connotations, extensions, and generally accepted understandings of the *International Regulations for Preventing Collisions at Sea, 1972* (hereinafter referred to as "the Rules"), as for the duration from the moment the two vessels meet each other in a crossing situation at sea to the moment a collision occurs, it can be divided into several stages [4], and

different plans should be taken by the give-way vessel at different stages. In sailing practice, pilots take geometric methods to work out and execute collision-avoiding plans based on collision-avoiding rules, ordinary practice of seamen, as well as their own knowledge, skills, experience, and so on. In this process, human beings are intelligent and able to make intelligent decisions and determine collision-avoiding plans for the specific stages according to the situations. But automatic collision avoidance needs to rely on computers, which are not intelligent, to finish the whole process, with judgments being made based on precise division of stages, only after which can the collision-avoiding plans be formulated. Therefore, all stages shall be defined strictly so as to make machine judgments possible. In the meanwhile, quantitative calculations shall be conducted on collision risk, close situation, and immediate danger in a crossing situation. According to the *Rules* and ordinary practice of seamen, this study focused on quantitative calculation models and proposed automatic collision-avoiding plans, in which MMG vessel maneuvering motion model and vessel domain theory were taken as the basis, and definitions or generally accepted understandings of collision risk, close situation, and immediate danger in crossing situations of vessels were applied.

MODELING OF AUTOMATIC COLLISION AVOIDANCE

HYPOTHESES AND DEFINITIONS

Hypothesis 1: The environment where a vessel is maneuvered is open water of a still water environment; according to features of the water, maneuverability of large vessels, and Article VIII of the *Rules*, the hypothesis of avoidance by reducing speed is not considered when the vessel is avoiding collision; no considerations are given to coordinative avoidance; position, course and speed of the approaching vessel are known;

Hypothesis 2: No considerations are given to the effects of roll, pitch, or heave;

Definition 1: Current Vessel/Approaching Vessel: give-way vessel/stand-on vessel in a crossing situation.

Definition 2: Vessel Domain and Arena: the definitions of References [5, 6] are adopted.

Definition 3: Close Situation: In such a situation, the approaching vessel will also enter the domain of the current vessel when the current vessel makes a turn by putting the rudder fully right. At a certain time or position point, the close situation generates a critical point where the current vessel makes a turn by putting the rudder fully right and the approaching vessel is tangent to the boundary of the current vessel's domain.

Definition 4: Time to Close Situation (TCS): The duration between the current moment and PCSE.

Definition 5: Collision Risk, referring to a situation under the following conditions: 1) with speed and course being kept, the approaching vessel enters in the domain of the current vessel; 2) the approaching vessel enters in the arena of the current vessel; 3) $TCS \leq 20$ minutes. Final Collision Risk refers to a risk that the two vessels will collide finally with unchanged speed and course no matter whether currently there is a collision risk or not.

Definition 6: Immediate Danger refers to the situation that the two vessels will also collide even if the current vessel makes a turn by putting the rudder fully right. Point Immediate Danger Formed (PIDF) refers to the last point before which the two vessels will avoid collision if the current vessel turns right by putting the rudder fully right. Collision refers to that the distance between the centers of gravity of the two vessels is less than half of the sum of two vessels' lengths.

Definition 7: Time to Immediate Danger (TID): The period between the current moment and the point immediate danger formed.

ANALYSIS OF VESSELS' MEETING SITUATIONS

The period from the meeting of two vessels at sea to their collision can be divided into the following stages [4]:

- 1) Free sailing stage before a collision risk forms;
- 2) Stage from the point collision risk forms to the point close situation forms;
- 3) Stage from the point close situation forms to the point immediate danger forms;
- 4) Stage from the point immediate danger forms to the occurrence of a collision.

MODELING FOR QUANTITATIVE CALCULATIONS OF ELEMENTS OF COLLISION-AVOIDING SITUATIONS

COORDINATE SYSTEM

To make calculations easy, the coordinate system shown in Fig. 1. is used in this paper:

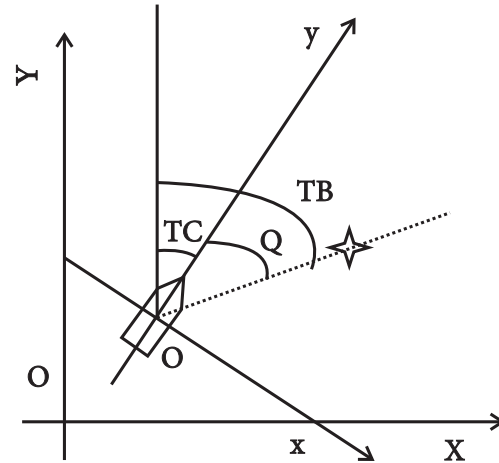


Fig. 1. Coordinate system

- 1) XOY is the earth-fixed coordinate system, where the positive Y-axis points North, and the positive X-axis points East, with right as the positive direction;
- 2) XOY is the vessel moving coordinate system, where the positive y-axis points bow, and the positive x-axis point's starboard, with right as the positive direction;

The angle between the two coordinate systems is the current vessel's course TC, which has the following relations with the object's bearing TB and the relative bearing Q:

$$TB = Q + TC \quad (1)$$

Coordinate transformation relations:

$$[X, Y] = [x, y] * \begin{bmatrix} \cos(TC) & -\sin(TC) \\ \sin(TC) & \cos(TC) \end{bmatrix} \quad (2)$$

According to the simulation process, this coordinate system, more suitable for sailing practice, has more advantages over other coordinate systems.

VESSEL DOMAIN MODEL

According to References [5–8], an off-centering circular vessel domain model is used as the vessel domain model.

The center of the circle of the vessel domain is where the virtual vessel is located, and the real vessel is on the left rear of the virtual vessel. Radius of vessel domain, offset of real vessel position from the center of vessel domain, and other parameters can be selected according to different vessel features, sailing environments, and so on. The simulation object in this paper was a 76,000 DWT full loaded bulk carrier, of which the radius R in the open water was considered as 6 times of the ship length, the off-centering direction was 199° , and the distance was 3 times of ship length.

VESSEL MOTION MODEL

Since the studies of pitch, heave and roll in the collision-avoiding process had only limited significance, studies were only performed on motions of the ship in longitudinal, transverse and yaw directions in still water. Thus MMG three-degree-of-freedom vessel motion model was adopted in this paper. Details about the meanings of symbols in the equation are described in References [9–10].

$$\begin{cases} (m + m_y)\dot{u} - (m + m_y)vr = y_H + y_P + y_R + y_F \\ (m + m_x)\dot{v} - (m + m_x)ur = x_H + x_P + x_R + x_F \\ (I_{ZZ} + J_{ZZ})\dot{r} = N_H + N_R + N_F \end{cases} \quad (3)$$

Through transformation and processing of the above equation of motion, eventually forces, moments, accelerations, angular accelerations, velocities, and angular velocities were expressed as functions of time t . Vessel coordinates were calculated based on the above model, with Runge-Kutta method being adopted.

QUANTITATIVE CALCULATION MODEL FOR COLLISION-AVOIDING ELEMENTS

QUANTITATIVE CALCULATION OF PCSF

Suppose the distance from another ship to the boundary in the direction of the vessel domain center is Dis at the moment t when the current situation begins; the time of putting the rudder fully right is t_m ; and thus, Dis is a function of the two variables of t and t_m . To find the solution of PCSF is to find $t_m = t_m^0$ satisfactory to the conditions that: when the vessel starts to sail at initial speed and on initial course from the current moment, the vessel is kept putting the rudder fully right to make a turn, and the approaching vessel is tangent to the domain of the current vessel. Thus, it is to find the solution of $t_m = t_m^0$:

$$\min \left(\frac{Dis}{t_m = t_m^0} \right) = \min (f(t, t_m^0)) = 0 \quad (4)$$

Specific expression of the function $Dis=f(t, t_m)$

$$\begin{cases} Dis^t = \left\| (X_0^t - X_R^t)^2 + (Y_0^t - Y_R^t)^2 \right\|^{0.5} - R \\ X_0^t = x_0^t + 0.25R_{\text{lingyu}} \cdot \sin(TC_0^t + 19) \\ Y_0^t = y_0^t + 0.25R_{\text{lingyu}} \cdot \sin(TC_0^t + 19) \end{cases} \quad (5)$$

(X_R^t, Y_R^t) is determined by the following equation:

$$(X_R^t, Y_R^t) = (X_R^0, Y_R^0) + (\sin(TC_R), \cos(TC_R)) * t * v_R \quad (6)$$

If $t \leq t_m$, then:

$$(x_0^t, y_0^t) = (x_0^0, y_0^0) + (\sin(TC_0), \cos(TC_0)) * t * v_0 \quad (7)$$

If $t > t_m$, then:

Taking $(x_0^{t_m}, y_0^{t_m})$ as the initial condition, as the time, and rudder angle as 35° , (x_0^t, y_0^t) is calculated as per according to equation (3). R is the radius of the vessel domain circle.

Superscript t represents the moment t ; subscript 0 represents the current vessel, and R represents the approaching vessel; v represents the speed, and TC represents the course; (x, y) and (X_R, Y_R) are the center of the current vessel's domain and the position of the approaching vessel.

Judging from the physical significance of the problem, $Dis=f(t, t_m)$ has the following attributes:

- 1) When $\exists t_1 > 0, t_2 > 0, t_m \in [t_m^0 - t_1, t_m^0 + t_2]$, $\min (f(t, t_m))$ decreases monotonically;
- 2) If the approaching vessel is far away and it will eventually enter in the domain of the current vessel if not steered, therefore $\min (f(t, 0)) > 0, \min (f(t, TCPA)) < 0$;
- 3) $\min (f(t, t_m^0)) = 0$ has just one solution in $t_m^0 \in [0, TCPA]$ therefore, bisection method can be used to find the solution of t_m^0 . The specific method is shown in the simulation calculation process.

QUANTITATIVE CALCULATION OF PIDF

Same as PCSF, a mathematical model was built for PIDF, with the vessel domain being changed into a circular area centered on the current vessel's center of gravity, with the radius being half of the sum of the two vessels' lengths.

COLLISION RISK

For judging whether there will be a final collision risk or not, the criterion is to see whether the approaching vessel will enter in the domain of the approaching vessel or not. Thus, with course and speed being kept, the conclusion can be reached based on the distance from the approaching vessel to the boundary of the vessel domain in the direction of the vessel domain center at different moments, namely, $Dis=f(t)=D(t)-R$, in which $D(t)$ represents the distance from the vessel domain center to the approaching vessel at moment t . If its minimum value: $\min (f(t)) \leq 0$, it means that at some moment, the approaching vessel enters the vessel domain and there will be a final collision risk; if $TCS \leq 20$ min and the approaching vessel is in the arena of the current vessel, a collision risk forms; if $\min (f(t)) \geq 0$, and the approaching vessel does not enter the domain of the current vessel, there will be no final collision risk.

COLLISION-AVOIDING PLANS OF THE GIVE-WAY VESSEL IN A CROSSING SITUATION

According to the time points determined based on element definitions and numerical solutions in a crossing situation, the crossing situation was divided into different stages, and the corresponding avoiding measures to be taken were analyzed as follow.

If there is no final collision risk, no plan needs to be executed. Otherwise,

- (a) Stage 1, a collision risk has not formed. An early avoiding plan can be executed freely (leftward or rightward).
- (b) Stage 2, a collision risk has formed but a close situation has not formed. Making a right turn can ensure the vessels pass

by each other at a safe distance, and therefore, according to the responsibility clauses and the generally accepted understandings about actions deviating from the *Rules*: if taking an action as per the *Rules* can avoid an immediate danger, the *Rules* shall be followed, and the procedures shall specify that the ship shall make a right turn.

- (c) Stage 3, a close situation has formed, an imminent danger has not formed, and a sharp turn to the right cannot ensure the vessels pass by each other at a safe distance. According to the responsibility clauses, both vessels shall deviate from the *Rules* so as to avoid the immediate danger, if necessary. According to the Collision-avoiding Rule 17, Action by Stand-on Vessel, when a stand-on vessel take actions alone, it shall avoid turning left when meeting a vessel on its own port side: if it can pass by the other vessel at a safe distance when turning left, it shall deviate from the rule and turn left to the largest extent and even turn round so that the collision can be avoided; if turning left cannot make it pass by the other at a safe distance either, the direction of avoidance shall be decided through comparison between the shortest distances from it to the approaching vessel in the cases of left and right full rudders.
- (d) Stage 4, an imminent danger has formed, at which stage, the action most helpful in avoiding the collision shall be taken, and meanwhile, whether the vessel makes a turn to the starboard side or the port side should be determined based on the shortest distances in the two collision avoidance cases of turning right and left respectively.

SIMULATION CALCULATION

SIMULATION DIGITAL VESSEL MODEL DESIGN

With the vessel in Section 2.2 as the simulation object, MATLAB programming was used to check the precision of the digital model. Comparison was made among full rudder maneuverings at different rotational speeds and at full speed respectively (as shown in Tab. 1.). According to the results, the vessel speed performance and maneuverability of the digital vessel model could be very close to those of a real vessel by adjusting different factors.

Tab. 1. Speed compare of MMG model and ship

Rotational Speed (rpm)	77.7	84.9	92.2	99.8
Speed (Kn)				
Hydrodynamic model	10.7	12.0	13.2	14.3
Real vessel (vessel model)	11.0	12.0	13.0	14.0

DESIGN OF SIMULATION PROCEDURES

Digital simulation was conducted with the vessel in Section 2.2 as the simulation object. Initial conditions: target vessel: relative bearing: 045°, distance: 5.6 nautical miles, speed: 12 kn, and course: 270°; current vessel: initial speed: 12 kn, and course: 000°. Output results: a close situation formed at 5513 m / 919 s. Immediate danger formed at 1097 s / 6584 m.

PROCEDURES OF JUDGING THE STAGES OF THE GIVE-WAY VESSEL IN A CROSSING SITUATION

In this paper, with translation of central arena being done according to Reference [6], the radius was 2.7 nautical miles, offset of the center was 1.9 nautical miles, and the bearing was a relative bearing of 199°. Under the conditions that for the target vessel, the relative bearing was 045°, the distance was 5.656 nautical miles, speed was 6m/s, and course was 270°, and for the current vessel, the initial speed was 6m/s and the course was 000°, a simulation was conducted, and the calculation results were output as follows:

- 1) TCS<20 min;
- 2) DCPA=0, TCPA=1234.7s;
- 3) there would be a final collision risk;
- 4) when TRC=644, and DRC=3864, the approaching vessel entered the arena;
- 5) the approaching vessel was outside the arena and there would not be a collision risk for now.

CONCLUSIONS

According to the simulation results, the mathematical model used in this study was reliable, and the algorithm would converge fast and reliably when a small value (5m) was taken by using the bisection method; the precision met the requirement of automatic collision-avoiding studies and sailing practice of vessels. The study results provided collision avoidance plans for different stages of the give-way vessel in a crossing situation. A complex sailing model, which was a combination of this model and the steering model, could develop possible collision-avoiding plans specific to different time points, optimize all plans, and eventually determine the optimal automatic collision-avoiding plans suitable for collision-avoiding rules and ordinary practice of seamen.

ACKNOWLEDGEMENTS

This project is partially supported by Natural Science Foundation of China “Research on Mechanism of Ship-Entropy Catastrophe Response to Seafarer-Ship-Environment Misadjust” (51379170), Research and Innovation Team of WTCC (CX2018A04).

REFERENCES

1. Zhongyi Zheng. *Research on automatic collision avoidance decision-making system of ships* [D], Dalian maritime university, 2000.
2. *The discuss on automatic collision avoiding decision for Muti-ships* [J]. Journal of NANTONG VOCATIONAL & TECHNICAL SHIPPING COLLEGE, Vol 4, No 3, Feb. 2005, pp. 52–53, 81.
3. Ming-Cheng Tsou. Chao-Kuang Hsueh, THE STUDY OF SHIP COLLISION AVOIDANCE [J]. Journal of Marine Science and Technology, Vol. 18, No. 5, pp. 746–756, 2010.
4. A.N. cockcroft, J.N.F. la major. *Guidelines for the rules of navigation*. Fourth edition [M]. Dalian: Dalian maritime institute press. 1992.132-134.
5. Goodwin, E. M. *A statistical study of ship domains*. [J]. Journal of Navigation, 28, 328, 1971.
6. DAVIS P V, DOVE M J, STOCKEL C T. *A computer simulation of marine traffic using domains and arenas* [J]. Journal of Navigation, 1980, 33: 215-222.
7. QI Le, ZHENG Zhongyi, Li Gouping. *AIS-data based ship domain of ships in sight of one another*. [J]. Journal of Dalian Maritime University Vol 37, No 1, Feb. 2011, pp. 48–50
8. R. Szlapczynski, *Solving Multi-Ship Encounter Situations by Evolutionary Sets of Cooperating Trajectories* [J]. TRANSSNAV, Volume 4, Number 2, 2010.
9. Li Wenkui, Chen Yongbing, Tian Weifeng et al. *Real-time simulation of ship motion control based on MATLAB* [J]. Journal of system simulation, volume 19, 19, October, 2007.4424-4427, 4433.
10. Y. Yavin, C, Frangos. *Computation of Feasible Control Trajectories for the Navigation of a ship around an Obstacle in the Presence of a Sea Current* [J]. Mathl. Comput. Modelling Vol. 21, No 3, 1995, pp. 99–117.

CONTACT WITH THE AUTHOR

Yixiong He, Ph. D.

e-mail: 584202921@qq.com

tel: 13163294652

School of Navigation

Wuhan University of Technology

Wuhan, Hubei, China 430063

Logistics Institute

Wuhan Technical College of Communications

Wuhan, Hubei

CHINA

EXPERIMENTAL STUDY OF THE AERODYNAMICS OF SAIL IN NATURAL WIND

Zeng Xiangming, Associate Professor

Zhang Huawu, Lecturer

Merchant Marine College, Shanghai Maritime University, Shanghai, China

ABSTRACT

In order to evaluate the impacts of a motor vessel after installing wind sails, the aerodynamics of the sail should be accurately calculated. However most of the research on sails are based on stable wind instead of natural wind which is changing horizontally and vertically. In this paper wind tunnel tests are carried out based on stable wind field and simulated natural wind field, the results shown that there are 16–44% decrease in natural wind in terms of lifting coefficient and 11–42% decrease for drag coefficient. This would provide a valuable reference to the effectiveness evaluation of the impact of sails for sail assisted ships.

Keywords: Natural wind, Wind sail; Aerodynamics; Sail assisted ship

INTRODUCTION

With the rising of oil price and the enter into force of IMO (International Maritime Organization) regulations on Green House Gas emission control, sail assisted shipping technology once again becomes a hot topic of shipping researches. Undoubtedly sails could be used as ship propulsion source to reduce the fuel consumption of engine, however, modern motor ship has tremendous differences compared with traditional sail ship in terms of structure and propulsion system. For sail assisted motor ship, sail is just an auxiliary propulsion plant, the working principle of wind sail is also different with pure sail ship because sails on motor ships are mainly working under transverse wind similar to aerofoil [1]. It makes the aerodynamic characteristics of the sail crucial to the efficiency of propulsion, i.e. to provide as much as possible thrust force and at the same time reduce the transverse force to limit the adversely impact to the ship stability and maneuvering.

By literatures [2, 3, 4, 5, 6], researches of sail for motor ships in recent years mainly focus on sail model selection and the interaction between sail and ship, including design, optimization

of model and aerodynamic analysis of sails of different structures and materials, routing plan and economic performance forecast, computation analysis of sail structure strength and its influences on ship stability, and interaction between sail and ship and between sails. The core of all these researches is to develop an accurate recognition of sail's aerodynamic performance. That is to say, if sail's stress situation is unclear, subsequent study of structure, stability, controllability and economic benefit is nothing but a false proposition.

Sail aerodynamic performance is an important basis for selection of sail model. Good sail type can make a sail of the same size generate higher ship thrust. During initial researches, Japanese scholars M. Ueno proposed a soft-hard-combined compound sail design, which is proven able to reach a thrust coefficient of 2.46 by wind tunnel experiment researches [7]. Fujiwara T. did the research of square soft sail's aerodynamic performance by both CFD and wind tunnel test[8]. Ouchi K. carried out research of optimization of sail type, and proposed that hard sail has the aerodynamic performance better than that of soft sails and will be the direction of development in the future [9]. French scholar Armand J. L. carried out wind tunnel experiment of 3100-ton product oil tanker with sail by the 1/50

proportion of reduction to research the ship model's aerodynamic performance, and proposed an initial scheme for adoption of sail for sail assistance in modern commercial ship [10]. Spanish scholar Guerri O. used numerical simulation model to CFD simulation research of the turbulence of elliptic sail [11]. British scholar Burden A. proposed a design concept of feeder container vessel with sail assistance, which has the sail system able to save energy by 6% at the 15-knot sailing speed [12].

However, in terms of literatures, current simulation researches of sail's aerodynamic performance are all based on the premise of stable wind field. Previous sail test researches were basically executed in low-speed wind tunnel with even wind speed and stable wind direction and did not simulate the influence of wind field change on sail stress situations under natural wind state [7, 8, 9, 10, 11]. However, actual sail working environment is natural wind field, the wind speed is fluctuating, and can be classified into stable average wind speed and fluctuating wind speed with characteristics of zero-mean stationary random process. In addition, in order to obtain higher thrust, sails of ships are always designed to be very large. For example, in the research of design of sail-assistance feeder container vessel by British University of Southampton, the sail had the width and height of 26.5 m and 25 m as an upright structures [12]. In natural wind environment, as surface boundary layer exists, wind speed in vertical direction often presents logarithmic or exponential distribution, namely wind speed will decrease strikingly with the fall of the height. Therefore, in actual sailing, the wind speed and direction on sail is under the action of wind force changing in the horizontal direction, but also the change of wind force in vertical direction, which will surely make great influence on sail stress. For this reason, to accurately understand stress situation of sail in actual use, aerodynamic performance of sail in natural wind environment must be studied.

This paper, on the basis of initial researches of the sail assistance research group of Shanghai Maritime University, explored natural wind simulation researches and carried out aerodynamic performance test of the elliptic aerofoil sail designed by the research group under natural wind state.

NATURAL WIND SIMULATION

Simulation experiment of natural wind is generally realized through boundary layer wind tunnel. By wind tunnel design characteristics, the experiment method could be divided into natural simulation and artificial simulation [13]. The natural simulation method relies on extension of the test section of common wind tunnel to let wind form certain turbulence and wind profile in the test section, thus to simulate characteristics of natural wind. This method is not used generally, because it needs changing of wind tunnel structure. The artificial intervention can be carried out through passive simulation or active simulation [14]. The passive simulation mainly features adding some components generating turbulence before the test section of wind tunnel, such as baffle and spire, so as to generate the wind field characteristics similar to atmospheric boundary layer. As shown in Fig. 1., in wind tunnel, plate-type

grilles are mounted with different intervals [15]. By adjusting grille distance distribution and plate-type scale, different atmospheric boundary layer characteristics can be simulated. This method is commonly used in early atmospheric boundary layer simulation wind tunnel.

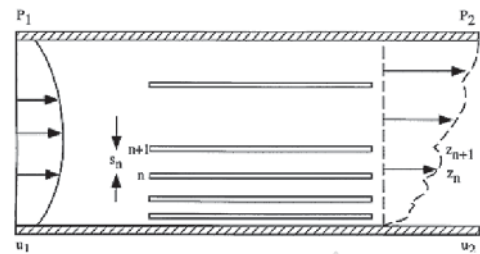


Fig. 1. Boundary Layer Wind Tunnel with Plate-type Grille

Relatively recent atmospheric boundary layer wind tunnels mostly use spires and roughness elements to simulate wind field characteristics of atmospheric boundary layer [16]. As shown in Fig. 2., spires were arranged in wind tunnel in a row, to make turbulence in wind tunnel. Meanwhile, with the structure as shown in Fig. 3., the spires can form wind profile. In addition, according to actual situations of the scene to be simulated in the experiment, some rectangular blocks can be arranged at the bottom of the wind tunnel, to increase surface roughness.

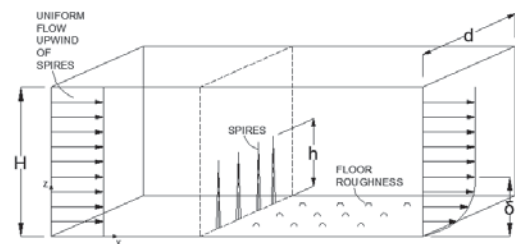


Fig. 2. Boundary Layer Wind Tunnel with Spire and Roughness Element

Active simulation method features adding jet or deformed spire block in wind tunnel, tests the flow field wind speed spectrum in the test section to control the additional incoming flow energy provided by jet or multiple fans or change shape of spire blocks, for example, letting spire be able to vibrate under computer control, to generate experiment-needed turbulence and realize accurate simulation of wind field characteristics. For example, University of Miyazaki's multi-fan wind tunnel adopts 11 conversion-controlled small fans, and relies on adjustment of the rotating speed of every fan to generate the wind simulating characteristics of atmospheric boundary layer wind field. In the test section, the hot-wire anemometer collects the wind speed spectrum of downstream wind field as the feedback information for control system and finally obtain the wind field needed for test [17]. Active simulation method is characterized by high requirements for wind tunnel hardware and control and high initial investment. Therefore, it is rarely used in actual application.

In order to understand the difference of stress situation of sail between natural wind environment and stable wind field, this paper, on the basis of initial research by the sail assistance

research group of Shanghai Maritime University, modified the University's low-speed revolution wind tunnel with the size and performance as follows:

- Test section size: 6 m (L) × 1.4 m (W) × 2 m (D)
- Area covered by the wind tunnel: L × W=22 m × 7.08 m
- Wind tunnel use: research of sailing ship, particularly sail stress
- Design wind speed: 1~40 m/s
- Factory building space: W 12 m × D 7.7 m × L 24 m
- The air-flow pressure in the wind tunnel is 1 bar and operates under normal pressure.
- Wind speed adjustment range and control accuracy
- 1.0~25 m/s, measurement accuracy: (error < 0.1%)

In this test, two spires as shown in Fig. 3. are added before the wind tunnel test section to increase test section turbulence and form wind speed profile. To test the aerodynamics of ship sails, we should simulated wind field on the sea, which is based the landforms with the lowest surface roughness. Therefore, roughness element is not used to increase roughness. Spire size is as shown in Fig. 3., and the front view shows the windward side of spire. The spire has a base 250 mm wide and 1800 mm high. The bottom supporting board behind the spire is trapezoidal, and the trapezoidal bottom's length of side is 318 mm. In order to better support spires, an adjustable carrier role is designed at the top of spires, to firmly fasten spires and take advantages of some inclination and rely on wind tunnel body to clamp spires firmly.

Before experiment execution, test spire firmness, which should be able to bear at least 30 m/s wind speed and satisfy the whole range of wind speed needed in this experiment. Spires are erected in the following manner: Spires are erected at the entrance to the experimental section of wind tunnel. In order not to influence normal wind speed control and adjustment of wind tunnel, spires are arranged behind the entrance wind tunnel hot-wire anemometer, with two spires erected at the place 30 cm from wind tunnel side, by the interval of 30 cm. Experimental spires are erected as shown in Fig. 4.

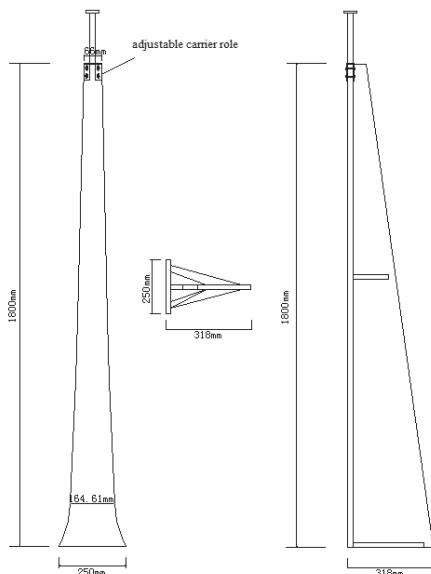


Fig. 3. Spire shape and size



Fig. 4. Real picture of spire erection

Tab. 1. Turbulivity Distribution at Different Wind Speeds before and after Modification

Wind speed		15 m/s	20 m/s	25 m/s
Turbulivity at the Height of 40 cm	Original	2.42	2.56	1.49
	Modified	27.68	27.39	27.39
Turbulivity at the Height of 50 cm	Original	1.49	0.93	0.76
	Modified	24.41	24.92	23.84
Turbulivity at the Height of 60 cm	Original	0.83	1.09	2.57
	Modified	22.05	20.31	20.31
Turbulivity at the Height of 70 cm	Original	1.53	0.58	1.74
	Modified	21.18	19.65	19.41
Turbulivity at the Height of 80 cm	Original	3.36	3.63	2.32
	Modified	18.16	19.75	18.16

Before and after modification, hot-wire anemometer was used to measure wind speed at all points on the 60 cm plane ahead of the test component. The comparison of turbulivity and standard variance at different wind speeds before and after modification is shown as in Tab. 1. and Tab. 2. The data indicate that before modification, the wind field in the wind tunnel had a very good evenness, low turbulivity and very low wind speed average variance. After the spires are added, the turbulivity in the wind tunnel increase by more than 10 times, and the average variance also increased by nearly 10 times, indicating that after modification, the flow field in the wind tunnel was no longer even and developed the fluctuating characteristics similar to natural wind.

Tab. 2. Wind speed Standard Variance Distribution at Different Wind Speeds before and after Modification

Wind speed		15 m/s	20 m/s	25 m/s
Turbulivity at the Height of 40 cm	Original	0.39	0.54	0.39
	Modified	3.73	4.88	5.95
Turbulivity at the Height of 50 cm	Original	0.22	0.19	0.19
	Modified	3.57	4.84	5.83
Turbulivity at the Height of 60 cm	Original	0.13	0.23	0.68
	Modified	3.48	5.34	5.34
Turbulivity at the Height of 70 cm	Original	0.23	0.12	0.45
	Modified	3.47	4.3	5.29
Turbulivity at the Height of 80 cm	Original	0.52	0.8	0.62
	Modified	5.29	4.61	5.29

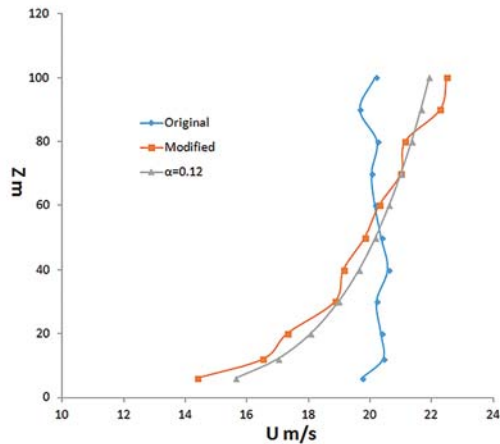


Fig. 5. Comparison of wind speed at Different Height

In vertical direction, Fig. 6. shows the speed distribution before and after modification within the testing height which is 6–100 cm as the height of model is only 62 cm in this experiment. Under the setting speed of 20 m/s, the original wind speed in the wind tunnel test section is closely constant in vertical direction. After modification, due to influence of spire shape, wind speed presented fundamental change at the testing height, very close to the wind profile curve with the index of $\alpha=0.12$ if the height of atmospheric boundary layer is set at 300 m and the scale is 1:100, just enough conforming to the surface distribution law of natural wind on the sea [18].

Tab. 3 shows the mean speed distribution at different transverse positions, namely at different positions 40 cm vertically from the wind tunnel's longitudinal centre line. It is clearly indicated that in the area nearest to sail model, the change of wind speed in transverse distribution was not obvious, which also conforms to the characteristics in maritime natural wind field.

Tab. 3. Wind speed at different transverse positions

Distance to the centre line		0 cm	15 cm	30 cm	50 cm
Set Speed 15 m/s	Original	15.14	15.82	16.12	15.14
	Modified	14.79	15.57	15.14	14.79
Set Speed 20 m/s	Original	20.53	20.64	20.44	20.53
	Modified	20.26	19.84	20.54	20.26
Set Speed 25 m/s	Original	25.13	26.27	25.92	25.13
	Modified	25.55	25.13	24.74	25.55

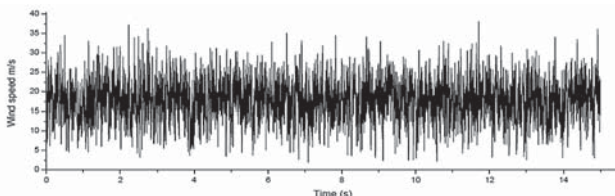


Fig. 6. Curve of the Wind Speed actually Measured in the Wind Tunnel

In order to understand the process of transient change of wind speed, the test adopted measurement of 1000 Hz sampling frequency, to record wind speed change at all points in the wind tunnel with hot wire anemoscope. The wind speed time-interval curve is as shown in Fig. 6. The measurement points were at

the centre line of the test section of the wind tunnel, 40 cm away from the ground and 60 cm away from the test piece. The wind speed power spectrum analysis is shown in Fig. 7 and it indicated that measured wind speed power spectrum is similar with Davenport spectrum [19].

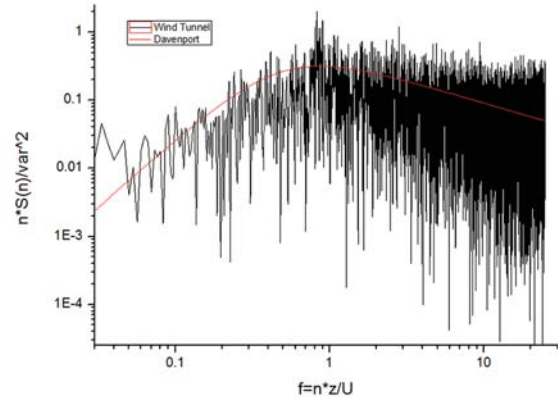


Fig. 7. Wind speed spectrum comparison

WIND TUNNEL TEST

In order to check influences of fluctuating wind field on sail's aerodynamic performance, this paper, on the basis of initial researches by the research group, carried out contrast test of aerodynamic performance in stable wind field and fluctuating wind field of elliptic arc Type D sail model [20]. The testing sail model's geometric size is as shown in Tab. 4. and the sail model is as shown in Fig. 8.

Tab. 4. Geometric Size of Sail Model

Type	Chord	Mast height	Sail height	Max. thickness	Max. camber
Ellipse Arc Wing Sail	36 cm	10 cm	52 cm	4.3 cm	7.2 cm



Fig. 8. Sail model in the wind tunnel

During the test, the wind speed is set at 20 m/s, and the aerodynamic load on the model consists of the forces and moment components decomposed from the wind axis coordinate system. Wind attacking angle α is the included angle between wind speed vector and sail plane direction as shown in Fig. 9.

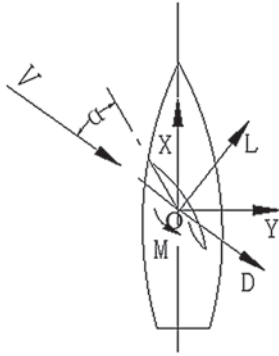


Fig. 9. Wind tunnel test stress coordinate system

Directions of the testing wind and the stress are as shown in Fig. 9, and the wind axis coordinate system is a right angle coordinate system O-LDZ, with the origin O at the center of the model baseboard and Axis Z upward vertically. According to the aerofoil theory, under action of the wind speed with the incoming flow attack angle of α , sail's aerodynamic force is disintegrated into Lifting Force F_l and Drag force F_d as two components, which are expressed as follows with Aerodynamic Coefficient C_L and C_D , respectively:

Lift coefficient

$$C_L = \frac{L}{\frac{1}{2}\rho S V^2} \quad (1)$$

Drag coefficient

$$C_D = \frac{D}{\frac{1}{2}\rho S V^2} \quad (2)$$

ρ — air density;

S — area of the sail;

V — wind speed.

Though testing, lift coefficient and drag coefficient of the same sail under stable wind field and fluctuating wind field conditions are as shown in Fig. 10. As the wind speed in fluctuating wind field had a high fluctuation, there was certain fluctuation in the lifting force and drag force through the testing. The Table shows the means on the basis of 5000-times automatically acquired data in 60 seconds. The wind speed used in formula 1 and 2 are measured at the height of 40 cm on the center line of the wind tunnel and in 60 cm plane before the model.

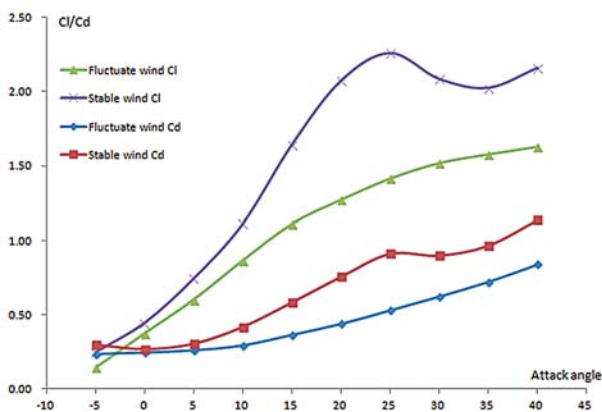


Fig. 10. Lift coefficient and the drag coefficient under stable and fluctuating wind field

As shown in Fig.10 and Tab. 5, there is 16–44% decrease of lift coefficient and 11–42% decrease of drag coefficient of the sail model measured in fluctuating wind field compared with that of stable wind field. The reasons for this phenomena may be of two aspects: on the one hand, with existence of wind profile, fluctuating wind field generally show a wind speed in vertical direction lower than that in stable wind field, so as to reduce sail stress. On the other hand, with existence of massive turbulence and vortex in fluctuating wind field, the distribution of randomly-distributed vortex in sail pressure field will cause loss of some energy and finally leading to decrease of sail stress.

Tab. 5. Comparison of Lift coefficient and the drag coefficient under stable and fluctuating wind field

Attack angle α	Stable wind		Fluctuating wind		Comparison	
	Cl	Cd	Cl	Cd	Cl	Cd
-5°	0.25	0.3	0.14	0.23	44%	23%
0°	0.45	0.27	0.38	0.24	16%	11%
5°	0.75	0.3	0.6	0.26	20%	13%
10°	1.11	0.42	0.87	0.29	22%	31%
15°	1.64	0.58	1.11	0.36	32%	38%
20°	2.07	0.76	1.27	0.44	39%	42%
25°	2.26	0.91	1.41	0.53	38%	42%
30°	2.09	0.9	1.52	0.62	27%	31%
35°	2.03	0.97	1.57	0.72	23%	26%
40°	2.16	1.14	1.63	0.84	25%	26%

CONCLUSIONS

Previous researches of sail's aerodynamic characteristics were carried out in stable wind field, while the real sail is working under natural wind field. By modification of the wind tunnel with stable wind field, this paper simulated the wind field in line with characteristics of natural wind on the sea, and carried out comparison test of sail model's aerodynamic characteristics in two conditions. The results show that in fluctuating wind field, both lift coefficient and drag coefficient of the sail model presented significant falling, which also indicates that to more accurately analyze ship sail's aerodynamic characteristics, natural wind speed fluctuation and wind profile in the atmospheric boundary layer cannot be neglected.

REFERENCES

1. Wang H M, Sun P T, Huang L Z, et al.: *The Analysis of Sail-assisted Ship Based on Aerofoil Theory*. Ship Engineering, Vol. 33(3), pp. 34–37, 2011.
2. Yi-Huai, H. U., Song-Yue, L. I., & Zeng, X. M.: *Study of airfoil sail's aerodynamic characteristics*. Ship Engineering, Vol. 33(4), pp. 20–24, 2011.

3. He, J., Hu, Y., Tang, J. J., & Xue, S.: *Research on sail aerodynamics performance and sail-assisted ship stability*. Journal of Wind Engineering & Industrial Aerodynamics, Vol. 146, pp. 81–89, 2015.
4. Fujiwara, T., Hearn, G. E., Kitamura, F., Ueno, M., & Minami, Y.: *Steady sailing performance of a hybrid-sail assisted bulk carrier*. Journal of Marine Science & Technology, Vol. 10(3), pp. 131–146, 2005.
5. Yang, X., & Li, X. S.: *Analysis and design on course control for sail-assisted ship*. Advanced Materials Research, Vol. 1008–1009, pp. 556–561, 2014.
6. Liu, Y.-F & Huang, L.-Z & Li, Y.-K & Fu, C.: *Analysis on available wind power resources around typical routes of sail-assisted ship*. Journal of Dalian Maritime University Vol. 42, pp. 51–56, 2016.
7. M. Ueno et al.: *Fundamental research for development of an advanced sail-assisted ship*. OCEANS MTTTS/IEEE TECHNO-OCEAN 04, Vol. 2, pp. 1102–1109, 2004.
8. Fujiwara T, Hirata K, Ueno M, et al.: *On Aerodynamic Characteristics of a Hybrid-Sail with Square Soft Sail*. Journal of Marine Science & Technology, 2003.
9. Burden A, Hearn G E, Lloyd T, et al.: *Concept design of a fast sail assisted feeder container ship*. Naval Architecture Shipbuilding, Marine Engineering, 2010.
10. Armand J L, Marol P.: *Aerodynamics of Sail-Assisted Propulsion of Commercial Ships: A Preliminary Study*. British Maritime Technology, 1982.
11. Ouchi K, Uzawa K, Kanai A.: *Huge hard wing sails for the propulsion of next generation sailing vessel*. Second International Symposium on Marine Propulsion. 2011.
12. Guerri O, Liberge E, Hamdouni A.: *Numerical Simulation of the Turbulent Flow around an Oval-Sail*. Journal of Applied Fluid Mechanics, Vol. 9(4), 2016.
13. Shui, L. M., Hua, W. W., & Xin, C.: *Boundary layer simulation in the first test section of 8m×6m wind tunnel*. Experiments & Measurements in Fluid Mechanics, Vol. 16(2), pp. 63–66, 2002.
14. Peng, H.: *Research of passive simulation method of atmospheric boundary layer in tj-2 wind tunnel*. Journal of Tongji University, Vol. 27, pp. 136–145, 1999.
15. Owen, P. R, & Zienkiewicz, H. K.: *The production of uniform shear flow in a wind tunnel*. Journal of Fluid Mechanics, Vol. 2(6), pp. 521–531, 1957.
16. Irwin H P A H.: *The design of spires for wind simulation*. Journal of Wind Engineering & Industrial Aerodynamics, Vol. 7(3), pp. 361–366, 1981.
17. Matsuda, Y., Nishi, A., Hirano, K., Ozono, S., Miyagi, H., & Cao, S., et al.: *Control of turbulence in a multiple-fan wind tunnel part5, reproduction of spatial strutures in an atmospheric boundary layer*. Journal of Wind Engineering. Vol. 83(2), pp. 189–196, 2000.
18. Mason, P.: *Atmospheric boundary layer flows: their structure and measurement*. Boundary-Layer Meteorology, Vol. 72 (1–2), pp. 213–214, 1995.
19. Davenport, A. G.: *The spectrum of horizontal gustiness near the ground in high winds*. Quarterly Journal of the Royal Meteorological Society, Vol. 87 (372), pp. 197–198, 1961.
20. Hu, Yihuai; Zeng, Xiangming; Li, Songyue.: *Research on the aerodynamic characteristics of ellipse wing sail*. Advanced Materials Research, Vol. 347–353, pp. 2249–2254, 2012.

CONTACT WITH THE AUTHOR

Zeng Xiangming

e-mail: xmzeng@shmtu.edu.cn

tel: 0086-21-38282979

Shanghai Maritime University
Shanghai 201306

CHINA

THE INFLUENCE OF SHIP ROLLING MOTION ON TAKE-OFF AERODYNAMIC CHARACTERISTICS OF AIRCRAFT

He Zheng¹, Ph. D.

Sun Xiao-yu^{1*}, Ph. D.

Gu Xuan^{1*}, Ph. D.

¹College of Aerospace and Civil Engineering, Harbin Engineering University, Harbin 150001 China

ABSTRACT

Ship motion is an important factor affecting on the safety of ski-jump take-off. The simplified frigate ship SFS1 was numerically simulated, and the results were compared with the experimental data, the feasibility of the calculation method was verified; Meshless method and WALE turbulence model were used to simulate the process of aircraft ski-jump take-off, aerodynamic characteristics under different rolling conditions during the aircraft ski-jump take-off process were presented. The results showed that: the influence of ship rolling motion on lift coefficient, drag coefficient and pitching moment was small, side force and rolling moment were greatly affected by rolling motion; the region of downwash with the maximum speed was about 10 m from the bow; the safety of ski-jump take-off was greatly affected when aircraft was close to the bow within 20 m.

Keywords: Ship rolling motion; Ski-jump take-off; Meshless method; WALE turbulence model; Aerodynamic characteristics

INTRODUCTION

Ski-jump take-off is one of the most important methods of aircraft take-off. Because of the limited ship size, the six degree of freedom motion of the ship and the upwash flow near the bow, taking off on ship is more complex than taking off on land, the security of ski-jump take-off has attracted increasing attention [1, 2]. While researching, not only the aerodynamic characteristics of the aircraft at different wind directions, wind speeds, the speed of departure and the angle of attack should be considered, the effects of ship rolling, pitching and heaving are also considered [3]. Hong W. H. established various forms of superstructure and changed the vertical layout of the superstructure, numerical simulations were respectively carried out, the flow field is analyzed and observed, and the characteristics of the flow field were compared [4]. Wang W. J. aimed at the characteristics of the aircraft taking off on the skid deck, the fitting relationship between the performance and quality of the aircraft and deck parameters was analyzed based on the changing process of the force polygon and the effect of the deck shape on the pitching rotation, the mechanical

mechanism of the aircraft establishing the angle of attack in the early departure at low speed was presented [5]. Liu W. W. established a general mathematical model of aircraft take-off based on tensor [6]. Wang M. H. and Zhao B. described the different methods of aircraft take-off and landing process, some key factors in the take-off and landing process are presented [7]. The take-off speed and the landing speed were estimated and analyzed based on the characteristics of the aircraft by Chen B. and Ang H. S. [8]. Gregory Imhof and William Schork discussed the influence of the skid deck curve on the take-off of the aircraft, and the optimization is carried out [9]. P. Shrikant Rao and Amitabh Saraf proposed a method for analyzing the performance of ski-jump take-off, some flight parameters were optimized and a set of feedback control system is designed [10]. The distribution of airflow around the warship was studied by Gao Y. and Xie H. S. [11]. The difference of the airflow distribution in different conditions was obtained, the influence during the course of the aircraft ramp ski-jump take-off on the airflow distribution on the deck was also considered. The result showed that the airflow distribution around the warship was considerably complicated and the influence on the air dynamic characteristics for the aircraft take-off can't be

neglected [12]. The sideslip wind would greatly enhance the airflow's turbulent intensity on the deck. Bi Y. Q. and Sun W. S. established a mathematical model of aircraft take-off and carried out a numerical simulation for a certain fighter aircraft [13]. The effect of take-off mass, take-off angle of attack, deck wind, take-off distance and other factors on the performance of the ski-jump take-off was quantitatively analyzed. Xiao H. introduced the principle and motility characteristics of the ski jump take-off, the mathematical model of ski jump take-off was given [14]. Take-off performance of aircraft under different configurations was simulated, the influence of take-off distance, take-off weight and flight trim on the ski jump take-off performance was analyzed. Gao Y. used dynamic mesh technology and the Spalart-Allmaras turbulence model to simulate aircraft ski-jump take-off from a ramp deck [15]. Aerodynamic characteristics during the aircraft ski-jump take-off process were analyzed under many different conditions. The result shows that improvements in the take-off aerodynamic characteristics for aircraft require taking off at an optimal airspeed. Bai S. G. established the six degrees of freedom model of aircraft in the condition of static balance, with the influences of carrier movement, deck wind and the airflow interference on aircraft considered [16, 17]. The static balance of aircraft in different situations was simulated, and the motion law of aircraft under different conditions was analyzed.

Overall, the research of aircraft ski-jump take-off is mainly focused on the following aspects: ramp deck curvature optimization, take-off decision, the analysis of aircraft motion characteristics, the influence of superstructure layout on airflow field and so on [18]. The research on the influence of ship rolling on the aircraft take-off is relatively less.

In recent years, many international scholars propose and develop the mesoscopic theories combining the macroscopic fluid mechanics with the microscopic molecular dynamics. Mesoscopic numerical models based on the Boltzmann equation of molecular motion theory are developed to reproduce the gas flow problem with a characteristic scale of micron and nanometer, Lattice Boltzmann method (LBM) is one of them [19, 20]. Compared with the traditional computational fluid dynamics method, this method can deal with more complicated boundary conditions and there is no need to mesh in the fluid domain. It has a great advantage in the CFD calculation of complex geometry. In this paper, the influence of ship rolling motion on the aerodynamic characteristics of aircraft during take-off is studied.

CALCULATION METHOD

LATTICE BOLTZMANN METHOD (LBM)

The Lattice Boltzmann Method (LBM) makes use of statistical distribution functions with real variables, preserving by construction the conservation of mass, linear momentum and energy. The collision operator is simplified under the Bhatnagar-Gross-Krook (BGK) approximation, it's defined as follows:

$$\Omega_i^{BGK} = \frac{1}{\tau} (f_i^{eq} - f_i) \quad (1)$$

Where τ is the relaxation characteristic time (which is related to the macroscopic viscosity) and f_i^{eq} is the local equilibrium function.

The equilibrium distribution function usually adopts the following expression:

$$f_i^{eq}(\gamma, t) = t_i \rho \left[1 + \frac{c_{i\alpha} v_\alpha}{c_s^2} + \frac{v_\alpha v_\beta}{2c_s^2} \left(\frac{c_{i\alpha} c_{i\beta}}{c_s^2} - \delta_{\alpha\beta} \right) \right] \quad (2)$$

Where c_s is the sound speed, v is the macroscopic velocity, δ is the Kronecker delta, and t_i are built preserving the isotropy in space.

WALE TURBULENCE MODEL

WALE model is chosen to be turbulence model This model recovers the asymptotic behavior of the turbulent boundary layer when this layer can be directly solved and it does not add artificial turbulent viscosity in the shear regions out of the wake. The WALE model is formulated as follows:

$$\nu_{\text{turbulent}} = \Delta^2 \frac{(G_{\alpha\beta}^d G_{\alpha\beta}^d)^{3/2}}{(S_{\alpha\beta} S_{\alpha\beta})^{5/2} + (G_{\alpha\beta}^d G_{\alpha\beta}^d)^{5/4}} \quad (3)$$

$$S_{\alpha\beta} = \frac{1}{2} \left(\frac{\partial v_\alpha}{\partial r_\beta} + \frac{\partial v_\beta}{\partial r_\alpha} \right) \quad (4)$$

$$G_{\alpha\beta}^d = \frac{1}{2} (g_{\alpha\beta}^2 + g_{\beta\alpha}^2) - \frac{1}{3} \delta_{\alpha\beta} g_{\gamma\gamma}^2 \quad (5)$$

$$g_{\alpha\beta} = \frac{\partial v_\alpha}{\partial r_\beta} \quad (6)$$

$$\Delta = C_w \text{Vol}^{1/3} \quad (7)$$

Where Δ is the filter scale, S is the strain rate tensor of the resolved scale, and C_w (the WALE constant) is typically 0.2.

VERIFICATION CALCULATION

PHYSICAL MODEL

Simplified frigate ship SFS1 is the simulation model of Verification Calculation. The model measures about 138.7 m long \times 13.7 m wide \times 16.8 m deep, its specific dimensions refer to the reference documentation. Simplified frigate ship SFS1 is shown in Fig. 1.

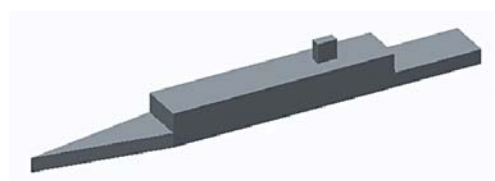


Fig. 1. SFS1 model

CALCULATION CONDITIONS AND SETTINGS

The computational domain uses the virtual wind tunnel in the simulation of simplified frigate ship SFS1. The ship model remains stationary and the wind direction is windward. The inlet wind speed is 20 m/s, the surface of the ship is no-slip wall, and the sea level is set as frictionless wall.

CALCULATION RESULTS AND ANALYSIS

A horizontal line is chosen in the computational domain. It's on the vertical plane in the middle of the flight deck, and the line is same height as the top of the hangar.

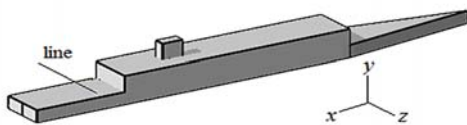


Fig. 2. Schematic diagram of monitoring line

The simulation results are compared with the literature, as shown in Fig. 3. The X axis is the ratio of the Z direction coordinate to the flight deck width, and the Y axis is the dimensionless ratio of the velocity component.

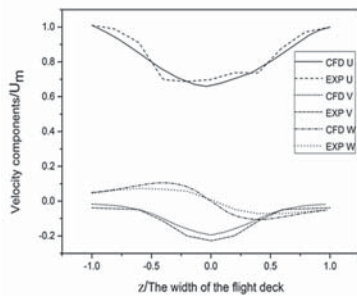


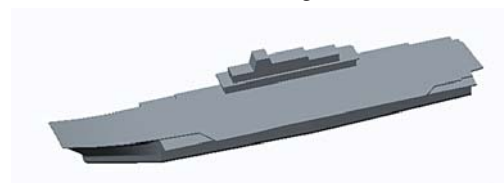
Fig. 3. Dimensionless velocity components in the middle of flight deck

From the Fig. 3., the simulation results are in good agreement with the experimental data, the calculation method is verified. The result of Z directional velocity component shows that the directions of velocity on both sides are opposite, airflow flows from side to the middle, and the velocity magnitude is symmetrical. The result of Y directional velocity component shows that there is downwash above the flight deck.

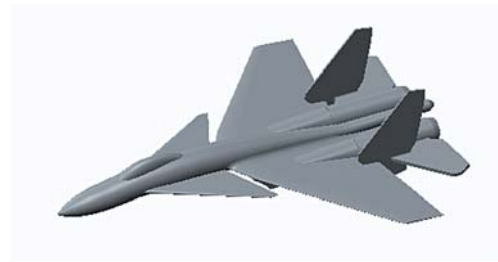
SIMULATIONS IN DIFFERENT SHIP ROLLING CONDITIONS

PHYSICAL MODEL

Simulation model is shown in Fig.4:



(a) aircraft carrier model



(b) aircraft model

Fig. 4. Simulation model

CALCULATION CONDITIONS AND SETTINGS

The computational domain uses the virtual wind tunnel in the simulation of aircraft take-off. The ship model remains stationary and the wind direction is windward. The inlet wind speed is 25 m/s, and the initial velocity of aircraft is 0 m/s. Aircraft moves and leaves the deck with 40 m/s² acceleration, the total movement time is 2.4 s. In this process, the rolling motion of the aircraft carrier accords with the sine function, the swing amplitude is 3° (the angle toward to starboard is positive, otherwise it's negative), and the rolling period is 8 s. The surface of ship and aircraft is no-slip wall, and the sea level is set as frictionless wall. There is a refinement region around aircraft and the bow, as shown in Fig. 5.

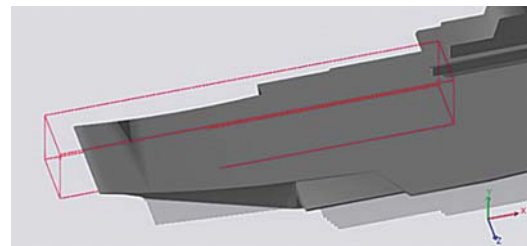


Fig. 5. Schematic diagram of refinement region

In order to analyze conveniently, the landing process of aircraft is divided into two sections: horizontal deck section (0 s–1.5 s) and skid deck section (1.5 s–2.4 s).

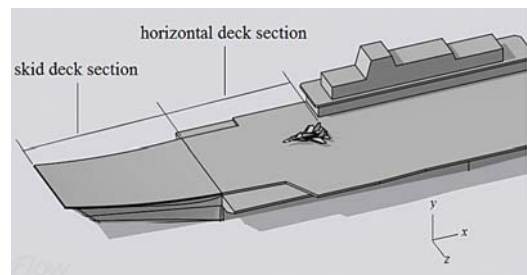


Fig. 6. Schematic diagram of aircraft

CALCULATION RESULTS AND ANALYSIS

Because the aircraft take-off time is smaller than ship rolling period, different rolling conditions should be considered. There are 8 calculation conditions in this paper. In order to facilitate the analysis, the calculation condition which ship remains stationary is represented as JZ, the rest of them are shown in Tab. 1.

Tab. 1. Ship rolling calculation conditions

Calculation conditions		Initial rolling angle				
		-3°	-1.5°	0°	1.5°	3°
Rolling direction	Starboard (R)	R-3	R-1.5	R0	R1.5	—
	Port (L)	—	L-1.5	L0	L1.5	L3

When the initial angle of the hull is 0° and deflects to the starboard, the vortices of the carrier takeoff process are shown in Fig. 7.

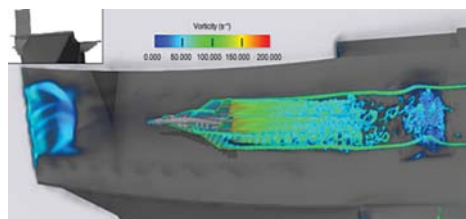
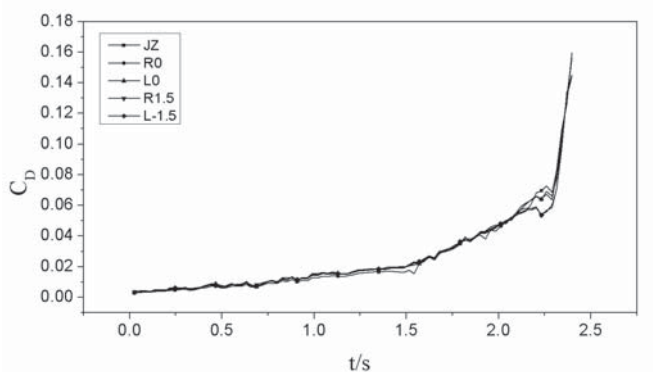
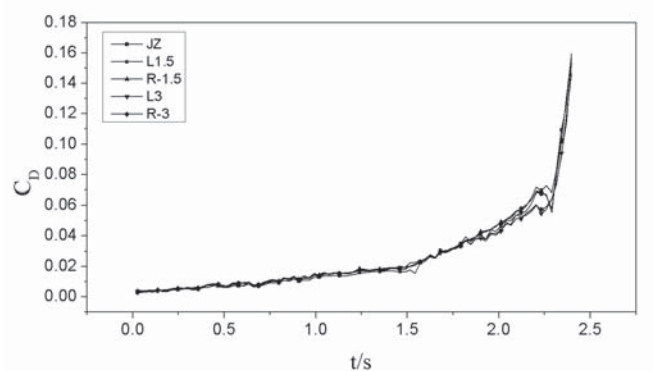


Fig. 7. Vorticity contours in 2 s

It can be seen from Fig. 7. that the larger vorticity region is mainly present on the carrier's tail and the route of its movement. In addition, there is a significant vortex structure in the bow part, which is caused by the flow around the ship, and the aerodynamic characteristics and force of the aircraft will change when the carrier is slipping off the area near the bow. Since the calculation is only encrypted around the flight path, the vortices on both sides of the bow are less noticeable than the encrypted area.

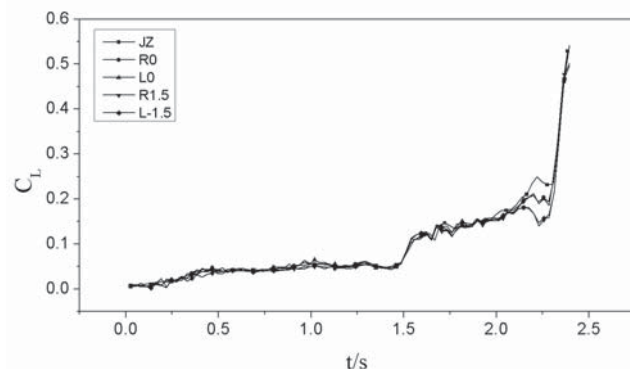


(a)

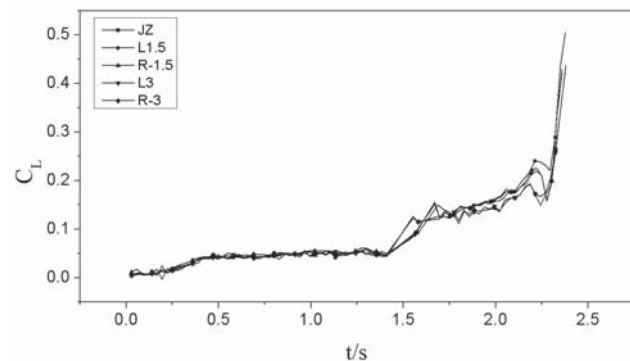


(b)

Fig. 8. The drag coefficient



(a)



(b)

Fig. 9. The lift coefficient

Fig. 8. and Fig. 9. show the drag coefficient and lift coefficient of carrier-based aircraft under different roll conditions. Compared with the calculated results, it can be found that the variation of the drag coefficient and the lift coefficient are basically the same under different working conditions. In the horizontal deck section (0–1.5 s), because the aircraft angle of attack is zero, the resistance coefficient and the lift coefficient are increasing with the speed increases slowly; In the skid deck section (1.5–2.4 s), the speed of the aircraft is increasing, and the angle of attack is also increasing, relative to the horizontal deck section, the resistance coefficient and the lift coefficient rise faster. In addition, it can be seen from the curve of the lift coefficient of the skid deck section, which shows that the growth rate of the front lift coefficient is much smaller than that of the rear, which shows that the aerodynamic characteristics of the aircraft in the front of the skid deck are relatively poor.

On the skid deck, the six horizontal monitoring lines shown in Figure 10 are 20 m in length ($z = -10$ m to $z = 10$ m), and the height of the skate deck surface is 2 m, line 1–6 $Z = 13.1$ m, profile $x = -142$ m, $y = 13.9$ m, profile $x = -148$ m, $y = 14.8$ m, section $x = -146$ m, $y = 12.4$ m, $X = -154$ m, $y = 15.8$ m, profile $x = -160$ m, $y = 16.9$ m.

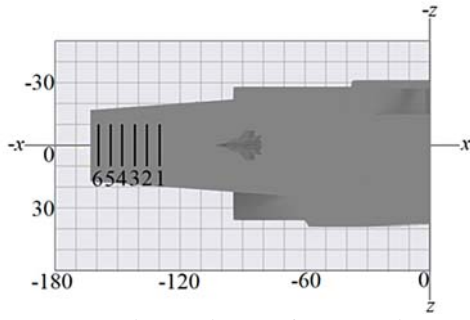


Fig. 10. Schematic diagram of monitoring line

The velocity component (ie velocity component v) of the six monitoring lines on the monitoring line at $t = 1.7$ s is shown in Fig. 11. when the hull does not roll motion.

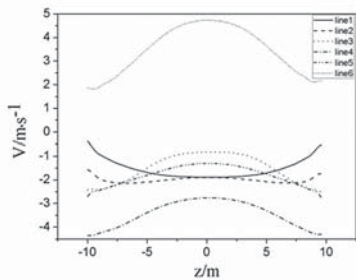


Fig. 11. Velocity components of Y direction in different monitoring line

It can be seen from the figure, 1–5 line at the existence of the next wash gas flow, and the next washing air flow rate is fastest in the 5th line, and there is the 6th line on the wash stream. When the aircraft slides through line 1–5, it is affected by the underwind airflow. When it continues to travel to line 6, it will be affected by the upper airflow. The lift factor of the skid deck will show as shown in Fig. 9.

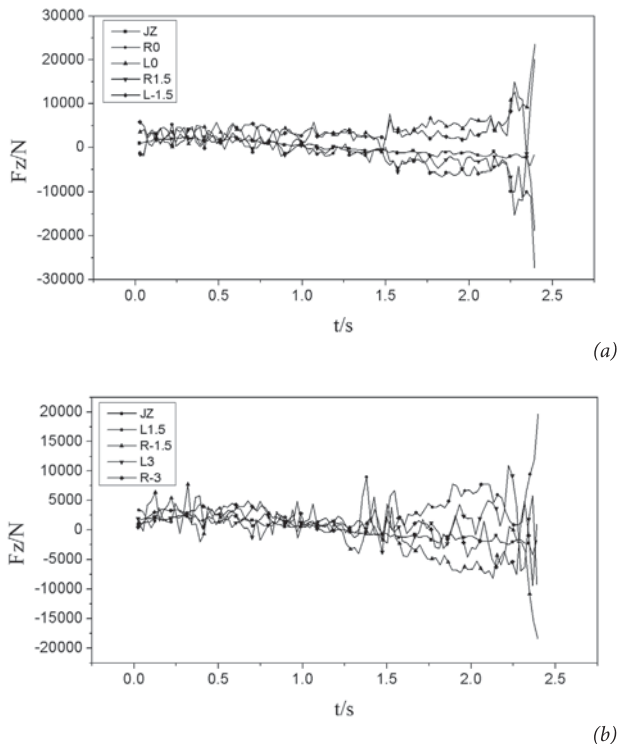


Fig. 12. Side force of aircraft

It can be seen from the figure, the aircraft carrier does not occur when the roll, due to the wind direction for the wind, the aircraft by the lateral force relative to the roll movement is very small, and little change; when the aircraft carrier roll. The lateral force in the horizontal deck section is relatively small and the lateral force in the skid deck section is greater, especially in the period of $t = 2.2$ s to $t = 2.4$ s, which is due to the fact that the aircraft is traveling. To the skid deck section, due to their own deflection angle and the impact of the bow airflow disturbance, in the skid deck section of the greater the angle of the aircraft carrier, the greater the lateral force of the aircraft. In addition, the aircraft carrier roll movement, the aircraft in the skid deck section by the direction of lateral force and roll deflection direction is basically the same, that is, when the aircraft carrier to the deck on the right side, the body force is also biased to the right, and vice versa also else.

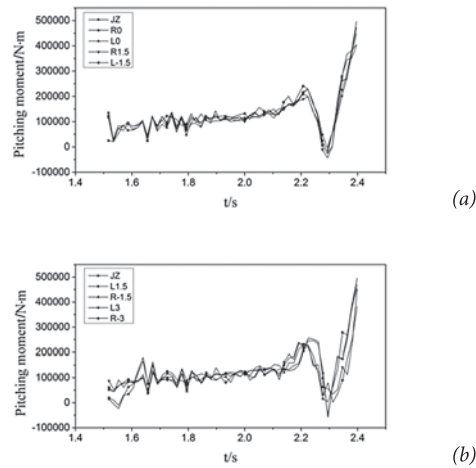


Fig. 13. Pitching moment of aircraft (Skid deck section)

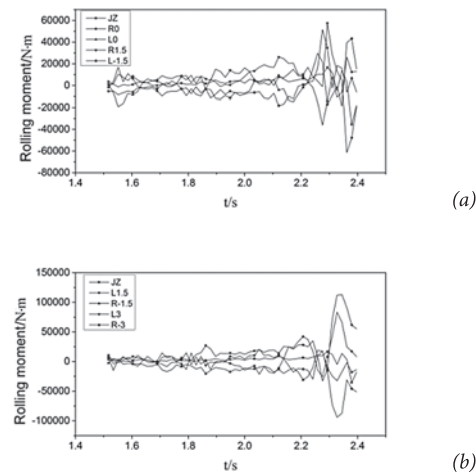


Fig. 14. Rolling moment of aircraft (Skid deck section)

As can be seen from Fig. 13. and Fig. 14., the roll motion of the aircraft carrier has little effect on the pitch torque of the aircraft in the skid deck section and has a greater effect on the roll torque, especially at $t = 2.2$ s to $t = 2.4$ s during the period of time, the aircraft through the $x = -144$ m to $x = -164$ m deck area.

CONCLUSION

The impact of the carrier roll on the lift coefficient, drag coefficient and pitching torque of the aircraft during the takeoff of the carrier is small, which has a great influence on the lateral force and the rolling moment.

When the aircraft enters the skid deck section, it is affected by the underwash airflow, which is affected by the upper airflow near the bow, resulting in a relatively small lift coefficient of the aircraft in the front of the skid deck. The aerodynamic characteristics are relatively The area where the maximum velocity of the lower wash airflow is located is about 10 m from the bow.

(3) In the case of a roll, the lateral force of the aircraft in the horizontal deck section is much smaller than that of the skid deck. The greater the deflection angle in the skid deck section, the greater the lateral force of the aircraft. In addition, when the aircraft carrier is rolling, the lateral force and the rolling moment of the aircraft are large and change rapidly in the area of about 20 m from the bow to the end of the skid deck. The area is the most affected by the flight.

ACKNOWLEDGEMENTS

This work is supported financially by the National Natural Science Foundation of China(No. 11602066).

REFERENCES

1. W. H. Hong, Z. F. Jiang, T. Wang.: *Influence of Upper Building Form and Layout on Ship's Air Flow Field*, Chinese Ship R., Vol. 2, no. 2, pp. 53–68, 2009.
2. W. J. Wang, L. L. Guo, X. J. Qu.: *Analysis of Mechanics Mechanism of Skidding*, Beijing University.Aero. Astron.J., Vol. 34, no. 8, pp. 887–889, 2008.
3. W. W. Liu, X. J. Qu.: *Kinetic Modeling of Slip – like Takeoff Based on Tension*, Chinese Aero.J., Vol. 18, no. 4, pp. 326–335, 2005.
4. M. H. Wang, B. Zhao.: *Study on the Dynamics of Shipborne Aircraft*, Chinese Aircraft Design.J., Vol. 2, no. 1, pp. 23–33, 1997.
5. B. Chen, H. S. Ang.: *Characteristics and Performance Analysis of Shipborne Aircraft*, Chinese Jiangsu Airlines. J., Vol. 3, no. 3, pp. 2–5, 2011.
6. I. Gregory, S. William.: *Using simulation to optimize ski jump ramp profiles for STOVLE aircraft*, AIAA-2000-4285, Vol. 2, no. 2, pp. 53–58, 2000.
7. R. P. Shrikant, S. Amitabh.: *Performance analysis and control design for ski-jump take off*, AIAA-2003-5412, Vol. 4, no. 2, pp. 43–48, 2003.
8. Y. Gao, H. S. Xie.: *Numerical Simulation of Flow Field around Hull in Slip – off Process*, Chinese Aero.J., Vol. 26, no. 4, pp. 513–518, 2008.
9. Y. Q. Bi, W. S. Sun.: *Preliminary Analysis on Take – off Performance of a Certain Type of Fighters*, Flight mech.J., Vol. 26, no. 4, pp. 18–21, 2006.
10. H. Xiao, S. M. Yang, J. Y. Yu.: *Simulation Analysis of Takeoff Performance of a Certain Type of Aircraft*, Flight mech. J., Vol. 27, no. 4, pp. 78–80, 2009.
11. Y. Gao, X. Gu, H. S. Xie, Z. He.: *Optimum Selection and Pneumatic Characteristic of Take – off Parameters of Shipboard Sliding*, Harbin Engineer University.J., Vol. 29, no. 10, pp. 1040–1045, 2008.
12. S. G. Bai, M. Q. Hu, J. T. Dun.: *Six – degree – of – freedom static balance analysis of carrier – borne ejection*, Air Force Engineer University.J., Vol. 13, no. 3, pp. 21–24, 2012.
13. D. Tian.: *The Principle and Application of Lattice Boltzmann Method*, Daqing: Daqing Petrol.Instit., China, 2009.
14. Y. H. Qian, D. D'humieres, P. Lallemand.: *Lattice BGK models for Navier-Stokes equation*, Europhysics L., Vol. 17, no. 6, pp. 479–484, 1992.
15. S. Y. Chen, G. Doolen.: *Lattice Boltzmann method for fluid flows*, Fluid Mech Annual.R., Vol. 30, no. 2, pp. 329–364, 1998.
16. S. Succi.: *The Lattice Boltzmann Equation for Fluid Dynamics and Beyond*. Clarendon Press, United Kingdom, 2001.
17. M. Liu, X. P. Chen, N. Kannan. Premnath.: *Comparative Study of the Large Eddy Simulations with the Lattice Boltzmann Method Using the Wall-Adapting Local Eddy-Viscosity and Vreman Subgrid Scale Models*, Chinese Phys.L., Vol. 29, no. 10, pp. 104706–104710, 2012.
18. D. M. Roper, I. Owen, G. D. Padfield, S. J. Hodge.: *Integrating CFD and piloted simulation to quantify ship–helicopter operating limits*, Aero.J., Vol. 110, no. 119, pp. 419–428, 2006.
19. James Forrest, I. Owen.: *An investigation of ship airwakes using Detached-Eddy Simulation*, Comp.Fluid.J, Vol. 39, no. 4, pp. 656–673, 2010.
20. S. M. Zhou.: *Simulation Analysis on the Influence of Carrier Deck Movement on Shipboard Carrier*, Aircraft design.J., Vol. 32, no. 6, pp. 28–32, 2012.

CONTACT WITH THE AUTHOR

Sun Xiao-yu, Ph.D.

e-mail: sunxiaoyu520634@163.com

tel: 13258668951

College of Aerospace and Civil Engineering Harbin

Engineering University

Harbin 150001

CHINA

MARINE FOUR-STROKE DIESEL ENGINE CRANKSHAFT MAIN BEARING OIL FILM LUBRICATION CHARACTERISTIC ANALYSIS

Teng XianBin, Ph. D.,

Zhang JunDong, Ph. D.

School of Marine Engineering, Dalian Maritime University, Dalian, Liaoning, China

ABSTRACT

The Craig-Bampton modal synthesis method was used to establish the dynamic model of marine four-stroke diesel engine body and crankshaft. Based on the Greenwood / Tripp microlong contact theory considering the surface roughness and the generalized Reynolds equation considering the oil filling rate, the elasto-hydrodynamic lubrication model of the main bearing of the four - stroke diesel engine is found. At the rated speed, the lubrication performance of the main bearing is simulated and analyzed by the maximum dynamic pressure, the minimum oil film thickness and the friction power. The results show that the oil pressure of 4 # main bearing is the largest and the maximum oil film pressure is in the 4 # main bearing position. The friction load of 4 # main bearing is the largest. The average oil film thickness of 4 # main bearing is the smallest and the minimum oil film thickness also occurred in the 4 # main bearing position; it can be seen 4 # bearing the most bad lubrication conditions.

Keywords: Marine four – stroke diesel engine; Main bearing; Elastic hydrodynamic lubrication.

INTRODUCTION

Marine four stroke diesel engine is usually used as the active power of the medium and small power ship or the generator set of the large ship. The ship in the ocean or inland coastal navigation process, usually in a trim and heel of the complex working conditions, so compared to land-based diesel engine, four stroke diesel engine crankshaft main bearing for ship lubrication reliability requirements more stringent. At present, the simplified method is usually used in the hydrodynamic lubrication of the main bearing, which does not take into account the deformation of the engine block and crankshaft, surface roughness and so on. With the progress of the complex work condition and the numerical simulation technology, the main influence factors of the main bearing of the modern marine diesel engine are taken into account, and the lubrication characteristics of the main bearing are judged more comprehensively.

Ebrat O [1] present a comprehensive formulation for the dynamics of a rotating flexible crankshaft coupled with

the dynamics of an engine block through a finite difference elasto-hydrodynamic main bearing lubrication algorithm. Jun Sun [2] investigate the effect of deformation of the whole engine block on the hydrodynamic lubrication performance of main bearings. Cai, X. X [3] analysis the crankshaft bearing elastic fluid dynamic lubrication for a four-stroke four-cylinder internal combustion engine crankshaft main bearing, considering the influence of the deformation of the body. Lei Jilin [4] built a three-dimensional lubrication simulation model of the main bearing with AVL Excite Power Unit software, based on the elastic fluid dynamic lubrication theory. Wei, Lidui [5–6] put forward a two-stroke diesel engine main bearing thermo-elastic hydrodynamic TEHD mixed lubrication model, considering the deformation of flexible body. At present, there are few reports on the study of the mixed lubrication characteristics of marine four stroke diesel engine main bearings.

In this paper, based on the theory of elasto-hydrodynamic lubrication and the theory of structural dynamics, the lubrication simulation model of marine 6 cylinder diesel engine crankshaft bearing system is established. Under the rated speed,

the lubrication performance of the main bearing is simulated and analyzed, which provides the basis for the optimal design of the bearing.

MULTI BODY DYNAMICS MODEL OF CRANKSHAFT BODY

According to the Craig-Bampton modal synthesis method, the number of freedom degrees of flexible body and crankshaft structure is reduced. The relationship between the physical coordinates and modal coordinates is as follows:

$$\mathbf{x}^b = \begin{pmatrix} \mathbf{x}_i^b \\ \mathbf{x}_r^b \end{pmatrix} = \begin{pmatrix} \mathbf{X}^b & \mathbf{T}^b \\ \mathbf{0} & \mathbf{I} \end{pmatrix} \cdot \begin{pmatrix} \boldsymbol{\alpha}^b \\ \mathbf{x}_r^b \end{pmatrix} = \boldsymbol{\phi} \cdot \begin{pmatrix} \boldsymbol{\alpha}^b \\ \mathbf{x}_r^b \end{pmatrix} \quad (1)$$

The equation of motion of the body is,

$$\mathbf{M}^b \cdot \ddot{\mathbf{x}}^b + \mathbf{C}^b \cdot \dot{\mathbf{x}}^b + \mathbf{K}^b \cdot \mathbf{x}^b = \mathbf{I} \quad (2)$$

Substituting equation(1) into equation (2), the body modal reduction motion equation is given as follows,

$$\overline{\mathbf{M}}^b \cdot \begin{bmatrix} \ddot{\boldsymbol{\alpha}}^b \\ \ddot{\mathbf{x}}_r^b \end{bmatrix} + \overline{\mathbf{C}}^b \cdot \begin{bmatrix} \dot{\boldsymbol{\alpha}}^b \\ \dot{\mathbf{x}}_r^b \end{bmatrix} + \overline{\mathbf{K}}^b \cdot \begin{bmatrix} \boldsymbol{\alpha}^b \\ \mathbf{x}_r^b \end{bmatrix} = \mathbf{I} \quad (3)$$

Considering the influence of the large range of rigid body motion rotation inertia crankshaft, crankshaft motion equation is reduced to,

$$\overline{\mathbf{M}}^c \cdot \mathbf{q}_a^c + \overline{\mathbf{C}}^c \cdot \mathbf{q}_a^c + \overline{\mathbf{K}}^c \cdot \mathbf{q}_a^c = \overline{\mathbf{Q}}^c \quad (4)$$

Where, x is the physical coordinates, subscript r, i are reservations of degrees of freedom (including all load points and degrees of freedom) and internal degrees of freedom respectively, θ is the crankshaft rotation coordinates, α is the main modal coordinates (also known as modal participation factor, q is a generalized displacement vector. Superscript b, c represent the body and the crankshaft respectively. M, C, K represent mass matrix, damping matrix and stiffness matrix respectively, and the upper line represents reduced physical quantities. T is a static reduction matrix. ϕ, Φ are the coordinate transformation matrix of the body and the crankshaft. The force F includes the external load vector, the oil film force and the asperity contact force.

MAIN BEARING ELASTIC HYDRODYNAMIC IUBRICATION THEORY

Main bearing of crankshaft in the actual operation, can produce hydrodynamic pressure of oil film to support the crankshaft rotation. Local high pressure makes the oil film of lubricating oil viscosity increases sharply, as well as the engine block of significant local deformation. These effects will significantly change the geometry of the oil film area, which

in turn affect the contact area pressure distribution at the same time. Therefore, in the elastic hydrodynamic lubrication, the sliding bearing oil film pressure distribution, distribution of oil film thickness and surface roughness, influence and elastic deformation distribution is a coupling problem.

THE OIL FILM THICKNESS

In the main bearing lubrication characteristics analysis, the elastic deformation and surface roughness factors are considered, the main bearing oil film thickness is expressed as:

$$h(\theta) = h_{\min}(\theta) + \Delta h(\theta) + \delta h(\theta) + \sigma h(\theta) \quad (5)$$

Where, $h_{\min}(\theta)$ is the minimum oil film thickness under rigid bearing hypothesis. $\Delta h(\theta)$ is the difference between the oil film thickness and $h_{\min}(\theta)$, only with the geometry factors. $\delta h(\theta)$ is elastic deformation caused by the oil film. $\sigma h(\theta)$ is the lubrication oil film thickness produced by surface roughness. θ is for the oil filling rate.

THE GENERALIZED REYNOLDS EQUATION

Main bearing lubricating oil film thickness in the process of work only a few microns, the influence of surface roughness on the lubrication performance need to be considered. So the elastic generalized Reynolds equation of hydrodynamic pressure lubrication are as follows [7]:

$$\frac{\partial}{\partial x} \left(\frac{1}{12\mu} h^3 \theta \frac{\partial p}{\partial x} \right) + \frac{\partial}{\partial z} \left(\frac{1}{12\mu} h^3 \theta \frac{\partial p}{\partial z} \right) = \theta \frac{u_1 + u_2}{2} \frac{\partial h}{\partial x} + h \frac{u_1 + u_2}{2} \frac{\partial \theta}{\partial x} + \frac{\partial h \theta}{\partial t} \quad (6)$$

p is the oil film pressure, MPa . μ is the oil dynamic viscosity, $Pa \cdot s$. u_1, u_2 are the journal, bearing the circumferential speed, $u_1 = V, u_2 = 0$, m/s. Generalized Reynolds equation shows the relationship between the dynamic bearing force and the dynamic external load, which shows the relationship between the pad diameter, the pad width, the axial trajectory, the oil dynamic viscosity and the oil film pressure in time and space. Boundary conditions are extended boundary conditions.

ASPERITY CONTACT MODEL

Greenwood / Tripp microlite contact theory is applied, bearing surface asperity contact pressure equation [8]:

$$P_b(h) = KE^* F (4 - h/\sigma_s) \quad (7)$$

P_b is the contact pressure; K is the elastic contact factor; σ_s is the integrated surface roughness; F is the film thickness function; E^* is the integrated elastic modulus.

When $(4 - h/\sigma_s) \geq 0$, it is determined that the contact area is rough and in the mixed friction state. When $(4 - h/\sigma_s) < 0$, it is determined that the contact area is fully lubricated and in the fluid dynamic lubrication state.

THE BODY – CRANKSHAFT – THE MAIN BEARING SIMULATION MODEL

Solidworks is used to build three-dimensional model of marine four-stroke diesel engine, including diesel engine body, crankshaft, main bearing, connecting rod and so on, as shown in Fig.1.

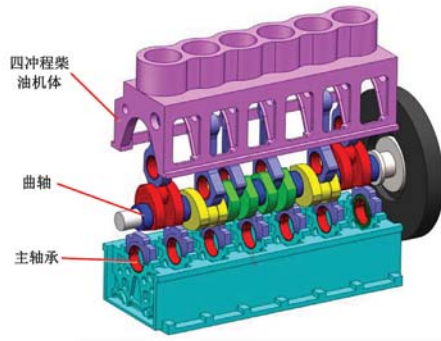


Fig. 1. Three – dimensional model of marine four – stroke diesel engine

The finite element model of the body-bearing is established by using the finite element software Abaqus, as shown in Fig. 2.

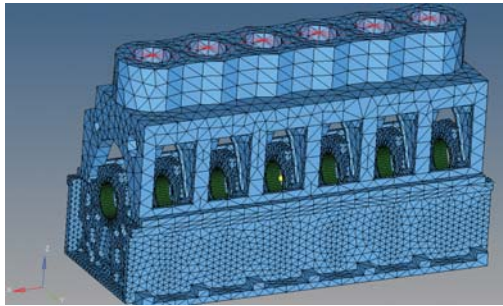


Fig. 2. Finite element model of body – bearing

The AVL-EXCITE SHAFTER MODELER module is used to build the crankshaft reduction dynamics model. The finite difference model of main bearing is established in ALV-EXCITE. The main bearing oil film surface mesh is divided into axial $17 \times$ circumferential 97. The finite element model of diesel engine body is introduced into AVL-EXCITE by modal reduction. Crankshaft power reduction model and the main bearing finite difference model are combined, the marine four-stroke diesel engine body – crankshaft bearing oil film dynamic lubrication model was established using AVL-EXCITE module, as shown in Fig. 3.

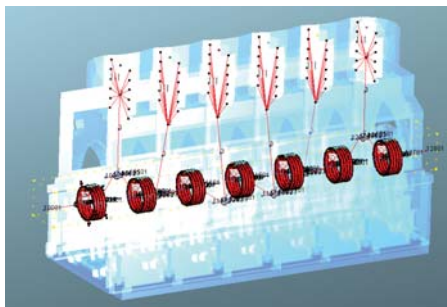


Fig. 3. Marine four-stroke engine block-crankshaft-main bearing lubrication and multibody dynamics model

THE CRANKSHAFT MAIN BEARING MIXED LUBRICATION CHARACTERISTICS ANALYSIS

The simulation calculation, the explosion gas pressure piston, piston components, and the calculation in the inertial force of connecting rod load was applied on the crankshaft crank pin. The average reverse torque on the crank flywheel end are imposed. Crankshaft ignition order is 1-5-3-6-2-4. Each cylinder gas force curve as shown in figure 4.

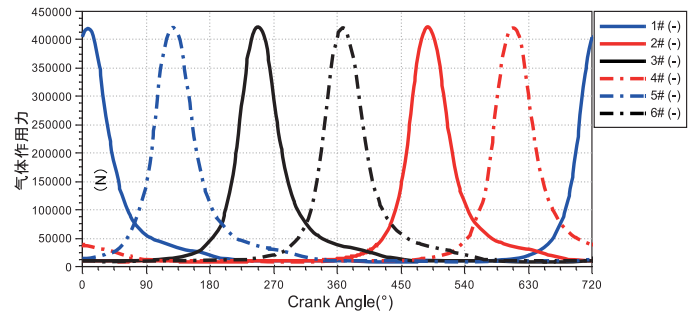


Fig. 4. Each cylinder indicator diagram

The specific structure parameters and working condition of the main bearing as shown in Tab. 1.

Tab. 1. Main bearing operating parameter

Parameter	Value
Journal radius	90 mm
Bearing radius clearance	0.135 mm
Bearing width	70 mm
Oil groove width	8 mm
Oil groove angle	220°
Bearing pad / Journal Surface roughness	0.8/0.4
Lubricating oil grades	SAE-15W-40
Oil supply pressure	0.45
Oil supply temperature	40°
Journal speed	900 rpm

The above parameters are input to the simulation model. Four stroke diesel engine main bearing oil film pressure, the minimum oil film thickness and friction power consumption data is obtained by AVL multi-body dynamics simulation iterative calculation.

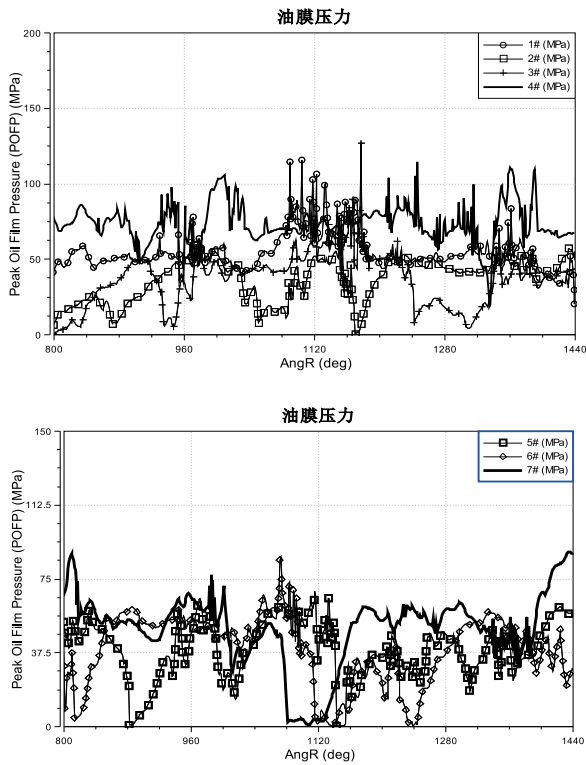


Fig. 5. The peak bearing oil film pressure distribution

As can be seen from Fig. 5., the average oil film pressure from large to small sort, 4#(72.9 MPa), 1#(50.8 MPa), 7#(50.3 MPa), 5#(39.7 MPa), 6#(39.6 MPa) > 3#(37 MPa) > 2#(34.6). It can be seen that the 4# main bearing average oil film pressure is the largest, reaching 72.9 MPa, and the maximum oil film pressure occurs in the 4# main bearing position, reaching 114.4 MPa. 1# and 7# main bearing average oil film pressure is close to the 4# main bearing.

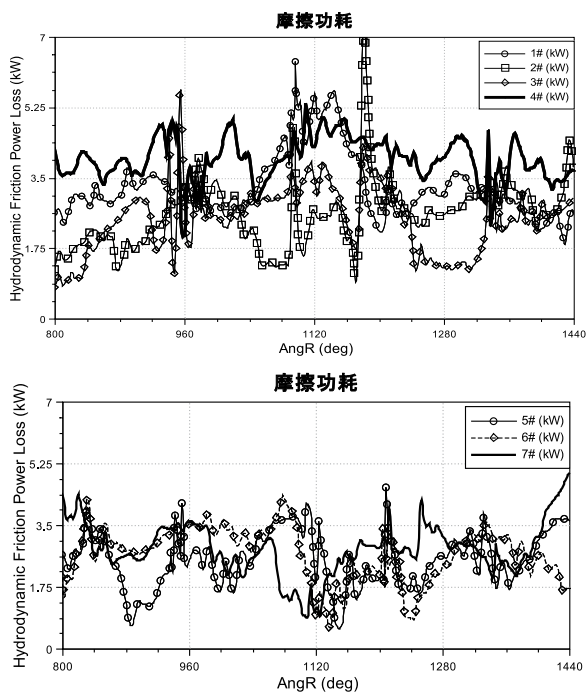


Fig. 6. The bearing friction power

As shown in Fig. 6., the order of the average frictional power consumption is 4#(4.27 KW) > 1#(3.2 KW) > 7#(3.0 KW) > 2#(2.78 KW) > 6#(2.7 KW) > 5#(2.73 KW) > 3#(2.71 KW). It can be seen, 4 # main bearing oil friction power consumption of the largest, reaching 4.27 KW. 1 # and 7 # main bearing average oil film pressure is similar, only less than 4 # main bearing. The rest of the main bearing friction power consumption is not much difference.

As can be seen from Fig. 7., the average minimum film thickness from large to small sort, 4#(0.0049 mm) < 1#(0.0073 mm) < 5#(0.0085 mm) < 3#(0.01 mm) < 7#(0.01 mm) < 6#(0.0114 mm) < 2#(0.0127 mm). It can be seen that the 4 # main bearing average minimum film thickness is the smallest, reaching 0.0049 mm, and the minimum film thickness occurs in the 4 # main bearing position, reaching 0.0014 mm. 1 # and 5 # main bearing average minimum film thickness is similar, only more than 4 # main bearing.

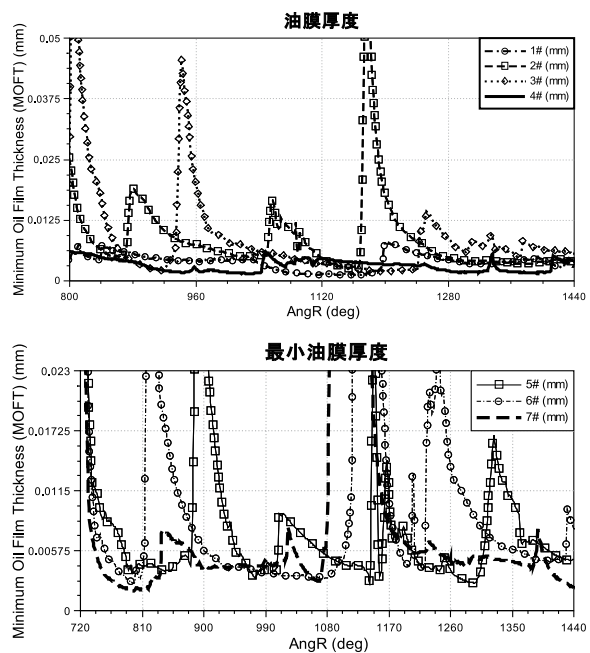


Fig. 7. Each bearing minimal oil film thickness

CONCLUSIONS

Elastic hydrodynamic lubrication theory and structural modal reduction dynamics theory are applied. The roughness of the bearing body and crankshaft is considered. The lubrication simulation model of the 6-cylinder four-stroke diesel engine crankshaft-bearing was established considering the flexible deformation of the body and the crankshaft.

At the rated speed, the lubrication performance of the main bearing is simulated and analyzed by the maximum dynamic pressure, the minimum oil film thickness and the friction power. The results show that the oil pressure of 4 # main bearing is the largest and the maximum oil film pressure is in the 4 # main bearing position. The friction load of 4 # main bearing is the largest. The average oil film thickness of 4 # main bearing is the smallest and the minimum oil film The thickness also occurred in the 4 # main bearing position; it can be seen 4 # bearing the most bad lubrication conditions.

This paper provides a reference for the optimization design of the main bearing of 6-stroke diesel engine. According to the above results of the main bearing simulation, 4 # main bearing structural parameters, materials and lubrication characteristics should be focused on the optimization design.

ACKNOWLEDGEMENTS

This project is partially supported by the Fundamental Research Funds for the Central Universities (No. 3132015337).

REFERENCES

1. Sun, Jun, X. Cai, and L. Liu. *On the elastohydrodynamic lubrication performance of crankshaft bearing based on the effect of whole engine block deformation*. Industrial Lubrication and Tribology 64.1(2012):60–65.
2. Cai, X. X., et al. *Elastohydrodynamic lubrication analysis of main bearing for internal combustion engine considering block deformation*. Tribology 30.2(2010):118–122.
3. Lei, Jilin, et al. *Analysis on influence factors of main bearing lubrication characteristics for horizontal diesel engine*. Transactions of the Chinese Society of Agricultural Engineering volume 28.17(2012):19–24(6).
4. Wei, Lidui. *Thermo-elasto-hydrodynamic Mixed Lubrication of Main Bearings of Marine Diesel Engines, Based on Coupling between Flexible Engine Block and Crankshaft*. Journal of Mechanical Engineering 50.13(2014):97.
5. Wei, L., S. Duan, and H. Wei. *TEHD lubrication analysis of the main bearings of a marine diesel engine based on the flexible engine block*. Journal of Harbin Engineering University (2015).
6. Saša Bukovnik;Günter Offner, et al. *Thermo elasto hydrodynamic lubrication model for journal bearing including shear rate-dependent viscosity*. Lubrication Science 19.4(2007):231–245.
7. Greenwood J. A., Tripp J. H. *The contact of nominally flat rough surface [J]*. Proceedings of the Institution of Mechanical Engineers, 1970, 185(46):625–633.
8. Greenwood J. A., Tripp J. H. *The contact of nominally flat rough surface [J]*. Proceedings of the Institution of Mechanical Engineers, 1970, 185(46):625–633.

CONTACT WITH THE AUTHOR

Teng XianBin, Ph.D.

e-mail: Tengx101@163.com

tel: 18988921593

School of Marine Engineering

Dalian Maritime University

Dalian, Liaoning 116026

CHINA

RESEARCH ON DRUM WATER LEVEL CONTROL OF MARINE AUXILIARY BOILER BASED ON ADRC

Hui-bing Gan, Ph.D.

Bo Lv, Master.

College of Marine Engineering, Dalian Maritime University, Liaoning, Dalian, China

ABSTRACT

The active disturbance rejection control (ADRC) exhibits strong robustness and adaptability in the presence of strong interference of a large class of uncertain systems. In order to better control the water level of the auxiliary boiler drum, this paper applies the ADRC to improve its control precision, robustness and timeliness. Firstly, the change of drum water level in a large oil tanker auxiliary boiler is analyzed and the dynamic equation is established. After the mathematic changes, the dynamic equation is transformed into a two-order system. Aiming at the characteristics of nonlinear, time-varying and strong disturbance of the boiler water level control system in marine auxiliary boiler, studying the ADRC that includes tracking differentiator (TD), extended state observer (ESO), nonlinear feedback (NLSEF) and disturbance compensation of four parts. The establishment of two kinds of two-order ADRC controller to control the drum level. Through the theoretical analysis and simulation experiment test, and comparing with the cascade control strategy, the experimental results show that the active disturbance rejection controller satisfies the steady state response index of the system, and has good timeliness and accuracy to the control of water level of the drum.

Keywords: ADRC; Robustness; Adaptability; Drum water level; Marine auxiliary boiler

INTRODUCTION

Drum water level is an important monitoring of boiler operation parameters, it is indirect reflects the boiler load and water balance, maintaining the water level is to maintain the drum important conditions for the safe operation of the boiler [1]. At present, most of the large oil tanker auxiliary boiler drum water level control system with high control accuracy is two impulses cascade control and three impulses cascade control. However, in the two impulses control or the three impulses control, there is a coupling between the feedforward loop of the steam flow and the feedback loop of the water supply valve due to the feedback error of the water level error, and the PID parameter will need to be retuning as the boiler conditions change. Digital method and advanced signal processing are usually incorporated into the PID to improve the PID controller's poor robustness, large overshoot and poor timeliness to improve its control performance.

Nowadays, many control strategies combined with PID applications have been proposed in the boiler. K.B. Lee et al.

analyzed the dynamic characteristics of the power plants boiler water level of the drum, and applied fuzzy control in the drum water level control system [2, 3, 4]. Hamed Moradi et al. applied sliding mode control to the control of the power plants boiler drum water level system [5]. These control schemes described above have improved the control effect, but there are still some problems.

Active disturbance rejection control is a non-linear control strategy proposed by Jing-qing Han, China [6]. ADRC achieves real-time estimation and compensation of disturbance by establishing the extended state observer, thus avoiding the defects of integral action and improving the adaptability of the system. According to the direction and size of the state error to carry out nonlinear feedback to improve the stability and fastness of the system [7]. Based on the analysis of the uncertainty of the water level system, this paper designs two ADRC methods for the drum water level of the boiler. The simulation results show that the control method has the advantages of high precision and fast response.

ADRC OF DRUM WATER LEVEL

ADRC is composed of tracking differentiator (TD), extended state observer (ESO), non-linear error feedback (NLSEF) and disturbance compensation [8].

The research on the water level of the drum of a large oil tanker boiler can obtain the dynamic equation of the change of drum water level [9]:

$$T_1 T_2 \frac{d^2 h}{dt^2} + T_1 \frac{dh}{dt} = (T_w \frac{du_w}{dt} + k_w u_w) - (T_D \frac{du_D}{dt} + k_D u_D) \quad (1)$$

In Eq. (1):

$T_w \frac{du_w}{dt} + k_w u_w$ — water disturbance;

$(T_D \frac{du_D}{dt} + k_D u_D)$ — steam disturbance;

h — drum water level;

T — time constant.

The function of (1) can write as.

$$\frac{d^2 h}{dt^2} = \frac{1}{T_1 T_2} \left[-T_1 \frac{dh}{dt} + (T_w \frac{du_w}{dt} + k_w u_w) - (T_D \frac{du_D}{dt} + k_D u_D) \right] \quad (2)$$

Using the two-order ADRC controller to study the water level of the drum.

Take the two-order object as an example, the dynamic equation of the controlled object can be described as:

$$\dot{x}^2 = f(\dot{x}, x, w, t) + bu \quad (3)$$

In Eq. (3):

w — external disturbance;

f — the generalized perturbation of the system;

b — system compensation;

u — system control input.

ADRC CONTROLLER FOR DRUMWATER LEVEL

In the ADRC system of the drum water level, all the uncertain factors (including the perturbation disturbance and external disturbance) of the drum water level are attributed to the generalized disturbance. Generalized disturbance quantities are estimated by ESO and through compensated by feedforward. The tracking signal of a given water level obtained by TD is compared with the estimated value of the system state variable obtained by ESO, and the control input signal of the system is obtained by NLSEF [8].

Drum water level ADRC controller algorithm is as follows.

1) Tracking Differentiator(TD)

$$\begin{cases} e = v_1 - v \\ v_1 = v_1 + h v_2 \\ v_2 = v_2 + h f_{han}(e, v_2, r_0, h_0) \end{cases} \quad (4)$$

In Eq. (4):

v — given signal;

v_1 — the tracking signal;

v_2 — the tracking speed;

r_0 — the speed factor;

e — the deviation of the tracking signal from the given signal;

h — the sampling step;

h_0 — the filter factor;

f_{han} — the optimal integrated control function [6].

The function of f_{han} can be defined as

$$f_{han}(e, v, r, h) = \begin{cases} -r \text{sign}(a), & |a| \geq d \\ -ra/d, & |a| \leq d \end{cases} \quad (5)$$

Where: $d=rh$; $d_0=hd$; $y=e+hv$

$$a_0 = \sqrt{d^2 + 8r|y|} \quad (6)$$

$$a = \begin{cases} v + \text{sign}(y)(a_0 - d)/2, & |y| > d_0 \\ v + y/d, & |y| \leq d_0 \end{cases}$$

2) Extended State Observer(ESO)

Aiming at two-order system with external disturbance and uncertainties.

$$\dot{x}^2 = f(\dot{x}, x, t) + w(t) + b_0 u(t) \quad (7)$$

In Eq. (7):

$f(\dot{x}, x, t)$ — an unknown function;

$w(t)$ — the external disturbance;

$u(t)$ — control input;

b_0 — a constant.

order:

$$\begin{cases} \dot{x}_1(t) = x(t) \\ \dot{x}_2(t) = \dot{x}(t) \\ \dot{x}_3(t) = f(x, \dot{x}, t) + w(t) \end{cases} \quad (8)$$

The system (7) can be expressed as

$$\begin{cases} \dot{x}_1(t) = x_2(t) \\ \dot{x}_2(t) = x_3(t) + b_0 u(t) \\ \dot{x}_3(t) = \xi(t) \end{cases} \quad (9)$$

In Eq. (9):

$\xi(t)$ — an unknown function.

Establish a nonlinear system:

$$\begin{cases} \dot{z}_1(t) = z_2(t) - g_1(z_1(t) - x_1(t)) \\ \dot{z}_2(t) = z_3(t) - g_2(z_1(t) - x_1(t)) + b_0 u(t) \\ \dot{z}_3(t) = -g_3(z_1(t) - x_1(t)) \end{cases} \quad (10)$$

In Eq. (10):

The function of $g_1(e_1)$, $g_2(e_1)$, $g_3(e_1)$ is the proper nonlinear continuous function of the construction, according to (9) and (10), there are,

$$\begin{cases} \dot{e}_1(t) = e_2(t) - g_1(e_1(t)) \\ \dot{e}_2(t) = e_3(t) - g_2(e_1(t)) \\ \dot{e}_3(t) = -\xi(t) - g_3(e_1(t)) \end{cases} \quad (11)$$

In Eq. (11):

$$e_i(t) = z_i(t) - x_i(t) (i=1, 2, 3)$$

For arbitrarily changed within a certain range $\xi(t)$, if and only when the nonlinear continuous function $g_1(e_1), g_2(e_1), g_3(e_1)$ satisfies,

$$e_1 g_i(e_1) > 0, \forall e_1 \neq 0, g_i(0) = 0 (i=1, 2, 3) \quad (12)$$

The system (12) is stable at the origin. Therefore, provided the appropriate nonlinear continuous function is constructed $g_1(e_1), g_2(e_2), g_3(e_3)$, the state of the system (8) able to track the state of the system (9), namely,

$$z_1(t) \rightarrow x_1(t), z_2(t) \rightarrow x_2(t), z_3(t) \rightarrow x_3(t) \quad (13)$$

According to the definition in formula (8), $x_3(t)$ is equal to an unknown function $f(x, \dot{x}, t)$ plus external disturbance $w(t)$. As long as the function satisfies the condition of (12) $g_1(e_1), g_2(e_2), g_3(e_3)$ satisfies the condition of (12), then the output of the system (10) z_{n+1} can be estimated $x_{n+1}(t)$ in real time, so the nonlinear system (10) is the ESO, ESO acquisition signal is derived from the input and output signals of the controlled object, For the n order controlled object to establish the $n+1$ order estimation state system, the parameter selection can make the observer real-time accurate state of the controlled object estimate. Because of $x_{n+1}(t)$ is the extended state, it is equivalent to the acceleration of the system, which can reflect the dynamic, disturbance and uncertain information of the system. It's can be seen that the ESO is independent of the concrete form of the object description function [10].

To study the object of two-order uncertainty system.

$$\begin{cases} \dot{x}_1^{(2)} = f(\dot{x}_1, x_1, w(t) + b_0 u \\ y = x_1 \end{cases} \quad (14)$$

In Eq. (14):

Order $x_2 = f(x_1, \dot{x}_1, w(t))$ is a new state of system (14), the new system as

$$\begin{cases} \dot{x}_1 = x_2 + b_0 u \\ \dot{x}_2 = \xi(t) \\ y = x_1 \end{cases} \quad (15)$$

Where:

The function of $\xi(t)$ is derivative of the x_2 , the unknown function. When $\xi(t)$ have the bounded, that is $|\xi(t)| < \xi_0$, the application fal function is used to construct the appropriate function, the ESO of the system (15) according to equation (10),

$$\begin{cases} e = z_1 - y \\ \dot{z}_1 = z_2 - \beta_{01} e \\ \dot{z}_2 = z_3 - \beta_{02} fal(e_1, a_1, \delta_1) + b_0 u \\ \dot{z}_3 = -\beta_{03} fal(e_2, a_2, \delta_2) \end{cases} \quad (16)$$

Where:

$0 < a_1 < a_2 < 1, \beta_{01}, \beta_{02}, \beta_{03}$ is gain of the observer, the magnitude of derivative $\xi(t)$ varies with the change in the uncertainty of the system (14), and when the part changes rapidly, $\xi(t)$ is large. On the contrary, it is very small.

The fal function is a non-smooth function as follows:

$$fal(x, \alpha, \delta) = \begin{cases} |x|^\alpha sign(x), |x| > \delta \\ x / \delta^{1-\alpha}, |x| \leq \delta \end{cases} \quad (17)$$

3) Non-linear Error Feedback (NLSEF)

$$\begin{cases} e_1 = v_1 - z_1, e_2 = v_2 - z_2 \\ u_0 = \beta_1 e_1 + \beta_2 e_2 \end{cases} \quad (18)$$

Where:

The coefficient of β_1, β_2 is the gain factor.

4) Disturbance Compensation

$$u = u_0 - z_3 / b_0 \quad (19)$$

Where:

The coefficient of b_0 is the compensation factor.

ADRC structure shown in Fig. 1. [6].

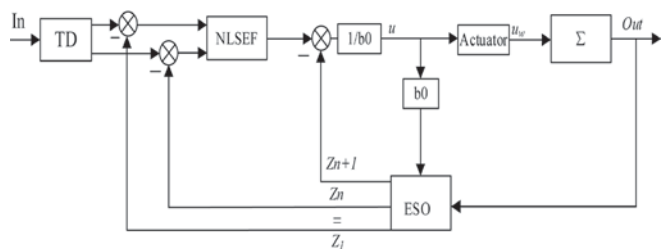


Fig. 1. Diagram of boiler water level control on ADRC

PARAMETER TUNING OF THE ADRC CONTROLLER

ADRC parameter tuning: First, for power parameters a_i , Usually in the ESO to take $a_1=0.5, a_2=0.25$ In the nonlinear feedback $0 < a_1 \leq 1.0, a_2 \geq 1.0$, usually to take $a_1=0.75$ or $0.5, a_2=1.25$ or 1.5 .

The parameter r of the TD is related to the excessive process time T_0 :

$$r = \frac{4(x_1 - x_0)}{T_0^2}$$

Where the coefficient of x_1 is the set value of TD, v is the input value, and x_{01} is the initial value of v . r to determine the tracking signal and speed, in order to suppress overshoot, generally taken $r < 1$.

The ADRC controller's gain factor β_1, β_2 corresponds to the proportional derivative gain of the PID controller, and the compensation factor b_0 is equivalent to the integral gain of the PID controller [15]. To adjust the parameters in the extended state observer $\beta_{01}, \beta_{02}, \beta_{03}$, the system by the sampling time to determine the three parameters. Where β_{03} is the most critical, the greater the value, the system lag is smaller, but β_{03} too large will cause oscillation, so in the adjustment process, the first adjustment β_{03} until the observer tracking effect is better, and then fine tune β_1 and β_2 to Enhance the performance of the observer [11]. b_0 is the compensation of the disturbance, it can refer to the PID control strategy in the differential and integral items to be adjusted.

SIMULATION OF CONTROL PROCESS OF DRUM WATER LEVEL ADRC

Fig. 2. is ADRC cascade three impulse working principle [12].

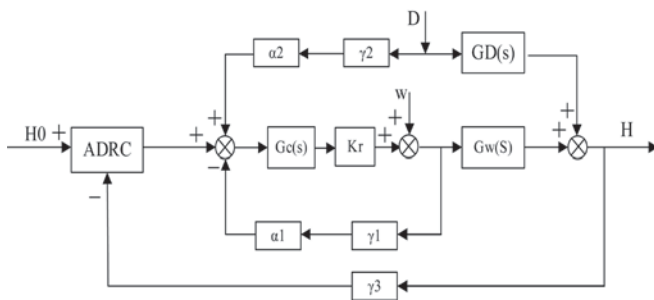


Fig. 2. The working principle of ADRC with cascade three impulses

Fig. 2., H, H_0 is the water level and its given value respectively. w is the water flow and D is the steam flow, $G_w(s), G_D(s)$ they are steam flow and the water flow of the transfer function of drum level.

Where:

$$G_w(s) = \frac{0.037}{s(30s+1)}, G_D(s) = \frac{3.6}{15s+1} - \frac{0.037}{s},$$

$$\gamma_1 = \gamma_2 = 0.083, \alpha_1 = \alpha_2 = 0.21, \gamma_3 = 0.033, K_r = 20.$$

At the same time on the PID controller parameter tuning. $K_{p1} = 0.5, K_{i1} = 0.0025, K_{d1} = 8, K_{p2} = 1, K_{i2} = 0.2, K_{d2} = 0$

Design two kinds of ADRC, and compare the performance of both.

1) ADRC without Tracking Differentiator

By simulation debugging, get a better set of parameters is: ESO: $\beta_{01} = 6, \beta_{02} = 12, \beta_{03} = 8$; NLSEF: $\beta_1 = 0.05, \beta_2 = 0.8$. disturbance compensation: $b_{01} = 0.0023$. In the simulation experiment, take the sampling step $h = 0.2s$. The secondary PID parameter is: $K_p = 1.45, K_i = 0.0055, K_d = 0$.

In the simulation experiment, the simulation time $t = 800s$ is added to the 35% feed water flow disturbance, the simulation

time $t = 1200s$ is added to the 30% steam flow disturbed. The control goal is to stabilize the drum level to 10 per unit. The corresponding unit step response curve is shown in Fig. 3.

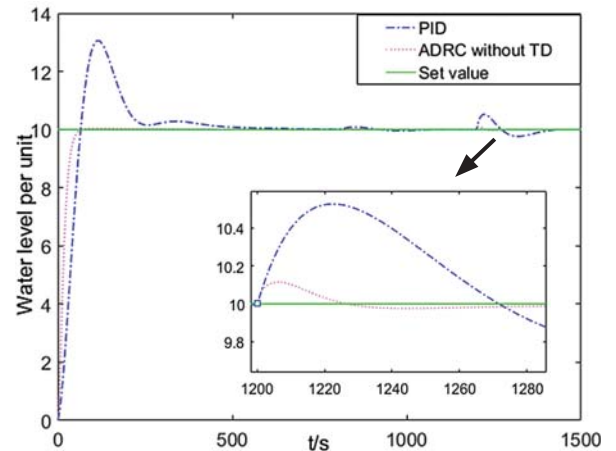


Fig. 3. The cascade three impulses of ADRC without tracking differentiator

As can be seen from Fig. 3., the ADRC step response without TD is fast and no overshoot, the system takes a short time to reach steady state, the PID control overshoot is large and the timeliness is poor. When adding water flow perturbation has little effect on PID and ADRC without TD has no change in steady state. When adding the steam flow perturbations, the contribution of the control flow to the control system has apparently overshoots. It can be seen from enlarged picture that the ADRC control system without TD is obviously smaller than the PID control system in transition time and overshoot.

2) ADRC with tracking differentiator

By simulation debugging, get a better set of parameters is: TD: $r = 5, h = 0.2$; ESO: $\beta_{01} = 100, \beta_{02} = 50, \beta_{03} = 10$; NLSEF: $\beta_1 = 5, \beta_{01} = 25$; disturbance compensation: $b_0 = 0.0023$. The secondary loop of the PID parameters as above. As shown in Fig. 4.

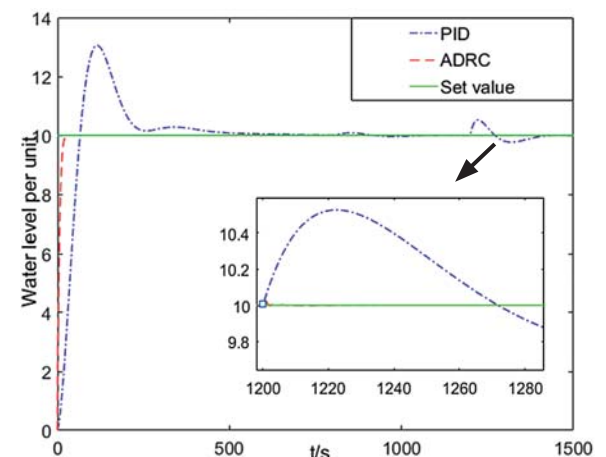


Fig. 4. The cascade three impulses of ADRC

It can be seen from Fig. 4. that the response speed of ADRC is fast and there is no overshoot. When adding water flow disturbances have little effect on the two controllers, when adding steam flow disturbances have almost no effect on ADRC, it can be seen from the enlarged graph that overshoot

is very small, the entire controller showed a good adaptability and timeliness.

3) Experimental Comparison of Two Kinds of Active Disturbance Rejection Controllers

The simulation results are shown in Fig. 5.

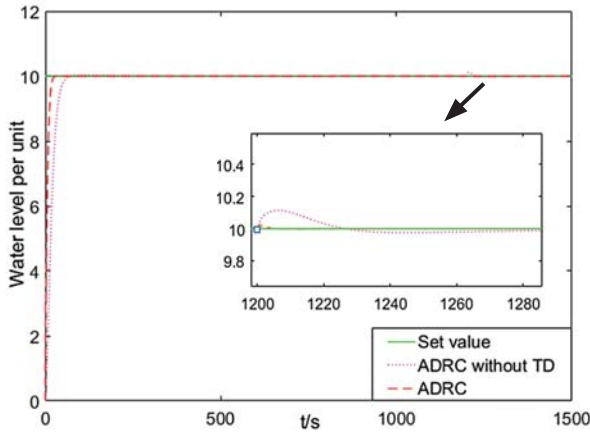


Fig. 5. Comparison of ADRC with tracking differentiator and without tracking differentiator

As can be seen from Figure 5, the ADRC with TD rises faster and reaches the steady state faster than the ADRC without TD as the step response curve is rising. However, there has jitter as the ADRC with TD is on the rise, while the ADRC without TD is more stable during the ascent. When adding water flow disturbances have no effect on these two ADRC controllers. When adding the disturbance of steam flow, the ADRC control system without TD has larger the overshoot than ADRC with TD. The more robust of the ADRC control system with TD, and the superior control performance of the two controllers compared to PID control, showing a very strong robustness.

To change the condition, when the time constant of the controlled object model increases 67%, the proportional coefficient increases 35%, the controlled object becomes

$$G_w(s) = \frac{0.05}{s(50s + 1)}$$

The simulation results are shown in Fig. 6.

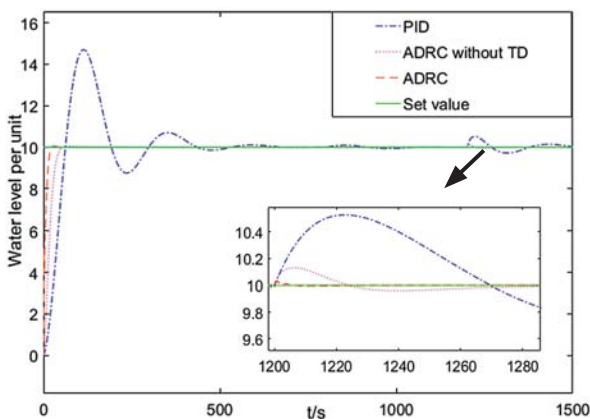


Fig. 6. ADRC under Changing Conditions

The simulation results are not changed, as shown in Fig. 7.

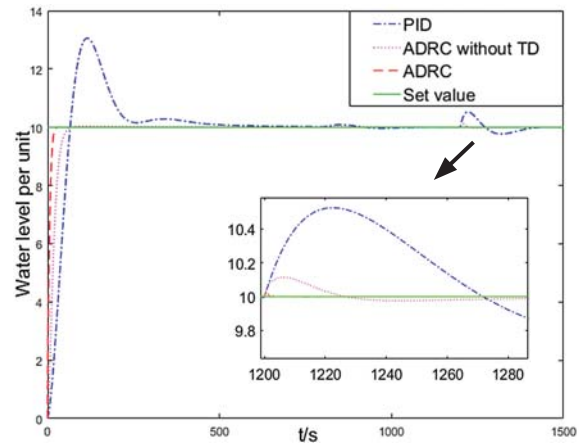


Fig. 7. ADRC without changing conditions

From Fig. 6. and Fig. 7. we can see that when the transfer function of feedwater flow changes, the overshoot of PID control becomes larger and the time for the system to reach steady state becomes longer. The ADRC controller with TD and the ADRC controller without TD adjust the feed water flow disturbance suppression ability is strong, no overshoot. To establish two kinds of ADRC control system can restrain the influence of a variety of uncertainties in the system well, with high control precision, fast response, strong adaptability, good robustness and so on.

CONCLUSION

This paper analyzes the dynamic change of the drum level of a large oil tanker and establishes the two-order model. By applying the ADRC control theory to the drum level control system of a large oil tanker auxiliary boiler, two kinds of ADRC controllers are designed and implemented. One is the traditional ADRC controller, and the other is to remove the TD simplified ADRC controller. Firstly, two kinds of drum water level cascade three-impulse ADRC algorithm are designed according to the non-linear, time-varying and strong interference of the drum water level system after obtaining the mathematical model of the water level of the three impulse drums. The performance of the control algorithm is tested based on the experimental model. It can be seen from the simulation results that the ADRC system can suppress the influence of various uncertainties in the system, and has the advantages of high control precision, fast response speed. Although the controller has shown the strong robustness and adaptability and achieves the expected results, it is necessary to further study in the future application due to the complexity of the control model and many parameters that need to be adjusted in the controller.

ACKNOWLEDGMENTS

The project is supported by “Liaoning Provincial Natural Science Foundation of China” (NO.201602071), also supported by “the Fundamental Research Funds for the Central Universities” (NO.3132016316). The authors also gratefully acknowledge the helpful comments and suggestions of the reviewers, which have improved the presentation.

REFERENCES

1. Hong-jun Liu, Pu Han, Dong-feng Wang.: *Simulation of Boiler Drum Water Level System DMC-PID Cascade Control*. Journal of System Simulation, 2004 (03): 450–453.
2. Xiao Feng.: *Fuzzy self-adapting PID control of drum water level in a power plant*, IFAC Proceedings Volumes, Volume 40, Issue 8, 2007, pp. 77–83.
3. Nan-hua Yu, Wen-tong Ma, Ming Su.: *Application of adaptive Grey predictor based algorithm to boiler drum level control*, Energy Conversion and Management, Volume 47, Issue 18, 2006, pp 2999–3007.
4. Jing-tao Zhang, Wei Wang, Tian-you Chai, et al.: *Intelligent Fuzzy Control of the Power Plant Boiler Water Level*, IFAC Proceedings Volumes, Volume 32, Issue 2, 1999, pp. 7241–7246.
5. Hamed Moradi, Majid Saffar-Avval, Firooz Bakhtiari-Nejad.: *Sliding mode control of drum water level in an industrial boiler unit with time varying parameters: A comparison with – robust control approach*, Journal of Process Control, Volume 22, Issue 10, 2012, pp. 1844–1855.
6. Jing-qing Han.: *Auto disturbance rejection control technique*. Frontier Science, 2007, 1(1): 24–31.
7. Hai-sheng Li.: *Research on Parameter Tuning and Optimization of Active Disturbance Rejection Controller*, Control Engineering. 2004,11(5): 419–423.
8. Hong Chen, Jian Zeng, Guang-jun Wang.: *Active Disturbance Rejection Control of Steam Generator Water Level Proceedings of the CSEE*, 2010, (32): 103–107.
9. Ju-yuan Jiang, Li-jing Li.: *The research on the new boiler water level automatic control system*. Mechanic Automation and Control Engineering (MACE), 2011 Second International Conference on, 2011.
10. Jing-qing Han.: *Auto disturbance rejection control technique*. Beijing: National Defense Industry Press, 2009: 255-262,280-286 (in Chinese).
11. Yong-chun Fang, Hui Shen, Xiu-yun Sun, Xu Zhang, Bin Xian.: *Control of Active Disturbance Rejection Control of Unmanned Helicopter*. Control Theory and Applications, 2014, 31(02): 238–243.
12. Chang-mei Hu, Jun Ren.: *Research and application of linear ADRC on cascade three-impulse control of drum water level*. Electric Power, 2014, 47 (12): 28–31.
13. Lin Fei, Hu Sun.: *A new type of extended state observer with a measurement noise system*. Control Theory and Applications. 2005, 22(6): 995–998
14. Zhi-qiang Gao.: *Scaling and bandwidth-parameterization based controller tuning Proceeding of the American Control Conference*. United States: IEEE, 2003: 4989–4996.
15. Simna Surendran, Vimal Kumar.: *Neural Network Based PI Controller Parameter Calculation on a Boiler Drum Level System*, Procedia Technology, Volume 24, 2016, pp. 1616–1622
16. Hai-sheng Li.: *Research on Parameter Tuning and Optimization of Active Disturbance Rejection Controller*. Control Engineering. 2004, 11(5): 419–423.
17. Jing-qing Han.: *Active disturbance rejection controller and its application*. Control and Decision, 1998, (01): 19–23.
18. Yuan-qing Xia, Li Dai, Meng-yin Fu, et al.: *Application of active disturbance rejection control in tank gun control system*, Journal of the Franklin Institute, Volume 351, Issue 4, 2014, pp. 2299–2314.
19. Fei Xia, Hao Zhang, Gui Zhang, et al.: *Image Processing in the Monitor of Boiler Drum Water Level on Power Plant*, Energy Procedia, Volume 17, 2012, pp. 266–272.
20. Jing-qing Han.: *Auto disturbance rejection control technique Frontier Science*, 2007, 1(1): 24–31.
21. Sun, K., L.P. Huang and Y. Mei.: *A nonlinear auto-disturbance rejection control for matrix converter fed induction motor drive system*. Transactions of China Electro technical Society 2007, 22(12), 39–45.
22. Jing-qing Han, Wen-ge Zhang.: *Active Disturbance Rejection Control for Large Delay Systems*. Control and Decision, 1999, (04): 67–71.
23. Xin Leng, Qi-dan Zhu.: *Multi-model Predictive Control of Boiler Water Level for Marine Boiler Based on Radial Basis Function Neural Network Dynamic Compensation*. Journal of Jilin University (Engineering and Technology Edition) 2011, 41(05): 1450–1455.

24. Hang Yi, Luo ZW, Svinin M, et al.: *Extended state observer technique for control of robot systems*. The Proc. of the 4th IEEE World Congress on Intelligent Control and Automation. Shanghai, 2002.
25. Y. Huang, H. Wan, J.L. Song, *Analysis and Design for Third Order Nonlinear Continuous Extended Status Observer*. Proceeding of 19th Chinese Control Congress. Hong Kong, China, 2000: 677–681.
26. Min Xu, Shao-yuan Li, Wen-jian Cai, *Cascade generalized predictive control strategy for boiler drum level*, ISA Transactions, Volume 44, Issue 3, 2005, pp. 399–411.

CONTACT WITH THE AUTHOR

Hui-bing Gan, Ph. D.
e-mail: ghbzq@dlmu.edu.cn
Faculty of Marine Engineering College
Dalian Maritime University
Dalian
CHINA

STUDY ON STRIKING SHIP WITH LOADING IMPACT ON THE PERFORMANCE OF THE DOUBLE HULL OIL TANKER COLLISION

Wenfeng Wu, Ph. D.

Yubin Yang, M. S.

Jianwei Zhang, Ph. D.

Jinshu Lu, Ph. D.

School of Port and Transportation Engineering, Zhejiang Ocean University, Zhoushan, Zhejiang, China

ABSTRACT

Due to the great danger of the collision of oil tankers, lots of research on the collision of oil tankers has been carried out. But, at present, the research on the collision of oil tankers mainly focuses on the loading condition of the struck ship, ignores the impact on the loading condition of the striking ship. However, during the actual oil tanker collision, the striking ship is generally in the state of loading. Therefore, it is necessary to carry out the analysis of the impact of the loading condition of the striking ship on the collision damage of the oil tanker. In this paper, the effect of striking ship with loading on the impact performance of the side structure during the collision of the cargo double hull oil tanker has been investigated. The ship collision model was established by using the finite element software ANSYS/LS-DYNA which is based on 7000 tons of double hull oil tankers. Based on the analysis of the collision force, impact of striking speed changes, impact of striking deep changes and structural energy absorption during the collision process, the influence of the striking ship with loading on the damage mechanism and the impact performance of the double shell oil ship side structure was expounded. The results show that the influence of the striking ship with loading can be great to the damage to side hull during the research of the collision performance of the oil tanker.

Keywords: Ship collision; Fluid-structure interaction; Impact parameters; Numerical simulation

INTRODUCTION

With the rapid development of the world economy, the maritime trade has become more and more busy, prompting a surge in the number of navigating ships, the increasing speed of ships and the more crowded route, which makes the probability of collisions between ships. As a complex and huge offshore movable building, the consequences of a collision are often catastrophic. Especially, the collision of a large oil tanker can not only cause damage to the hull structure, but also cause severe economic loss and potential environmental damage [1, 2]. Therefore, it is of great significance to carry out the research on the collision performance of the oil tanker, which is for the safety of navigation and the protection of the environment.

In the past, due to the complexity of the collision problem of oil tankers and the limitations of technical solutions, the research on the structural crash performance of oil tankers generally focused on the plastic deformation and failure mechanisms of the

structures, ignored the influence of liquid cargo [3, 4, 5, 6, 7, 8]. Recently, with the in-depth study of the mechanism of collision damage and the development of calculation power and sophistication of the software, some scholars have discussed the collision of oil tankers under the condition of loading.

Recently, the researches on the collision problem of liquid cargo tanker mainly focus on the sloshing interaction in ship collisions and the research object is mainly struck ship. Zhang [9] used three kinds of numerical simulation methods to study the interaction between fluid and structure of an oil tanker under impact load. The results show that the Lagrange Euler method is reasonable. It has a lower computational cost and can be used as a practical engineering application. Cui [10] analyzed the impact of liquid cargo on the anti-impact performance of the side structures and found that the liquid cargo had some influence on the side impact performance of the ship. Wu [11] analyzed the influence of tank sloshing on the crashworthiness of side structures of double-hull tankers with numerical software

ANSYS /LS-DYNA. The results show that the impact of liquid cargo can not be ignored in the study of the collision of double hull tanker.

In addition, a preliminary study of the impact on striking ship with loading has been carried out. Tabri [12] studied the collision performance of ships under the influence of sloshing by model tests and found that the sloshing of fluid in partially filled tanks influenced the collision dynamics and lowered the energy available for structural deformations. Rudan [13] used the arbitrary Eulerian-Lagrangian finite element method to analyze the sloshing interaction in ship collisions and found the free-surface elevation inside the partially filled tanks was well predicted with the numerical approach. However, none of these studies have deeply analyzed the mechanism of liquid sloshing on structural damage.

The aim of this paper is to investigate the impact of liquid cargo impact on the collision damage characteristics of double hull tankers. In order to get more intuitive results, four groups are set as follow: striking ship no load, striking ship single cabin loading with 80% of high-filling level, striking ship double cabin loading with 80% of high-filling level, striking ship triple cabin loading with 80% of high-filling level. Numerical simulations of a collision between two identical double-hull tankers are carried out by using the finite element software ANSYS/LS-DYNA. Through the comparative analysis of collision force and structural damage and deformation, the general rule of impact on the collision damage characteristics of double hull tankers with liquid cargo is obtained.

COLLISION SCENARIO

In this paper, a 7,000DWT double-hull tanker is selected as the research object. The striking ship is vertically centered at 4m/s and hit a stationary double hull tanker. The main dimension of the collision ships are presented on Tab. 1.

Tab. 1. Main dimensions of collision ships

Struck ship		Striking ship	
Item	Value	Item	Value
Spacing between transverse web frames	2.6 m	The height from bulb bow to baseline	6.3 m
Spacing between longitudinal girders	2.6 m	The length of bulb bow	3.07 m
Plate thickness	0.016 m		

In addition, in order to explore the impact characteristics of striking ship with loading on the collision damage of double-hull tankers, the loading conditions of the impact ship are four different states: no-load, single-cabin load, double-cabin load and three-cabin load. Ships collision scheme is shown in Tab. 2., the struck ship cabin distribution is shown in Fig. 1.

Tab. 2. Ship collision scheme

Group	Tonnage	Impact ship loaded condition
Case 1 (No load)	7000DWT	No liquid cargo loading
Case 2 (Single cabin loading)		First cabin loading liquid cargo
Case 3 (Double cabin loading)		First cabin and second cabin loading liquid cargo
Case 4 (Triple cabin loading)		Three cabin loading liquid cargo

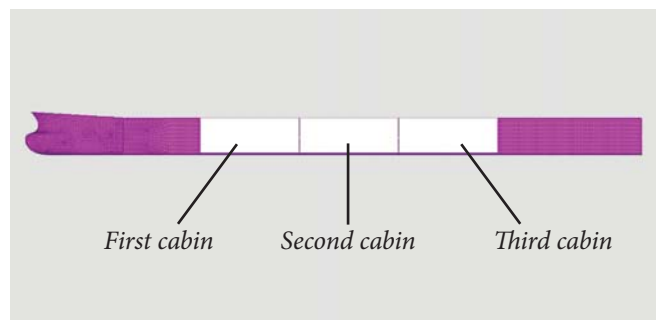


Fig. 1. Cabin distribution of struck ship

MODEL ESTABLISHMENT

SHIP COLLISION MODEL

Taking into account the partial characteristics of the ship collision and the computational efficiency calculation, the model is simplified in the process of establishing the ship model [14]. In this case, the struck ship is simplified into a cargo hold, and the center of the ship is guaranteed to be the center of mass and the center of gravity. The structure of the bow of the striking ship is consistent with the shape of the prototype bow and only the tank shell is retained in the side tank structure, but the centroid and weight of the striking ship are to be consistent with those of the actual ship. Ship collision numerical model is shown in Fig. 2.

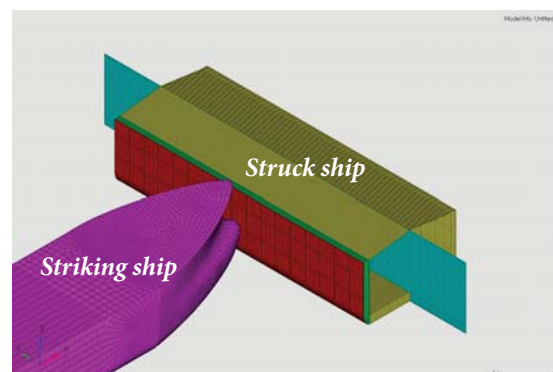


Fig. 2. Ship collision numerical model

In the collision of ships, the stiffness of the striking ship's bow is generally much higher than the side structure of the struck ship. Therefore, in this paper, a rigid material is used in the striking ship, and a plastic kinematics model is used in the struck ship. The parameters set in Tab. 3. Furthermore, the structure of collision ships are modeled with Belytschko-Tsay shell elements [15]. The contact between the striking ship and the struck ship is implemented by using a contact-automatic-to-surface formulation.

Tab. 3. Plastic kinematics material properties

Material properties	Value
Density	7800kg/m ³
Young's modulus	2.1×10 ¹¹ N/m ²
Poisson's ratio	0.3
Tangent modulus	1.18×10 ⁹ N/m ²
Yield stress	2.35×10 ⁸ N/m ²
Hardening parameter	0
Strain rate parameter(P)	5
Strain rate parameter(C)	40.4
Failure strain	0.15

CABIN CRUDE MODEL

Cabin crude oil model includes two parts, crude oil and air. The air and crude oil are modeled by using the eight-node solid elements. The model of crude oil in the cabin is shown in Fig. 3. In order to realize the fluid-structure interaction, the Arbitrary Lagrangian-Eulerian (ALE) algorithm is adopted. The interaction between the structure and the crude oil is defined by using the LS-DYNA coupling command "Constrained Lagrange in Solid" [16]. Besides, the material properties of the fluid model in this paper are mainly described by the NULL material model and the equation of state (EOS) in LS-DYNA.

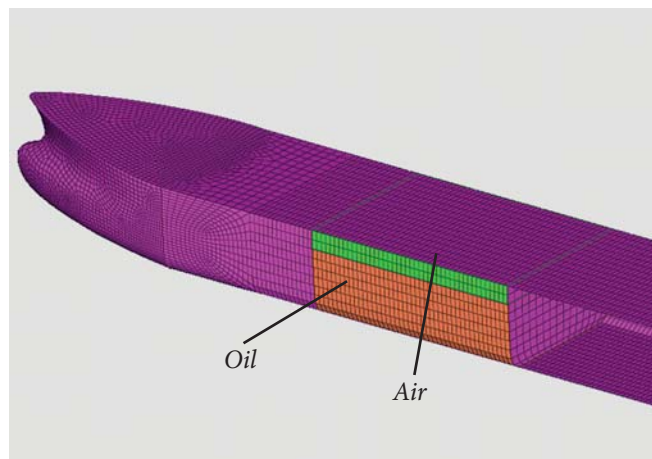


Fig. 3. Crude oil model

For air, the equation of state uses the linear polynomial equation of state provided by LS-DYNA and is described by the keyword "EOS LINEAR POLYNOMIAL". Air material parameters are listed in Tab. 4. The equation of state defines the pressure of the compressed material is shown in Eq. (1).

$$P = C_0 + C_1\mu + C_2\mu^2 + C_3\mu^3 + (C_4 + C_5\mu + C_6\mu^2)E \quad (1)$$

In Eq. (1):

P — Pressure;

$C_0, C_1, C_2, C_3, C_4, C_5$ and C_6 — Custom constants;

μ — The volume change rate;

E — The internal energy per initial volume.

Tab. 4. Air material parameters

Material properties	Value
Density	1.29 kg/m ³
Constant(C_0-C_3)	0
Constant(C_4, C_5)	0.4
Constant(C_6)	0

For crude oil, the equation of state uses the Gruneisen equation provided in LS-DYNA and is described by the keyword "EOS GRUNEUSEN". Crude material parameters are given in Tab. 5. The equation of state defines the pressure of the compressed material as shown in Eq. (2).

$$P = \frac{\rho_0 C^2 \mu \left[1 + \left(1 - \frac{\gamma_0}{2} \right) \mu \right]}{\left[1 - (S_1 - 1)\mu - S_2 \frac{\mu^2}{\mu + 1} - S_3 \frac{\mu^3}{(\mu + 1)^2} \right]^2} + (\gamma_0 + \alpha\mu)E \quad (2)$$

In Eq. (2):

P — Pressure;

ρ_0 — The initial fluid density;

C — The intercept of v_s-v_p curve;

ρ — The density of the fluid;

μ — The specific volume, $\mu = \rho/\rho_0 - 1$;

γ_0 — The Gruneisen gamma;

S_1, S_2, S_3 — The coefficients of the slope of the v_s-v_p curve;

E — The internal energy per initial volume.

Tab. 5. Crude oil material parameters

Material properties	Value
Density	0.855 × 10 ³ kg/m ³
Curve intercept (C)	1.5 × 10 ³
Kinematic viscosity	1.019 × 10 ⁻⁵ m ² /S
Slope coefficient (S_1)	1.921
Slope coefficient (S_2)	-0.096
Gruneisen gamma	0.5

SIMULATION RESULTS AND ANALYSIS

ANALYSIS OF THE SPEED CHANGE OF COLLISION SHIP

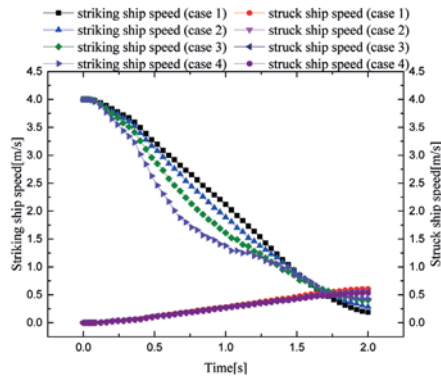


Fig. 4. Ship speed versus time for different loading of the striking ship

Fig. 4. is the curve for collision ships speed versus time for different loading of the striking ship. As shown in the figure, the speed of the collision ships includes the striking ship speed and the struck ship speed. It can be seen from the figure that the trend of the struck speed of each model is basically consistent with time.

The speed changes of the striking ship are mainly divided into three stages: the first stage of the impact time is 0.38 s ago, the striking ship is in contact with the struck ship in this stage. The speed variation of the striking ship is not quite different because of the lack of timely response of the liquid cargo and the similar collision situation in the initial collision ship. The second stage of the impact time is about 0.38 s to 1.7 s, through the post-processing software, it is found that the fluid in the cabin begin to respond at this time. It can be seen that the liquid cargo starts to respond at the time. The specific response is reflected in the more impact cargo, the faster the speed of impact ship changes. The main reason of this response is the impact of liquid cargo sloshing. In the third stage, the impact time is about after 1.7 s, the drift speed of the struck ship is greater than the speed of the striking ship, and the interaction between the striking ship and the struck ship is weakened.

PENETRATION DEPTH CHANGE ANALYSIS

Fig. 5. is the collision ship penetration depth versus time curve. As can be seen from Fig. 5., the penetration depth changes are mainly divided into three stages.

In the first stage, the impact time is about 0.38 s ago. During this phase, the striking ship's bulb bow contacts the side structure of the struck ship but do not crash the inner shell of the struck ship. The collision energy is transferred to the struck ship through the side structure deformation. In this case, due to the short collision time, there is no obvious response to the liquid cargo in the striking ship. In addition, the quality and structure of the collision are consistent, so the penetration depth is basically consistent with the time changes. The second phase of the impact time is about 0.38 s to 1.7 s, as time increase, the more liquid

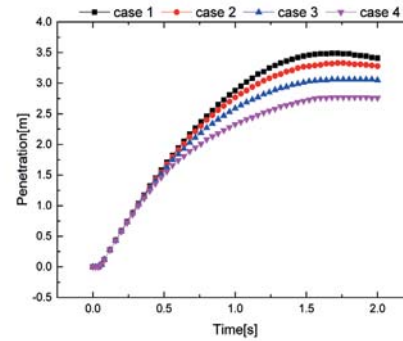


Fig. 5. Penetration versus time for different loading of the striking ship

cargo the striking ship carries, the shallower the penetration depth is. It is mainly due to the collision energy produced by the striking ship partially absorbed by the sloshing of liquid cargo in the cabin resulting from the sudden drop in impact speed of the striking ship. The third stage is after 1.7 s, the penetration depth changes very slowly and has a downward trend. At this stage, the collision speed of the struck ship is faster than the speed of the striking ship, the interaction between the striking ship and the struck ship is weakened. The striking ship and the struck ship slowly are separated at this stage.

COLLISION FORCE ANALYSIS

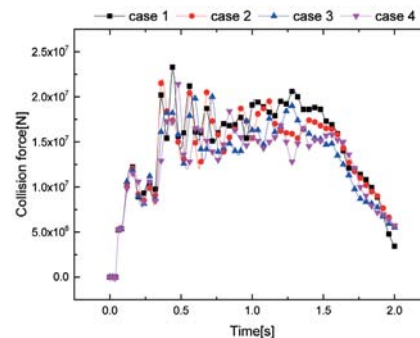


Fig. 6. Collision force versus time for different loading of the striking ship

Fig. 6. shows the curve for collision force versus time with different loading of the striking ship. As shown in the figure, the model collision force can be divided into three stages.

The first stage of collision time is about 0.38 s ago, the striking ship impacts the struck ship, but this collision is not the role of the inner shell. This stage is 0.17 s ago, the collision force is significantly increased due to the deformation of the side structure of the ship being struck against the propulsion of the striking ship. In the period of 0.17 s to 0.38 s, due to the rupture of the struck ship's out shell, the striking ship has a direct contact with the longitudinal girders and transverse web frames but has not yet directly interacted with the inner shell. Because of the weak response of liquid cargo in striking ship cabin at this stage and the impact conditions in each collision scene are the same, the collision force of each model in this stage is basically the same.

The second stage of collision time is about 0.38 s to 1.7 s, due to the striking ship contact with the inner shell of the struck ship, the collision force rises rapidly until the inner shell

is damaged, then the collision force decreases. Besides, with the continued impact of the striking ship, there is a certain fluctuation in the collision force.

In the third stage, when the collision time reaches to 1.7 s, the collision force begins to drop. At this time, the collision between the striking ship and the struck ship are weakened because the striking ship speed is less than the speed of the struck ship. Due to the complexity of the collision process at this stage, the impact on the striking ship with loading does not have a significant effect on the impact.

ENERGY ABSORPTION ANALYSIS

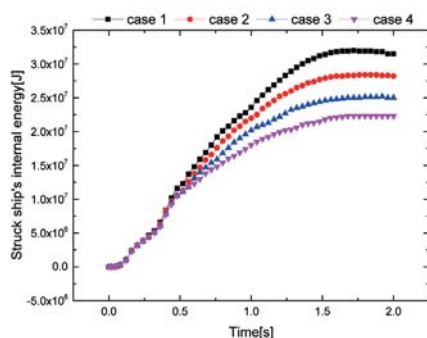


Fig. 7. Struck ship's internal energy versus time for different loading of the striking ship

Fig. 7. shows the internal energy of the struck ship varies with time. It can be seen from the figure that in the initial stage of the collision, that is, before the collision time is about 0.38 s, whether the striking ship laden with liquid cargo or not, it will have little effect on the internal energy change in the struck ship. At this moment, there is no obvious response to the liquid cargo in the striking ship's cabin, and the collision modes are basically the same. Therefore, the internal energy produced by the structural deformation of the struck ship during this stage is less related to the loading state of the striking ship. At the later stage of the collision, that is, after the collision time is about 0.38 s, it can be seen from Fig. 4. that at this moment, due to the obvious response of liquid cargo, the collision speed of striking ship is obviously different to the striking ship under the loading condition. The more liquid cargo the striking ship loads, the faster the speed of striking ship decreases, the shallower the penetration depth is, which leads to a smaller internal energy of struck ship.

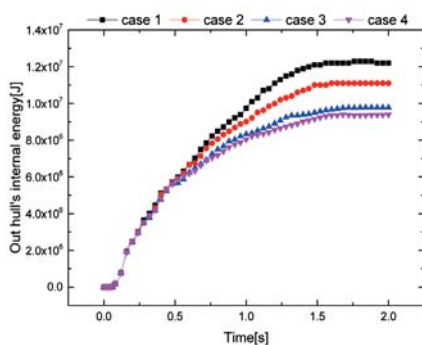


Fig. 8. Out hull's internal energy versus time for different loading of the striking ship

Fig. 8. reflects the out hull's internal energy of the struck ship versus time for four different loading of the striking ship. It can be seen from the figure that the changes of the out hull's internal energy of the four kinds of collision cases are basically the same before the collision time is about 0.38 s. The main reason is that the liquid cargo in the cabin does not play a significant role in the beginning of the collision. After the collision time is about 0.38 s, with the increase of the penetration depth, the shell continues to bend and deform in the direction of collision, out hull's internal energy increases gradually. As can be seen from Fig. 4., in the period of 0.38 s to 1.7 s, the impact velocity decreases with the decrease of liquid cargo of the striking ship, and the degree of the deformation of the shell structure is relatively low. After 1.7 s, due to the separation of the striking ship and the struck ship, the impact of the striking ship on the struck ship is rapidly reduced and the deformation energy is absorbed by the struck ship's side structure is basically completed. As a result, the internal energy of the out hull of the struck ship tends to be gentle.

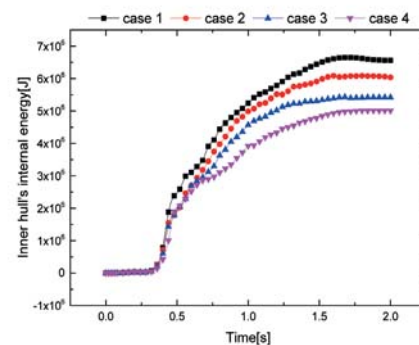


Fig. 9. Inner hull's internal energy versus time for different loading of the striking ship

Fig. 9. reflects the inner hull's internal energy of the struck ship versus time in different loading of the striking ship. It can be seen from the figure that before the time is about 0.38 s, the striking ship does not have a significant effect on the inner shell, and the internal energy of inner shell increases gently. With the impelling of the collision time, the striking ship contacts with the inner shell, and the internal energy of inner shell increases rapidly. At this time, the internal energy of inner shell is mainly derived from the inner shell deformation caused by the collision. The more liquid cargo the striking ship loads, the more obvious speed the striking ship falls, the shallower the penetration depth is, the less energy the deformation of the inner shell absorbs, the lighter the ship will be. To sum up, during the collision of ships, the more the striking ship carries liquid cargo, the less the energy absorbed by the shell plates and the whole ship, which indicates that striking ship with loading has an important impact on the collision damage of the ships.

CONCLUSION

In this paper, taking the double-hull tankers as the research object, using the application of ANSYS / LS-DYNA to compare the impact of ship collision on the side shell of double hull oil tankers, the main conclusions are as follows:

(1) In the early stage of collision, under the loading condition of the striking ship has little impact on penetration depth, collision force and structure energy absorption, etc. It can ignore the influence of side structure damage which is caused by the loading striking ship.

(2) In the later stage of collision, the collision of cargo loading striking ship has an obvious influence on the collision of double hull oil tankers, which is mainly reflected in the impact of cargo ship collision relative to no-load, the shallower penetration depth the striking ship is, the less energy the side structure of the struck ship absorbs. With the striking ship carries more cargo, the penetration depth and the structure energy absorption can reduce accordingly. Therefore, the study of the collision of double-hull oil tankers can not ignore the influence of striking ship which is under the condition of loading.

However, due to the limitations of the research method, the impact of striking ship with loading on ship collision has not been given quantitatively in this paper. In subsequent research, the quantitative relationship between the loading condition of the striking ship (liquid properties, filling ratio and liquid viscosity) and the damage condition of the struck ship (structural deformation, collision depth and structural energy absorption) are worthy of further study.

ACKNOWLEDGEMENTS

This project is partially supported by Zhejiang Provincial Natural Science Foundation Youth Fund (LQ16E090003, LQ14E090001) and the project of bureau of science and technology of Zhoushan (2015C41009).

REFERENCES

1. Haris S., Amdahl J.: *Analysis of ship-ship collision damage accounting for bow and side deformation interaction*. Marine Structures. No 7, Vol. 32, 2013, pp.18–48.
2. Liu B., Soares C.G.: *Assessment of the strength of double-hull tanker side structures in minor ship collisions*. Engineering Structures. Vol. 120, 2016, pp. 1–12.
3. Prabowo A.R., Dong M.B., Sohn J.M., Zakki A.F., Cao B., Wang Q.: *Analysis of structural damage on the struck ship under side collision scenario*. Alexandria Engineering Journal. 2017.
4. Liu B.: *Analytical method to assess double-hull ship structures subjected to bulbous bow collision*. Ocean Engineering. Vol. 142, 2017, pp. 27–38.
5. Liu B., Villavicencio R., Zhang S., Soares C.G.: *Assessment of external dynamics and internal mechanics in ship collisions*. Ocean Engineering. Vol. 141, 2017, pp. 326–336.
6. Lee S.G., Lee J.S., Lee H.S., Park J.H., Jung T.Y.: *Full-scale Ship Collision, Grounding and Sinking Simulation Using Highly Advanced M&S System of FSI Analysis Technique*. Procedia Engineering. Vol. 173, 2017, p.1507-1514.
7. Gagnon R.E., Wang J.: *Numerical simulations of a tanker collision with a bergy bit incorporating hydrodynamics, a validated ice model and damage to the vessel*. Cold Regions Science and Technology. No 5, Vol. 81, 2012, pp. 26–35.
8. Yu Z., Amdahl J., Storheim M.: *A new approach for coupling external dynamics and internal mechanics in ship collisions*. Marine Structures. Vol. 45, 2016, pp. 110–132.
9. Zhang A., Suzuki K.: *A comparative study of numerical simulations for fluid-structure interaction of liquid-filled tank during ship collision*. Ocean Engineering. No 5, Vol. 34, 2007, pp. 645–652.
10. Jie C., Zhang A.M., Yao X.L., Yang S.T.: *Influence of liquid cargo in tank on crashworthiness of double-skin side structure*. Journal of Ship Mechanics. No 3, Vol. 15, 2011, pp. 259–268.
11. Wu W.F., Yang Y.B., Lu J.S., Deng J.J., Zhu F.X.: *Study on liquid cargo sloshing impact on the performance of the double hull oil tanker collision*. China Shiprepair. No 6, Vol. 29, 2016, pp.10–14.
12. Tabri K., Matusiak J., Varsta P.: *Sloshing interaction in ship collisions—An experimental and numerical study*. Ocean Engineering. No 17, Vol. 36, 2009, pp. 1366–1376.
13. Rudan S., Tabri K., Klarić I.: *Analysis of sloshing interaction in ship collisions by means of ALE finite element method*. In: Proceedings of fifth International Conference on Collision and Grounding of Ships, Espoo, Finland, 2010, pp. 229–234.
14. Sun B., Hu Z., Wang G.: *An analytical method for predicting the ship side structure response in raked bow collisions*. Marine Structures. Vol. 41, 2015, pp. 288–311.
15. Belytschko T., Lin J.I., Chen-Shyh T.: *Explicit algorithms for the nonlinear dynamics of shells*. Computer Methods in Applied Mechanics and Engineering. No 2, Vol. 42, 1984, pp. 225–251.
16. Song M., Ma J., Huang Y.: *Fluid-structure interaction analysis of ship-ship collisions*. Marine Structures. Vol. 55, 2017, pp. 121–136.
17. Rudan S., Volarić D.: *Fluid structure interaction analysis of a ship collision*. In: Proceedings of the ICCGS 2016, Ulsan, Koreja, 2016.

CONTACT WITH THE AUTHOR

Jianwei Zhang, Ph. D.

e-mail: zhangjianwei@zjou.edu.cn

tel: 18858397351

School of Port and Transportation Engineering

Zhejiang Ocean University

Zhoushan Zhejiang 316022

CHINA

SIMULATION AND EXPERIMENTAL STUDY OF SCR INJECTION SYSTEM

Jun Du, Prof.

Yan Zhang, Postgraduate

Zeliang Cai, Postgraduate

College of Energy and Power, Jiangsu University of Science and Technology, Jingkou, Zhenjiang, China

ABSTRACT

According to actual engineering test, we design a linear controlled spray ammonia grille, and apply it to the SCR injection system of ship tail gas treatment. In this paper, the geometric model of ammonia injection grid was built in the flue of diesel engine, and the effects of spray atomization, ammonia uniformity and urea droplet distribution on spray atomization were simulated. Then the test bench was set up to observe the injection status of the ammonia injection grille. The NO_x content of the outlet was measured by the original data of the flue gas, and the experimental data were processed. We calculate the denitrification rate by taking the average value to verify the correctness of the spray ammonia grille scheme.

Keywords: Ammonia grille; Flow field; Uniformity; SCR test; The denitrification rate

INTRODUCTION

In order to achieve a good catalytic effect, the SCR reactor needs to control the change of parameters of the front-end of the catalytic converter. The reactor gas mixing state and system denitrification rate and reducing agent distribution uniformity is important link of ammonia, the distribution uniformity of NH_3 depends on the atomization quality of urea. This would require the SCR injection system for structural optimization, by using the high quality of urea [1], control suitable injection amount, good atomization effect, reasonable structure design and so on methods to improve the spray atomization effect, the effect of jet atomization in order to improve the removal rate of NO_x .

At present, the SCR system has a key research object besides the catalyst study, which is the injection system, there are many people working on the simulation of ammonia grille and its corresponding bench experiment [2]. Many SCR denitrification experiments use air to replace the exhaust gas produced by diesel engines [3, 4] replacing NH_3 with carbon oxide, explore the mixing uniformity of waste gas and NH_3 , and the distribution of flow field, concentration field and pressure field in the flue, and obtain the optimal design scheme of the injection device in the

SCR catalytic reaction system [5, 6, 7]. Subhasish Bhattachajee used Fluent to simulate the fluidity of air flow within the SCR catalytic reactor and its effect on the concentration distribution of NH_3 in the first layer catalyst [8]. The result is that the larger the flow resistance in the catalytic converter, the better the uniformity of NH_3 . Adams B established the CFD model and simulated NH_3 injection [9], the results show that the injection speed of NH_3 can be adjusted in a certain range, and the concentration distribution of NH_3 at the entrance of the catalyst is more uniform. Naqvi simulated the effect of spraying ammonia grille on velocity uniformity in the flue of SCR system [10]. Enrico Tronconi simulated the distribution of ammonia injection and concentration field in the SCR injection system by simulation software, and proposed the optimal design scheme [11]. Tao Qiu used the energy conservation equation and SCR reaction model, proposing a method for estimating the downstream exhaust temperature of the catalyst [12]. Ossi Tapani Kaario established a single droplet simulation phase diagram, which predicted the optimal operation area of the SCR system and verified the HLR method at high Reynolds number [13].

In this paper, NO_x is used to determine the amount of NO_x in flue gas under stable condition of diesel engine by NO_x

sensor to calculate the amount of urea solution that needs to be sprayed. Then, a suitable geometrical model for the injection of ammonia grille was established to simulate the effect of spray atomization flow field distribution, ammonia uniformity and urea droplet distribution on the result of spray atomization. And the test bench was built to observe the injection status of the injection grate and calculate the denitrification rate to verify the correctness of the injection.

THE BASIC MODEL

At present, there are three main types of Ammonia-Injection Grid used in industry: vortex static mixing type, linear control type and zoned control type. According to the actual engineering test, this paper designs a linear control type of injection grate, which is arranged in the flue, the axial jet, 4 rows \times 6 holes, and the aperture is 1.06 mm. The layout of the injection of ammonia grille in the flue is shown in Fig. 1.

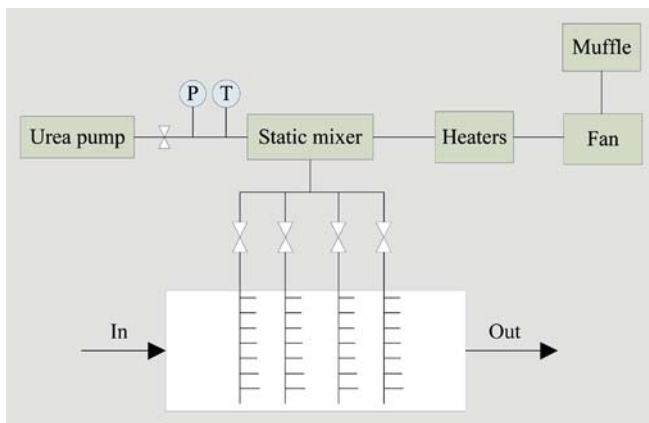


Fig. 1. Spray ammonia grid piping layout

THE TAB MODEL

The TAB model is a common model for simulating droplet collision and crushing in FLUENT simulation system, and also called Taylor ratio model [14]. This kind of model is suitable for low speed spray, due to fluid flow and collision between the droplet surface wave droplets produced force in the process of collision, and amplitude increases, this is a major cause of droplet breakage. The force equation of the droplet surface in TAB model is as follows:

$$F_a - F_\mu - F_\sigma = \frac{d^2 y}{dt^2} \quad (1)$$

$$F_a = -\frac{C_F \rho_a}{C_b \rho_d \gamma^2} |\mu_a - \mu_d|^2 \quad (2)$$

$$F_\mu = C_d \frac{\mu_d}{\rho_d \gamma^2} \frac{dy}{dt} \quad (3)$$

$$F_\sigma = C_k \frac{\sigma y}{\rho_d \gamma^3} \quad (4)$$

In Eq. (1), (2), (3) and (4):

F_a — the aerodynamic force on the droplet surface of the atomizing liquid N/m;

F_σ — surface tension on the surface of a droplet, N/m;

F_μ — the viscous force on the surface of a droplet, N/m;

r — the initial droplet radius, m;

μ_d — the kinetic viscosity of liquid drop, kg/(m·s);

C_F, C_k, C_d — dimensionless parameters.

DISCRETE PHASE MODEL

The urea solution is injected into the flue, and atomized into fine droplets, but its content is the exhaust flow accounted for less, so the use of spray process is described DPM discrete model, have occurred due to heat transfer and evaporation of liquid droplets and gas mixing phenomenon in the process of heat and mass transfer effects, hence there is a need to consider the droplet discrete and continuous gas phase between. Firstly, in the absence of discrete phase on the basis of the continuous phase to continuous phase after the simulation calculation results as the initial conditions, the activation of discrete items, for each source of jet flow field simulation calculation.

THE CHEMICAL REACTION MECHANISM OF UREA DECOMPOSITION

The pyrolysis reaction and hydrolysis of isocyanate will occur in the flue, and Yim et al. studied the reaction rate of urea decomposition and the experimental verification. Therefore, this paper USES the law to simulate the pyrolysis and hydrolysis rate of urea [15]. The equations are as follows:

$$r_1 = A_1 \exp\left(\frac{-E_1}{RT}\right) C_{(NH_2)_2CO} \quad (5)$$

$$r_2 = A_2 \exp\left(\frac{-E_2}{RT}\right) C_{HNCO} \cdot C_{H_2O} \quad (6)$$

In Eq. (5) and (6):

r_1 — the reaction rate of urea pyrolysis;

r_2 — the reaction rate of urea hydrolysis;

A_1, E_1, A_2, E_2 — the reaction rate constant;

$A_1 = 4900 \text{ m}^3 \cdot \text{kmol}^{-1} \cdot \text{s}^{-1}$;

$E_1 = 2.3033 \times 10^7 \text{ J} \cdot \text{kmol}^{-1}$;

$A_2 = 2.5 \times 10^8 \text{ m}^6 \cdot \text{kmol}^{-2} \cdot \text{s}^{-1}$;

$E_2 = 6.222 \times 10^7 \text{ J} \cdot \text{kmol}^{-1}$.

DESIGN OF PARAMETER

DETERMINATION OF UREA DEMAND

This paper takes a type of Marine diesel engine as an example, measured the volume flow of flue gas under stable condition of diesel engine was $V=49211 \text{ m}^3/\text{h}$ and the concentration of the NO_x was $\rho=600\text{ppm}$, and calculated the amount of urea solution to be sprayed from this.

It is assumed that the mole ratio of NO₂ to NO in the exhaust gas of a marine diesel is 1/9, and the Molar mass are M_{NO} = 30g/mol; M_{NO₂} = 46g/mol, then the calculation formula of the NO_x's average Molar mass is:

$$\overline{M} = 0.1 \times M_{NO_2} + 0.9 \times M_{NO} = 31.6 \text{ g/mol}$$

In this formula,

M_{NO} — the Molar mass of NO, value as 30g/mol;

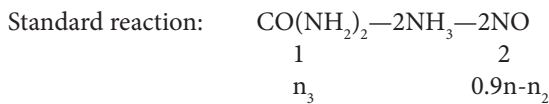
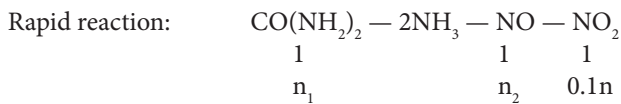
M_{NO₂} — the Molar mass of NO₂, value as 46g/mol.

Therefore, the mass of NO_x in unit time is:

$$m = \rho \times \frac{\overline{M}}{M_V} \times V = 600 \times \frac{31.6}{22.4} \times 49211 = 41.65 \times 10^6 \text{ mg} = 41.65 \text{ kg}$$

In this formula, \overline{M}_V — the average molar volume of NO_x; under standard condition the molar volume of gas is 22.4L/mol.

The relationship between the four reactants CO(NH₂)₂, NH₃, NO and NO₂ is as follow.



In this formula: n — the amount of substance of NO_x in exhaust gas; n₁ — the amount of urea material substance required for NO_x's rapid reaction; n₂ — the amount of NO substance involved in rapid reactions; n₃ — the amount of urea material substance required for NO_x's standard reaction.

It can be obtained by the proportional formula: n₁ = 0.1n; n₂ = 0.1n; n₃ = 0.4n.

The SCR injection system is responsible for mixing urea solutions with exhaust emissions from the main engine after the urea solution is injected into the flue pipe by a jet pump. Generally, the power of a diesel engine is greater in a ship's sailing work, the internal temperature of the engine room is high, and the SCR system space is limited, therefore, the urea solution with mass concentration of 40% and density of 1.1 kg/m³ is chosen as SCR denitrification reducer in this paper, its freezing point is 0 degrees centigrade, so it can be stored in the ship's cabin for a long time. And it avoids occurrence of ice during the flight, affecting the jet effect.

Therefore, the amount of urea required to spray per unit of time:

$$m_{\text{urea}} = (n_1 + n_3) \times 60 \div 40\% = 0.5 \times \frac{41.65}{31.6} \times 60 \div 40\% = 98.85 \text{ kg/h}$$

BASIC ASSUMPTIONS

In order to achieve the atomization effect of SCR injection system and easy to operate, this chapter makes the following assumptions about the simulation process:

- (1) Exhaust gas from the diesel engine is considered an ideal gas;
- (2) Because the import and export temperature of the SCR

system is small, and the thermal loss of the gas in the whole process is not considered, the whole simulation process is set up as an adiabatic system;

(3) Assuming that the flue gas flow in the catalyst channel is constant and incompressible flow;

(4) Set the wall of the flue as viscous flow, no slip and no heat conduction on the wall surface.

BOUNDARY CONDITION SETTING

The numerical simulation of flue gas mixing with NH₃ is divided into two velocity inlets and one pressure outlet condition:

Tab. 1. Inlet flue gas parameter setting

NO concentration in inlet flue gas	Velocity of flow	Temperature	The mole fraction of each component (%)				
			NO	O ₂	H ₂ O	CO ₂	N ₂
ppm	m/s	K					
600	14.8	623	0.001	0.036	0.097	0.148	0.718

Relevant studies show that the mixing rate is well when the urea injection rate is equal to the exhaust gas exhaust rate [16], V_{injection} = V = 14.8m/s.

Tab. 2. Setting of reducing agent inlet parameters

Velocity of flow	Temperature	Turbulent intensity	Hydraulic diameter	The mole fraction of each component (%)		
				NH ₃	O ₂	N ₂
m/s	K	%	mm			
14.8	300	10	0.5	0.05	0.2	0.75

The export boundary conditions are pressure outlet, wall insulation, viscous flow, no slip, and no heat conduction.

THE SIMULATION ANALYSIS OF THE INJECTION OF AMMONIA GRILLE

The flow field distribution of the flue and the first layer of SCR catalysts entrance section is presented in Fig. 2.

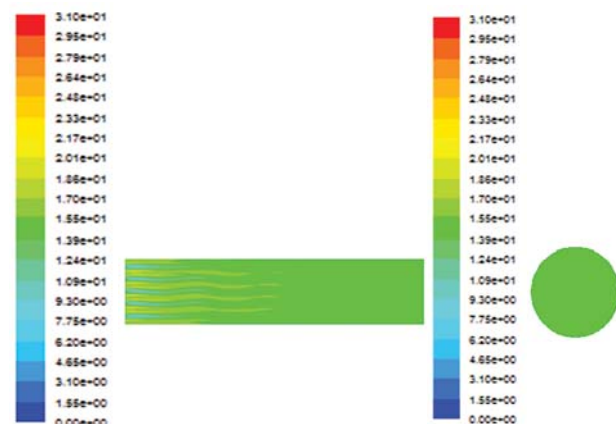


Fig. 2. Flow field Profile

The internal flow diagram after joined the spraying ammonia grille is presented in Fig. 2. The maximum velocity of export is 18.7 m/s, due to the size of the ammonia injection grid compared to the size of the whole flue is much smaller, so when the flue gas flows through the ammonia injection grid, the ammonia injection grid has little effect on flow field and the resistance loss is small, There isn't form vortex area and velocity deviation in flue area. Obviously, the influence of spraying ammonia grille flow field is smaller.

The concentration distribution of NH_3 in flue is presented in Fig. 3.

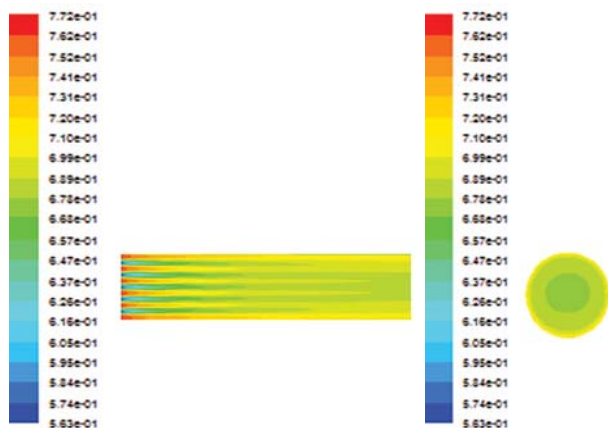


Fig. 3. NH_3 concentration profile

The concentration distribution of spraying ammonia grille NH_3 is presented in Fig. 3. We can found that the flue near the wall of ammonia concentration is higher than that of the middle section, there is a certain deviation. Uneven distribution of ammonia concentration said that the reductant and the flue gas has failed to fully mix, it is easy to affect denitrification efficiency of the system. Accordingly, decorate spraying ammonia grille can increase the disturbance of flue, improve the ammonia concentration distribution, and improve the denitrification efficiency. After ammonia by multiple nozzle, mainly concentrated in the vent and spread slowly. From the full degree and the uniformity, the type of ammonia injection method is much better and the use of the pipeline space is full. The urea droplet density distribution in the flue is shown in Fig. 4.

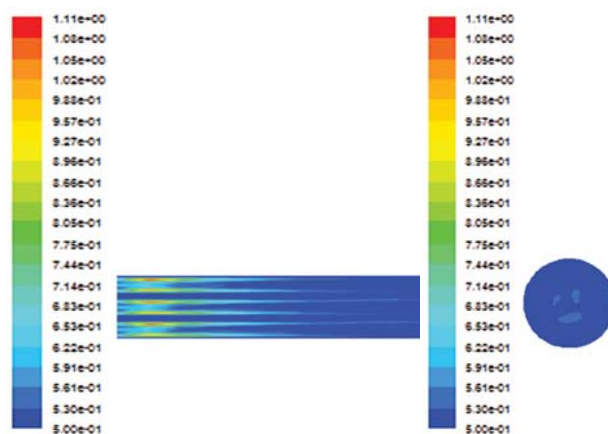


Fig. 4. The density distribution of urea droplet density

The urea droplet distribution of concentration field in the flue after join the ammonia injection grid is presented in Fig. 4. When more than one axis of the nozzle spray, the spray range is wide, the urea solution atomization effect is good and the droplets uniformity is good. The droplet content is higher near the export, by the time the speed is slowly. At the entrance of the first layer of the catalyst residual, only a small amount of urea, the urea aqueous solution evaporates pyrolysis effect is very good, reductant spray are uniformly mixed with the flue gas and can effectively improve the rate of catalytic reduction reaction.

Based on the analysis above, the ammonia injection grid, NH_3 concentration distribution and flow field distribution uniformity droplets in both injection effect is better than a single nozzle, the efficiency of urea pyrolysis generating NH_3 is higher, gas mixed more evenly before entering the SCR catalyst layer, it will improve the NO_x 's conversion rate and reduce the reductant's leak of NH_3 .

EXPERIMENTAL STUDY

SCHEME DESIGN

According to the design of the ammonia injection grid injection effect is good, we will be the device installed in the flue, combination of urea pump, SCR catalytic reactor, control and detection system, such as a test bench, the flow chart is shown in Fig. 5.

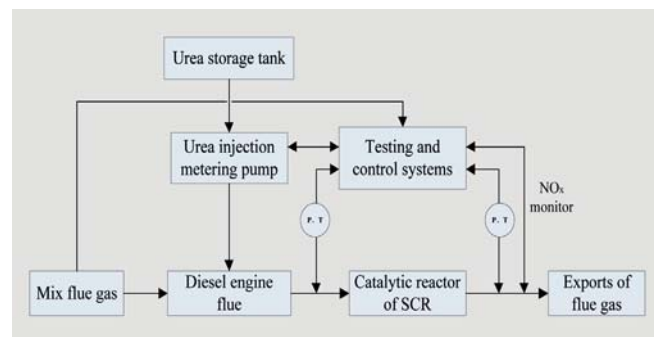


Fig. 5. Experimental flowchart

The equipment includes NO_x sensor, temperature controller, pressure sensor, gas mixing heater, etc. Before starting the experiment, the injection of the sprayed ammonia grille designed by this paper is conducted to observe the injection status. After that, the measuring instruments used in all experiments are calibrated separately, and the flow control apparatus, thermocouple and sensors are tested to ensure the correctness of the experimental results. Connect all the experimental devices to the test system for normal operation. Turn on the computer, connect the test system with the computer test software, and initialize the test instrument. Adjust the gas flow after entering the equilibrium gas N_2 . The sealing of the test system is checked to ensure that the connection between each device and the flue is well sealed. Open the electric heater, the gas mixer and SCR reactor were heated to the experimental

temperature, to reach the set value of flue gas temperature, open the steel cylinder control valve, access the supplied mixed gas, the gas flow balance after a period of time, start the experiment. The details of the experimental scheme are as follows:

Tab. 2. Setting of reducing agent inlet parameters

Test plan	Gas flow(kg/h)	NO _x content (ppm)	Exhaust temperature (k)	Flow velocity (m/s)
A	43490	473	537	13.92
B	61570	541	592	14.1
C	80214	600	623	14.8
D	102733	849	704	15.76

INJECTION TEST OF SPRAY AMMONIA GRILLE

Before the experiment, the performance of the ammonia jet grille designed in this paper was tested, the injection of urea water solution is shown in Fig. 6.



Fig. 6. Injection test diagram of injection of ammonia grille

It can be seen from Fig. 6., the spraying of ammonia grille is better, the liquid squirts out and becomes a tiny droplet of mist, spray mist like to stretch around the center axis, irregular cone, the edges of the droplets are content is significantly lower than the center position, the lower the content of the closer it gets to the surrounding area. But the spray uniformity is good, the injection Angle is large, meet the experiment requirement.

SCR EXPERIMENT DENITRIFICATION RATE

The urea injection metering pump was started based on the previous urea injection, open the control valve and conduct five experiments for each program, record the NO_x content of the five flue gas outlet, and find the average value, the experimental data is shown in the Table 4.

Tab. 2. Setting of reducing agent inlet parameters

Test plan	Urea discharge (kg/h)	jet velocity	Export NO _x content (ppm)	Export NO _x content average (ppm)
A	42.25	13.92	21.88	28.75
			29.09	
			34.75	
			26.40	
B	68.43	14.1	31.63	49.62
			50.21	
			36.65	
			41.00	
C	98.85	14.8	57.19	53.18
			63.05	
			57.66	
			63.05	
D	179.17	15.76	41.83	131.79
			51.16	
			52.20	
			107.33	
			142.80	
			155.04	
			132.10	
			121.68	

According to the experimental data in Table 5 and Table 6, the rate of denitrification of each scheme is calculated according to the formula of catalytic reaction rate of SCR system (bottom 7). The results are shown in Fig. 7.

$$\eta_{NO} = \frac{NO_{in} - NO_{out}}{NO_{in}} \times 100\% \quad (7)$$

In Eq. (7):

NO_{in} — the concentration of NO at the inlet of SCR reactor, mg/m³;

NO_{out} — the concentration of NO at the exit of the SCR reactor, mg/m³.

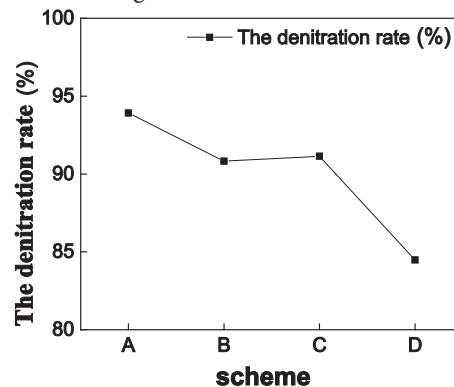


Fig. 7. Denitrification of different schemes

The denitrification rate of the four diesel engine flue gas flow schemes is different. Programme A has the largest denitrification rate of 93.92 %, at this time, the denitrification efficiency of the SCR reactor is optimal. Plan D denitrification rate is the lowest, at 84.48 %, this is because the plan D maximum flow, high temperature, a part of NH_3 easy to oxidation, lead to part of NO_x is not oxidation, so the denitrification rate is low. Although the catalytic efficiency of programme D is less than that of the other three schemes, it is more than 80 % and meets the emission requirements.

CONCLUSIONS

In this paper, NO_x is used to determine the amount of NO_x in flue gas under stable condition of diesel engine by NO_x sensor to calculate the amount of urea solution that needs to be sprayed. And then we build the appropriate geometric model of the injection grid, the effect of spray atomization flow field distribution, ammonia uniformity and urea droplet distribution on atomization results was simulated. Set up the test bench to observe the injection status of the injection grate, by testing the correctness of the scheme, the experimental data are processed and the following conclusions are drawn.

In the simulation, we found that the spray atomization effect of the 4×6 sprayed ammonia grille designed in this paper is better. Before starting the experiment, ammonia injection grid carried out the external experiment of the system, and the spray atomization effect was better, which met the requirements of the system. To calculate the denitrification rate of the SCR system experiment, the denitrification rate of four diesel engine flue gas flow schemes is different, but it is more than 80 % and meets the emission requirements.

ACKNOWLEDGEMENTS

This project is partially supported by Jiangsu University of Science and Technology.

REFERENCES

- Baik J H, Yim S D, Nam I S, et al., *Control of NO_x emissions from diesel engine by selective catalytic reduction (SCR) with urea* [J]. Topics in Catalysis, 2004, 30–31(1–4): 37–41.
- Lei Z, Wen C, Chen B., *Optimization of internals for Selective Catalytic Reduction (SCR) for NO removal* [J]. Environmental Science & Technology, 2011, 45(8): 3437–3444.
- Chen, Ming, and S. Williams. *Modelling and Optimization of SCR-Exhaust Aftertreatment Systems*. SAE 2005 World Congress & Exhibition, 2005.
- Weltens, Herman, et al., *Optimisation of Catalytic Converter Gas Flow Distribution by CFD Prediction*. International Congress & Exposition, 1993.
- Ho Jeong Chae, 500Tac Choo, Hoon Choe, et al., *Direct use of Knetic parameters for modeling and simulation of a selective catalytic reduction Process* [J] Ind. Eng. Chem. Res. 2000 39(5): 1159–1170.
- Tronconi E, Beretta A, Elmi A S, et al., *A complete model of scr monolith reactors for the analysis of interacting NO_x , reduction and SO_2 , oxidation reactions* [J]. Chemical Engineering Science, 1994, 49(24): 4277–4287.
- Upadhyay D, Nieuwstadt M V. *Model Based Analysis and Control Design of a Urea-SCR de NO_x Aftertreatment System* [J]. Journal of Dynamic Systems Measurement & Control, 2006, 128(3): 737–741.
- Bhattacharjee S, Haworth D C, Moores R. *CFD modeling of processes upstream of the catalyst for urea SCR NO_x reduction systems in heavy-duty diesel applications* [J]. Sae Technical Papers, 2011.
- Adams B, Cremer M, Valentine J, et al., *Use of CFD Modeling for Design of NOx Reduction Systems in Utility Boilers* [C]. International Joint Power Generation Conference. 2002: 695–702.
- Naqvi Mughis Meyer Chris. *Gas-Gas Mixing as Applied to SCR's* [C].NETL conference Pittsburgh Pennsylvania 2003: 1–30.
- Enrico Tronconi, Andrea Cavanna, Carlo Orselligo, Pio Forzani, *Transient Kinetics of SO_2 Oxidation Over SCR-De NO_x Monolith Catalysts*. Industrial & Engineering Chemistry Research, 1999, 38(7): 2593–2598.
- Tao Qiu, Xuchu Li, Hong Liang, Xinghua Liu, Yan Lei. *A method for estimating the temperature downstream of the SCR (selective catalytic reduction) catalyst in diesel engines* [J]. Energy, 2014, 68.
- Ossi Tapani Kaario, Ville Vuorinen, Lei Zhu, Martti Larmi, Ronghou Liu. *Mixing and evaporation analysis of a high-pressure SCR system using a hybrid LES-RANS approach* [J]. Energy, 2016.
- Amsden A A, Orourke P J, Butler T D. *KIVA-2: A computer program for chemically reactive flows with sprays* [J]. Nasa Sti/recon Technical Report N, 1989, 89.
- Yim S D, Kim S J, And J H B, et al., *Decomposition of Urea into NH_3 for the SCR Process* [J]. Industrial & Engineering Chemistry Research, 2004, 43(16): 4856–4863.
- Weili Zhang. *Study on the urea storage and injection unit of the ship SCR system*. Dalian Maritime University. 2012: 1–62.

CONTACT WITH THE AUTHOR

Jun Du, Associate professor.

e-mail: dujun9988@163.com

tel: +86-15996805827

Jiangsu University of Science and Technology

23-102 Mengxi Road 6

Zhenjiang City Jiangsu Province

212003

CHINA

HIGH-SPEED CATAMARAN'S LONGITUDINAL MOTION ATTENUATION WITH ACTIVE HYDROFOILS

Kaiye Hu, Ph. D.

Yong Ding, Ph. D.

Hongwei Wang, Ph. D.

College of shipbuilding Engineering, Harbin Engineering University, Harbin, Heilongjiang, China

ABSTRACT

This paper mainly studies the longitudinal motion prediction method and control technology of high-speed catamaran using the active hydrofoils. To establish the longitudinal motion equations of the ship basing on the 2.5D theory. Using the CFD software to obtain the hydrodynamic data of the hydrofoil. Bring the hydrodynamic expression of hydrofoils into the longitudinal motion equations of the ship. Predicting the longitudinal motion of High-speed catamaran before and after added the hydrofoils. A specific catamaran has been predicted with this approach, the result indicates this approach is workable and this prediction approach provides the theoretical basis for assessing the stabilization ability of appendages and possess the engineering practical value.

Keywords: High-speed catamaran; Longitudinal motion attenuation; 2.5D theory; Hydrofoil

INTRODUCTION

As an important member of high-performance ships, high-speed catamaran attracted widespread attention and research in the industry, high-speed catamaran have advantages of good stability, large open deck and high speed, so this kind of ship has a broad application prospect in the field of military and civilian [1–5]. The high-speed catamaran will bring sharp longitudinal oscillation motion (heaving and pitching) when sailing in the sea with high speed. This is a big problem which the rapid development of the high-speed catamaran will facing. It will bring the worse performance of motion and safety for high-speed catamaran. Adding stabilizer appendage can effectively improve the intense longitudinal oscillation of the high-speed catamaran. This paper study the method to predict longitudinal motion of high-speed catamaran with active hydrofoils.

This paper set up the longitudinal motion equation for high-speed catamaran based on the 2.5D theory [6–9]. Establish hydrofoil hydrodynamic model and adding hydrodynamic force of hydrofoil to the longitudinal motion equations of catamaran. Solving and programming these equations in regular waves and irregular waves, the stabilization capability of hydrofoils are assessed.

LONGITUDINAL MOTION EQUATIONS

Ships are partially submerged objects with six degrees of freedom for their motion (with constraints related to its interaction with water). Three of the referenced motions are rotational: pitch, roll and yaw. The other three are translational: heave, surge and sway. Each motion can be described with a differential equation, with terms induced by the other motions (there are couplings between motions due for instance to gyroscopic effects). For the sake of simplicity, let us disregard deformations of the ship, due for example to flexible modes. Supposing the ship is divided into symmetric parts by the X-Z vertical plane, the six differential equations can be grouped into two decoupled sets: one is related to longitudinal motions (surge, heave and pitch), the other is related to lateral motions (sway, roll and yaw). The interest in this paper is centered on longitudinal motions.

Analysis of experimental data shows that heave and pitch motions are the most relevant for the purpose of the research, while surge motion has negligible effects. The signs of heave and pitch are as follows: Pitch angle is positive when the bow goes down the horizontal. Heave position is positive from the origin upwards along axis Z.

From the point of view of physics, the longitudinal motion equations are [10]:

$$(a_{33} + m)\ddot{z} + b_{33}\dot{z} + c_{33}z + a_{35}\ddot{\theta} + b_{35}\dot{\theta} + c_{35}\theta = F_3(t) \quad (1)$$

$$(a_{55} + I_y)\ddot{\theta} + b_{55}\dot{\theta} + c_{55}\theta + a_{53}\ddot{z} + b_{53}\dot{z} + c_{53}z = F_5(t) \quad (2)$$

The left-hand side of the equations constitutes a model of the ship's dynamics (the semi submerged body). In this paper, this part will be denoted as the forces-to-motions model. The right-hand side of the equations will be denoted as the waves-to-forces model, giving the forces due to waves. In Eq. (1) and Eq. (2):

m — the mass of the ship (tonne);

θ — pitch angle (deg);

z — heave translation (m);

I_y — pitch moment of inertia (tonnem²);

a_{33}, a_{55} — the added mass (a_{33} tonne, a_{55} tonnem²);

b_{33}, b_{55} — the damping coefficient (b_{33} kN s/m, b_{55} kN ms/rad);

c_{33}, c_{55} — the restoring coefficient (c_{33} KN/m, c_{55} KNm/rad);

F_3, F_5 — waves forces (F_3 : heave kN/m, F_5 : pitch kN).

All of the above hydrodynamic coefficients and wave force are obtained by the 2.5D theory [9], through the two-dimensional time domain source distribution method.

HYDRODYNAMIC OF HYDROFOIL

HYDROFOIL SELECTION

Hydrofoils mounted below the bow position of catamaran, when the high-speed catamaran sailing on the waves, the water will be at a certain angle of attack relative to the flow of the hydrofoil surface, and generates movement in the opposite direction of the ship's force, effectively inhibited the longitudinal motion of the vessel.

The selected hydrofoil is NACA0021, shown in Figure 1. The mounted position is shown in Figure 2.

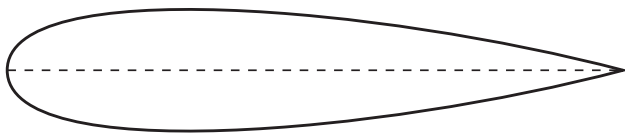


Fig. 1. NACA0021 airfoil

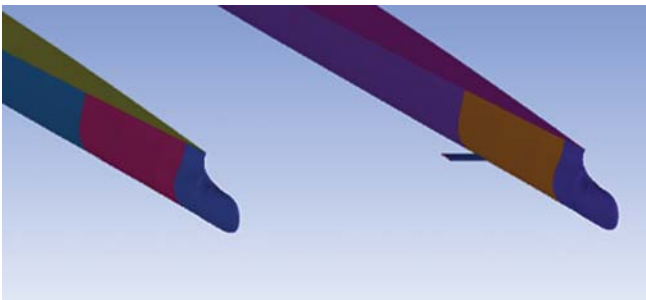


Fig. 2. Mounted position of hydrofoil

HYDRODYNAMIC FORCE OF HYDROFOIL

Based on the hydrodynamic theory, the lift force of hydrofoil is

$$F_F = \frac{1}{2} \rho U^2 A C_L \quad (3)$$

where ρ (kg/m³) is fluid density, U (m/s) is ship speed, A (m²) is projected area of hydrofoil and C_L is the lift coefficient of hydrofoil.

C_L is related with the attack angle of hydrofoil, in a wide range of attack angles (less than angle of stall), lift coefficient and angle of attack is linear relationship, it can be expressed as:

$$C_L = \frac{dC_L}{d\alpha} \cdot \alpha \quad (4)$$

where α is effective angle of attack, $\frac{dC_L}{d\alpha}$ is the slope of hydrofoil lift coefficient curve, which is obtained by the fitting curve based on the computational fluid dynamics calculation. The fitting curve of hydrofoil lift coefficient is shown in Figure 3.

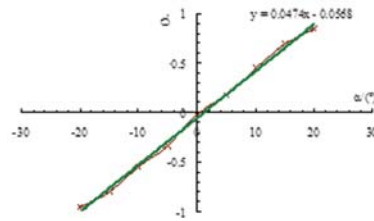


Fig. 3. Fitting curve of hydrofoil lift coefficient

The lift force formula of hydrofoil is:

$$F_F = \frac{1}{2} \rho U^2 A \frac{dC_L}{d\alpha} \cdot \alpha \quad (5)$$

so the lift moment formula of hydrofoil is:

$$M_F = (-l_F) \frac{1}{2} \rho U^2 A \frac{dC_L}{d\alpha} \cdot \alpha \quad (6)$$

where l_F (m) is the horizontal distance between the lift point of hydrofoil and center of gravity of the ship.

The actual movement of hydrofoil is unsteady. But generally speaking, the impact of unsteady movement of hydrofoils is small, so we can calculate the hydrofoil lift assume the hydrofoil movement is steady. When we calculate the real attack angle of hydrofoil, we need consider the extra angle caused by the heave, pitch of ship body. For active hydrofoil, the actual effective attack angle of hydrofoil including 3 parts: the swinging angle of the hydrofoil φ , the pitching angle θ of hydrofoil together with the ship body, an additional angle θ_F course by the movement of ship body. So the formula for the real attack angle of hydrofoil is

$$\alpha = \varphi - \theta + \theta_F \quad (7)$$

According to the research of Esteban S. [11], considering the combined action of the instantaneous heave speed of ship \dot{z} , vertical velocity of wave on hydrofoil ζ , angular velocity of pitch $\dot{\theta}$ and ship speed v , θ_F can be written as follow:

$$\theta_F = \arctan \frac{l_F \dot{\theta} - \dot{z} + \dot{\zeta}}{U} \quad (8)$$

θ_F is a small value, so it can be simplified to

$$\theta_F = \frac{l_F \dot{\theta} - \dot{z} + \dot{\zeta}}{U} \quad (9)$$

The final expression for the effective angle of attack:

$$\alpha = \varphi - \theta + \frac{l_F \dot{\theta} - \dot{z} + \dot{\zeta}}{U} \quad (10)$$

Substitute Eq. (10) into Eq. (5), we can get

$$F_F = \frac{1}{2} \rho U^2 A \frac{dC_L}{d\alpha} (\varphi - \theta + \frac{l_F \dot{\theta} - \dot{z} + \dot{\zeta}}{U}) \quad (11)$$

When the model of hydrofoil has chosen, $\rho U^2 A \frac{dC_L}{d\alpha}$ is a constant value under a certain ship speed U , suppose this constant value is K_F , because the catamaran has two hydrofoils, the total control force acting by hydrofoil can be expressed as

$$F_F = K_F (\varphi - \theta + \frac{l_F \dot{\theta} - \dot{z} + \dot{\zeta}}{U}) \quad (12)$$

the total control moment is

$$M_F = (-l_F) K_F (\varphi - \theta + \frac{l_F \dot{\theta} - \dot{z} + \dot{\zeta}}{U}) \quad (13)$$

THE STABILIZATION PRINCIPLE OF HYDROFOILS

The stabilization principle is the control force and moment which produce by hydrofoils can counteract the wave exciting force and moment [12], adding the control force and moment to the longitudinal equations of ship motion, we can get:

$$\begin{aligned} (m + a_{33})\ddot{z} + b_{33}\dot{z} + c_{33}z + a_{35}\ddot{\theta} + b_{35}\dot{\theta} + c_{35}\theta \\ = F_3 + K_F (\varphi - \theta + \frac{l_F \dot{\theta} - \dot{z} + \dot{\zeta}}{U}) \\ (I_y + a_{55})\ddot{\theta} + b_{55}\dot{\theta} + c_{55}\theta + a_{53}\ddot{z} + b_{53}\dot{z} + c_{53}z \\ = F_5 - K_F l_F (\varphi - \theta + \frac{l_F \dot{\theta} - \dot{z} + \dot{\zeta}}{U}) \end{aligned} \quad (14)$$

LONGITUDINAL MOTION PREDICTING METHOD OF HIGH-SPEED CATAMARAN WITH HYDROFOILS

Solving the steady-state solution of the longitudinal motion equations of catamaran with hydrofoils in frequency domain. Firstly, use heave equations of catamaran with hydrofoils as an example, the simplification equation is:

$$\begin{aligned} (m + a_{33})\ddot{z} + (b_{33} + \frac{K_F}{U})\dot{z} + c_{33}z + a_{35}\ddot{\theta} \\ + (b_{35} - K_F \frac{l_F}{U})\dot{\theta} + (c_{35} + K_F)\theta = F_3 + K_F \varphi + \frac{K_F}{U} \dot{\zeta} \end{aligned} \quad (15)$$

The key problem is to determine the swinging angle φ of the hydrofoil, using PID control method, the size of the swing angle φ is determined by the value of ship movements [13–15], that is

$$\varphi = -K_{p\theta T} \ddot{\theta} - K_{i\theta T} \dot{\theta} - K_{d\theta T} \theta - K_{pzT} \dot{z} - K_{lzT} z - K_{DzT} \ddot{z} \quad (16)$$

This is the ideal form of PID control method, $K_{p\theta T}$, $K_{i\theta T}$, $K_{d\theta T}$ are controller's control parameters of hydrofoil corresponding to the pitch angular velocity $\dot{\theta}$ of ship body, K_{pzT} , K_{lzT} , K_{DzT} are controller's control parameters of hydrofoil corresponding to the heave velocity \dot{z} of ship body. Select certain value of PID control parameters which have good anti-pitching effecting, use fixed PID parameters, this allows us moved the control force and control moment which generated by the swing angle φ of hydrofoil to the left side of Eq.(15), Eq.(15) become:

$$\begin{aligned} (a_{33} + K_{Tj} K_{DzT})\ddot{z} + (b_{33} + K_{Tj} K_{pzT} + \frac{K_{Tj}}{U})\dot{z} \\ + (c_{33} + K_{Tj} K_{lzT})z + (a_{35} + K_{Tj} K_{D\theta T})\ddot{\theta} \\ + (b_{35} + K_{Tj} K_{p\theta T} - \frac{K_{Tj} l_F}{U})\dot{\theta} \\ + (c_{35} + K_{Tj} K_{i\theta T} + K_{Tj})\theta = F_3 + \frac{K_{Tj} \dot{\zeta}}{U} \end{aligned} \quad (17)$$

In the right side of Eq. (17), the heave velocity of wave on hydrofoil surface $\dot{\zeta}(t) = \omega_0 \cdot \zeta_a \cdot e^{kz} \cdot e^{i(\omega t - kx)}$, where ω_0 is wave circular frequency, ζ_a is amplitude of wave and k is wave number.

When theoretical calculation of regular waves, wave exciting force, heave, pitch angle can express as $F_3 = F_0 e^{i\omega t}$, $z(t) = z_0 e^{i\omega t}$, $\theta(t) = \theta e^{i\omega t}$. Substitute these expression to the heave equation, eliminate time items $e^{i\omega t}$, use complex expression and separate real part and imaginary part, we can get two equations:

$$\begin{aligned} [-\omega^2 (a_{33} + K_{Tj} K_{DzT}) + (c_{33} + K_{Tj} K_{lzT})]z_{0r} \\ - \omega (b_{33} + K_{Tj} K_{pzT} + \frac{K_{Tj}}{U})z_{0i} + [-\omega^2 (a_{35} + K_{Tj} K_{D\theta T}) \\ + (c_{35} + K_{Tj} K_{i\theta T} + K_{Tj})]\theta_{0r} - \omega (b_{35} + K_{Tj} K_{p\theta T} - \\ \frac{K_{Tj} l_F}{U})\theta_{0i} = F_0 + \frac{K_{Tj} \omega_0 \zeta_a e^{kz_0}}{U} \cos kx_0 \end{aligned} \quad (18)$$

$$\begin{aligned} [-\omega^2 (a_{33} + K_{Tj} K_{DzT}) + (c_{33} + K_{Tj} K_{lzT})]z_{0i} \\ + \omega (b_{33} + K_{Tj} K_{pzT} + \frac{K_{Tj}}{U})z_{0r} + [-\omega^2 (a_{35} + K_{Tj} K_{D\theta T}) \\ + (c_{35} + K_{Tj} K_{i\theta T} + K_{Tj})]\theta_{0i} + \omega (b_{35} + K_{Tj} K_{p\theta T} - \frac{K_{Tj} l_F}{U})\theta_{0r} \\ = F_0 - \frac{K_{Tj} \omega_0 \zeta_a e^{kz_0}}{U} \sin kx_0 \end{aligned} \quad (19)$$

Similarly we can obtain two equations using the same method to the pitch equation, solve these four equations we can get heave amplitude z_{0F} and pitch amplitude θ_{0F} , the wave and heave displacement phase difference ε_{zF} , the wave and pitch phase difference $\varepsilon_{\theta F}$.

EXAMPLES

CATAMARAN AND HYDROFOIL MODEL

Now predict the longitudinal motion of a specific catamaran, the principal dimension of selected hydrofoil and catamaran are shown in Table 1. and Table 2.

Tab. 1. Principal dimension of hydrofoil

Stabilization appendage	Items	Unit	Quantitative value
hydrofoil	wing chord	m	1.414
	wing span	m	2.828
	max thickness	m	0.297

Tab. 2. Principal dimension of catamaran

Items	Unit	Quantitative value
Lpp	m	97.177
BWL (side hull)	m	5.24
B _{wL}	m	28.115
Draft	m	3.62
Z _G	m	8.733
X _G	m	-5.258
∇	m ³	2398.8
Inertia radius of pitching	m	26.0125

Select ITTC two parameters wave spectrum:

$$S_{\zeta}(\omega) = \frac{173H_{1/3}^2}{T_1^4\omega^5} \exp\left[-\frac{691}{T_1^4\omega^4}\right] \quad (m^2 \cdot s) \quad (20)$$

where $H_{1/3}$ (m) is significant wave height, T_1 (s) is characteristic period, ω (s^{-1}) is circular frequency.

The ship forward speed is 30 kn.

RESULTS

The following figures are frequency response prediction of longitudinal movement of high speed catamaran with and without hydrofoils. In these figures, β is the angle of wave direction, Z is the frequency response of heave of catamaran without hydrofoils, Z_{gf} is the frequency response of heave of catamaran with fix hydrofoils, Z_{df} is the frequency response of heave of catamaran with active hydrofoils, θ is the frequency response of pitch of catamaran without hydrofoils, θ_{gf} is the frequency response of pitch of catamaran with fix hydrofoils, θ_{df} is the frequency response of pitch of catamaran with active hydrofoils

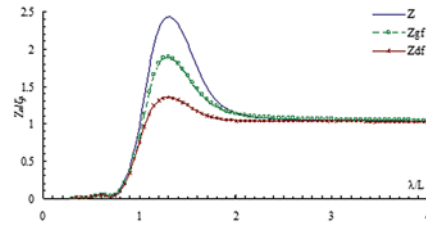


Fig. 4. Frequency response of heave ($\beta=180^\circ$)

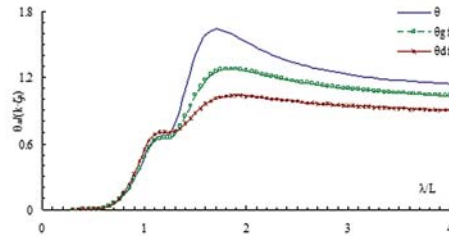


Fig. 5. Frequency response of pitch ($\beta=180^\circ$)

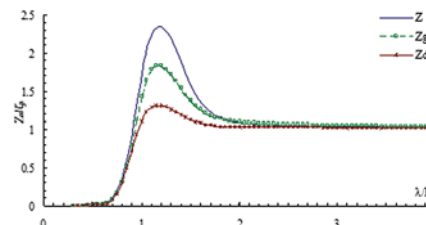


Fig. 6. Frequency response of heave ($\beta=150^\circ$)

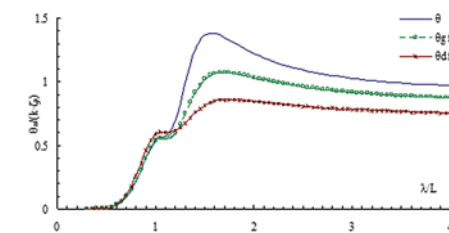


Fig. 7. Frequency response of pitch ($\beta=150^\circ$)

Statistical values of longitudinal motion of catamaran in irregular wave and stabilization effectiveness are shown in Tab. 3. and Tab. 4.

CONCLUSION

In regular waves, the fixed hydrofoils have obvious stabilization effectiveness, active hydrofoils have better stabilization effectiveness than fixed hydrofoils. In short wave length region, the longitudinal motion response basically did not change with hydrofoils, in resonance region, the hydrofoils have good stabilization effectiveness, in long wave length region, the heave motion response basically did not change with hydrofoils but pitch motion response reduce a lot. In irregular waves, the stabilization effectiveness decreases with the sea state increase.

This paper provides a reference to research the automatic control model of stabilization for high speed catamaran longitudinal motion.

Tab. 3 Statistical values of heave of catamaran with and without hydrofoils and stabilization effectiveness

Working condition		Sea state		Statistical values of heave and effectiveness				
U (kn)	β (°)	$H_{1/3}$ (m)	T_1 (s)	Z_s (m)	Z_{s+GF} (m)	η_{GF} (%)	Z_{s+DF} (m)	η_{DF} (%)
30	180	1.25	6.13	0.670	0.543	18.90	0.417	37.69
		2.50	7.20	1.665	1.375	17.37	1.081	35.09
		4.00	8.21	2.760	2.342	15.13	1.905	30.97
		5.00	9.10	3.381	2.943	12.96	2.472	26.89
		6.00	10.51	3.794	3.421	9.84	2.999	20.96
	150	1.25	6.13	0.719	0.588	18.20	0.454	36.81
		2.50	7.20	1.671	1.399	16.24	1.115	33.25
		4.00	8.21	2.697	2.326	13.75	1.927	28.55
		5.00	9.10	3.274	2.898	11.49	2.481	24.22
		6.00	10.51	3.668	3.359	8.41	2.996	18.30

Tab. 4. Statistical values of pitch of catamaran with and without hydrofoils and stabilization

Working condition		Sea state		Statistical values of pitch and effectiveness				
U (kn)	β (°)	$H_{1/3}$ (m)	T_1 (s)	θ_s (°)	θ_{s+GF} (°)	η_{GF} (%)	θ_{s+DF} (°)	η_{DF} (%)
30	180	1.25	6.13	0.933	0.813	12.87	0.818	12.34
		2.50	7.20	2.549	2.132	16.38	2.004	21.37
		4.00	8.21	4.492	3.722	17.15	3.373	24.92
		5.00	9.10	5.627	4.666	17.08	4.152	26.20
		6.00	10.51	6.263	5.226	16.55	4.584	26.81
	150	1.25	6.13	0.975	0.840	13.87	0.833	14.54
		2.50	7.20	2.487	2.069	16.82	1.923	22.70
		4.00	8.21	4.212	3.480	17.38	3.125	25.80
		5.00	9.10	5.160	4.271	17.24	3.771	26.92
		6.00	10.51	5.626	4.687	16.69	4.082	27.45

ACKNOWLEDGEMENTS

This project is partially supported by the Basic scientific research of national defense of China (Grant No. B2420132001)

REFERENCES

1. Wu Y.S, Ni Q.J., Ge W.Z.: *Advances in Technology of High Performance Ships in China*. Journal of Ship Mechanics, Vol. 12, no. 6, pp. 1022–1028, 2008.
2. Pohler C.H., Deppa R.W., Corrado J.A., Graner W.R.: *Advanced Composite Structures for High Performance ships*. Naval Engineers Journal, Vol. 87, no. 2, pp. 189–197, 2010.
3. Fach K., Bertram V.: *High-performance simulations for high-performance ships*. Ships & Offshore Structures, Vol. 2, no. 2, pp. 105–113, 2007.
4. Ren J.S.: *High-Speed Hydrofoil Ship Motion Control*. Science Press, Beijing, 2015.
5. Fossen T.I.: *Guidance and Control of Ocean Vehicles*. Wiley, New York, 1994.
6. Duan W.Y., Ma S., Song J.Z.: *Hydrodynamic Properties of High-Speed Catamarans*. Journal of Harbin Engineering University, Vol. 23, no. 1, pp. 9–14, 2002.

7. Faltinsen O., Zhao R.: *Numerical predictions of ship motions at high forward speed*. Philos. Trans. R. Soc. Lond, A, Vol. 3, no. 34, pp. 241–252, 1991.
8. Ma S., Duan W.Y.: *A time domain simulation method for nonlinear motion and wave loads of fast ships*. International Shipbuilding Progress, Vol. 56, no. 1, pp. 59–93, 2009.
9. Ma S., Duan W.Y. Song J.Z.: *An efficient Numerical Method for Solving '2.5D' Ship Seakeeping Problem*. Ocean Engineering, Vol. 32, no. 8–9, pp. 937–960, 2005.
10. A.R.J.M.Lloyd.: *Seakeeping: Ship Behavior in Rough Weather*, A.R.M.J.Lloyd, Gosport, Hampshire, U.K., 1998
11. Giron-Sierra, J.M., Esteban S., De Andres B., Diaz J.M., Riola J.M.: *Experimental study of controlled flaps and T-foil for comfort improvement of a fast ferry*. In Proceedings IFAC Intl. Conf. Control Applications in Marine Systems CAMS2001, Glasgow, 2001.
12. Faltinsen O.: *Hydrodynamics of high-speed marine vehicles*. Cambridge University Press, Cambridge, 2005.
13. Lopez R., Santos M.: *Neuro-fuzzy system to control the fast ferry vertical acceleration*. 15th Triennial World Congress, Barcelona, Spain, 2002.
14. Bhushan, S., Stern, F., Doctors, L.J.: *T-Craft calm water resistance and motions, and seakeeping in regular waves*. In: Proceedings of the 11th International Conference on Fast Sea Transportation, FAST2011, Honolulu, Hawaii, USA, 2011.
15. Esteban, S., De la Cruz, J.M., Giron-Sierra, J.M., DeAndres Toro, B., Diaz, J.M., Aranda J.: *Fast Ferry Vertical Acceleration Reduction with Active Flaps and T-foil*. Proc. IFAC Int. Symp, MCMC2000, Aalborg, 2000.

CONTACT WITH THE AUTHOR

Kaiye Hu, Ph. D.

e-mail: hukaiye@126.com

tel: 15545187318

College of Shipbuilding Engineering
Harbin Engineering University
Harbin Heilongjiang, 150001
CHINA

A SHIP NETWORK DYNAMIC ROUTING ALGORITHM BASED ON VECTOR NETWORK

Jianguang Zhao^{1, 2}

Jingjing Fan¹

¹Institute of Information Science, Beijing Jiaotong University, Beijing, China

²Information Engineering Institute, Hebei Institute of Architectural and Civil Engineering, Zhangjiakou, Hebei, China

ABSTRACT

In view of the characteristics of low speed mobile ship network, strong network dynamics and large signal interference, this paper proposes a low-rate mobile sensor network routing algorithm. In mobile wireless sensor networks, network topology changes frequently is a new challenge for resource constrained sensor node. Constantly updated network topology, sensor nodes need to exchange data frequently in order to maintain fresh route, resulting in sensor nodes consume a lot of energy. To solve this problem, to reduce control overhead is considered to be an effective strategy. In this paper, we present a vector network-based dynamic routes (VNDR) scheme aims to minimize the control cost of the sensor nodes. We propose data exchange based on binary-coded vector address to reduce the control cost, moreover, we present a set of communication rules that govern the routes search procedure thereby requiring little cost of packet analysis to determine the next hop of node. VNDR performance was compared with well known scheme such as SPIN and DD. Simulation results show that, our VNDR scheme reduced the network control overhead and improved network lifetime.

Keywords: Ship network; Vector Network; Vector address; Routes discovery; Wireless Sensor Network

INTRODUCTION

In the “13th Five-Year Plan”, the state explicitly proposed the development of the marine economy. Ocean communication is also an important and crucial technology in the livelihood of the people and marine militaries. It is also a key discipline developed and paid attention by the state in recent years. It is also the goal that the marine science and technology circles have been pursuing for many years. Wireless sensor networks are widely used in the fields of reconnaissance, environmental monitoring and target location. They can sense, collect and process the object information within the network coverage in real time and send them to the observer. It has the advantages of wide coverage, remote monitoring, high monitoring accuracy, fast and low-cost network.

Wireless Sensor Network (WSN) – a self-organized network of smart dust which has limited computing and storage power, has widely used in Military areas and production and living areas [1]. In WSN, there is an enormous number of sensor nodes

are deployed to collect, process and forwarding sensing data with wireless channels. [2] These battery-powered sensor nodes worked cooperatively to monitor and report the interesting information to base station or sink. In order to reduce energy consumption and prolong network lifetime, various routing protocols had proposed so far. Most of these routing protocols assumed sensor nodes to be immobile in the WSN implementation. However, there are applications environments naturally require mobile node to complete the monitoring mission, [1] e.g., in a individual combat system, a battlegroup need search forward holding formation. Therefore everyone need communication with each other to improve battlegroup manoeuvrable. Each soldier moves with low-speed so as not to expose themselves to be discovered by the enemy. Similar, in an Intelligent Transport System (ITS), a lot of immobile sensor nodes are deployed at car park, rockfall area, and traffic entrance as ITS infrastructure. In contrast, there are numerous moving vehicle in ITS. Some scholars named it Internet of Vehicles, which is constituted by mobile nodes, Vehicle position, speed, and infrastructure.

Because of node mobility, the network topology changes frequently, it brings new challenges for data transmission and routing protocols. Hence, network topology need to constantly update, leading to frequent data transmission and more energy consumption. So far, routing protocols have been proposed are most based on immobile, these ones not suitable for mobile scenario. To cope with the dynamic network topology, new routing scheme should be presented to accommodate the mobility of nodes.

In this paper, a novel scheme called Vector Network-Based Dynamic Routes(VNDR) is proposed for low-speed mobility WSN. The scheme is suitable for small scale low-speed and high real-time requirements scenario. The proposed scheme enables nodes to maintain optimal multiple routes with each other. Each node in the network has a unique ID, which by binary encoding to form vector address. Moreover, packet transmission scheme using multi-hop transmission, route information contained in the data packet. Thus, when a node receives a packet, from the vector cut a sub-vector to determine next hop. It aims to optimize transmission delay and energy consumption and quality of service performance using vector address. Simulation results reveal decreased transmission delay, control data overhead and energy consumption of VNDR compared to other state-of-the art.

The rest of this paper is organized as follows: Part II describes the related work about mobile WSN. Part III presents VNDR routing mechanism. To evaluate the new proposed scheme, simulation and performance compare are presented in Part IV. Section V concludes the paper, finally.

RELATED WORK

Several schemes have been proposed for mobile WSN in the last decade. Abdul et al. [1] presented a Virtual Grid-Based Dynamic Routes Adjustment Scheme for Mobile Sink-Based Wireless Sensor Networks(VGDRA) that constructs a virtual grid aim to minimize the routes reconstruction overhead and balance the nodes energy dissipation. In this scheme, a mobile sink moving around the border-line of sensor field. However, nodes along the border line spends high energy consumption thereby causing hot-spot problem. Yet another similar approach can be found in [11], which places a application of WSN-based smart grid(WSN-SG).

B.B et al. [6] proposed a new clustering algorithm Distributed load balancing Unequal Clustering in wireless sensor networks using Fuzzy approach (DUCF) in that make use of fuzzy logic to elect cluster head (CH). DUCF although improves the network lifetime, however, it employs residual energy, node degree and distance to BS as fuzzy input variables, and chance and size as fuzzy output variables. Due to less number of fuzzy inference parameters, it can not accurately reflect the real network. An Efficient Multipath Dynamic Routing Protocol for Mobile WSNs (M-DART) [2] which constructs multipath routing protocols for Mobile WSN by Distributed Hash Tables (DHTs). A similar approach has also been proposed in Optimizing LEACH clustering algorithm with mobile sink

and rendezvous nodes (LEAH-SR)[10] which constructs a mobile sink(MS) as a way to reduce energy consumption and a rendezvous node(RN) to act as a store node. Proactive Highly Ambulatory Sensor Routing (PHASeR) protocol for mobile wireless sensor networks proposed by T.H and F.H in [12], proactively constructs a hop-count metric to implement dynamic and robust routing in mobile WSN.

Tab.1 presents a performance comparison of the variously discussed schemes. We evaluated each scenario by comparing parameters mobile node, delay, complexity and simulation tools. The mobile node specifies the type of mobile node, including ordinary nodes and sink. The second parameter provides an estimate of the network delay involved in communicating and holding routing updates. Similarly, the complexity is an estimate the difficulty of implementation of the scheme. Finally, the last parameter indicate simulation tools used in each paper.

Based on the above literature, it is observed that the mobile node brings topology update speed up and network delay increase. Though these related works has been improved the performance of mobile WSN, still no scenario is discovered to reduce the network delay and control overhead, simultaneously, prolongs network lifetime. The main contribution of this paper is reducing the network control data overhead by encoding node ID to vector address. It offers a novel solution for route discovery without too many constrains for real nodes. Compared to existing schemes, the VNDR is a viable choice in mobile WSN.

Tab. 1. Performance comparison of discussed schemes.

Scheme	Mobile Node	Delay	Complexity	Simulation Tools
VGDR [1]	Sink	Moderate	Low	NS-2
WSN-SG [11]	Sink	High	Low	No
DUCF [6]	None	High	High	MATLAB
M-DART [2]	All	High	High	NS-2
LEAH-SR [10]	Sink	Moderate	Low	MATLAB
PHASeR [12]	All	High	High	OPNET

THE PROPOSED SCHEME

In this section, we detail our proposed solution, including how to encode vector address and how to discover route by cutting vector address. We design a new network layer architecture including data plane, control plane and management plane. The main innovation in the data plane and some work about control plane, management plane inherited the art.

This mechanism is divided into two stages: the route discovery phase and data forwarding phase as show in Fig. 1. The mission of route discovery phase is to complete the routing update, the stage is divided into route acquisition phase and route filtering phase. Furthermore, the data forwarding phase is a data communication phase, the minimum length of vector addresses is preferred to reduce traffic and delays.

Fig. 1. is Operational diagram of VNDR.

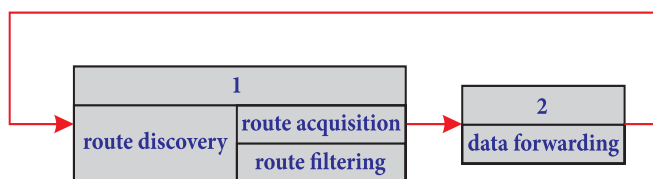


Fig. 1. Operational diagram of VNDR

NETWORK FEATURES

It is necessary to highlight the assumptions of the mobile WSN, before a detailed discussion VNDR scheme. Some of the main features of VNDR are as follows:

- The number of nodes is not too much, and all nodes are of homogeneous architecture.
- Nodes are randomly deployed and all nodes moving at a lower speed.
- All nodes move throughout in its communication radius.
- The sensor field is not too large.
- The scheme is suitable for high real-time requirements scene, and has a weak quality of service.

THE VECTOR ADDRESS CONSTRUCTION

The VNDR scheme constructs the Vector Address (VA) by encoding all branches of any node which called Virtual Port Number (VPN). VA is an swiching address based on the VPN of nodes. The input and output port numbers (I/OPN) numbered from 1 started, called Virtual Port Number (VPN). The communication path information included in the packet of VN. The path information is a sequence of virtual port numbers, each node on the path corresponding to a virtual port number in sequence. The next-hop is determined by output virtual port number of nodes on the route. Network topology as shown in Fig. 2., virtual port number were constructed by each node according to the network topology.

Fig. 2. is an example of virtual port number were constructed.

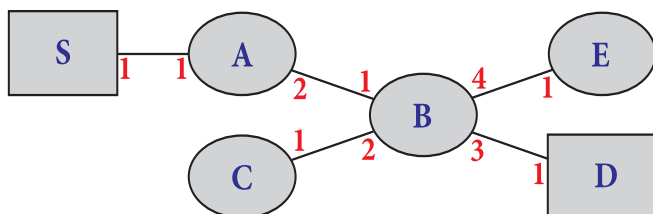


Fig. 2. An example of virtual port number were constructed

Each node builds the virtual port number depending on the degree of a node, take A for example, the degree of A is 2, similily, the degree of B is 4. Therefore, based on the above assumptions, we can build the vector address. Vector Addresses are divided into two types: Forward Vector Address(FVA) and back Backward Vector Address(BVA).Easy to deduce, Forward Vector Address(route) from the source node S to the destination node D $V_{SD}=123=\{1,2,3\}$. Fig. 3. shows an example of the construction for Vector address V_{SD} .

Fig. 3. is an example of construction for Vector address V_{SD} .

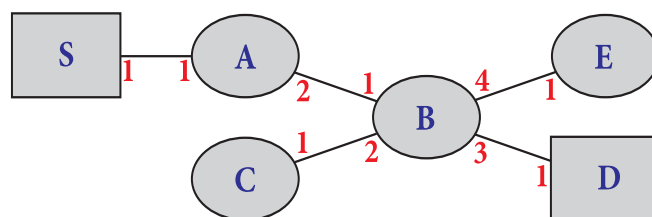


Fig. 3. An example of construction for Vector address VSD

Similarly, $V_{CE}=14$, $V_{SE}=124$, $V_{SC}=122$. Similarly, BVA is the sequence of reverse virtual port number sequence. Therefore, the reverse route of S->D $BV_{SD}=111$. Bidirectional path represented by a vector address as Expression 1.

$$(f_1, b_1; f_2, b_2; \dots f_n, b_n) \quad (1)$$

Where, $(f_1; f_2; \dots f_n)$ represent forward vector address, and $(b_1; b_2; \dots b_n)$ denotes backward vector address; n denotes the total number of hops.

After construction of vector address, coding of the vector address is setup using binary encoding. Thus, the representation of the vector address into binary form, $V_{SD}=123=\{1,2,3\} \rightarrow \{1,10,011\}$ that is, 110011. Each node encode virtual port numbers into binary code according to their degree. The virtual port numbers of All nodes from 1 to start coding, for example, the degree of B is equal to 4, thence, the coding range of 001-100.

CUTTING VECTOR ROUTING ALGORITHM

After the vector coding, every node get route by cutting vector from packet. Fig. 4. shows the packet format of vector network.

Fig. 4. is Packet format of vector network.

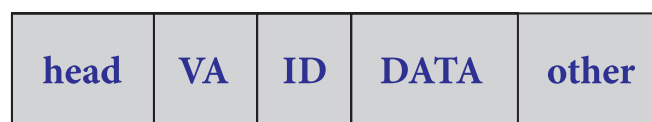


Fig. 4. An example of virtual port number were constructed

Where, head denotes head of packet, ID is increasing along with the packet forwarding and it used to indicate the freshness of the packet, like the same in AODV scheme. After a node receives a packet, firstly, separate the first component of VA and assigned to the variable sentto; secondly, remove the separated components from the VA field; thirdly, send packets to virtual port sentto. Fig. 5. show an example of cutting vector.

The steps of the algorithm are described as follows:

- When first start algorithm, all nodes periodically broadcast **ROUTE_PROBE** to all neighbor nodes to establish a network topology.
- Construction of the virtual port number(VPN) for all nodes based on network topology and encode VPN to vector address.

- Each nodes computes the length of the vector, and the minimum length of 10 vector paths are stored as set S.

Fig. 5. is an example of cutting vector.

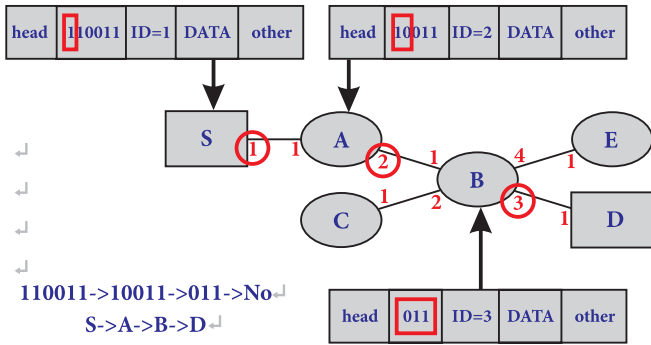


Fig. 5. An example of virtual port number were constructed

- All nodes Periodically update the routing. During routing updating, the node in S is preferentially chosen to be the next hop. Node sends data, after successfully updated routing. If $S = \emptyset$, goto 1. Detail of the same algorithm in **Algorithm 1**.

Algorithm 1 VNDR Algorithm:

- N = Total number of nodes
- j = a sensor node in the network
- $j.VPN$ = total number of virtual port
- Vector = virtual port encode as a binary vector
- s = the shortest path set
- this = pointer to current node
- If ($s = \emptyset$)
-
- for $i = 1:N$
- Send ROUTE_PROBE to all neighbor nodes
- x = list of all ROUTE_PROBE from neighbor
- $j.VPN$ = Get the VPN of node
- $j.vector$ = virtual port encode as a binary vector address
- if ($this.length(vector) < length(i.vector)$)
- if ($s.Count < 10$)
- add this.vector into s
- else
- Sent ROUTE_PROBE to a node in s
- if (receive REPLY_PROBE)
- NEXT_HOP = cut vector(this.vector)
- sent data to NEXT_HOP
- else
- goto 10

SIMULATION AND RESULTS

In this section, we present the simulation results using NS - 3. The proposed algorithm is compared with SPIN and DD. SPIN (Sensor Protocol for Information via Negotiation) is a data-centric adaptive routing communication protocol, and DD (Directed Diffusion) is a query-based routing algorithm, also is wireless sensor network protocol based on data related. We varied the total number of sensor nodes from 50 to 400

which are randomly deployed in a sensor field of A circular area with a radius of 50 m. Wireless signal transmission model using the free space model, the propagation loss is calculated by the Formula 2. Furthermore, we uses the energy consumption model used in [1]. Sending and receiving energy consumption as Formula 3 and Formula 4.

$$L_p = \left(\frac{\lambda}{4\pi d} \right)^2 \quad (2)$$

$$E_t = k \times E_{elec} + k \times E_{amp} \times d^2 \quad (3)$$

$$E_r = k \times E_{elec} \quad (4)$$

In Eq (2), (3) and (4), L_p is the path energy loss, d is the distance between sender and receiver, λ is the wavelength of the signal, E_{elec} is the cost of wireless transmitter and receiver, E_{amp} is the spent of wireless transmission amplifier, k is the packet length. In our experiment, set $E_{elec} = 50nJ/bit$, $E_{amp} = 100pJ/bit \times m^2$ and $k = 10bits$. Initially, all nodes in the network is powered by two battery-powered, and have a unified energy 5000 J (Because a battery can release 2500 J energy). Simulation parameters and values are listed in Tab2.

We compared VNDR scheme with SPIN and DD from the following aspects: route discovery cost, route signaling cost, average network energy consumption and average network lifetime.

Tab. 2. Simulation parameters and values.

Parameters	Values
Sensor field radiu	100m
E_{elec}	50nJ/bit
E_{amp}	100pJ/bit $\times m^2$
k	10bits
Initially energy per node	5000J
v	2m/s

THE ROUTE DISCOVERY COST

The Route Discovery Cost is used to estimate the cost of establishing a network topology consuming energy. Fig. 6. compares the per round route discovery cost for different network sizes.

As demonstrated in Fig. 6., spend less energy use the VNDR algorithm for establishing the network topology. In the network initialization phase, three schemes make use of flooding to discovery route. For small-scale network, VNDR, DD and SPIN energy consumption difference is not large, but from Fig. 6. can clearly see that the energy consumption of SPIN is twice than VNDR, and energy consumption of DD between VNDR and SPIN. In DD, each node needs to maintain a Interest Message List (IML) consuming more energy, therefore can not be used for large-scale networks and dynamic topology networks. In SPIN, each node should be carry out consultation by sending

metadata before transmit the packet, this will result in large data transmission delay. In our proposed VNDR, each node uses vector cutting to achieve route discovery, which greatly reducing the overhead. As presented in Fig. 6. our proposed VNDR scheme has superior performance in route discovery cost.

Fig. 6. is Comparing the Per Round Route Discovery Cost for different network sizes.

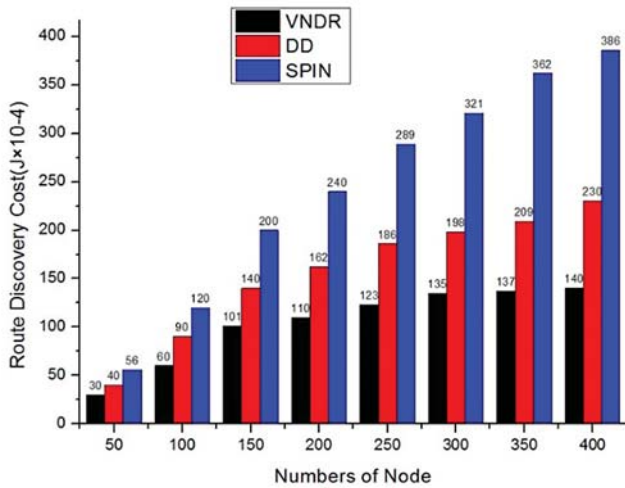


Fig. 6. Comparing the Per Round Route Discovery Cost for different network sizes

THE ROUTE SIGNALING COST

The Route Signaling Cost used to measure the proportion of the network control signal and redundant data in the total amount of data, and it consists of two parts: signaling and overhead. The VNDR scheme employs Vector Address to control dynamic topology, corresponds to SPIN uses ADV packet for routing control which contains metadata and its own address, and DD make use of Gradient for topology control which consists of the transmission rate and transmission direction. As shown in Fig. 7., along with the network size grows, gradually increasing the signaling overhead. Moreover, our VNDR scheme demonstrated superior performance than SPIN and DD. Although VNDR to maintain the 10 shortest vector, since each vector address employ binary code to save a lot of storage space and control overhead.

THE AVERAGE NETWORK ENERGY CONSUMPTION

As shown in Fig. 8., spend less energy use the VNDR algorithm for establishing the network topology. With the number of nodes in the network increases, VNDR, SPIN and DD energy consumption are gradually increasing. When the number of nodes is small, VNDR, SPIN and DD energy consumption is very close. For example, when the number of nodes equal to 30, VNDR and DD energy consumption is very close to, but SPIN energy consumption slightly higher. The VNDR scheme complete route discovery by the vector address binary coding, and this method effectively reduces the duty cycle of the control data, thereby reducing the energy consumption of route discovery. Similarly, DD by sending

node interest to complete routing discovery. The node interest described by structure, which takes up more resources than binary vector address, thus, DD has more cost. Also, the SPIN wasting more energy by dropping packets when the packets is not required.

Fig. 7 is Comparing the Per Round Route Signaling Cost for different network sizes.

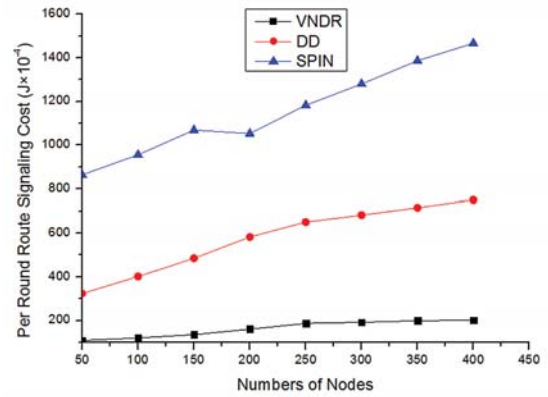


Fig. 7. Comparing the Per Round Route Signaling Cost for different network sizes

THE AVERAGE NETWORK LIFETIME

The average network lifetime used to measure the length of the network life, is the period of time from the network initialization to any node death due to the energy depletion. In our experiments, we use numbers of round to measure the average network lifetime. As presented in Fig. 8, with the increase in numbers of nodes, the numbers of rounds is in decreasing. Our VNDR algorithm with better performance on the number of rounds than other solutions. The VNDR network lifetime is four times SPIN, and is DD two times. Using our VNDR scheme, effectively extending the life of network. This is mainly attributed to employing Virtual Port and vector addresses, that result in effectively reduce the control overhead, reduces the amount of data transmission, and prolong the network lifetime.

Fig. 8. is Comparing node average energy consumption for network working time.

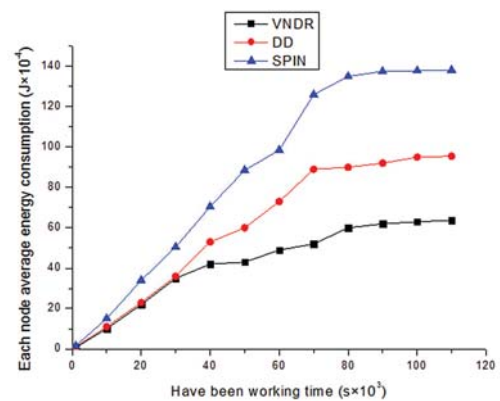


Fig. 8. Comparing node average energy consumption for network working time

Fig.9 is Comparing the Number of Rounds for different network sizes.

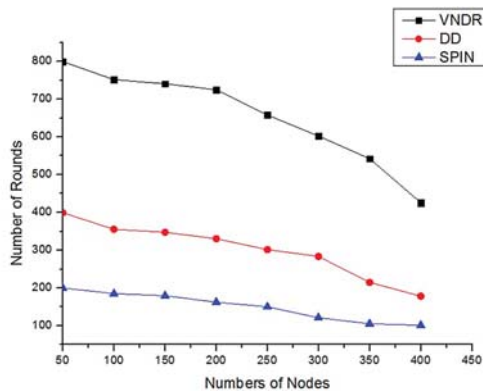


Fig. 9. Comparing the Number of Rounds for different network sizes

CONCLUSION

A new dynamic routes scheme VNDR is proposed for mobile WSN using vector address in this paper. Our VNDR scheme, first construct vector address based on virtual port number of node, and then embedded vector address in the packet. In data transfer phase, the next hop formed by cutting the vector algorithm. The simulation results reveals the VNDR reduced the control overhead and prolonged the network lifetime. In future, we will develop a test bed for VNDR scheme and hardware simulation.

ACKNOWLEDGEMENTS

This work was financially supported by National Natural Science Foundation Project, project number: U1636109, and National 863 Project, project number: 2007AA01Z203, and Hebei provincial science and technology plan special work projects, NO: 16236004D-8, and Project of 2016 Science and Technology Program of Zhangjiakou City, NO: 1611059B.

REFERENCES

1. Abdul Waheed Khan, Abdul Hanan Abdullah, Mohammad Abdur Razzaque, and Javed Iqbal Bangash. *VGDR: A Virtual Grid-Based Dynamic Routes Adjustment Scheme for Mobile Sink-Based Wireless Sensor Networks*, IEEE SENSORS JOURNAL, VOL. 15, NO. 1, JANUARY 2015
2. Ravinder Kaura, Kamal Preet Singhb. *An Efficient Multipath Dynamic Routing Protocol for Mobile WSNs*, International Conference on Information and Communication Technologies (ICICT 2014), Procedia Computer Science 46 (2015) 1032–1040
3. Tapan Kumar Jain, Davinder Singh Saini, and Sunil Vidya Bhooshan. *Lifetime Optimization of a Multiple Sink Wireless Sensor Network through Energy Balancing*. Journal of Sensors Volume 2015, Article ID 921250, 6 pages
4. Jiliang Wang, Wei Dong, Zhichao Cao, and Yunhao Liu. *On the Delay Performance in a Large-Scale Wireless Sensor Network: Measurement, Analysis, and Implications*. IEEE/ACM TRANSACTIONS ON NETWORKING,
5. Gabriel Mujica, Jorge Portilla, Teresa Riesgo. *Performance evaluation of an AODV-based routing protocol implementation by using a novel in-field WSN diagnosis tool*. Microprocessors and Microsystems 39 (2015) 920–938
6. B. Baranidharan, B. Santhi. *DUCF: Distributed load balancing Unequal Clustering in wireless sensor networks using Fuzzy approach*. Applied Soft Computing 40 (2016) 495–506
7. Mohammad Hammoudeh, Robert Newman. *Adaptive routing in wireless sensor networks: QoS optimisation for enhanced application performance*. Information Fusion, Volume 22, March 2015, pp. 3–15
8. Fatemeh Mansourkiaie, Mohamed H. Ahmed. *Per-Node Traffic Load in Cooperative Wireless Sensor Networks*. IEEE COMMUNICATIONS LETTERS, VOL. 20, NO. 2, FEBRUARY 2016
9. Suraj Sharma and Sanjay Kumar Jena. *Cluster based Multipath Routing Protocol for Wireless Sensor Networks*. ACM SIGCOMM Computer Communication Review, Volume 45, Number 2, April 2015
10. Saeid Mottaghi, Mohammad Reza Zahabi. *Optimizing LEACH clustering algorithm with mobile sink and rendezvous nodes*. Int. J. Electron. Commun. (AEÜ) 69(2015)50–514
11. Etimad Fadel, V.C. Gungor, Laila Nassef, Nadine Akkari, M. G. Abbas Malik, Suleiman Almasri, Ian F. Akyildiz. *A survey on wireless sensor networks for smart grid*. Computer Communications 71 (2015) 22–33
12. José J. Anaya, Edgar Talavera, Felipe Jiménez, Francisco Serradilla, José E. Naranjo. *Vehicle to Vehicle GeoNetworking using Wireless Sensor Networks*. Ad Hoc Networks 27 (2015) 133–146
13. T. Hayes, F.H. Ali. *Proactive Highly Ambulatory Sensor Routing (PHASeR) protocol for mobile wireless sensor networks*. Pervasive and Mobile Computing 21 (2015) 47–61
14. Zhang Shuai, Liang, Man-Gui, Jiang Zhong-Yuan, Li Hui-Jia. *Improved efficient static weighted routing strategy on two-layer complex networks*, International Journal of Modern Physics C, 2015, 26(1).
15. An, Wenjuan, Liang, Mangui, Liu, He. *An improved one-class support vector machine classifier for outlier detection*, Proceedings of the Institution of Mechanical Engineers, Part C: Journal of Mechanical Engineering Science, 2015, 229(3): 580–588.

16. Jiang Zhong-Yuan, Liang Man-Gui, An Wen-Juan. *Effects of efficient edge rewiring strategies on network transport efficiency*, Physica A: Statistical Mechanics and Its Applications, 2014, 394: 379–385.
17. Zhang Shuai, Liang Man-Gui, Jiang Zhong-Yuan, Wu Jia-Jing. *Effective strategy of adding links for improving network transport efficiency on complex networks*, International Journal of Modern Physics C, 2014, 25(6).
18. Liu He, Liang Mangui. *Privacy-preserving registration protocol for mobile network*, International Journal of mmunication Systems, 2014, 27(10): 1653–1671.
19. Wang Shujuan, Liang Mangui. *An Efficient Multicast Strategy for On-Demand Data Dissemination in Wireless Networks*, Journal of Internet Technology, 2014, 15(4): 557–564.
20. Zhang Shuai, Liang Man-Gui, Li Hui-Jia. *Method to enhance traffic capacity for two-layer complex networks*, Canadian Journal of Physics, 2014, 92(12):1599–1605.
21. Jiang Zhong-Yuan, Liang Man-Gui, Wu Jia-Jing. *Dynamic Source Routing Strategy for Two-Level Flows on Scale-Free Networks*, PLoS One, 2013, 8(12).

CONTACT WITH THE AUTHOR

Liang Mangui, Ph. D.

e-mail: mgliang@bjtu.edu.cn

tel: 13801166970

Institute of Information Science

Beijing Jiaotong University

Beijing 100044

CHINA

PASSIVE LOCALIZATION FOR MIXED-FIELD MOVING SOURCES

Chunxian Gao, Ph.D,

Hui Liu, Ph.D,

Communication Engineering Department, Xiamen University, Xiamen, Fujian, China

ABSTRACT

Due to the mobility of underwater equipment, high-precision underwater positioning technology will face two technical challenges: dealing with mixed-field signals composed of near-field signals and far-field signals; adapting to variable component of mixed-field signals considering the mobility of equipment. Under this condition, an effective method based on MUSIC is addressed in this paper. After distinguishing far-field signal subspace from mixed-field signal subspace, estimations of DOAs and powers of far-field sources are carried out. Then the corresponding far-field and noise signal components can be eliminated from the signal subspace. After that, based on path-following algorithm, modified 2D-MUSIC is performed for DOA and range estimations of near-field sources. The performance of the proposed method is verified and compared with the other methods through computer simulations. Reasonable classification of source types and accurate localization estimation can be achieved by using the proposed method.

Keywords: underwater positioning; passive localization; mixed-field sources; MUSIC algorithm

INTRODUCTION

Underwater smart equipment has technical advantages in marine environmental monitoring, seabed mineral exploration, and harbor monitoring, which mostly includes UUVs, ROVs and AUVs. With the advancement of underwater communication technology and battery technology, more and more underwater equipment has been deployed to offshore ports and open ocean areas, which has driven the rapid development of the marine industry. With the release of a large number of equipment, high-precision underwater positioning technology has become the core technology for underwater equipment monitoring, joint operation and equipment autonomous operation.

Source localization based on array signal is a fundamental problem in many fields such as radar, sonar, communications, and seismic exploration [1]. In the past decades, a great deal of work has been carried out in this field and various algorithms have been proposed for either far-field sources [1]-[3] or near-field sources [4]-[8]. However, in most practical applications, sources may be spread over a wide area, creating a mixed-field signal environment. In some special cases, some of the sources may switch between far-field and near-field range continuously due to random movement of sources in that area. Most methods aforementioned may fail or deteriorate in such environment.

Recently, passive localization under mixed-field sources environment has been explored, and several efficient methods

are available. A two-stage MUSIC method [9] was proposed by Liang and Liu, to solve the mixed-field sources localization problem. Wang and Sun [10] reconstructed and utilized the sparsity of mixed-field signal subspace, and the better performance of accuracy and resolution were proved. He and Swanmy [11] introduced second-order statistics (SOS) to their solution and improved computation efficient. By implementing matrix difference technology, two-stage localization algorithm was proposed by Liu and Sun [12]. However, these methods are dependent on the hypothesis that the exact numbers of far-field sources or near-field sources are known in advance and keep invariant. In reality the exact numbers remain in a state of flux because of the possible motion of sources. Thus, these methods would encounter the failure problem or unsatisfactory performance.

In this paper, a new method was proposed for the mixed-field sources environment where some of them may be in motion. By exploring the difference of MUSIC spectral features between far-field and near-field signals, an estimator, termed as far-field distinguisher, is constructed to distinguish far-field signals from mixed-field signals. Azimuth DOAs and powers of far-field sources are estimated and eliminated from the mixed signal subspace. Based on path-following algorithm, azimuth DOAs and ranges information of near-field sources are obtained via Strip-2D-MUSIC searching. Computer simulation proves that the proposed method avoids the estimation failure problem and provides a more accurate estimation performance.

The remainder of the paper is organized as follows. Section II describes the signal model for localization estimation of mixed-field sources. Section III derives the algorithms involved in the proposed method and introduces its main implementation steps. Section IV shows the computer simulation results. Section V is the conclusion of the whole paper.

SIGNAL MODELS

There are M uncorrelated narrowband sources under mixed-field sources scenarios, among which there are M_N near-field signals and $(M - M_N)$ far-field signals. The sensor array is a symmetric uniform linear array and consists of $L = 2N + 1$ sensors with inter-sensor spacing d . The phase reference point of the sensor array is set in its center. The sample signal received by sensor array can be written as [11, 12]

$$\mathbf{x}(t) = \mathbf{A}_N \mathbf{s}_N(t) + \mathbf{A}_F \mathbf{s}_F(t) + \mathbf{n}(t) \quad (1)$$

where

$$\mathbf{s}_N = [s_1(t) \cdots s_m(t) \cdots s_{M_N}(t)]^T \quad (2)$$

$$\mathbf{s}_F = [s_{M_N+1}(t) \cdots s_{M_N+m}(t) \cdots s_M(t)]^T \quad (3)$$

$$\mathbf{A}_N = [\mathbf{a}(\theta_1, r_1) \cdots \mathbf{a}(\theta_m, r_m) \cdots \mathbf{a}(\theta_{M_N}, r_{M_N})] \quad (4)$$

$$\mathbf{A}_F = [\mathbf{a}(\theta_{M_N+1}) \cdots \mathbf{a}(\theta_{M_N+m}) \cdots \mathbf{a}(\theta_M)] \quad (5)$$

\mathbf{s}_N and \mathbf{s}_F are near-field and far-field source signal vectors, respectively. \mathbf{A}_N and \mathbf{A}_F are the array steering matrices of near-field and far-field sources, respectively. $\mathbf{a}(\theta_m, r_m)$ and $\mathbf{a}(\theta_m)$ are the array steering vectors for near-field and far-field sources, respectively.

$$\mathbf{a}(\theta_m, r_m) = [e^{j(-N\gamma_m + N^2\phi_m)}, \dots, 1, \dots, e^{j(N\gamma_m + N^2\phi_m)}]^T \quad (6)$$

$$\mathbf{a}(\theta_m) = [e^{-jN\gamma_m}, \dots, 1, \dots, e^{jN\gamma_m}]^T \quad (7)$$

$$\gamma_m = -2\pi(d/\lambda) \sin \theta_m \quad (8)$$

$$\phi_m = \pi[d^2/(\lambda r_m)] \cos^2 \theta_m \quad (9)$$

where λ is the wavelength of the source signal, θ_m and r_m stand for DOA and range of the m th signal source. $\mathbf{n}(t)$ is additive sensor noise and modeled as zero-mean Gaussian which is spatially uniformly white and statistically independent of all the signals.

Based on (1), the array covariance matrix can be calculated as

$$\begin{aligned} \mathbf{R} &= E\{\mathbf{x}(t)\mathbf{x}^H(t)\} \\ &= \mathbf{A}_N \mathbf{S}_N \mathbf{A}_N^H + \mathbf{A}_F \mathbf{S}_F \mathbf{A}_F^H + \sigma_n^2 \mathbf{I} \\ &= \mathbf{R}_N + \mathbf{R}_F + \sigma_n^2 \mathbf{I} \\ &= \mathbf{A} \mathbf{S} \mathbf{A}^H + \sigma_n^2 \mathbf{I} \end{aligned} \quad (10)$$

Where \mathbf{S} , \mathbf{S}_N and \mathbf{S}_F are diagonal matrices and diagonal elements represent power of corresponding sources. σ_n^2 indicates the sensor noise power.

PROPOSED SOLUTION

NOISE POWER ESTIMATION

The proposed solution assumes that the value of M is known, but the actual number of far-field or near-field sources remains unknown because of the possible motion of sources. The array covariance matrix can be eigen decomposed as

$$\mathbf{R} = \mathbf{U}_S \Delta_s \mathbf{U}_S^H + \mathbf{U}_N \Delta_n \mathbf{U}_N^H \quad (11)$$

where $\Delta_s \in \mathbb{R}^{M \times M}$ is a diagonal matrix and its diagonal elements are the M largest eigenvalues of \mathbf{R} , $\Delta_n \in \mathbb{R}^{(L-M) \times (L-M)}$ is a diagonal matrix and its diagonal elements are the rest eigenvalues of \mathbf{R} , $\mathbf{U}_S \in \mathbb{C}^{L \times M}$ spans the signal subspace which consists of the eigenvectors related to the M largest eigenvalues, and $\mathbf{U}_N \in \mathbb{C}^{L \times (L-M)}$ spans the noise subspace which consists of the eigenvectors related to the rest. Based on the MUSIC subspace theory [2], power of noise can be calculated as

$$\tilde{\sigma}_n^2 = \frac{1}{L-M} \text{tr}(\Delta_n) \quad (12)$$

Then $\tilde{\mathbf{R}}_{FN}$ can be reconstructed which only contains the far-field and near-field signal information.

$$\tilde{\mathbf{R}}_{FN} = \mathbf{U}_S (\Delta_s - \tilde{\sigma}_n^2 \mathbf{I}_{M \times M}) \mathbf{U}_S^H \quad (13)$$

It can be seen from (13) that sensor noise is well eliminated, and its influence is effectively reduced.

DOA ESTIMATION FOR FAR-FIELD SOURCES

According to 2D-MUSIC pseudo-spectrum scalar function [4], far-field source signal will exhibit peaks at the range $r = \infty$ with corresponding azimuth. 2D-MUSIC pseudo-spectrum scalar function defined as

$$V(\theta, r) = [\mathbf{a}^H(\theta, r) \tilde{\mathbf{U}}_{FNn} \tilde{\mathbf{U}}_{FNn}^H \mathbf{a}(\theta, r)]^{-1} \quad (14)$$

where $\tilde{\mathbf{U}}_{FNn}$ represents the noise eigenvector matrix of $\tilde{\mathbf{R}}_{FN}$. This indicates that the DOAs of the far-field sources can be obtained by screening all peaks from the following 1D-MUSIC pseudo-spectrum function,

$$P(\theta) = [\mathbf{a}^H(\theta, \infty) \tilde{\mathbf{U}}_{FNn} \tilde{\mathbf{U}}_{FNn}^H \mathbf{a}(\theta, \infty)]^{-1} \quad (15)$$

In our scenarios, there are two fatal flaws in (15). Firstly, there exists spurious peaks among real peaks due to the interference from near-field signals or noise, which is deduced and simulated in paper [13]. The phenomenon of spurious peaks would lead to estimation failure. Secondly, the number of far-field sources remains unknown during estimating. Sorting out the first k maximum peaks or using conventional methods, which would not solve far-field estimation problem. For confirming estimations from (15), further processing need to be carried out. For each azimuth θ_i and corresponding pseudo-spectrum value $V(\theta_i, \infty)$ from (15), we do another 1D searching on range dimension, termed as far-field signal distinguisher,

$$V(\theta_i, r_i) = \max_r \{ [\mathbf{a}^H(\theta_i, r) \tilde{\mathbf{U}}_{FNn} \tilde{\mathbf{U}}_{FNn}^H \mathbf{a}(\theta_i, r)]^{-1} \} \quad (16)$$

where $r \in [0.62(D^2 / \lambda)^{1/2}, 2D^2 / \lambda]$ and D represents the array aperture. Finally, far-field sources classification and DOA estimation are fulfilled based on the following criteria,

$$\begin{cases} \tilde{\theta}_F = \theta_i, \text{ far-field, if } V(\theta_i, \infty) > V(\theta_i, r_i) \\ \text{spurious peak, if } V(\theta_i, \infty) \leq V(\theta_i, r_i) \end{cases} \quad (17)$$

POWER ESTIMATION FOR FAR-FIELD SOURCES

After processing of (13), far-field signals become the largest interference sources for the parameters estimation of near-field sources. Removal of far-field signals from mixed-field signals subspace is helpful to improve the accuracy of near-field parameters estimation. Similar to the mathematical derivation in paper [13], the power of mth far-field signal can be estimated as,

$$\begin{aligned} \tilde{\sigma}_m^2 &= \frac{1}{\tilde{\mathbf{a}}^H(\tilde{\theta}_m) [\mathbf{A} \mathbf{S} \mathbf{A}^H] \tilde{\mathbf{a}}(\tilde{\theta}_m)} \\ &= \frac{1}{\tilde{\mathbf{a}}^H(\tilde{\theta}_m) [\tilde{\mathbf{R}}_{FN}]^+ \tilde{\mathbf{a}}(\tilde{\theta}_m)} \end{aligned} \quad (18)$$

where $\tilde{\sigma}_m^2$ is mth far-field source power estimation and $\tilde{\mathbf{a}}(\tilde{\theta}_m)$ is the corresponding estimated steering vector, superscript + denotes the pseudo inverse operation. After power estimation of all far-field sources, $\tilde{\mathbf{R}}_N$ which only contains near-field information can be reconstructed as

$$\begin{aligned} \tilde{\mathbf{R}}_N &= \tilde{\mathbf{R}}_{FN} - \tilde{\mathbf{R}}_F \\ &= \tilde{\mathbf{R}}_{FN} - \tilde{\mathbf{A}}_F \text{diag}(\tilde{\sigma}_1^2, \dots, \tilde{\sigma}_{M-M_N}^2) \tilde{\mathbf{A}}_F^H \end{aligned} \quad (19)$$

DOA AND RANGE ESTIMATION FOR NEAR-FIELD SOURCES

According to path-following method [13, 14], the algebraic relation between the azimuth $\tilde{\theta}_i$ from 1D MUSIC pseudo-spectrum function and the actual azimuth θ_i and range r_i for near-field source satisfies

$$\sin \theta_i = \sin \tilde{\theta}_i + 0.5 \times (1 - \sin^2 \tilde{\theta}_i) (D / r_i) \quad (20)$$

The numerical difference between $\tilde{\theta}_i$ and θ_i is small which is proved in paper [14]. Azimuth estimation from 1D MUSIC pseudo-spectrum function can be regard as rough azimuth estimation for near-field source. Based on this assumption, we propose Strip-2D MUSIC for parameters estimation for

near-field sources. Firstly, M_N azimuths are estimated from 1D MUSIC pseudo-spectrum function,

$$P(\theta) = [\mathbf{a}^H(\theta) \tilde{\mathbf{U}}_{Nn} \tilde{\mathbf{U}}_{Nn}^H \mathbf{a}(\theta)]^{-1} \quad (21)$$

where $\tilde{\mathbf{U}}_{Nn}$ represents the noise eigenvector matrix of $\tilde{\mathbf{R}}_N$. Each estimated azimuth θ_{i_rough} is termed as rough azimuth estimation for near-field sources. Then, 2D search zone based on rough azimuth estimations is set up,

$$\begin{cases} r \in [0.62(D^2 / \lambda)^{1/2}, 2D^2 / \lambda] \\ \theta \in [\theta_{i_rough} - \Delta\theta, \theta_{i_rough} + \Delta\theta] \end{cases} \quad (22)$$

Finally, 2D MUSIC search on each zone is carried out, and DOA and range estimation for near-field sources are fulfilled.

$$V(\theta_i, r_i) = \max_{\theta, r} \{[\mathbf{a}^H(\theta, r) \tilde{\mathbf{U}}_{Nn} \tilde{\mathbf{U}}_{Nn}^H \mathbf{a}(\theta, r)]^{-1}\} \quad (23)$$

Compared with traditional 2D MUSIC, Strip-2D MUSIC avoids whole plane searching, and its computational complexity is far less than the traditional method.

E. DESCRIPTION OF THE PROPOSED METHOD

We can summarize the proposed method as follows.

- Step 1: Compute the array covariance matrix \mathbf{R} by (10).
- Step 2: Eigen decompose \mathbf{R} , and obtain the power estimation of noise by (12), then eliminate noise by (13).
- Step 3: Eigen decompose $\tilde{\mathbf{R}}_{FN}$, and obtain all peaks by (15), then do range dimension search for each estimated azimuth value by (16), finally fulfill far-field signal classification and azimuth DOA estimations by (17).
- Step 4: Obtain far-field power estimations by (18), and eliminate far-field signals by (19).
- Step 5: Eigen decompose \mathbf{R}_N , and obtain M_N peaks by (21), then set up search zones by (22), finally do Strip-2D MUSIC by (23).

COMPUTER SIMULATION RESULTS

In this section, the feasibility of the proposed method is verified by computer simulation. A nineteen-element ULA with a quarter-wavelength inter-sensor spacing is used. Before the start of the simulation, there are 5 signal sources to be located. Among them there are three far-field sources and two near-field sources. Three far-field sources are assumed to have the following azimuths: $\{-33^\circ, 22^\circ, 60^\circ\}$ and two near-field sources are assumed to be located at $(-25^\circ, 12\lambda)$ and $(13^\circ, 7\lambda)$. In order to simulate the motion of sources, the position of the source is disturbed before each independent estimation,

and the amount of disturbance is assume as $(x \cdot \Delta\theta, x \cdot \Delta\lambda)$ and $x \sim U(-1, 1)$. The additive noise is assumed to be spatial white complex Gaussian, and the SNR is defined relative to each signal. For comparison, both the SOS based method (SOS) [11] and the Matrix-Differencing based method (MD) [12] are also presented. The application of SOS or MD depends on the number information of far-filed and near-field sources. At each estimation, SOS and MD is provided with the accurate number of sources, but the proposed method is kept in the state of blind estimation. The presented results are evaluated by the estimated root mean percent square error (RMPSE), defined as

$$RMPSE = \sqrt{\frac{1}{N} \sum_{i=1}^N \left(\frac{E_i - R_i}{R_i} \right)^2} \times 100\% \quad (24)$$

where denotes the estimated value, denotes the real value and denotes the number of independent estimations.

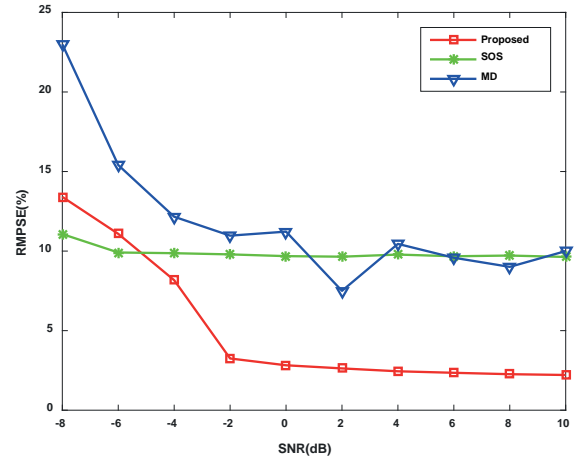


Fig. 1. The RMPSEs of azimuth estimations for far-field sources versus SNRs, the snapshot number is 500, 500 independent trials.

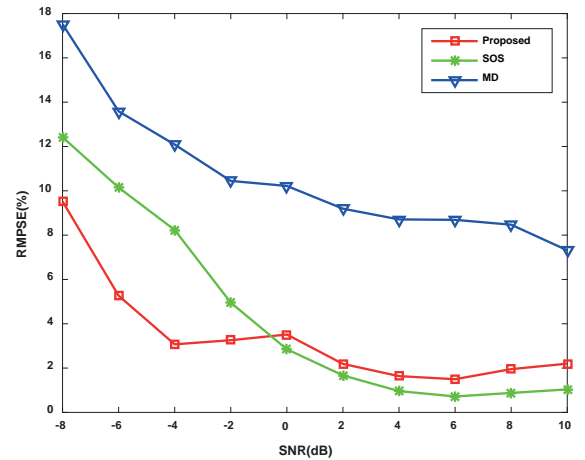


Fig. 2. The RMPSEs of azimuth DOAs estimations for near-field sources versus SNRs, the snapshot number is 500, 500 independent trials.

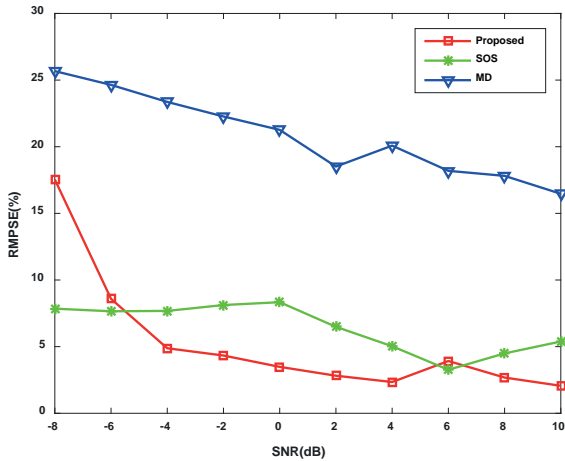


Fig. 3. The RMPSEs of range estimations for near-field sources versus SNRs, the snapshot number is 500, 500 independent trials.

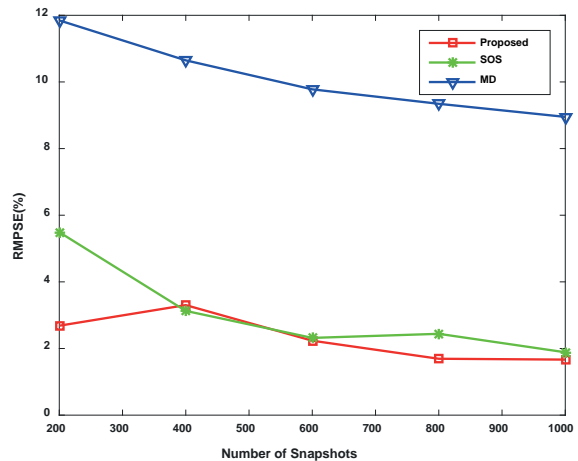


Fig. 5. The RMPSEs of azimuth DOAs estimations for near-field sources versus snapshot number, SNR=0dB, 500 independent trials.

In the first experiment, we examine the performance of three methods under various SNR. Figs. 1–3 respectively show the RMPSE simulation results of far-field sources azimuth estimation, near-field sources azimuth estimation and near-field sources range estimation under various SNR conditions. From the simulation results, it can be seen that the estimation performance of the three methods has been improved with the increase of SNR. Among them, the performance of the proposed and SOS is better than that of MD in all kinds of SNR conditions. For far-field azimuth estimation and near-field range estimation, the performance of the proposed is slightly lower than that of SOS at low SNR condition (<-6dB), but with the increase of SNR, the performance of the proposed is better than that of SOS. For near-field azimuth estimation, the performance of the proposed is superior to or equivalent to that of SOS at all SNR conditions. In general, the comprehensive performance of the proposed in all kinds of SNR conditions is better than that of SOS or MD, showing the robustness of the method.

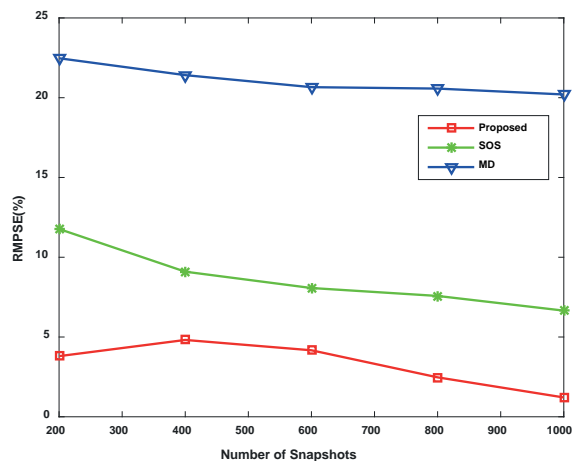


Fig. 6. The RMPSEs of range estimations for near-field sources versus snapshot number, SNR=0dB, 500 independent trials.

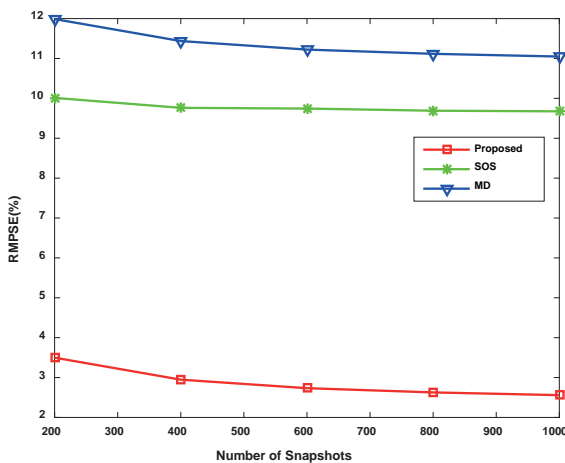


Fig. 4. The RMPSEs of azimuth DOAs estimations for far-field sources versus snapshot number, SNR=0dB, 500 independent trials.

Secondly, we assess the performance of the proposed method versus the number of snapshots. The simulation conditions are similar to the first experiment except that the SNR is set at 0dB, and the number of snapshots is evenly spaced from 200 to 1000 with interval 200. The RMPSE simulation results are respectively displayed in Figs. 4–6. The estimation RMPSE for three methods declines monotonously with the increase of snapshot size. Increasing the size of snapshot does improve the performance of three estimation methods. In the smaller snapshot zone, the performance is improved obviously with the increase of snapshot size. However, when the snapshot size reaches a certain value, the effect of the increase in size tends to be slow.

CONCLUSION

We have presented a method for mobile sources localization problem under mixed-field scenarios. Our investigation has shown that the proposed method is capable of yielding

reasonably good estimates of the azimuth and the range estimation for both the far-field and near-field sources.

BIBLIOGRAPHY

1. H. Krim and M. Viberg, "Two decades of array signal processing research: The parametric approach," *IEEE Signal Process. Mag.*, vol. 13, no. 4, pp. 67–94, Jul. 1996.
2. R. O. Schmidt, "Multiple emitter location and signal parameter estimation," *IEEE Trans. Antennas Propag.*, vol. AP-34, pp. 276–280, Mar. 1986.
3. R. Roy and T. Kailath, "ESPRIT-estimation of signal parameters via rotational invariance techniques," *IEEE Trans. Acoust., Speech, Signal Process.*, vol. 37, pp. 984–995, Jul. 1989.
4. Y. D. Huang and M. Barkat, "Near-field multiple sources localization by passive sensor array," *IEEE Trans. Antennas Propag.*, vol. 39, pp. 968–975, Jul. 1991.
5. A. J. Weiss and B. Friedlander, "Range and bearing estimation using polynomial rooting," *IEEE J. Ocean. Eng.*, vol. 18, no. 2, pp. 130–137, Apr. 1993.
6. E. Grosicki, K. Abed-Meraim, and Y. Hua, "A weighted linear prediction method for near-field source localization," *IEEE Trans. Signal Process.*, vol. 53, no. 10, pp. 3651–3660, Oct. 2005.
7. W. Zhi and M. Y. W. Chia, "Near-field source localization via symmetric subarrays," *IEEE Signal Process. Lett.*, vol. 14, no. 6, pp. 409–412, Jun. 2007.
8. Y. Wu, H. C. So, and J. Li, "Passive localization of near-field sources with a polarization sensitive array," *IEEE Trans. Antenna Propag.*, vol. 55, no. 8, pp. 2402–2408, Aug. 2007.
9. J. Liang and D. Liu, "Passive localization of mixed near-field and far-field sources using two-stage music algorithm," *IEEE Trans. Signal Process.*, vol. 58, no. 1, pp. 108–120, Jan. 2010.
10. B. Wang, J. Liu, and X. Sun, "Mixed sources localization based on sparse signal reconstruction," *IEEE Signal Process. Lett.*, vol. 19, no. 8, pp. 487–490, Aug. 2012.
11. J. He, M. N. S. Swamy, and M. O. Ahmad, "Efficient application of MUSIC algorithm under the coexistence of far-field and near-field sources," *IEEE Trans. Signal Process.*, vol. 60, no. 4, pp. 2066–2070, Apr. 2012.
12. G. Liu and X. Sun, "Two-Stage Matrix Differencing Algorithm for Mixed Far-Field and Near-Field Sources Classification and Localization," *IEEE Sensors J.*, vol. 14, no. 6, pp. 1957–1965, Jun. 2014.
13. D. Storer and A. Nehorai, "Passive Localization of Near-Field Sources by Path Following," *IEEE Trans. Signal Process.*, vol. 42, no. 3, Mar. 1994.
14. J. H. Lee, C.-M. Lee, and K.-K. Lee, "A path-following algorithm using a known algebraic path," *IEEE Trans. Acoust., Speech Signal Process.*, vol. 47, no. 5, pp. 1487–1490, May 1999.

CONTACT WITH THE AUTHORS

Hui Liu, Ph.D

email: lh@xmu.edu.cn

tel.: +86-13860494875

Communication Engineering Department

Xiamen University

Xiamen Fujian, 361005

CHINA

THE CAVITATION NUCLEI TRANSIENT CHARACTERISTICS OF LENNARD-JONES FLUID IN CAVITATION INCEPTION

Fu Qiang, Dr.

Zhang Benying, M.S.

Zhao Yuanyuan, Dr.

Zhu Rongsheng, Prof. Dr.

Liu Gang, M.S.

Li Mengyuan, M.S.

National Research Center of Pumps, Jiangsu University, Zhenjiang, Jiangsu, China

ABSTRACT

In the field of ocean engineering, cavitation is widespread, for the study of cavitation nuclei transient characteristics in cavitation inception, we applied theoretical analysis and molecular dynamics (MD) simulation to study Lennard-Jones (L-J) fluid with different initial cavitation nuclei under the NVT-constant ensemble in this manuscript. The results showed that in cavitation inception, due to the decrease of liquid local pressure, the liquid molecules would enter the cavitation nuclei, which contributed to the growth of cavitation nuclei. By using molecular potential energy, it was found that the molecular potential energy was higher in cavitation nuclei part, while the liquid molecular potential energy changes greatly at the beginning of the cavitation nuclei growth. The density of the liquid and the surface layer changes more obvious, but density of vapor in the bubble changes inconspicuously. With the growth of cavitation nuclei, the RDF peak intensity increased, the peak width narrowed and the first valley moved inner. When cavitation nuclei initial size reduced, the peak intensity reduced, the corresponding r_{bin} increased. With the decrease of the initial cavitation nuclei, the system pressure and total energy achieved a balance longer, and correspondingly, they were smaller. In addition, at the beginning of the cavitation nuclei growth, the total energy and system pressure changed greatly.

Keywords: Cavitation nuclei; Molecular dynamics simulation; Lennard-Jones fluid; Cavitation inception; Nucleation

INTRODUCTION

Cavitation is a complex flowing physical phenomenon in liquid involving multiphase flow, compressibility and exchange of multiple aspects. In the field of ocean engineering, cavitation is widespread, such as propellers, high-speed underwater weapons, and so on[1]. How to reduce and control the occurrence of cavitation and reduce the negative effects of cavitation is an important research direction in the field of ocean engineering. Cavitation is often accompanied by hydrodynamic disturbance, decline of performance, erosion on solid surface, increase of water resistance, pressure fluctuation, vibration, noise, and so on [2,3]. Therefore, it is

extremely important to study the microcosmic mechanism of cavitation.

Cavitation is one of the key research in fluid mechanics, especially the micro cavitation bubble nucleation. In recent years, the research on micro bubble nucleation mainly is focus on theoretical analysis, experimental research and molecular dynamics (MD) simulations. In the latest theoretical analysis, based on the classical nucleation theory, Kyoko[4], who combined experimental study and numerical results, set up a complete equation about the nucleation rate, and revised Thomas coefficient. Besides, he also found that the improved equation and the classical nucleation theory vary several orders on the bubble nucleation parameter. In the process

of cavitation nuclei experimental research, Mørch, combining theoretical and experimental method, discussed tensile strength and bubble nuclei generation[5], and then studied the bubble nuclei nucleation on solid-liquid interface[6], and verified the experimental results. In addition, Anders Andersen[7] made an experimental and theoretical study on cavitation interface, whose results showed that the cavitation nuclei in experiment were smaller than those were calculated.

With the rapid development of MD simulation, a large number of researchers have carried on MD simulations study of bubble nucleation in L-J fluid. For homogeneous nucleation, Kinjo[8], Yasuoka[9] and Wu[10], investigated cavitation nucleation process of the stretched L-J liquids in homogeneous liquid. According to the simulation results, stable bubbles appeared, when the L-J liquid was stretched to a certain extent to cause liquid density being lower than the certain critical value. Then Sekinea[11] and Vladimir[12,13], also studied the bubble nucleation process in L-J fluid by using the same method, and calculated the system bubble nucleation rate. The results showed that the actual bubble nucleation rate was greater than the predicted value of classical nucleation theory, and indicated that the size effect was not considered in the classical nucleation theory. In addition, Raymond analyzed the bubble nucleation in boiling and cavitation[14], and the results showed that the bubble was non-spherical at initial state, and with the growth of the bubble, it gradually became spherical. The most important was that bubble growth process was in accordance with Rayleigh-Plesset equation. Based on the research of homogeneous nucleation in L-J fluid, there have been some results of heterogeneous nucleation simulation[15,17]. Tsuda discussed the difference in bubble nuclei growth rule between one-component liquid and two-component liquid, and the results showed that coalescence of bubble nuclei appeared frequently in one-component liquid than that in two-component liquid, and the bubble nuclei were more stable near the heterogeneous atoms[17]. In the research of nucleation on the metal surface, Kirandid not only study the bubble nuclei nucleation in L-J fluid with hot nanoparticles by using MD simulation, but also described the formation and rupture of the cavity nanobubbles, and at last concluded the thermodynamic parameters of cavitation formation and rupture of different nanoparticles[18]. In recent years, more and more researchers focus on liquid water bubbles nuclei nucleation[19]. Yijin Mao studied nanobubbles generation and collapse in water by using the MD simulation[20]. And then, Mitsuhiro described the bubble surface tension on bubble nuclei nucleation in water, and found that the surface tension formula of the nanobubbles conformed to the Yong-Laplace (Y-L) equation[21].

In summary, although there has been a certain degree of understanding of bubble nuclei nucleation in the current study, the research on the cavitation mechanism and the influencing factors at a molecular level is not perfect enough. So this manuscript studied bubble nuclei nucleation transient characteristics in cavitation inception and analyzed the changing mechanism of cavitation nuclei and the thermodynamic parameters.

SIMULATION PARAMETERS SETTING

THE LENNARD-JONES POTENTIAL ENERGY

Because the parameters value are very small in MD simulation, each parameter was converted into dimensionless number to calculate and analyze conveniently. The specific conversion relations were shown in Tab. 1.

Tab. 1. Parameters Dimensionless Relationship[22]

Dimensionless quantity	Transformation relation
Length L^*	L/σ
Number density ρ^*	$\rho\sigma^3$
Time t^*	$(\epsilon/m\sigma^2)^{1/2}t$
Temperature T^*	$k_B T/\epsilon$
Energy E^*	E/ϵ
Pressure p^*	$p\sigma^3/\epsilon$

L-J fluid was employed as the simulation study object, which might be caused by the reason that structure of L-J fluid is relatively simple, and it is not involved effect of the bond angle and coulomb force. In addition, it is also an important reason that the experimental data is relatively abundant, and the intermolecular forces between the liquid and gas can be described by using it.

The L-J potential energy function u_{LJ} , which is a function of intermolecular distance r , is given by[17]

$$u_{LJ}(r) = 4\epsilon \left[\left(\frac{\sigma}{r} \right)^{12} - \left(\frac{\sigma}{r} \right)^6 \right] \quad (1)$$

where the potential well depth ϵ and the characteristic length σ are potential energy parameters. In this manuscript, the potential energy parameters of argon atoms are set as $\epsilon/k_B = 115.5\text{K}$, $\sigma = 0.3385\text{nm}$, where k_B is Boltzmann's constant [17]. In order to reduce the computational cost, the cut-off processing was adopted for the potential energy model in this manuscript, and the simulation was conducted with a cut-off distance $r_c = 2.5\sigma$.

Permanent gas bubble nuclei are a necessary condition of the cavitation initial nucleation process in liquids, so the helium is applied as non-condensed gas nuclei, and its potential energy parameters are set as $\epsilon_s/k_B = 10.2112\text{K}$, $\sigma_s = 0.2556\text{nm}$. The interaction parameters between two different kinds of molecules, ϵ_{AB} and σ_{AB} are obtained by the Lorentz-Berthelot rules[22], that are calculated from

$$\sigma_{AB} = \frac{1}{2}(\sigma + \sigma_s) \quad (2)$$

and

$$\epsilon_{AB} = \sqrt{\epsilon \cdot \epsilon_s} \quad (3)$$

SIMULATION PARAMETER SETTINGS

The computational domain was filled with 64000 argon atoms in the simulation, which was built with the face-center cubic (FCC) unit of cubic lattice distribution at the initial position. The center of the computational domain was set to be the cavitation nuclei, whose initial size of dimensionless radius $R^*= 2,5,10$ respectively and its slices of the model were showed in Fig.1. In the simulation process, canonical ensemble (NVT) was adopted in this research, which acquired that number of molecules N , computational domain volume V and temperature T were constants in the computational domain. And in the process of cavitation, temperature can be thought to be constant, while system pressure and total energy would change with cavitation nuclei growth. The influence of pressure change is very important to research cavitation in liquid, so the NVT was used to control the system temperature. Because of inertia in the liquid, generally, the volume and quality of liquid around the cavitation nuclei are considered constant in a very short time, therefore NVT was used to fix system volume in this study. Other conditions were as follows: the initial velocity of each argon atom distribution was a series of random numbers under an absolute temperature in the system, which was in accordance with Maxwell distribution. Periodic boundary conditions were applied in the calculation model, and verlet leap frog method was adopted to calculate Newton equations. The method of interval sampling was used, and simulation steps were 1.0fs. The total time was set to be 1000ps.

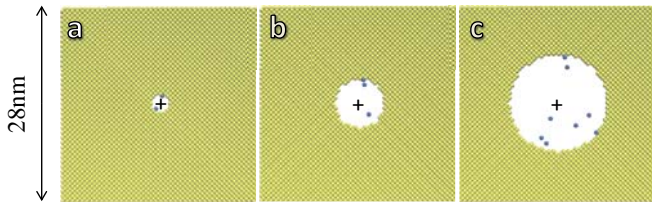


Fig.1. Model section. The section thickness is 0.1nm, where the blue particles gas molecules, and the '+' markers indicate their center-of-masses; a) $R^*=2$; b) $R^*=5$; c) $R^*=10$

Simultaneously, the temperature control system was introduced in the computational domain to correct the velocity of two kinds of molecules, which ensured a constant temperature. Here, the temperature and pressure are calculated from[17]

$$T = \frac{2}{3Nk_B} \sum_i \frac{1}{2} m v_i^2 \quad (4)$$

and

$$p = \rho k_B T - \frac{1}{3V} \sum_{i<j} \sum_j r_{ij} \frac{\partial u_{JJj}}{\partial r_{ij}} \quad (5)$$

where m is the molecular mass, ρ is density, N is the total number of molecules in the computational domain, V is the

volume of the computational domain, v_i is the speed of atom No. i , k_B is the Boltzmann's constant, u_{JJ} is the potential energy function, and i and j is different molecules number.

In order to accurately obtain the transient characteristics of cavitation nucleation, molecular structure was set to be stable before the calculation, so relaxation time and energy minimization method was carried out. In the relaxation time, the temperature and pressure were key to characteristic parameters whether the system was stable. The total steps of relaxation time were set to be 5000ps.

The change of the system temperature and pressure was shown in Fig.2 with the dimensionless number density $\rho^*=0.5924$ at the temperature $T=84K$. From the temperature curve (see Fig.2(a)), the system temperature reached equilibrium stage (III) after 1200ps, so the computational domain was regarded as reaching equilibrium before the liquid argon overheated. The eventual equilibrium temperature value was almost a constant, which fluctuated at about 84.05K. From the pressure curve (see Fig.2(b)), The pressure tended to be balanced and at equilibrium stage (III). And the balanced pressure was not over 0MPa at equilibrium stage (III), which caused the system was in a tension state to guarantee the existence of cavitation nuclei. When cavitation nucleus appeared in liquid, the greater the cavitation nuclei were, the greater the pressure increase was, but finally the pressure equilibrium value was consistent with the others.

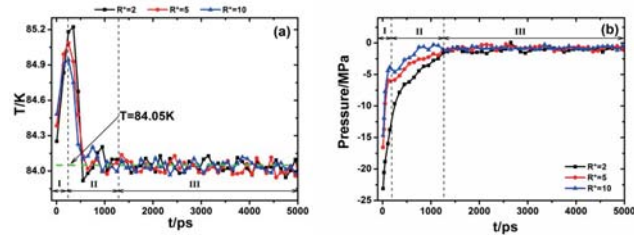


Fig.2. The system temperature (a) and pressure (b) change in relaxation process. I) initial stage; II) transition stage; III) equilibrium stage.

SIMULATION RESULTS AND ANALYSIS

CAVITATION NUCLEI EVOLUTION PROCESS

In cavitation inception, the mass and volume of the liquid around cavitation nuclei can be regarded as the constant in a very short time, which caused by the inertia of the liquid mass, accordingly the sampling and calculation of the liquid region with cavitation nuclei was carried out. When the saturation pressure of liquid argon reached overheated state, the growth of cavitation nucleus was shown in Fig. 3 under the NVT ensemble with a stable volume and temperature.

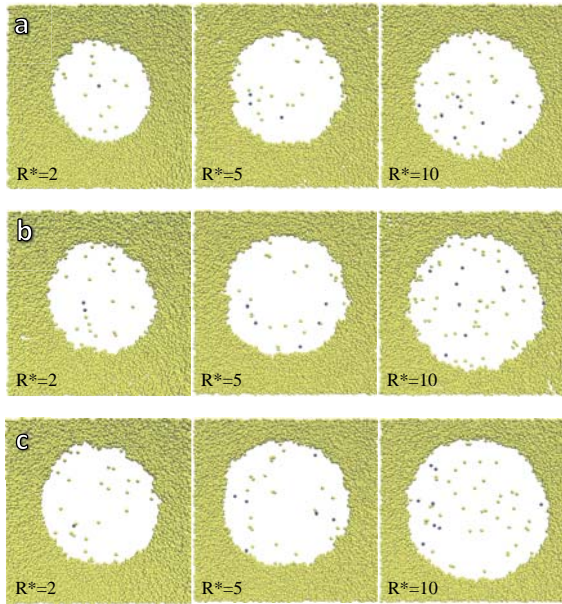


Fig.3. Time evolution of cavitation nuclei section. The section thickness was 0.1nm; a) $t=10ps$; b) $t=100ps$; c) $t=1000p$

From Fig.3, the radius of cavitation nuclei increased gradually with time, and the growth process of cavitation nucleus with different initial size was similar. Because the liquid and the vapor of argon molecules did not reach equilibrium state in the system, the change of argon molecules from liquid into cavitation nuclei occurred continuously with decreasing pressure at the beginning of the growth, and the cavitation nuclei radius would increase constantly to reach a certain value eventually. Owing to the restriction of computational domain, the cavitation nuclei could not increase infinitely. So the cavitation nuclei changed faintly at the later growth, which indicated the vapor and liquid reached dynamic equilibrium. The shape of cavitation nucleus tended to be spherical over time because of the intermolecular forces, and molecules was gather together by the intermolecular forces, which was the surface tension on the macro level. Therefore in the cavitation nuclei growth process, the shape of the cavitation nucleus was always spherical.

In Fig.3, the larger the cavitation nucleus initial size was, the larger the cavitation nuclei final size was. It was for the reason that the cavity volume and permanent gas molecules number were larger because of the larger cavitation nuclei initial size, which caused the frequent interaction increased between gas molecules and liquid molecules, and the activity enhancement of liquid molecular in the surface layer was carried out. That is to say, under the same condition, the probability for argon atoms entering the cavitation nuclei increased, so the final cavitation nuclei would be larger. The distribution in surface layer of cavitation nuclei was unsmooth, and uneven, which proved that surface layer molecules into the cavitation nuclei were not consistent. It was likely that the interfacial vaporization heat of one molecule in the surface layer was carried out, which led to potential energy of other molecules around it reducing, and activity

decreased. In addition, the probability for other molecules from the surface layer into cavitation nuclei decreased.

From Fig.3, it can be seen that there were cavitation nuclei containing permanent gas in liquid during the cavitation inception. Because of the liquid local pressure decreasing, the enhancement of the molecular activity was carried out in the surface layer, which caused the liquid molecules entered the cavitation nuclei continuously because of its vaporization, and the vapor molecules constantly condensed into liquid molecules. But the number of evaporative molecules was more than that the vapor molecules condensing into the liquid, which contributed to the growth of the cavitation nuclei. With the liquid molecules entering the cavity, the cavitation nuclei would constantly be expand, but their size wouldn't change dramatically because of the computational domain limitation, when the cavitation nuclei grew to a certain size. If the computational domain was large enough, the cavitation nuclei would become bubbles which continuously developed and eventually formed the cavitation on the macro level.

THERMODYNAMIC PARAMETERS CHANGE OF CAVITATION NUCLEI GROWTH

THE MOLECULAR POTENTIAL ENERGY CHANGE IN THE COMPUTATIONAL DOMAIN

Molecular potential energy was a key parameter to the stability of molecular structure, and it was one of the important indexes to distinguish vapor. So the molecular potential energy was analyzed and calculated with different time steps in this manuscript.

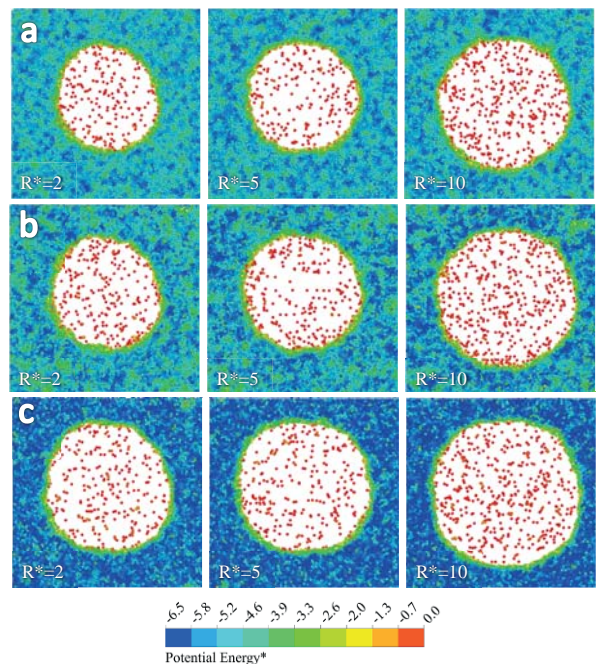


Fig.4. Molecular potential energy change section of cavitation nuclei growth. The section thickness was 0.1nm; a) $t=10ps$; b) $t=100ps$; c) $t=1000ps$

It was showed that the molecular potential energy variation of cavitation nucleus growth in Fig.4, and it can be seen that molecular potential energy was corresponding to cavitation nuclei evolution in cavitation inception. Comparing Figs. 3 with 4, we could see that the vapor potential energy increased gradually, which mainly caused by the liquid molecules continually entered the vapor region, resulting in a constant growth of cavitation nuclei. From the Boltzmann density distribution law, the vapor number density would decrease with the increase of the potential energy in conservative field, thus the potential energy in cavitation nuclei was considerably higher than that in other region. So, the position, the growth speed, the size and the shape change of cavitation nuclei would be judged according to the potential energy inside the liquid argon. Potential energy of surface layer was higher than liquid but lower than vapor significantly, which meant that the number density of the surface layer larger than liquid but smaller than vapor (verified in Fig.5). In addition, the average intermolecular distance in the surface layer was larger than liquid but smaller than vapor (validated in Fig.7). Since the attraction was greater than repulsion between adjacent molecules in the surface layer. Namely, net tangential attraction was existed in adjacent molecules in the surface layer, which was surface tension source.

From Fig.4, it can be found that the liquid potential energy in the computational domain decreased on the whole, while the potential energy in cavitation nuclei changed faintly with time going by. During the decrease of the liquid potential energy, the reducing speed of different radius was different: before $t=100\text{ps}$, the blue region changed least with $R^*=2$, but mostly with $R^*=10$. Therefore in cavitation nuclei growth, the decrease amplitude of liquid potential energy was different with various cavitation nuclei. So the larger the cavitation nuclei initial size was, the greater the reduction of liquid potential energy was at the same time. It was because the gravitational potential energy on the surface layer was proportional to the surface area, that is, the larger the initial size was, the larger the surface area was, which caused that potential energy of surface layer molecular was greater and molecular structure of the surface layer was more unstable. It meant that the molecular activity enhancement in the surface layer was carried out, which increased the probability of entering the cavity, resulting in the molecular potential energy reducing faster. There were some molecules with stronger activity in the surface layer because of high molecular potential energy, so the potential energy of the surrounding molecules must be lower, and its structure was more stable. Therefore, it verifies the surface layer was rough and coarse in the aspect of the potential energy.

With time going by, the molecular potential energy gradient between vapor and liquid tended to be concentrated, and the surface molecules were in an unbalanced state. Besides, the potential energy gradient changed greatly because of the effect of attraction. For different initial size of cavitation nuclei in the liquid, the variation of potential energy inside the surface layer was similar. This was because that although the cavitation nuclei surface were different, the radius of

curvature were similar, which contributed to a similar change of the molecular potential energy. Under the isothermal condition, the surface free energy was the sum of all molecules gravitational potential energy, so, the surface free energy had a tendency to decrease because of potential energy decreasing. Thus a shrinking tendency was carried out in surface layer, which showed why the bubbles were spherical from another aspect, and it was also the reason for a consistent surface potential energy distribution of cavitation nuclei.

To sum up, at the beginning of the cavitation nuclei growth, the molecular potential energy was larger and the molecular activity was stronger in the liquid and surface layer, in addition, the molecular internal structure stability was poorer, which caused that the liquid molecules escaped attraction of surrounding molecules to enter the vapor. With the cavitation nuclei growing, liquid density increased in a short time, thus causing that the molecular structure tended to be stable, which was characterized by the reduction of the liquid molecular potential energy.

COMPUTATIONAL DOMAIN DENSITY CHANGE IN THE CALCULATION DOMAIN IN CAVITATION INCEPTION

In order to have a closer look at the density variation, the spatial density profile was computed by averaging density in bubble center and radially bin which are built by uniformly chopping the simulation box in the horizontal direction; the final profile of density are shown in Fig. 5.

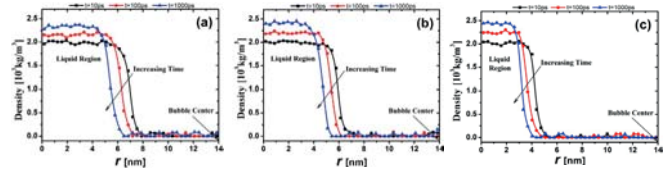


Fig.5. Computational domain density variation. a) $R^*=2$; b) $R^*=5$; c) $R^*=10$

From the density variation curves in Fig.5, with different initial size, the density curves variation was similar. It can be seen that liquid density kept increasing with liquid volume decreasing and the density of vapor in the bubble was constant, despite vapor volume increasing with time going by. The density variation of the surface layer was sharper, and its severity variation did not change with time. In cavitation inception, the density of liquid region surrounding cavitation nuclei was increasing in a short time, and corresponding to Fig.4. The greater the liquid density, the smaller the potential energy, which caused the molecular structure was more stable. The surface layer density was between the liquid and vapor, thus its potential energy was somewhere in between, which also confirmed indirectly that the Boltzmann distribution law was applicable even to the molecular level.

From 3 pictures in Fig.5, the smaller the initial size of cavitation nuclei, the longer the interval of the density variation curve in the surface layer, so the cavitation nuclei growing space here was bigger. While the liquid region was

on the contrary, the density curve interval was longer with the larger initial size of cavitation nuclei. The main reason was that the cavitation nuclei became larger with the smaller liquid region. But the inertia of liquid was still existed, so the density here became denser and the potential energy became smaller in a short time. That is to say if the initial size of cavitation nuclei was larger at first, then the liquid region density was larger in the final growth of cavitation nuclei. In addition, the potential energy here was smaller and the structure of liquid molecule around cavitation nuclei was more stable, but the growing space of cavitation nuclei was smaller. In Fig.5(c), the curve interval in the position of surface layer between $t=10\text{ps}$ and $t=100\text{ps}$ was wider than that between $t=100\text{ps}$ and $t=1000\text{ps}$, which showed that the growth rate here was reduced significantly in the latter of the simulation, when the cavitation nuclei initial size was $R^*=10$. Although the distance in the other two figures curves was not wide compared to the former, the growth of the other two kinds of cavitation nuclei was declined to some extent, since the time scale between the 2 curves was 10 times.

Thus, in cavitation inception, because the cavitation initial stage was very short, there was a time lag of the liquid surrounding cavitation nuclei moving, so the density variation of the liquid and the surface layer was more obvious, and the density of vapor in the bubble was constant.

THE CAVITATION NUCLEI DIAMETER CHANGES IN CAVITATION INCEPTION

In cavitation inception, the cavitation nuclei size change was the focus of researchers all the time, and the size change of the cavitation nuclei determined whether cavitation bubbles could be produced, so this manuscript monitored and analyzed the cavitation nuclei transient changes in cavitation inception.

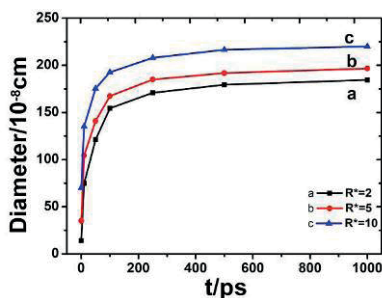


Fig.6. Cavitation nuclei diameter changes

Fig.6 showed the changing curve for cavitation nuclei diameter, and the three curves respectively represented the growth of different initial cavitation nuclei, which could be seen from the figure that the cavitation nuclei diameter had obvious changes. Before $t=200\text{ps}$, the three growth curves increased more sharply, but the curves increase reduced rapidly because of the limitation of the computational domain, which was consistent with the density variation (Fig.5), when time was between 200ps and 1000ps . There

was a certain difference among the three curves in the figure, since the cavitation nuclei final diameter depended on its initial radius, which caused that the larger the initial radius was, the greater the final diameter was. During the cavitation nuclei growth, under the same condition, the growth speed was relatively rapid if the initial radius of cavitation nuclei was large, on the contrary its growth was relatively slow if the initial radius was small.

Tab. 2. Cavitation nuclei diameter change

Type	$R^*=2$	$R^*=5$	$R^*=10$
Initial diameter D_0	14.016	35.04	70.08
Maximum diameter D_{\max}	184.537	189.586	219.998
Growth rate = $(D_{\max} - D_0)/D_0$	12.2857	4.2561	2.1514

As can be seen from table 2, the growth rate of $R^*=2, 5$ and 10 was $12.2857, 4.2561$ and 2.1514 , respectively. By contrast, it can be found that the growth space of cavitation nuclei was larger if its initial radius was smaller, but its final size was smaller than that of the cavitation nuclei with larger initial diameter. It showed that under the same external conditions, the smaller cavitation nuclei growth was same as the larger cavitation nuclei, but its growth needed a long time. With computational domain permitting, the cavitation nuclei surface area was greater, which caused the high resistance appeared, so the growth space of cavitation nuclei became smaller.

The rapid growth of cavitation nuclei was occurred so that cavitation nuclei grew into bubbles rapidly (calculation domain permitting) in cavitation inception, which confirmed a „sudden” cavitation inception rather than a „calm” one. Cavitation nuclei diameter was necessary to the cavitation on the micro level, and the larger the initial radius was, the faster its growth rate was.

THE MOLECULES RADIAL DISTRIBUTION FUNCTION (RDF) IN CAVITATION INCEPTION

The internal structure change of liquid was very important in the cavitation process, so this manuscript analyzed it by combining the RDF.

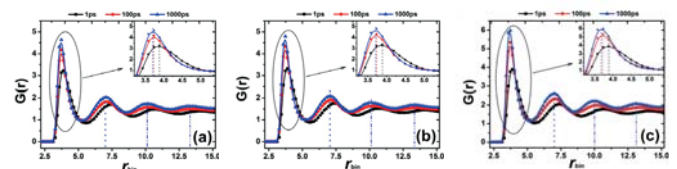


Fig.7. The changes of molecular RDF. a) $R^*=2$; b) $R^*=5$; c) $R^*=10$; r_{bin} was the intermolecular distance

The RDF changes of liquid argon molecules were shown in Fig.7.(a), (b) and (c), which showed that the RDF was 0 when $r_{\text{bin}} < 3.21\text{\AA}$, that is, the recent distance between adjacent molecules would not be less than 3.21\AA . When $r_{\text{bin}} = 3.9\text{\AA}$, $G(r)$ has reached the first peak, and this time, r_{bin} represented

the most likely distance of two adjacent liquid molecules in the cavitation nuclei growth, where the here r_{bin} was lowest point of the intermolecular interaction potential. As $r_{bin}=7.25\text{\AA}$, $G(r)$ reached the second peak which was the liquid molecules second shell peak, and at this time r_{bin} was corresponding to the distance between the center liquid molecule and that of the second shell. And the third peak appeared at about $r_{bin}=10.9\text{\AA}$, and the peak intensity gradually weakened. In addition, all the RDF tended to be a stable value when $r_{bin}>14.3\text{\AA}$, that is, when the distance exceeded 14.3\AA , the system molecules were similar to the uniform liquid. The above features reflecting the liquid had a short-range in order, long-range out of order. From (a), (b) and (c) in Fig.7, it can be found that in the entire growth of cavitation nuclei, the liquid RDF had several peaks, which represented the first coordination sphere, the second coordination sphere, et al respectively of the center molecule, and the peaks attenuated quickly with time going by. So it can be concluded that the orderly arrangement of liquid molecules disappeared with the increase of the intermolecular distance. And also, it can be said that the areal density, on average, was greater than the average density near the peak position. Although the cavitation nuclei initial size was different, the curve of RDF was roughly the same, that it, for the first peak, before $t=100\text{ps}$ and with time going by, the peak intensity of the RDF increased gradually, while the peak width narrowed gradually. When $t>100\text{ps}$, the two curves interval in the first peak became smaller, which indicated that the peak intensity and the peak width achieved a balance. This suggested that when $t<100\text{ps}$, at the maximal peak, the probability of liquid molecules appearance would increase with the extension of time. In addition, the density became bigger gradually, which caused that the molecular distribution was loose and out of order, and the internal structure stability was poor, that the vaporization of liquid molecules was serious. With the growth of cavitation nuclei, the peak intensity increased, the peak width narrowed and the first valley moved inner. The reason why the above features occurred were that the liquid molecular arrangement at the first coordination sphere became close, the molecular distribution became regularly and the internal liquid structure was stable, which led to the result that the vaporization of liquid molecules decreased gradually. By comparison from the former two peaks, the peak intensity of the second peak became larger with the increasing of cavitation nuclei initial size, while the change of peak width was not obvious, but the width was larger than the former one. The main reason was that the size of cavitation nuclei increased gradually with time going by, which made the volume of liquid region become smaller, the density become heavier and the performance of the peak intensity increase. With intermolecular distance of the second shell r_{bin} increasing, the molecular disorder became larger and the structure became more unstable, which was accord with the rules that short-range in order, and long-range out of order. Therefore, the performance of the second peak width in RDF did not change with time going by, but it was greater than the first peak width. For the two peaks in RDF, intermolecular

distance r_{bin} increased with cavitation nuclei initial size decreasing, which could get the following conclusion, with the increasing of pressure in cavitation nuclei, the distance between the liquid molecules were compressed to a certain degree, so the performance of intermolecular distance r_{bin} decreased in RDF.

Through the partial enlarged graphs in Fig. 7 (a), (b) and (c), by contrast, it can be found that the larger the cavitation nuclei initial size was, the greater the peak intensity of the RDF was, and the most important was that the increase amplitude of the peak intensity was similar. Moreover, the peak intensity of RDF was more different with the greater difference of cavitation nuclei initial size. The change trend of r_{bin} was contrary to the change of peak intensity: with the extension of time, the position of peak appearance was getting smaller, that the intermolecular distance of liquid was getting smaller, which proved that the liquid pressure was increasing gradually. When $t=100\text{ps}$, r_{bin} reached an equilibrium value, and it showed the intermolecular distance achieved a balance, which caused the liquid pressure was maintained in stable. The liquid intermolecular distance r_{bin} would decrease with the increase of the initial size, so the relative liquid pressure also enhanced. In Fig.7, (a), (b) and (c), the position of other peaks occurrence decreased with cavitation nuclei size increasing, but the peak intensity increased as cavitation nuclei size increased. The most obvious was that the greater the initial cavitation nuclei size was, the severer curves amplitude was. Through the analysis of the RDF, it can be concluded that the liquid molecular distribution of RDF was similar to the change rule of the liquid molecular potential energy. At the beginning of the cavitation nuclei growth, the vaporization of liquid molecules was rapid with its liquid volume decreasing, which, under the limit of the computational domain, caused the gradual increase of density, and stability of molecular structure. After that the cavitation nuclei size grew slowly, and the liquid volume and density changed faintly.

Therefore, in cavitation nuclei growth, the molecular distribution inside the liquid became orderly gradually and the liquid density changed over time. And the change of liquid peak has confirmed short-range in order, long-range out of order. At the early growth of cavitation nuclei, the vaporization of liquid molecules was relatively serious and intermolecular distance was greater. While in the later growth, the liquid molecular distribution was relatively regular and ordered with intermolecular distance decreasing to a balance. The peak of the RDF was greater with the larger initial size of cavitation nuclei, so the molecular distribution rule was more regular, which caused relative increase of pressure liquid.

THE SYSTEM PRESSURE AND TOTAL ENERGY VARIATION IN CAVITATION NUCLEI GENERATION

On the macro level, the occurrence of cavitation was because of the reduction of the external pressure, so it was a necessary condition for cavitation that the system pressure being lower than the saturated vapor pressure. So this

manuscript monitored the pressure of cavitation occurrence in the computational domain.

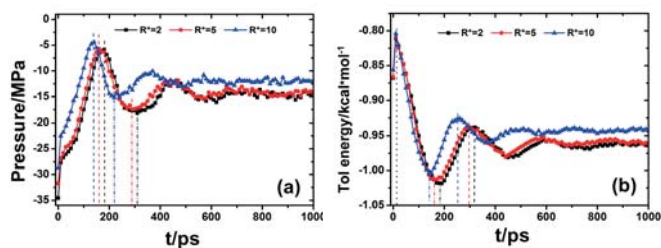


Fig.8. The system pressure (a) and the total energy (b) variation of cavitation nuclei growth.

The three curves in Fig.8 represented the system pressure variation of cavitation nuclei growth. It can be seen that, the system pressure was negative in the entire growth process, which indicated that the liquid region and the growth of cavitation nuclei was in a tension state in the whole computational domain. The absolute value of pressure system was getting maximum, which meant that the entire system was in the maximum tensile force at the initial state of cavitation nuclei growth. Before $t=100\text{ps}$, the absolute value of system pressure reduced continuously, which meant that tensile force been in system was reduced gradually. However, cavitation nuclei were in rapid growth at the initial state of cavitation nuclei growth, which might lie in that the average tensile force was larger. When $100\text{ps} < t < 680\text{ps}$, the system pressure has been in fluctuation, and the tensile force was changing constantly, but not affect cavitation nuclei growth with its growth rate decreasing. After $t=680\text{ps}$, the system pressure value reached a relatively balanced state, which indicated that the tensile force remained stable and cavitation nuclei growth was maintained at moderate speed. Therefore, the cavitation nuclei grew steadily, and finally became bubbles within the permission of the computational domain after $t=680\text{ps}$. The above features meant that before $t=100\text{ps}$, the liquid molecules were not stable, which might be attributed to the high potential energy. So it was easier that molecules from the surface layer into the cavitation nuclei, which caused the needed tensile strength decreased gradually. When $100\text{ps} < t < 680\text{ps}$, the liquid internal structure was stable, which might result from that liquid potential energy decreased, so the acquired tensile force increased gradually. But, the system pressure fluctuation was larger, which might lie in that it was a transition state. After $t=680\text{ps}$, the potential energy stability was achieved, and the liquid internal structure was more stable, which caused that the tensile force been in cavitation nuclei growth tended to be stable.

In the Fig.8 (a), the overall trend had no difference when $R^* = 2, 5$ and 10 , but it can be seen from the local pressure variation that the absolute value of system pressure was smaller, and the emergence of valley value was shorter, which might lie in that the initial size was greater. As the cavitation nuclei initial size decreased, the emergence of the valley value would be later, and their absolute value would be smaller. Moreover, the pressure balance would also be later in the

meantime. When the cavitation nuclei growth was stable, the absolute value of the system pressure would decrease with the increase of the initial size: The average pressure of $R^*=5$ was 0.8Mpa lower than that of $R^*=2$, 14.95Mpa , while the average pressure of $R^*=10$ was 12.35Mpa , which reduced 1.8Mpa compared with $R^*=5$, and the reduction amplitude increased 55.56% . This was mainly because the cavity in liquid was greater with the larger cavitation nuclei initial size, which jointly caused that tensile force needed for the cavitation nuclei growth became smaller, so the system pressure needed for phases change was smaller. It means that the cavitation occurrence was easier with the larger initial cavitation nuclei size, during external pressure reduced to a lesser extent, under the same external conditions.

Fig.8 (b) was the curve variation of the total energy with the changing of time. From Fig.8 (a) and (b), the total change trend of the system total energy was similar to the system pressure change. Before $t=100\text{ps}$, the overall trend reduced gradually. Moreover the total energy has been fluctuant with $100\text{ps} < t < 680\text{ps}$, and after $t=680\text{ps}$, the total energy value reached a relatively balanced state.

From the three curves in Fig.8 (b), the total energy firstly reached the maximum value before $t=150\text{ps}$, which was around 1.0186 kcal/mol . As the cavitation nuclei initial size decreased, the minimum value that the total energy achieved in the initial stage decreased gradually. And when $R^*=2$, the total energy had the least minimum value which was about 0.975 kcal/mol . As the difference of cavitation nuclei initial size became smaller, the difference of the minimum value would also be smaller like the first valley value of $R^*=2, 5$. This showed that when the cavitation nuclei appeared in the liquid, the total energy in the initial state has a decreasing process. And with the decrease of the initial cavitation nuclei size, the total energy decreasing process had a downward trend but it had a violent fluctuation before it achieved a balance.

From the Fig.8, it was almost same that the time for the total energy and pressure of the system achieving the best value. It can be seen that with the increase of the initial size, the occurrence time of the first peak reduced, the peak value also increased gradually, and the balanced time for the total energy was shorter. When $t=680\text{ps}$, the total energy achieved a balance which became larger with the increase of cavitation nuclei initial size. The total energy of $R^*=5$ was 0.007 kcal/mol larger than that of $R^*=2$, -0.965 kcal/mol , while it increased to -0.9404 kcal/mol when $R^* = 10$, which increased 0.0176 kcal/mol compared with $R^*=5$, and increasing extent increased by 60.23% .

Compared Fig.8 (a) with (b), it can be found that when there were cavitation nuclei inside the liquid argon, the changing trends of the system pressure and the total energy were similar, which would fluctuate before achieving a balance. As well as, the balance time for the system pressure and total energy would be shorter with the larger cavitation nuclei initial size. At the early stage of the cavitation nuclei growth, the pressure and total energy changed greatly, and they would be much more stable in the middle and the later period of the growth. This meant that, in cavitation inception,

the intermolecular structure in liquid was not stable, which would show a pressure and total energy fluctuation on the macro level. At the later growth stage, the intermolecular structure would be much more stable, which would show a balanced pressure and total energy, at that time, the cavitation nuclei reached a certain value with a stable growth, and finally achieved the cavitation within the permission of the computational domain on the macro level.

CONCLUSIONS

(1) In cavitation inception of L-J fluid, the larger the cavitation nuclei were, the larger they were finally in the computation domain. Under the influence of the surface tension, the final shape of the cavitation nuclei was spherical.

(2) In the evolution of cavitation nuclei, the potential energy in the vapor region was the highest, and the potential energy in the liquid region was constantly changing. At the beginning of the cavitation nuclei growth, the potential energy in the liquid region decreased with the increase of the cavitation nuclei. The molecular potential energy in vapor was significantly higher than that in the liquid region.

(3) The density of the liquid and the surface layer changes more obvious, but density of vapor in the bubble changes inconspicuously. It was easier for the cavitation nuclei to grow with the larger cavitation nuclei, and under the influence of the computational domain, finally the cavitation nuclei diameter increased first, and then tended to be certain.

(4) With the change of time, the peak intensity of the RDF first peak in liquid region increased gradually, and the peak width narrowed gradually.

(5) In cavitation inception of the L-J fluid, when the cavitation nuclei were growing, the total energy and the system pressure change fluctuated greatly. As the initial cavitation nuclei size decreased, the balance time for the system pressure and the total energy was later, the absolute value of the system pressure was smaller, and the equilibrium value of the total energy was greater.

ACKNOWLEDGMENTS

This project is partially supported by National Youth Natural Science Foundation of China (51509112), Natural Science Foundation of Jiangsu Province of China (BK20171302), Key R & D programs of Jiangsu Province of China (BE2015129, BE2016160, BE2017140), Prospective joint research project of Jiangsu Province of China (BY2016072-02).

BIBLIOGRAPHY

1. Zhu, R.S., Chen, Z.L., Wang, X.L., Chao, L.: *Numerical study on cavitation characteristics of CAPI400 nuclear main coolant pump*. Journal of Drainage and Irrigation Machinery Engineering. Vol. 34, no. 6, pp. 490-495, 2016.

2. Knapp, R.T., Daily, J.W., Hammitt, F.G.: *Cavitation*. McGraw-Hill Book Company, New York, 1970.

3. Brennen, C.E.: *Cavitation and Bubble Dynamics*. Oxford University Press, Oxford, 1995.

4. Tanaka, K.K., Tanaka, H., Angéilil, R., Diemand, J.: *Simple improvements to classical bubble nucleation models*. Phys Rev E Stat Nonlin Soft Matter Phys. Vol. 92, no. 2, pp.022401, 2015.

5. Mørch, K. A.: *Cavitation nuclei: experiments and theory*. Journal of Hydrodynamics. Vol. 21, no. 2, pp. 176-189, 2009.

6. Mørch, K. A.: *Cavitation inception from bubble nuclei*. Interface Focus. Vol. 5, no. 5, pp. 20150006, 2015.

7. Andersen, A., Mørch, K. A.: *Cavitation nuclei in water exposed to transient pressures*. Journal of Fluid Mechanics. no. 771, pp. 424-448, 2015.

8. Kinjo, T., Matsumoto, M.: *Cavitation processes and negative pressure*. Fluid Phase Equilibria. Vol. 144, no. 1-2, pp. 343-350, 1998.

9. Yasuoka, K., Matsumoto, M.: *Molecular dynamics of homogeneous nucleation in the vapor phase. I. Lennard-Jones fluid*. Journal of Chemical Physics. Vol. 109, no. 19, pp. 8451-8462, 1998.

10. Wu, Y. W., Chin, P.: *A molecular dynamics simulation of bubble nucleation in homogeneous liquid under heating with constant mean negative pressure*. Nanoscale and Microscale Thermophysical Engineering. Vol. 7, no. 2, pp. 137-151, 2003.

11. Sekine, M., Yasuoka, K., Kinjo, T., Matsumoto, M.: *Liquid-vapor nucleation simulation of Lennard-Jones fluid by molecular dynamics method*. Fluid Dynamics Research. Vol. 40, no. 7, pp. 597-605, 2008.

12. Baidakov, V. G., Bobrov, K. S.: *Spontaneous cavitation in a Lennard-Jones liquid at negative pressures*. Journal of Chemical Physics. Vol. 140, no. 18, pp. 184506, 2014.

13. Baidakov, V. G.: *Spontaneous cavitation in a Lennard-Jones liquid: Molecular dynamics simulation and the van der Waals-Cahn-Hilliard gradient theory*. Journal of Chemical Physics. Vol. 144, no. 7, pp. 074502, 2016.

14. Angéilil, R., Diemand, J., Tanaka, K. K., Tanaka, H.: *Bubble evolution and properties in homogeneous nucleation simulations*. Physical Review E Statistical Nonlinear & Soft Matter Physics. Vol. 90, no. 6, pp. 063301, 2014.

15. Maruyama, S., Kimura, T.: *A Molecular Dynamics Simulation of Bubble Nucleation on Solid Surface*.

Transactions of the Japan Society of Mechanical Engineers
Part B. Vol. 65, no. 638, pp. 3461-3467, 1999.

16. Tatsuto, K., Shigeo, M.: *Molecular dynamics simulation of heterogeneous nucleation of a liquid droplet on a solid surface*. Nanoscale and Microscale Thermophysical Engineering. Vol. 6, no. 1, pp. 3-13, 2002.
17. Tsuda, S. I., Shu, T., Matsumoto, Y.: *A study on the growth of cavitation bubble nuclei using large-scale molecular dynamics simulations*. Fluid Dynamics Research. Vol. 40, no. 7-8, pp. 606-615, 2008.
18. Sasikumar, K., Keblinski, P.: *Molecular dynamics investigation of nanoscale cavitation dynamics*. Journal of Chemical Physics. Vol. 141, no. 23, pp. 12B648_1-790, 2014.
19. Yamamoto, T., Ohnishi, S.: *Molecular dynamics study on helium nanobubbles in water*. Physical Chemistry Chemical Physics Pccp. Vol. 13, no. 36, pp. 16142, 2011.
20. Mao, Y. J., Zhang, Y. W.: *Nonequilibrium molecular dynamics simulation of nanobubble growth and annihilation in liquid water*. Nanosc Microsc Therm. Vol. 17, no. 2, pp. 79-91, 2013.
21. Matsumoto, M.: *Surface Tension and Stability of a Nanobubble in Water: Molecular Simulation*. Journal of Fluid Science & Technology. Vol. 3, no. 8, pp. 922-929, 2008.
22. Allen, M. P., Tildesley, D. J.: *Computer simulation of liquid*. Oxford: Clarendon Press, 1987.

CONTACT WITH THE AUTHORS

Zhao Yuanyuan, Ph.D.

email: ujjsfq@sina.com

tel.: 008651188780280

National Research Center of Pumps

Jiangsu University

Zhenjiang Jiangsu 212013

CHINA

RESEARCH ON RUB-IMPACT LOADS RESPONSE OF SHIP SHAFTING

DONG Liang-xiong, associate Prof. Dr.

SHI Yi-ran, Master.

WANG Shao-hua, Master.

Zhejiang Ocean University, Zhoushan, Zhejiang, China

ABSTRACT

The anti-impact ability of shafting affects stability and security of the ship power transmission directly. Moreover, it also cannot be ignored that the rub-impact loads have influence on the torsion vibration of ship shafting. In order to solve the problem of engineering application of reliability assessment under rub-impact loads, a test rig with rubbing generator is established. By carrying out the integrative analysis, the torsional vibration characteristics, such as vibration amplitude and orbit of axle center under the rub impact load are studied. According to the rub-impact conditions obtained through numerical simulation, the experimental verification is carried out on the test rig with rubbing generator. The results show that it is not obvious the influence of rub-impact loads upon the shafting torsion vibration except in special working conditions, that can be simulated by the rubbing generator. The maximum amplitude of torsional vibration is influenced by the radial rigidity as well as the friction coefficient of rubbing body, and the degree of influence is difference under conditions of continuous rubbing and serious rubbing. By adjusting the rigidity of stern bearing, the influence of rub-impact upon shafting can be weakened, which provides a theoretical reference for the safety evaluation of ship shafting.

Keywords: rub-impact; Torsional Vibration; Test Rig; Rubbing Generator

INTRODUCTION

The tail shaft is an important part of the marine propulsion system. The stern tube bearing supports not only its own gravity but also the weight of the propeller and thus withstands the largest load of the ship shafting. With the increasing scale of ship, the increasing hull deformation have generated many troubles of mutually affect between the ship shafting and hull structure. Besides, subjected to various wave loads, the ship shafting work under transient conditions such as variable load or variable inertia, which produce certain influence to the dynamic characteristics of propulsion system [1]. During the running of the ship shaft, as the ship shafting

misalignment or bending, the vibration amplitude of the stern shaft will be augmented. When the amplitude exceeds the gap between the bearing and the journal, the collision and friction between them will happen that are known as the rub-impact [2]. Rub-impact is one common phenomenon of large-scale rotating machinery that will wear the stern tube bearing, cause increase of the gap between bearing and journal, even lead to failure of propulsion system and then affect the safe operation of ship [3].

In order to study the rub-impact phenomenon, the test rig is generally adopted for experimental research. However, the phenomenon of rub-impact between journal and bearing under different marine environment are very complex [4],

and the effectiveness of the experimental research depends on the similarity between the working condition of the test rig and that of actual ship.

In this study, a mass-spring model was proposed for stern structure modeling, and the equivalent mechanical models of spring-vibrator-damper were given by mechanical equivalent principle. Considering the test of rub-impact is destructive, a rubbing generator is adopted to simulate rub-impact load between the tail shaft and the bearing [5]. And then, a variety of conditions of rub-impact load can be realized by adjustment of rubbing generator. By analyzing the rub-impact induced vibration response in both test rig and real ship, the influence of rubbing loads upon ship shafting can be obtained. The study can play a guiding role in solving practical engineering problems such as ship design and ship handling.

THE DYNAMICS CHARACTERISTICS OF SHAFTING SYSTEM

According to the construction features of ship propulsion system, the shafting can be simplified as a single disk system whose two ends are supported on the sliding bearing [6]. So, the mechanic model can be built as shown in Fig. 1.

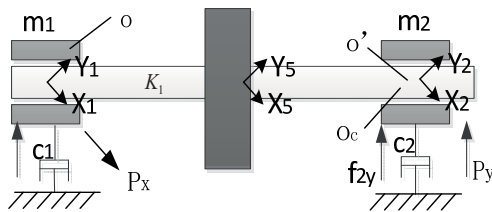


Fig. 1. The mechanical model of shafting

Furthermore, the model of single-disk motion can be obtained as shown in Fig. 2. The mass of disk is m ; the moment of inertia is J ; $o'(x, y)$ is coordinates of the geometrical center of disk; $o_c(x_c, y_c)$ is the ordinates of mass center of disk; The eccentric distances of disk is $|o'o_c| = e$; The axis ξ and the axis ζ are direction of the maximum and the minimum principal inertia axis of shaft. The k_ξ, k_ζ is the maximum and the minimum elastic axis stiffness of shaft in the two axes direction.

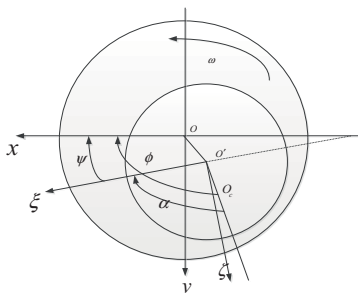


Fig. 2. The model of single-disk motion

In the two coordinate systems of Fig.2, the coordinate correspondence can be expressed as following:

$$\begin{cases} x_c = x + e \cos \phi(t) \\ y_c = y + e \sin \phi(t) \end{cases} \quad (1)$$

In Eq. (1):

ϕ – the angle between x-axis and the line that linked the geometrical center and the mass center of disk, $\phi(t)$ is determined by the following geometric relations:

$$\phi(t) = \psi(t) + a = \int_0^t \omega dt + a \quad (2)$$

In Eq. (2):

a – constant.

In normal operation, the rotational speed of shaft is constant. The disturbance loads can cause torsional vibration to the ship shafting, and then the flexural-torsional coupled resonance may occur.

The $\psi(t)$ can be expressed as follows:

$$\psi(t) = \omega t + \theta(t) \quad (3)$$

In Eq. (3):

θ – the distortion angle of shaft.

And then, the angular velocity and acceleration of disk can be expressed as follows:

$$\begin{cases} \phi(t) = \omega t + \theta + \alpha \\ \dot{\phi}(t) = \omega + \dot{\theta}(t) \\ \ddot{\phi}(t) = \ddot{\theta}(t) \end{cases} \quad (4)$$

The acceleration of the disc center of mass can be expressed as follows:

$$\begin{cases} \ddot{x}_c = \ddot{x} - e\ddot{\phi} \sin \phi - e\dot{\phi}^2 \cos \phi \\ \ddot{y}_c = \ddot{y} + e\ddot{\phi} \cos \phi - e\dot{\phi}^2 \sin \phi \end{cases} \quad (5)$$

The stiffness of propulsion shafting is associated with its principal axis of inertia and is a function that depends on the rotation angle [7]. The axis stiffness in the direction of both the maximum and minimum principal inertia axis is fixed, and the relationship between them can be expressed as:

$$\begin{pmatrix} k_x \\ k_y \end{pmatrix} = \begin{pmatrix} \cos^2 \psi & \sin^2 \psi \\ \sin^2 \psi & \cos^2 \psi \end{pmatrix} \begin{pmatrix} k_\xi \\ k_\zeta \end{pmatrix} = \begin{pmatrix} \cos^2(\phi - \alpha) & \sin^2(\phi - \alpha) \\ \sin^2(\phi - \alpha) & \cos^2(\phi - \alpha) \end{pmatrix} \begin{pmatrix} k_\xi \\ k_\zeta \end{pmatrix} \quad (6)$$

Due to the role of eccentric load, the rotary inertia force and gravity acted on the center of disc mass generate the rotational torque. Besides, there are other torque acted on the geometric center of the disc axle that are the torsion restore torque, torsional resistance torque, and the output torque of driving motor M . So, the moment equilibrium equations of the torsional vibration can be established as following:

$$\begin{aligned} (J+me^2)\ddot{\phi} &= me\ddot{x}\sin\phi - \\ m(\ddot{y} + g)e\cos\phi - k_n\theta + M \end{aligned} \quad (7)$$

Moreover, the dynamics equation of shafting-oil film-stern structure system^[4] can be expressed as follows:

$$M\ddot{u} + (C + G)\dot{u} + Ku = F \quad (8)$$

In Eq. (8), the following parameters are:

- M – the mass matrix;
- u – the matrix of center coordinates;
- G – the matrix of the gyro;
- C – the damping matrix;
- K – the stiffness matrix;
- F – loads matrix.

According to the above dynamics equation, the motion equations of the disk, the front and back journals can be established as follows:

$$\begin{aligned} m_1\ddot{X}_1 + c_1\dot{X}_1 + k_1(X_1 - X_2) &= f_{1x} + P_{1x} \\ m_1\ddot{Y}_1 + c_1\dot{Y}_1 + k_1(Y_1 - Y_2) &= f_{1y} + P_{1y} - m_1g \\ m_2\ddot{X}_2 + c_1\dot{X}_2 + k_1(X_2 - X_1) + k_1(X_2 - X_5) &= f_{2x} + P_{2x} \\ m_2\ddot{Y}_2 + c_1\dot{Y}_2 + k_1(Y_2 - Y_1) + k_1(Y_2 - Y_5) &= f_{2y} + P_{2y} - m_2g \\ m_5\ddot{X}_5 + c_5\dot{X}_5 + k_1(X_5 - X_2) &= m_5r\omega^2 \cos\omega t \\ m_5\ddot{Y}_5 + c_5\dot{Y}_5 + k_1(Y_5 - Y_2) &= m_5r\omega^2 \sin\omega t - m_5g \end{aligned} \quad (9)$$

In Eq. (9):

- (X_1, Y_1) – the center coordinates of the front journal axis;
- (X_2, Y_2) – the center coordinates of the back journal axis;
- (X_5, Y_5) – the center coordinate of the disk with the eccentricity r ;
- K_1 – the elastic axis stiffness;
- k_c – the stern structure stiffness;
- f_{1x} – the oil film force of the left bearing;
- f_{1y} – the oil film force of the right bearing.

So, iterative calculation can be carried by solving simultaneous equations (8) and (9). In Eq. (8), the nonlinear oil film force can be calculated base on the working conditions of short bearing in which the influence of circumferential flow in bearing have be neglected.

NUMERICAL SIMULATION OF RUB-IMPACT LOADS

According to the construction features of the ship shafting, When the rub-impact happen, the force acting point is on the center of disk mass [8]. The calculated mode of rub-impact loads can be obtained as shown in Figure 3.

Supposed the bearing deformation is small elastic deformation, the rub-impact force can be established as follows:

$$\begin{Bmatrix} P_x \\ P_y \end{Bmatrix} = -\frac{(e-\delta)k_c}{e} \begin{bmatrix} 1 & -f \\ f & 1 \end{bmatrix} \begin{Bmatrix} x \\ y \end{Bmatrix} \quad (14)$$

Where in:

P_x – the radial component of the rub-impact force;

P_y – the tangential component of the rub-impact force;

When $e < \delta$, both the radial force and tangential force are zero.

δ – the clearance between journal and bearing in the quiescent state;

e – the tail bearing radius clearance, and $e = \sqrt{x^2 + y^2}$;

k_c – the radial stiffness coefficient.

f – the friction coefficient.

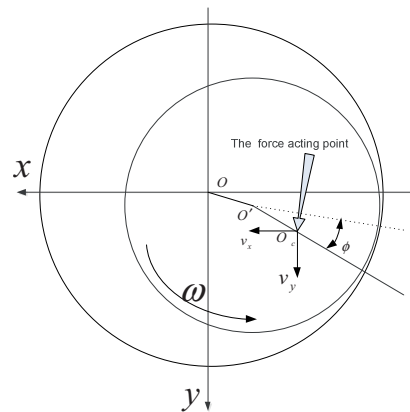


Fig.3. The diagram of rub-impact force

The numerical simulation can be carried by putting Eq. (14) in the Eq. (8) and (9). Initial parameters are set as: $m_1 = 100kg$, $m_2 = 80kg$, $m_3 = 200kg$, $c_1 = 5000N \cdot s / M$, $K_1 = 5 \times 10^6 N / m$, $k_c = 5 \times 10^6 N / m$, $r = 0.06mm$, the radius clearance of bearing $\delta = 0.2mm$ [10]. The initial values of the system kinetics parameters, such as $\dot{X}_1, \ddot{X}_1, \dot{X}_2, \ddot{X}_2, \dot{X}_5, \ddot{X}_5, \dot{Y}_1, \ddot{Y}_1, \dot{Y}_2, \ddot{Y}_2, \dot{Y}_5, \ddot{Y}_5$, are taken as zero. Sensibility analysis results show that the change of initial value had no effect on calculation accuracy.

With the achievements by the former researchers, the condition of slight rubbing, continuous rubbing and severe rubbing can be obtained by setting the different speed to 500, 800, 900r/min [9]. Carrying out the integrative analysis, the center orbits curve and the amplitude-time response curve can be taken as shown in Figure 4~7, and the following conclusions can be drawn:

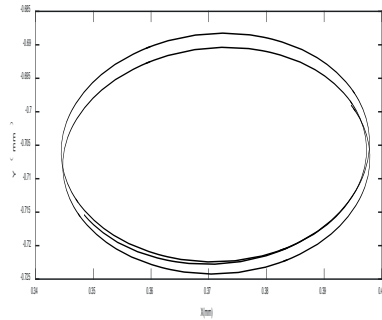


Fig. 4. The center orbits under slight rubbing

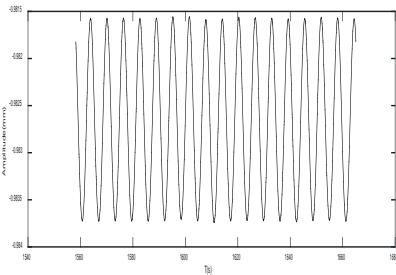


Fig. 5. The torsional vibration amplitude under slight rubbing

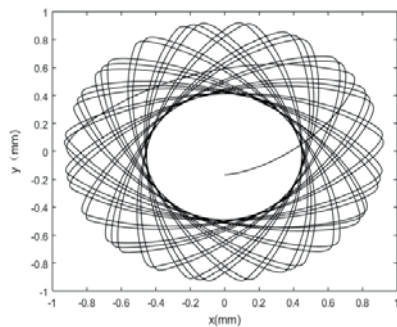


Fig. 6. The center orbits under continuous rubbing

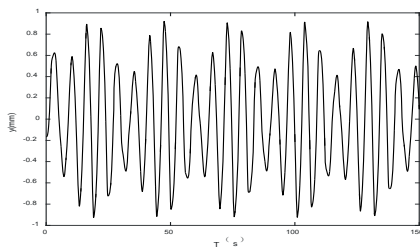


Fig. 7. The torsional vibration amplitude under continuous rubbing

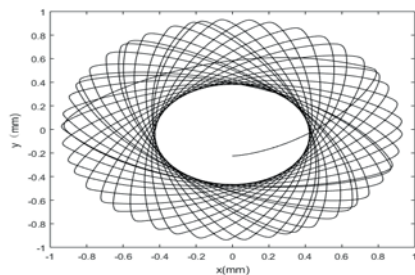


Fig. 8. The center orbits under serious rubbing

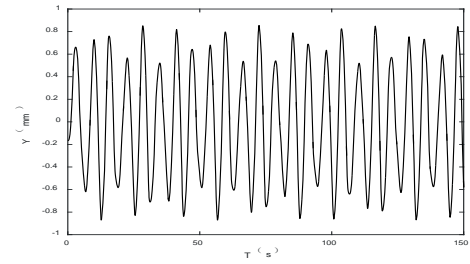


Fig. 9. The torsional vibration amplitude under serious rubbing

1. The rub-impact loads will disturb the motion of shafting bending vibration as show in Fig 4, 6 and 8. Under working conditions of slight rub-impact, the shaft can maintain the periodic motion and the center orbits of shafting is transient and cyclical as show in Fig 4 that the shaft is $4T$ cycle motion. When the rub-impact become serious, the instability of the system motion may result in almost periodic motion and chaotic motion as show in Fig 6 and 8 in which the frequency components of vibration include both low-frequency and high-frequency. And then, the center orbits of shaft under serious rubbing is more chaotic than that of continuous rubbing.

2. As shown in Fig.5, 7, 9, when shaft run under from the slight rubbing to the continuous rubbing, both the mode and the amplitude of torsional vibration change. In contrast, when the shaft run under from the continuous rubbing to the severe impact, the mode of torsional vibration change, the amplitude of torsion vibration almost remain unchanged.

It is obviously that rub-impact load had a real impact on torsional vibration. But the above conditions of rub-impact between the shaft and bearing require the shaft running at specific rotating speed. So, in order to obtain the law of torsional vibration in a wide variety of speed, it is necessary to simulate the working condition of rub-impact by experimental methods.

THE TEST RIG WITH RUBBING GENERATOR

Considering the auxiliary shaft structure can be used to transfer the external loads [11], a test rig with an adjustable auxiliary shaft is established as shown in Fig. 10.

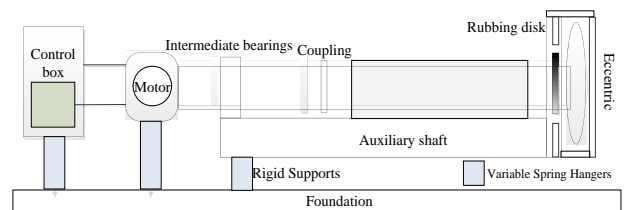


Fig.10. The structure diagram of test rig

In order to simulate the rub-impact load, a rubbing generator was attached to the test rig. The rubbing generator

produces various rub-impact loads that is transmitted to the auxiliary shaft and make it produce corresponding vibration and deformation. In the rig, the variable frequency motor is used to adjust the rotational speed of shafting, and the controlling and monitoring unit is applied to monitor the working condition of the shafting, and the force sensor are mounted on the bearing housing that can be used to obtain the force characteristic of the bearing oil film under different load conditions.

The rubbing generator with disk structuring is made of high quality carbon steel which can be installed and disassembled freely on the test rig [12]. Four adjustable bolts fixed on the rubbing generator under which is connected with the spring as shown in Fig. 11. When the length of bolts is adjusted, the rub-impact will happen sooner with certain gap between the journal and bearing. On the contrary, there is no gap in real state of rub-impact [13]. So, this test rig can simulate various rub-impact loads and is used to validate our model results and discussed later.

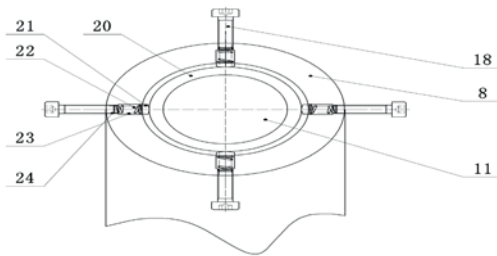


Fig.11. The structure of rubbing generator

Set the device stiffness $k_c = 10^5 N / m$, we test the reaction of the torsional amplitude to various rub-impact loads by measuring the maximum amplitude under different rotational speed. With the numerical simulation simultaneously, the observed value and the theoretical value are obtained as shown in Fig.12.

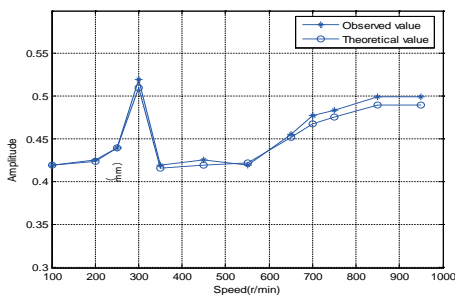


Fig.12. The maximum amplitude with speed

It can be see that the test rig and the real state had resemblance in the change regularities as shown that the observed value is accord with the theoretical value. When the shaft is at a lower speed and rub-impact haven't actually happened, the amplitude was in well keeping with the theoretical value. However, due to the gap between shaft

and bearing under rub-impact loads in the test rig, both the continuous rubbing and severe rubbing are happening sooner rather than real state impact. Accordingly, the maximum amplitude of torsional vibration caused by the rub-impact load is slightly reduced rather than real state impact.

RUB-IMPACT TEST BASED ON RUBBING GENERATOR

In order to evaluate the rub-impact condition of the test rig systematically, it is necessary to comparing the rules of change of maximum amplitude with the different rub-impact condition generated by rubbing generator [14].

In the experiment, the adjustment of rub-impact load is realized by adjusting the length of bolts or changing the spring stiffness of rubbing generator [15], that is changing the friction coefficient or elastic coefficient of rub-impact load. The condition of continuous rubbing and severe rubbing are obtained by choosing the speed to 700, 850r/min in Fig.12. And then, measuring the maximum amplitude at the front of the tail shaft under rub impact loads, the curve of the maximum amplitude with the friction coefficient and elastic coefficient can be taken as shown in Fig. 13 and 14. The experiment results show that the rub-impact loads affect ship shafting in a certain manner as follows:

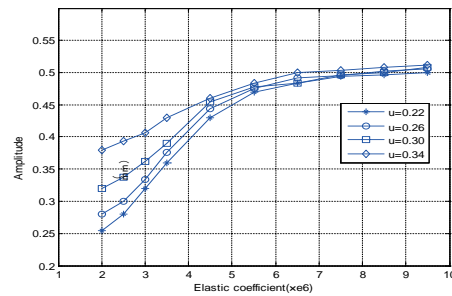


Fig.13. The maximum amplitude under continuous rubbing

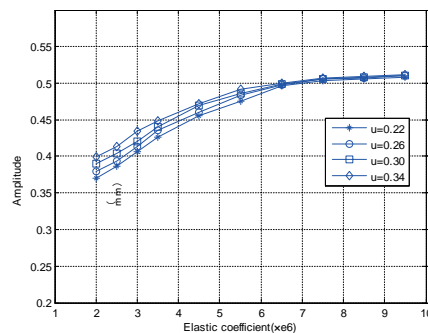


Fig.14. The maximum amplitude under serious rubbing

1. The rub-impact load had a real impact on torsional vibration under continuous rubbing than serious rubbing which is accord with the aforementioned theoretical analysis.

Furthermore, the biggest influence on torsional vibration under continuous rubbing is the friction coefficient, but that is elastic coefficient under serious rubbing.

2. When the coefficient of friction remained unchanged, the maximum amplitude of torsional vibration increases first fast and then slowly with the increase of elastic coefficients. The change speed of the maximum amplitude is different in different friction coefficients. As shown in Fig.14, the lower the friction coefficient is, the smaller the growth rate of the maximum amplitude is likely to be [16]. For example, when the friction coefficient is 0.22, the maximum amplitude has the fastest recovery speed which is not obvious when the coefficient is more than 0.34.

CONCLUSION

In order to simulate the dynamic characteristics of ship shafting system under rub-impact load, the system mechanical model can be regarded as a single disk system whose two ends are supported on the sliding bearing. Furthermore, a test rig that can simulate the rub-impact load is built to carry out experimental verification. The results of the numerical simulation and experiments are summarized as follows:

1. The rub-impact loads will disturb the motion of ship shafting with compromise in both torsion vibration and bending vibration. However, on the voyage, the influence of rub-impact loads to the shafting torsion vibration is not obvious except in special working conditions that can be simulated by test rig with rubbing generator. The rubbing generator has provided useful research methods for the torsional vibration characteristics of shafting under various rubbing loads.
2. The maximum amplitude of torsional vibration increases with the increasing of both the friction coefficient and elastic coefficient in different manners. According to the influences model respectively under continuous rubbing or serious rubbing, the rub-impact loads response on shafting can be weakened by adjusting the radial and tangential rigidity of stern bearing.
3. Due to the clearance between shaft and bearing in the test rig have exert an influence on the rub-impact loads response, there is still a certain difference in the working condition between rub-impact generated by rubbing generator and the actual rub-impact [17], so further studies on rub-impact loads response of ship shafting are necessary.

ACKNOWLEDGEMENTS

This research was supported by Zhejiang Provincial Natural Science Foundation of China under Grant No. LY16E090003.

REFERENCE DOCUMENTS

1. DONG L X, YANG Y, GAO J K, et al. Response mechanism of impact load based on marine shafting-oil film-stern

structure system [J]. Chinese Journal of Ship Research, Vol. 12, no. 1, pp. 122-127, 2017.

2. YANG L K. Study on the lubrication and rub-impact characteristics of stern bearing of ship [D]. Wuhan University of Technology, 2010.
3. LI H. Dynamic characteristics and fault analysis of RUB-impact rotor system [D]. North China Electric Power University, 2016.
4. ZHU Li, PANG Fu-zhen, WANG Xue-ren, etl. Coupled Vibration Mechanism of Equipment and Ship Hull Structure[J]. Journal of Ship Mechanics, Vol. 17, no. 6, pp. 680-688, 2013.
5. Zhang C, Tian Z, Yan, X P. Analytical analysis of the vibration of propulsion shaft under hull deformation excitations [J]. Journal of Vibroengineering, Vol. 18, no. 1, pp. 44-55, 2016.
6. MA Hui, YANG Jian, SONG Rong-ze, NAI Hai-qiang, etl. Review and prospect on the research of rub-impact experiment of rotor systems [J]. Journal of Vibration and Shock, Vol. 33, no. 6, pp. 1-12, 2014.
7. X.F. Wen, Q. Yuan, J. S. Lu, et al. Analysis of Propulsion Shafting Torsional Vibration of Vessels with Double Engines and Double Propellers[C]. 3rd International Conference on Manufacturing and Engineering, pp. 1423-1428, 2012.
8. PAUL S. The Interaction between diesel engine, ship and propeller during manouevring [D]. Netherlands: Technische Univeriteit Delft, 2005.
9. Lech Murawski. Shaft line alignment analysis taking ship construction flexibility and deformations into consideration[J]. Marine Structures, Vol.18, no.1, pp. 62-84, 2005.
10. Jung WooSohn, Seung-BokChoi, Heung SooKim. Vibration control of smart hull structure with optimally placed piezoelectric composite actuators[J]. International Journal of Mechanical Sciences, Vol.53, no.8, pp. 647-659, 2011.
11. Wilfried Schiffer. Advanced methods for static and dynamic shafting calculations [J]. Brodogradnja, Vol.58, no.2, pp. 115-122, 2007.
12. H. Hirani, M. Verma. Tribological study of elastomeric bearing for marine propeller shaft system[J]. Tribology international, Vol.42, no.2, pp.378 -390, 2009.
13. Z.G. Zhang, Z.Y. Zhang, X.C. Huang, et al. stability and transient dynamics of a propeller-shaft system as induced by nonlinear friction acting on bearing-shaft contact

interface[J]. Journal of sound and vibration, Vol.333, no.12, pp.2608-2630 2014.

14. S. Merz, R. Kinns, N. Kessissoglou. structural and acoustic responses of a submarine hull due to propeller forces[J]. Journal of sound and vibration, Vol.325, no.1, pp.266-286, 2009.
15. L. Della, Pietra, G. Adiletta. The squeeze film dam perover four decades of investigations Part I: Characteristics and operating features[J]. SAGE. The Shock and Vibration Dight, Vol.34, no.1, pp.3-26, 2002.
16. Zhao Wu. Investigations on detection model of large scale rotation shaft torsional vibration in precision heavy machinery [J]. International Asia Conference on Informatics in Control, Automation and Robotics, pp. 459-463, 2009.
17. PENU Cheng, DAVILA C, HOU G S. Vibration analysis and sensitivity analysis of stepped beams using singularity functions[J]. Journal of Structures, Vol.2014, no.5, pp. 1-13, 2014.

CONTACT WITH THE AUTHORS

Liangxiong Dong, associate Prof. Dr.

email: dongliangxiong@163.com

tel.: 18368097266

Zhejiang Ocean University

Zhoushan Zhejiang 316022

CHINA

RESEARCH ON SDG FAULT DIAGNOSIS OF OCEAN SHIPPING BOILER SYSTEM BASED ON FUZZY GRANULAR COMPUTING UNDER DATA FUSION

Ying Zhu^{1,2}, Ph. D.,

Liang Geng², Ph. D.,

¹School of Automation, Huazhong University of Science and Technology, Wuhan 430074, China;

²School of Science, Hubei University of Technology, Wuhan 430068, China;

ABSTRACT

The research work in this paper belongs to the application of granular computing, graph theory and its application in fault detection and diagnosis. It is a cross cutting and frontier research field in computer science, information science and graph theory. The results of this paper are of great significance to the application of the fault detection and diagnosis of the ocean boilers system. This research combines granular computing theory and signed directed graph, and proposes a new method of fault diagnosis, and applies it to the fault diagnosis of ocean ship boiler system.

Keywords: Granular computing; Symbolic digraph; Fault diagnosis; Fuzzy theory

INTRODUCTION

In the past few decades, the ocean boilers system has become increasingly complex, the probability of the failure of the system is increasing, and the occurrence of the fault is also more complex [1]. If the failure of the system fails to be detected in time and correctly, it may cause a major failure in the whole system and even the catastrophic consequences of the system. As a way to improve system reliability and safety, fault diagnosis technology is proposed which is based on modern sensing technology, information processing technology, computer technology, network technology, software engineering and AI. We expect to be able to infer the state according to the observation system from the current state of the system, which has extremely important practical significance to guarantee the safe operation of marine boiler system [2]. Fig. 1 is the scheme of the ship boiler system.

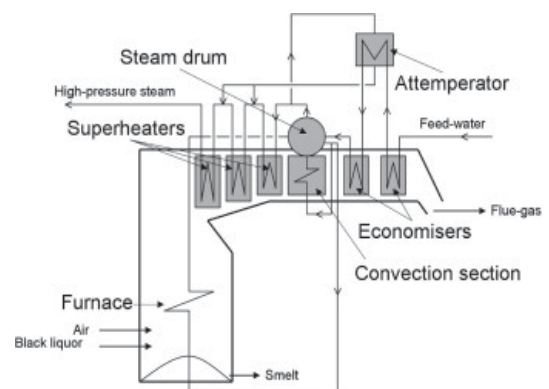


Fig. 1. Ship boiler system

When the fault diagnosis method based on the quantitative model cannot solve these problems, people start to kick the

other path and seek other methods. The fault diagnosis method based on qualitative model is qualitative description of system structure and function by using incomplete or imprecise knowledge of the system, and qualitative reasoning is carried out to realize system fault diagnosis [3]. The qualitative model based fault diagnosis method is widely applied because of its low requirement for the analytical model of the system [4].

The symbolic directed graph is a typical method of fault diagnosis based on the qualitative model. The SDG model effectively depicts the mechanism and relationship of the system through the nodes with clear physical meaning and directed edges. It is a schema abstraction of mathematical models or physical models of processes and devices. Fault diagnosis based on SDG is based on the strong expression ability of nodes and directed edges in the SDG model, and its unique reasoning method can be used for fault detection and location quickly and effectively [5,6,7].

Granular computing is a hotspot in current computational intelligence, is a new philosophical method to solve complex problems to simulate human thinking. For a complex problem, human beings have a strong global analysis ability. Granular computing can simulate human thinking from a different size (level) to abstract the perplexing problem into simpler problem. It has become a common means of solving complex problems, mass data mining, and pattern recognition. A major function of a knowledge reduction of granular computing can be under the premise of ensuring the same classification ability, remove redundant attributes decision table, minimum rules [8].

INFERENCE ALGORITHM FOR SDG FAULT DIAGNOSIS

As shown in Fig. 2 is the fault diagnosis system for the boiler system.

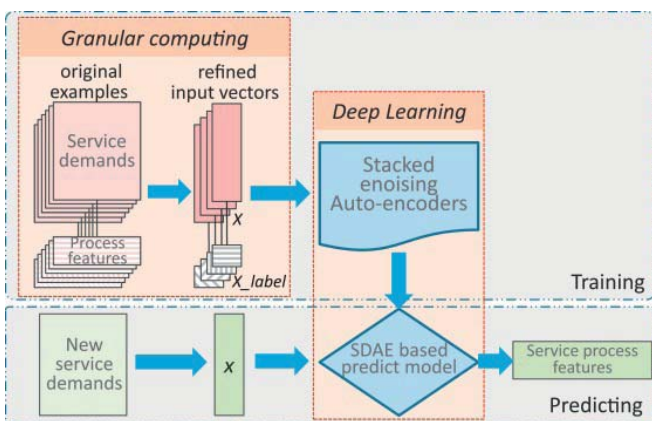


Fig. 2. Diagram for the fault diagnosis system of the boiler system

SDG is an important branch of the qualitative fault diagnosis method, at present has become a hot research topic in the field of intelligent fault diagnosis at present. Its

application is more and more widely over large systems, poor real-time and low resolution defect [9].

This chapter studies the search reasoning algorithm in SDG fault diagnosis. The characteristic of this way of reasoning is that it is both logical and set theory, and therefore, it has a strong superiority in the search reasoning based on artificial intelligence [10].

Fuzzy theory is a fuzzy concept expressed by mathematical method. It uses fuzzy things and introduces quantitative information into the operation of fuzzy concepts, making the results more intuitive and objective. Fuzzy mathematics can quickly deal with a large number of matrices and vectors, which is simple and fast as shown in Fig. 2.

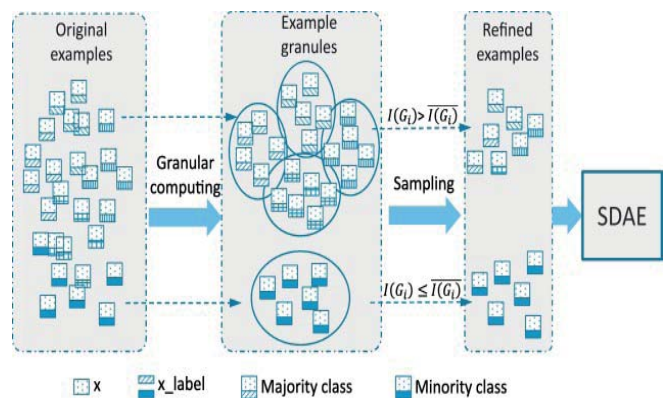


Fig. 3. Illustration of the refining examples based on granular computing

In Rough set theory, knowledge is artificially classified into objects in the field. Knowledge has granularity. So the reason for knowledge uncertainty is that knowledge granularity is too large [11, 12]. In other words, the larger the granularity of knowledge, the more rough the information set is. In the rough set, the representation of this granular structure of knowledge is the equivalent class, and the equivalent class is obtained by the method of the equivalence relation (the method of object division) [13-15]. The elements in the equivalent class obtained from the same equivalence relation are undistinguishable, that is, the undistinguishable relation between objects.

Any one particle is a particle statement, is composed of raw sugar logic formula and its semantics [16-18].

$$D = \{S(x_i, x_j) | x_i, x_j \in X\} = \{\lambda_1, \lambda_2, \dots, \lambda_m\} \quad (1)$$

The search reasoning of granular computing is to convert the traditional reasoning based on the rule of rule base into the grain Library in grain language.

$$E[X(\lambda_k)] = \sum_{i=1}^g \frac{|G_i|}{n} * I(G_i) \quad (2)$$

In reasoning, we can use logical method as well as set theory, which provides great convenience for reasoning process, especially in the field of artificial intelligence [19].

$$I(G_i) = -\sum_{ij} p_{ij} \log_2(p_{ij}) = \log_2(|G_i|) \quad (3)$$

Transforming the rules in the traditional rule library into particle language to the decision rule particles in the grain Library [20].

$$E[X(\lambda_k)] = \sum_{i=1}^g \frac{|G_i|}{n} * \log_2(|G_i|) \quad (4)$$

The matching of the information particles in the field and the conditions for all the particles in the grain Library.

$$\theta_e, \theta_d = \arg \min_{\theta_e, \theta_d} L(x, z) = \arg \max_{\theta_e, \theta_d} H(B(x) \| B(z)) \quad (5)$$

The search reasoning algorithm based on similarity is in the computer stored granular library, by finding a particle that reaches a certain threshold and has the highest similarity with the collection information, it gets the corresponding decision of the information collected at the scene [21].

$$H(B(x) \| B(z)) = -\sum_i [x^{(i)} \log z^{(i)} + (1-x^{(i)}) \log(1-z^{(i)})] \quad (6)$$

The search reasoning algorithm for granular computing is used for fault diagnosis, and a threshold is set here:

$$\theta_e, \theta_d = \arg \min_{\theta_e, \theta_d} J(x, z) = \arg \min_{\theta_e, \theta_d} J(x, g_{\theta_d}(f_{\theta_e}(x))) \quad (7)$$

DESIGN AND EVALUATION OF A SIMULATION PLATFORM FOR FAULT DIAGNOSIS

Generally speaking, a decision table of knowledge reduction is not the only one, that there may be a number of decision table reductions of knowledge. Knowledge reduction is achieved based on decision rules in decision table and attribute reduction in number directly affects the complexity of decision rules. In the fault diagnosis, the minimum reduction can be found through the expectation of knowledge reduction.

In this section, based on the knowledge reduction algorithm of granular matrix, we propose an attribute reduction algorithm based on the importance of node attributes. After computing the kernel reduction, we add one of the most

important attributes every time, until the attribute set meets the requirement of attribute reduction.

This model has 17 monitoring variables, respectively is the boiler water supply flow FR-01, superheated steam output flow FR-02, de-superheating water flow FI-03, softening water flow FR-04, gas flow, fuel oil flow rate of FR-07 and FI-06 to the catalytic deaerated water flow FI-08, furnace pressure PI-03, flue gas outlet pressure PI-05, oxygen content in flue gas AI-01, main steam high pressure gas pressure PIC-01, pressure PIC-02, pressure PIC-03, liquid hydrocarbon deaerator pressure PIC-04, SAIC LIC-01, packet level of deaerator water level LIC-02 and superheated steam temperature TIC-01.

8 common failures were considered: deaerator pressure failure CI, high pressure gas pressure fault C8, liquid hydrocarbon pressure failure C7, boiler full water F2, boiler water shortage F3, boiler fire extinguishing F4, power interruption F5, temperature reducer bad F6.

3 methods are applied to attribute reduction of typical fault sample set of boiler system, and get different results. Attribute reduction algorithm which is anxious for granular matrix and node importance is reduced to 5 attributes, and the other two methods are 6. This paper sorted the importance of the key nodes and the vulnerable nodes in the failure decision table, and used it as heuristic information to improve the efficiency of attribute reduction.

The fault 3 and the fault 9 in the system are the step changes and random changes of the temperature of the feed D of the reactor. After analysis, the temperature change of the feed D has little influence on the system variables. From the measured data, it can be seen that the temperature change of the feed D has no effect on the other variables. Fault 4 and fault 11 all change the inlet temperature of the cooling water of the reactor, one is step change, one is random change, and the compatible path is consistent. Fault 14 is the viscosity of the reactor cooling water valve. When the failure occurs, the system is in a stable state. From the measured data of the system, the occurrence of the fault has no effect on other variables of the system. Therefore, only the fault 4, 6, 11 of the fault occurred at various stages of the situation.

The knowledge base is the core of the expert system, which is stored and managed by the knowledge base. The rational distribution of knowledge base is beneficial to the retrieval and reasoning of knowledge, and improves the performance of the system. In this expert system, the knowledge base is composed of a text library, a picture library, and a database, which stores text, case pictures, and data tables, respectively.

The library includes: introduction of system flow, SDG reasoning process, particle similarity reasoning process, and detailed description of fault diagnosis (including the description of each node's condition, explanation of failure phenomena, and related maintenance and maintenance suggestions).

The picture library includes the core SDG diagram, the total SDG diagram, and the SDG part pattern of the fault diagnosis.

The database includes the full node decision table, the core node decision table, the node real-time monitoring data table, the node real-time monitoring data state value table and so on.

The rule of decision table in knowledge base is composed of conditional attribute and decision attribute. Conditional attribute is the state value of corresponding node variable when the fault occurs, and the decision attribute is the fault source.

For the expert system, the beginning of the design can be as brief as possible. Need to continuously improve the rules. Before the new rule is added, it is necessary to verify whether the rule satisfies the SDG model rules, such as whether the satisfaction is added or not, and the SDG model and the node threshold setting are improved. After adding the new rule, we need to store the new all node decision table, and use the reduction algorithm of granular computing to reduce it again, and get the new core node decision table.

In addition, the domain experts also need to modify the corresponding text library and picture library corresponding to the rule.

The query of the knowledge base mainly completes the query of all kinds of files (SDG diagram, text and so on) corresponding to the fault cases.

One of the most important indicators to measure the performance of an expert system is the consistency of knowledge base. The so-called knowledge base consistency refers to the consistency of each unit in the knowledge base which affects and interconnects each other, and there is no two meaning. The rules in the knowledge base to add, delete, modify, and must carry out the rules of consistency test, especially in a large number of rules, each unit of the knowledge between the mutual influence and mutual relations will become very complex, the knowledge base consistency test is very important. The main work of the knowledge management module is to check the knowledge base to ensure the consistency and integrity of knowledge.

By calling the MATLAB program, the whole node decision table in the database is transformed into the corresponding matrix form of MATLAB, and the matrix is reduced by using the particle knowledge reduction algorithm. The matrix form of the simplified decision table is saved to the core node decision table of the database.

Fault diagnosis system is mainly implemented in King View “application command language” centralized diagnosis algorithm. The programming command language in configuration is a programming language which is grammatically similar to C language. People can use these programming command languages to enhance the flexibility of applications, and do some arithmetic and operation calculations. The information table is shown in Tab.1.

Tab. 1. Information table

	a1	a2	a3	a4
u1	0	1	2	0
u2	1	2	0	2
u3	1	0	1	0
u4	2	1	0	1
u5	1	1	0	2

Command languages are executed by event triggered events, such as timing, data change, keypad press, click of the mouse, and so on. According to different events and functions, the programming command language is divided into application command language, event command language, hotkey command language, data change command language, semantic function command language, animation track command language and picture command language. These are the command language for editing input through the command language editor, was compiled in „King view” operating system.

After the operation of the background operation management part, when the fault occurs, the operation result of the program will be changed significantly by using the program command language, causing the event to trigger, pop up the cause of the failure display interface, point out the source of the failure, and give the corresponding maintenance or operation suggestion.

The main fault of the system found by the system is shown in Tab. 2:

Tab. 2. Fault Information table

Fault 1	1	0	0	1	0	0
Fault 2	1	0	0	1	0	0
Fault 3	1	1	0	1	0	0
Fault 4	1	1	0	1	1	0
Fault 5	1	1	0	0	0	1
Fault 6	1	1	0	0	0	0
Fault 7	1	1	1	0	0	0
Fault 8	1	0	1	0	0	0
Fault 9	1	0	1	0	1	0
Fault 10	0	0	1	0	1	0

Based on the above simulation results, the three methods based on similarity reasoning, which are based on similarity reasoning, have the fastest speed of diagnosis because of their simple method and convenient reasoning. Because of the „layering” thought, the hierarchical SDG fault diagnosis only searches in the lower layer when searching for the cause of the fault. It improves the diagnostic accuracy of the system while improving the diagnostic speed. Fault diagnosis based on fuzzy reasoning, fuzzy quantitative join in qualitative SDG, the qualitative knowledge and quantitative knowledge organically six, effectively improve the resolution of fault diagnosis based on similarity reasoning is not only superior, and two kinds of SDG fault diagnosis is better than the front.

Although the above several fault diagnosis methods have advantages and disadvantages, however, a fault in the system, such as 3, 9, 13–15 fault and other five kinds of fault are the correct diagnosis results failed to give, the main reason is the five failure of the system measurement variable data fault diagnosis method proposed in this paper is very little, not suitable for on the trouble, can use the principal component analysis method of mathematical statistics for fault diagnosis. The use of principal component analysis of the five kinds of fault diagnosis results are given in detail, and the method of fault identification is 4, 5, 7 and 10 of the rate is very low, the fault diagnosis method is proposed in this paper is very

good for the four kinds of fault diagnosis results, mainly due to a variety of variables influence the method proposed in this paper the faults were considered, including changes in reactant concentration, control variables change; fault diagnosis literature selected only 16 variables for a system of 22 continuous measurement variables for fault diagnosis. Such as fault 4, the controller under the control of the reactor temperature and reactor cooling water outlet temperature is almost constant, by continuously measuring the variables it is difficult to observe the change of system, this method takes into account the effects of the control variables, observed the change of the reactor cooling water valve V51, accurately diagnose the fault. Faults 5, 7, and 10 are similar. Therefore, fault diagnosis is a comprehensive and complex work. For a practical diagnosis system, multiple fault diagnosis methods are usually applied together to accomplish their diagnostic tasks. As shown in Fig.4, the learning efficiency of various systems are shown.



Fig. 4. Hyper-parameters setting experiments for deep neural network

CONCLUSIONS

In this paper, the principle of grain calculation and symbolic digraph is mainly studied and the application of the two groups in the fault diagnosis of the marine boilers system is also applied. Granular computing is a hotspot in current computational intelligence, is a new philosophical method to solve complex problems to simulate human thinking, the theory, rough set theory, a superset of quotient space theory. Granular computing abstracts the complicated problems from different granularity (level), and induces them into simpler problems. Then we analyze and solve these simple problems. A large function of grain computing - knowledge reduction can remove the redundant attributes of the decision table and derive the minimum rules, on the premise of ensuring that the classification ability is constant.

Sign directed graph is a kind of fault diagnosis method based on qualitative analysis, the relationship between the variables can effectively express complex system, the system has a strong relationship between the completeness

of the representation is also very complicated, some redundant variables also exist in the system, affect the speed of fault diagnosis. Therefore, we introduce granular computing to fault diagnosis based on signed digraph, and propose granular computing based SDG fault diagnosis method, and do some research on some key problems.

BIBLIOGRAPHY

1. Ciabattini, L., Ferracuti, F., Freddi, A. and Monteriu, A.: *Statistical spectral analysis for fault diagnosis of rotating machines*, Ieee Transactions on Industrial Electronics, Vol. 65, no. 5, pp. 4301-4310, 2018.
2. He, W., He, Y., Luo, Q. and Zhang, C.: *Fault diagnosis for analog circuits utilizing time-frequency features and improved vvrkfa*, Measurement Science and Technology, Vol. 29, no. 4, pp. 1-4, 2018.
3. Jack, Q., John, E. and Pan, Y.: *Multi-scale stochastic resonance spectrogram for fault diagnosis of rolling element bearings*, Journal of Sound and Vibration, Vol. 420, no. 2, pp. 174-184, 2018.
4. Khan, S., Gani, A., Wahab, A.W.A. and Singh, P.K.: *Feature selection of denial-of-service attacks using entropy and granular computing*, Arabian Journal for Science and Engineering, Vol. 43, no. 2, pp. 499-508, 2018.
5. Li, Y., Li, G., Yang, Y., Liang, X. and Xu, M.: *A fault diagnosis scheme for planetary gearboxes using adaptive multi-scale morphology filter and modified hierarchical permutation entropy*, Mechanical Systems and Signal Processing, Vol. 105, no. 4, pp. 319-337, 2018.
6. Wang, Y., Zheng, Y., Fang, H.-J., Wang, Y.-W.: *ARMAX model based run-to-run fault diagnosis approach for batch manufacturing process with metrology delay*. International Journal of Production Research, 2014, 52(10): 2915-2930.
7. Zheng, Y., Fang, H.-J., Wang, H.-O.: *Takagi-Sugeno fuzzy model-based fault detection for networked control systems with markov delays*. IEEE Transactions on System, Man and Cybernetics, Part B: Cybernetics, 2006, 36(3): 924-929.
8. Liu, H., Li, J., Guo, H. and Liu, C.: *Interval analysis-based hyperbox granular computing classification algorithms*, Iranian Journal of Fuzzy Systems, Vol. 14, no. 5, pp. 139-156, 2017.
9. Lung, J., Chen, Q., Mao, N. and Jack, P.: *Combining granular computing technique with deep learning for service planning under social manufacturing contexts*, Knowledge-Based Systems, Vol. 143, no., pp. 295-306, 2018.
10. Micheal, J., Zi, Y., Chen, J., Zhou, Z. and Wang, B.: *Liftingnet: A novel deep learning network with layerwise*

- feature learning from noisy mechanical data for fault classification*, Ieee Transactions on Industrial Electronics, Vol. 65, no. 6, pp. 4973-4982, 2018.
11. Pecht, M., Zhao, M., Kang, M. and Tang, B.: *Deep residual networks with dynamically weighted wavelet coefficients for fault diagnosis of planetary gearboxes*, Ieee Transactions on Industrial Electronics, Vol. 65, no. 5, pp. 4290-4300, 2018.
 12. Sheikhan, H., Delavar, M.R. and Stein, A.: *A gis-based multi-criteria seismic vulnerability assessment using the integration of granular computing rule extraction and artificial neural networks*, Transactions in Gis, Vol. 21, no. 6, pp. 1237-1259, 2017.
 13. Wang, J., Cheng, F., Qiao, W. and Qu, L.: *Multiscale filtering reconstruction for wind turbine gearbox fault diagnosis under varying-speed and noisy conditions*, Ieee Transactions on Industrial Electronics, Vol. 65, no. 5, pp. 4268-4278, 2018.
 14. Wang, L., Liu, Z., Miao, Q. and Zhang, X.: *Complete ensemble local mean decomposition with adaptive noise and its application to fault diagnosis for rolling bearings*, Mechanical Systems and Signal Processing, Vol. 106, no. 5, pp. 24-39, 2018.
 15. Wang, M., Hu, N.-Q. and Qin, G.-J.: *A method for rule extraction based on granular computing: Application in the fault diagnosis of a helicopter transmission system*, Journal of Intelligent & Robotic Systems, Vol. 71, no. 3-4, pp. 445-455, 2013.
 16. Wang, Q. and Gong, Z.: *An application of fuzzy hypergraphs and hypergraphs in granular computing*, Information Sciences, Vol. 429, no., pp. 296-314, 2018.
 17. Wu, H., Liu, Y., Yan, P., Fang, G. and Zhong, J.: *A frequent itemset mining algorithm based on composite granular computing*, Journal of Computational Methods in Sciences and Engineering, Vol. 18, no. 1, pp. 247-257, 2018.
 18. Xiahou, K.S. and Wu, Q.H.: *Fault-tolerant control of doubly-fed induction generators under voltage and current sensor faults*, International Journal of Electrical Power & Energy Systems, Vol. 98, no. 6, pp. 48-61, 2018.
 19. Yang, S.-C., Hsu, Y.-L., Chou, P.-H., Chen, G.-R. and Jian, D.-R.: *Online open-phase fault detection for permanent magnet machines with low fault harmonic magnitudes*, Ieee Transactions on Industrial Electronics, Vol. 65, no. 5, pp. 4039-4050, 2018.
 20. Yu, Y., Zhao, Y., Wang, B., Huang, X. and Xu, D.: *Current sensor fault diagnosis and tolerant control for vsi-based induction motor drives*, Ieee Transactions on Power Electronics, Vol. 33, no. 5, pp. 4238-4248, 2018.
 21. Zheng, B., Li, Y.-F. and Huang, H.-Z.: *Intelligent fault recognition strategy based on adaptive optimized multiple centers*, Mechanical Systems and Signal Processing, Vol. 106, no. 7, pp. 526-536, 2018.

CONTACT WITH THE AUTHORS

Ying Zhu, Ph.D.

e-mail: no2kenk98@sina.com

tel.: 18971840231

School of Automation

Huazhong University of Science and Technology

Wuhan Hubei 430074

CHINA

AN IMPROVED FEATURE EXTRACTION METHOD FOR ROLLING BEARING FAULT DIAGNOSIS BASED ON MEMD AND PE

Hu Zhang, Ph. D.,
Lei Zhao, Ph. D.,
Quan Liu, Ph. D.,
Jingjing Luo, Ph. D.,
Qin Wei, Ph. D.,

School of Information Engineering, Wuhan University of Technology, Wuhan 430070, China

Zude Zhou, Ph. D.,

Yongzhi Qu, Ph. D.,

School of Mechanical and Electronic Engineering, Wuhan University of Technology, Wuhan 430070, China

ABSTRACT

The health condition of rolling bearing can directly influence to the efficiency and lifecycle of rotating machinery, thus monitoring and diagnosing the faults of rolling bearing is of great importance. Unfortunately, vibration signals of rolling bearing are usually overwhelmed by external noise, so the fault frequencies of rolling bearing cannot be readily obtained. In this paper, an improved feature extraction method called IMFs_PE, which combines the multivariate empirical mode decomposition with the permutation entropy, is proposed to extract fault frequencies from the noisy bearing vibration signals. First, the raw bearing vibration signals are filtered by an optimal band-pass filter determined by SK to remove the irrelative noise which is not in the same frequency band of fault frequencies. Then the filtered signals are processed by the IMFs_PE to get rid of the relative noise which is in the same frequency band of fault frequencies. Finally, a frequency domain condition indicator FFR(Fault Frequency Ratio), which measures the magnitude of fault frequencies in frequency domain, is calculated to compare the effectiveness of the feature extraction methods. The feature extraction method proposed in this paper has advantages of removing both irrelative noise and relative noise over other feature extraction methods. The effectiveness of the proposed method is validated by simulated and experimental bearing signals. And the results are shown that the proposed method outperforms other state of the art algorithms with regards to fault feature extraction of rolling bearing.

Keywords: Improved Feature Extraction Method; Rolling Bearing Fault Diagnosis; MEMD and PE

INTRODUCTION

Rolling bearing is widely used in electric power industry, petrochemical industry, military industry and so on. However, rolling bearing is vulnerable and frequently falls out of service for various reasons. Bearing failures may further result in fatal breakdowns or even huge amount of economic losses and casualties. According to the bearing statistical data, about 70% of the mechanical faults are caused by the vibration faults, whereas among the vibration faults, 30% are due to the rolling bearing's failure [1]. Therefore, it is imperative to monitor the work condition of the rolling bearing. Since vibration signal contains much information about machine health condition, fault diagnosis methods based on the vibration signal analysis

are really prevalent in current literature. Recently, many signal processing methods to extract features from signals were proposed [2-5].

Rolling bearing is composed of rollers, outer races, inner races, as well as cages. The components of rolling bearing interact with each other to generate complex vibration signals. When the surface of one of these components develops a localized fault, the impacts, generated by other parts of rolling bearing periodically striking the damage spot, will excite bearing fault frequency. And the fault frequency will be further modulated by mechanical resonance of the whole mechanic structure [6]. Thus the measured signals from rolling bearing are usually have the characteristics of non-stationary and non-linear. Moreover, in the early stage

of rolling bearing's failure, the information of defects in the measured vibration signals is weak and is usually concealed by large background noise and other structural vibrations. Hence, it is a big challenge to extract the fault frequencies from the raw bearing vibration signals [7].

The fault vibration signals of rolling bearing are usually in the form of amplitude modulation or frequency modulation. So lots of signal analysis methods which are based on either frequency domain or time-frequency domain have been proposed to extract fault frequencies from the measured signals. In frequency domain, the spectrum of the rolling bearing fault vibration signals is composed of fault frequencies and other mechanical noise frequencies. On this basis, the fault frequencies can be obtained from the spectrum of rolling bearing vibration signal. Then, Envelope analysis method, which is one of spectrum analysis methods was presented by McFadden et al [8] to solve the problem of signal modulation in time domain. However, envelope analysis method is decreasingly effective when the signal-to-noise ratio of the rolling bearing vibration signals decreases. To tackle this problems, some optimal frequency-band selection methods based on wavelet and wavelet package [9] have been proposed to complete the function of the band-pass filter and acquire the signals whose frequencies are among the resonance frequency of fault frequencies. However, in order to obtain good decomposition results, the mother wavelet needs to be chosen carefully to ensure that the content of daughter wavelets is similar to the analysed signals. To tackle the disadvantage of wavelet and wavelet package methods, the empirical mode decomposition(EMD) was emerged.

The ensemble empirical mode decomposition(EEMD) was as an improved algorithm of EMD and was put forward by Wu and Huang in 2009 [10]. Many signal analysis methods based on EMD or EEMD [11] have been proposed to decompose the modulation signals into a number of sub-signals, which are also named as intrinsic mode functions(IMFs). However, these methods mentioned previously only decompose the complex signals into a finite number of sub-signals, but they fail to identify the specific sub-signals that contain most of the defect information, especially when the original signals are overwhelmed by large noise.

Spectral kurtosis(SK) is a statistical tool to quantify the presence of transient peak and locate the transients in the frequency domain [12]. The SK algorithm can determine the central frequency and frequency band where the bearing fault frequencies reside. Hence, an optimal band-pass filter can be designed based on the SK algorithm to recover the higher signal-to-noise ratio bearing fault signal from the raw bearing fault signal. Whereas the main drawback of the SK algorithm is that, only the noise which is out of the resonance frequency band of fault frequencies can be removed.

Recently, permutation entropy(PE) has been proposed by Bandt and Pompe in 2002 [13], which serves as a statistical indicator of the time series' complexity. Since PE is sensitive to the signal mutation and can characterize the small intrinsic dynamic changes of signal, it is applied to assist extracting the faults of rolling bearing effectively [14] used the PE as a tool

in status characterization of rolling bearing. They found that PE could detect and amplify the dynamic change of rolling bearing vibration signals.

In this paper, the SK algorithm is firstly applied to obtain the SOI signal, which contain mainly fault characteristics, and the residual signal which mainly contains noise. Then, the improved IMFs_PE method is used as a tool to recover the bearing fault signal of higher signal-to-noise ratio from the SOI signal. By using MEMD, a series of IMFs are obtained, which include noise, irrelevant components and the real bearing fault signal. Then, the reconstructed bearing fault signal is reconstructed from the IMFs through using the PE value as the criterion. Finally, obtain the fault frequencies by calculating the envelope spectrum of the reconstructed bearing fault signal, and verify the performance of the proposed method in this paper by comparing the FFR values of raw bearing signal and reconstructed bearing fault signal.

The structure of this paper is organized as follows: Section 1 is the introduction, it is mainly introduced the research background of this paper. In section 2, the theory of SK, MEMD and PE algorithms are introduced firstly. Furthermore, the procedure of the proposed feature extraction method based on MEMD and PE is described in detail. In section 3, the proposed method is validated by the simulation bearing signals and experimental bearing signals firstly. Then make comparisons of the proposed method in this paper with some other feature extraction methods to demonstrate the effectiveness of the proposed method. In section 4, the conclusion and discussion are drawn.

METHOD

Kurtosis is sensitive to the singular signals and is often used to detect the abnormal responses in the rotating systems. However, kurtosis is a global statistical indicator and sensitive to the noise. To tackle the drawback of kurtosis, spectral kurtosis (SK) was proposed by Dwyer, which is a spectral descriptor. SK is used as a statistic tool for processing the non-stationary signal, it can not only detect the non-stationary components in the signals, but also locate the non-stationary components in the frequency domain. The principle of SK method is to calculate the kurtosis value of each frequency line and then find out the frequency band where the non-stationary characteristics exist, and the definition is explained below:

(1) Taking account of the Wold-Cramer decomposition of conditionally non-stationary process, any a non-stationary signal $x(t)$ can be expressed as $Y(t)$ in frequency domain.

$$Y(t) = \int_{-\infty}^{+\infty} e^{j2\pi ft} H(t, f) dX(f) \quad (1)$$

When $H(t, f)$ is the time-varying transfer function of the system, and it is also a complex envelope. $X(f)$ is the spectrum of the $x(t)$.

(2) Since conditionally non-stationary process has the statistical property of time-independent, 2n-order instantaneous variable $S_{2nY}(t, f)$ is defined to calculate the energy of the complex envelope at time t and frequency f :

$$S_{2nY}(t, f) \triangleq E \left\{ |H(t, f)|^{2n} \mid \omega \right\} / df \quad (2)$$

$$= |H(t, f)|^{2n} \cdot S_{2nX}$$

On the condition that the complex envelope $H(t, f)$ has the properties of stationarity and ergodicity, 2n-order instantaneous variable $S_{2nY}(t, f)$ can be also defined as:

$$S_{2nY}(f) = \langle S_{2nY}(t, f) \rangle_t \quad (3)$$

$$\triangleq \lim_{T \rightarrow \infty} \frac{1}{T} \int_{-T/2}^{+T/2} S_{2nY}(t, f) dt$$

Where $\langle \bullet \rangle_t$ is the time-averaged operator.

(3) According to the definition above, the fourth-order spectral cumulant of conditionally non-stationary process $C_{4Y}(f)$ is defined as:

$$C_{4Y}(f) = S_{4Y}(f) - 2S_{2Y}^2(f) \quad (4)$$

(4) Finally, SK is generated by normalizing the fourth-order cumulant $C_{4Y}(f)$, namely the SK value is used to measure the peakiness of the probability density function of the conditionally non-stationary process at frequency f :

$$K_Y(f) \triangleq \frac{C_{4Y}(f)}{S_{2Y}^2(f)} = \frac{S_{4Y}(f)}{S_{2Y}^2(f)} - 2 \quad (5)$$

Antoni gave the further study of applying the SK to the vibratory surveillance and diagnostics of rotating machines after he gave the formal definition of SK in 2006. When a fault occurs in the rotating machine, the vibration signal of rotating machine usually has a periodic impulse-like repetitive nature. Since the SK algorithm has advantage of having a robust way of detecting and locating the periodic impulse-like signals even in the presence of large noise. The SK algorithm is used as a defect indicator to extract bearing fault signal out of the raw bearing signal overwhelming by large noise in this paper.

Empirical mode decomposition(EMD) is a fully data-driven method for multistate analysis of non-linear and non-stationary signals, so it is widely applied for signal analysis in time-frequency domain. The multivariate empirical mode decomposition (MEMD) algorithm is the extension of EMD for multivariate data, which was proposed by Rahman and Mandaic. MEMD method has the advantage of overcoming the mode alignment problem experienced with EMD by the joint analysis of multiple oscillatory components within a higher dimensional signal.

The detailed procedure of MEMD algorithm is summarized as follows:

(1) The input signal is $\{x(t)\}_{t=1}^T = \{x_1(t), x_2(t), \dots, x_n(t)\}$, and $d^k = \{d_1^k, d_2^k, \dots, d_n^k\}$ is projected vector according to the angle vector $\theta^k = \{\theta_1^k, \theta_2^k, \dots, \theta_{n-1}^k\}$ on an $(n-1)$ sphere.

(2) According to the Hamersley sequence[4], an appropriate set of sampling points on $(n-1)$ sphere is obtained.

(3) Calculate a projection $\{p^{\theta^k}(t)\}_{t=1}^T$, which is the projection of the input signal $\{x(t)\}_{t=1}^T$ along the direction vector d^k , for all k , giving $\{p^{\theta^k}(t)\}_{k=1}^K$ as the set of projections.

(4) Find all maxima of the set of projected signals $\{p^{\theta^k}(t)\}_{k=1}^K$ at time instants $\{t_i^{\theta^k}\}$. Then interpolate the sequences $[t_i^{\theta^k}, v(t_i^{\theta^k})]$ to obtain multivariate envelope curves $\{e^{\theta^k}(t)\}_{k=1}^K$. Finally, for a set of K direction vectors, calculate the mean $m(t)$ of the envelope curves as $m(t) = 1/K \sum_{k=1}^K e^{\theta^k}(t)$.

(5) Extract the detail signal $d(t)$ by using $d(t) = x(t) - m(t)$. If the detail signal $d(t)$ fulfills the stop criterion for a multivariate IMF, apply the above (2) procedure to $x(t) - d(t)$, otherwise apply it to $d(t)$.

In this paper, MEMD is used as a tool for decomposing the filtered bearing vibration signal by SK through adding extra channels containing independent white noise. By using MEMD, a series of IMFs are obtained.

Permutation entropy (PE) is a statistical method for measuring the complexity and detecting the dynamic changes of one dimensional time series, which was first proposed by Bandt and Pompe in 2002. PE has the advantage of simple and fast calculation. Furthermore, Yan et al had applied PE for status characterization of rotating machine and demonstrated that PE had the advantage of effectively characterizing the working status of rotating machine.

PE was calculated by the comparison of neighboring values and its definition is given as follows.

(1) For a given time series $\{x(i), i = 1, 2, 3, \dots, N\}$, according to the time delay τ and embedding dimension m , the m -dimensional reconstructed matrix Y^m is defined as Eq. (6):

$$Y^m = \begin{bmatrix} Y(1) \\ \vdots \\ Y(j) \\ \vdots \\ Y(N - (m-1)\tau) \end{bmatrix} = \begin{bmatrix} x(1) & x(1+\tau) & \cdots & x(1+(m-1)\tau) \\ \vdots & \vdots & \vdots & \vdots \\ x(j) & x(j+\tau) & \cdots & x(j+(m-1)\tau) \\ \vdots & \vdots & \vdots & \vdots \\ x(N - (m-1)\tau) & x(N - (m-2)\tau) & \cdots & x(N) \end{bmatrix} \quad (6)$$

(2) Rearrange the reconstructed matrix Y^m , each row in matrix Y^m $Y(i) = (x(i) \ x(i+\tau) \ \cdots \ x(i+(m-1)\tau))$ is rearranged in an increasing order as in Eq. (7).

$$\begin{aligned} x(i+(j_1-1)\tau) &\leq x(i+(j_2-1)\tau) \\ &\leq \dots \leq x(i+(j_m-1)\tau) \end{aligned} \quad (7)$$

Where j_1, j_2, \dots, j_m refer to the index of column in matrix $Y(i)$. If there are two same values in $Y(i)$, for example, if $x(i+(j_1-1)\tau) = x(i+(j_2-1)\tau)$, then the order can be rearranged by the value of j_1 and j_2 . That is to say, when j_1 is small than j_2 , it can be rearranged as $x(i+(j_1-1)\tau) \leq x(i+(j_2-1)\tau)$.

(3) After rearranging, each row $Y(j)$ of the matrix Y^m can be uniquely mapped into an ordinal permutation as Eq. (8).

$$S(l) = (j_1, j_2, \dots, j_m) \quad (8)$$

Where $l = 1, 2, \dots, K$, and $K \leq m!$.

(4) It is clearly that there is $m!$ permutations for m dimensional delay vectors at most. And each $S(l)$ represents a permutation pattern. Assume that the probability distribution of each permutation pattern can be calculated with Eq. (9)

$$P_l = \frac{\{\text{the number of } S(l)\}}{K} \quad (9)$$

Where $l = 1, 2, \dots, K, K \leq m!$.

(5) Finally the normalized permutation entropy is defined as Eq. (10):

$$0 \leq H_p = \frac{-\sum_{l=1}^K P(l) \ln P(l)}{\ln(m!)} \leq 1 \quad (10)$$

Thus H_p gives a complexity measure of a time series. The smaller the value of H_p , the more regular the time series is. Bandt and Pompe recommend that the value of m should be in the scope $m = 3, \dots, 7$.

As known, fault information of rolling bearings is mostly reflected by singular points of abrupt changing signals and is usually non-stationary and non-linear. PE is effective to detect the dynamic changes of non-stationary and non-linear signals in complex systems. Moreover, the PE is insensitive to the noise. In this paper, the PE is used as the criterion to select the corresponding IMFs of bearing fault signal to reconstruct the high signal-to-noise ratio bearing fault signal. The procedure of calculating PE is described as follows: First, the raw data is partitioned into blocks of data subsets with length w , which may overlap each other or not. Then the embedding dimension m and the delay time τ are determined. Finally, the permutation entropy H_p is calculated for each data subset, so its change with time varying is obtained. In this paper, the parameters are chosen as: $w = 1024, m = 5, \tau = 1$. For more details about the parameter selection, refer to Yan and Zheng.

In the process of extracting the fault frequencies of rolling bearing vibration signals, there are two big challenges that

we have to face. 1) the irrelevant interference which is not in the same frequency band of fault frequencies; 2) the relevant interference which is in the similar frequency band of fault frequencies. As for the irrelevant interference, since it has the property of the irrelevant interference having different frequency band range with the fault frequencies in frequency domain. Some time-frequency signal analysis methods have successfully removed the irrelevant interferences, such as SK, wavelet package transfer, EEMD and so on. And it has appeared large amount of excellent research achievements. However, there fewer research on solving the problem of getting rid of the relevant interferences except for blind source separation algorithm. On this basis, the IMFs_PE method in this paper is mainly aimed at removing the relevant interference. The improved feature extraction method based on the MEMD and PE in this paper take both irrelevant and relevant interferences into account. And it recover the bearing fault signal from the raw noisy bearing signal very well.

Before introducing the improved feature extraction method clearly, in order to validate the effectiveness of the proposed feature extraction method based on MEMD and PE quantitatively, the fault frequency ratio (FFR) is introduced firstly.

For a bearing fault signal $x(n)$, let $X(f) = F[x(n)]$, where F is the envelope spectral transform. Then the FFR is defined as:

$$FFR = \frac{|X(f_{fault})|}{\sum_{i=1}^N |X(f_i)|^2} \quad (11)$$

Where $|X(f_i)|$ is the modulus of $X(f_i)$, and f_{fault} is the fault characteristic frequency of the bearing fault signal.

In this paper, an improved feature extraction method applied to fault diagnosis of rolling bearing based on MEMD and PE is proposed, and the whole processing procedure is shown in Fig. 1. And the procedure of the proposed method is summarized as follows:

THE PROCEDURE OF FILTERING SIGNAL BY SK

Obtaining the central frequency f_c and bandwidth B_w by using the SK algorithm firstly. Then design the optimized band-pass filter and optimized band-stop filter according to the central frequency f_c and bandwidth B_w . Extracting the SOI signal by the optimized band-pass filter, and the SOI signal contains more of fault characteristics. Obtaining the residual signal by the corresponding band-stop filter. The procedure of filtering signal by SK is mainly to get rid of the irrelevant interference which is not in the same frequency band of the fault frequencies.

THE PROCEDURE OF PROCESSING SIGNAL BY MEMD AND PE

(a) Decompose the SOI signal by MEMD, and a series of IMFs are obtained;

(b) Calculate the PE value of each IMF to get PE_{IMFi} . Then calculating the PE value of the residual signal to get the $threshold_B^*$ and the PE value of the normal bearing vibration signal to get the $threshold_A^*$;

(c) Reconstruct the bearing fault signal from the IMFs by comparing the PE value of each IMF PE_{IMFi} with threshold values $threshold_A^*$ and $threshold_B^*$, the IMF which fulfil the equation $PE_{IMFi} > threshold_A^*$ and

$$|PE_{IMFi} - threshold_B^*| \text{ is maximum}$$

is used to reconstructed the bearing fault signal. The procedure of processing signal by MEMD and PE is mainly to remove the relevant interference which is in the similar frequency band of the fault frequencies.

THE PROCEDURE OF EXTRACTING THE FAULT FREQUENCY

Calculate the spectral envelope of the reconstructed bearing fault signal, and then calculating the FFR value of the reconstructed bearing fault signal based on the spectral envelope.

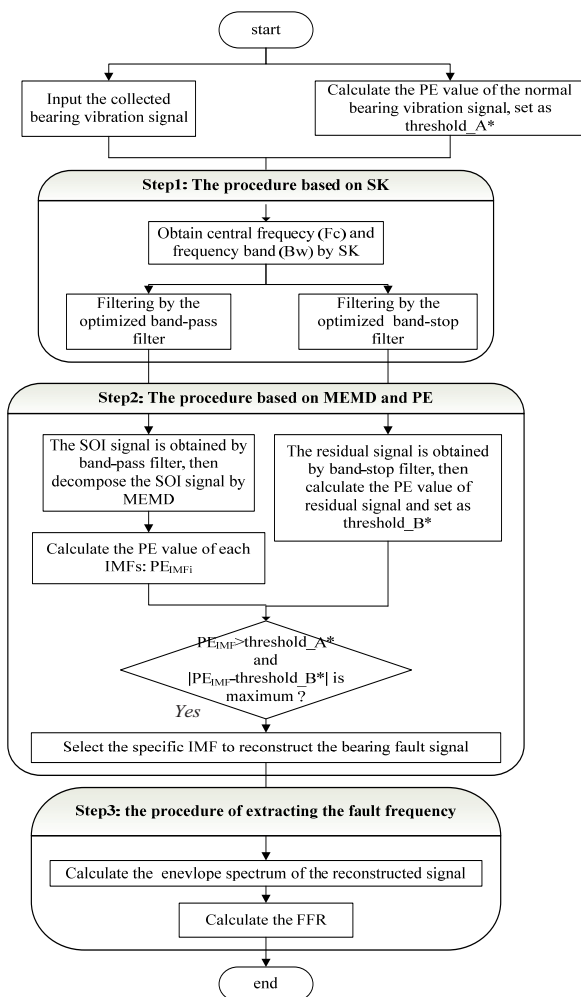


Fig. 1. The processing procedure of the proposed method

To verify the proposed feature extraction method in this paper, a simulated bearing fault signal is used to verify the correctness of the proposed method. According to the fault model of rolling bearing, the formula for inner fault model of rolling bearing under noise is defined as:

$$y(t) = [1 + Cx_{inner}(t)] * \cos(2\pi * f_z * t) + n(t) \quad (12)$$

Where f_z is the resonant frequency of the rolling bearing system, $n(t)$ is the noise, and $x_{inner}(t)$ is the inner fault signal, and the definition is as follows:

$$x_{inner}(t) = A * [1 + B * \cos(2\pi * f_a * t)] * \cos(2\pi * n * f_i * t), n = 1, 2, \dots \quad (13)$$

Where f_a is the rotating frequency, and f_i is the inner fault frequency.

The simulated bearing inner signal is shown as Fig.2(a), it is clearly that the fault frequency is 106.2Hz, which agrees with the theoretical value. Then the simulated signal is processed by the proposed method in this paper, and the de-noised simulated signal is obtained and is shown in Fig.2(b). In the envelope of the de-noised simulated signal, the fault frequency 106.2Hz is well preserved and the interferences are suppressed effectively. In order to describe the result intuitively, FFR is calculated and the results are shown in Table 1.

According to the Table1, the FFR value of the simulated signal is 0.5245, while the FFR value of the De-noised simulated signal which is obtained by the proposed method is 0.6682. It has improvement of 27.3% according to the FFR value of the simulated signal. In a word, the improved feature extraction method based on MEMD and PE is effective in the feature extraction of the rolling bearing vibration signals.

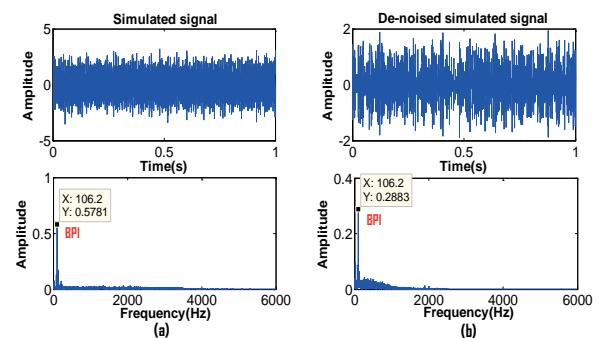


Fig. 2. The simulated inner fault signal; (a) The time domain and envelope spectrum of the simulated inner fault signal; (b) The time domain and envelope spectrum of the de-noised simulated signal which is obtained by the proposed method

Tab. 1. The FFR of inner fault simulated signal

Signal	FFR	ΔFFR
Simulated signal	0.5245	27.3%
De-noised simulated signal	0.6682	

EXPERIMENT AND RESULT

All the bearing vibration signals analyzed in this paper are downloaded from the Case Western Reserve University (CWRU) Bearing Data Centre. As shown in Fig. 3, the test stand consists of a 2 horsepower, three-phase induction motor (left), a torque sensor (middle), a dynamometer (right) and a self-aligning coupling (middle). The type of the tested bearing used in the experiment is the deep groove ball bearings 6205-2RS JEM SKF, and the information of the tested bearing are shown in Table 2. Single point fault is arranged in the bearing by electric discharging machining (EDM) technique and the defect size is 0.007inch in diameter, 0.0011inch in depth. The sampling frequency is 12KHZ and the shaft rotating speed of the motor 1730rpm. Under this environment, the normal bearing signal (NORM), the inner race fault bearing signal (IRF), the outer race fault bearing signal (ORF) and the rolling element fault bearing signal (REF) are collected by using the accelerometers. The time-domain waveforms of the four kind signals are shown in Fig. 4. In Table 3, the fault characteristic frequency (defect frequency) of the inner race fault, outer race fault and rolling element fault are listed.

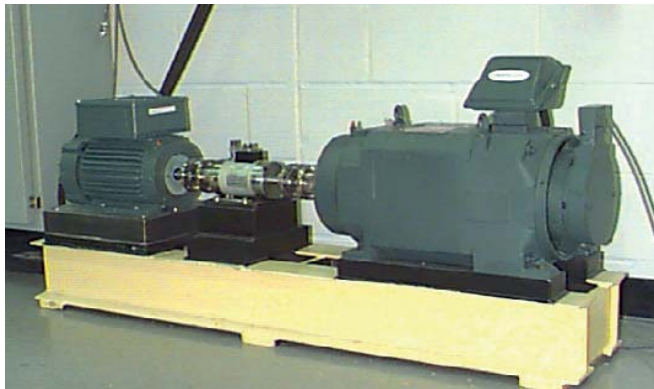


Fig. 3. The test stand of bearing

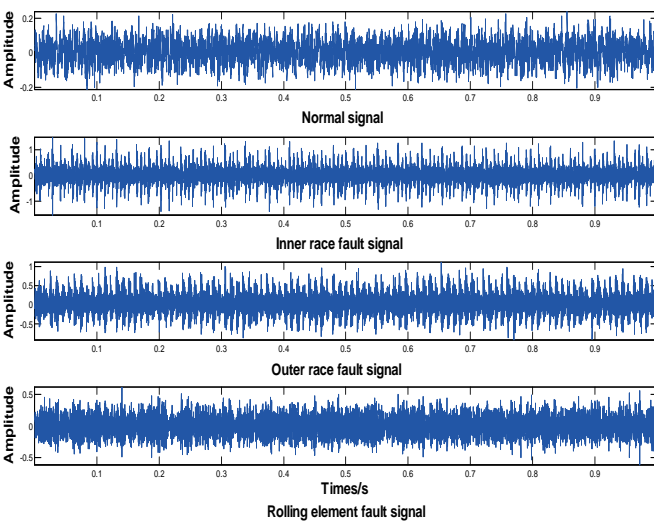


Fig. 4. NORM signal and IRF, ORF, REF fault signals

Tab. 2. The information of the tested bearings

Inside Diameter (inch)	Outside Diameter (inch)	Thickness (inch)	Ball Diameter (inch)	Pitch Diameter (inch)	Number of Balls (inch)
0.9843	2.0472	0.5906	0.3126	1.537	9

Tab. 3. Characteristic frequency of the tested bearing

Characteristic frequency	Rotating speed r(RPM)	Equation	Value (Hz)
Defect on inner race (BPI)	1721	$BPI = \frac{r}{2} \cdot N \cdot (1 + \frac{d}{D} \cos \alpha)$	155.3
Defect on outer race (BPO)	1725	$BPO = \frac{r}{2} \cdot N \cdot (1 - \frac{d}{D} \cos \alpha)$	103.6
Defect on rolling element (BS)	1722	$BS = \frac{r}{2} \cdot \frac{D}{d} \cdot (1 - (\frac{d}{D})^2 \cos^2 \alpha)$	67.6

Where N is the number of balls, d is the ball diameter, D is the pitch diameter, and α is the contact angle.

In this paper, PE is used as a criterion to select the IMF components which contain more fault information in the bearing vibration signals. First of all, the PE of the NORM signal, IRF signal, ORF signal and REF signal are studied, and the result are shown in Fig.5.

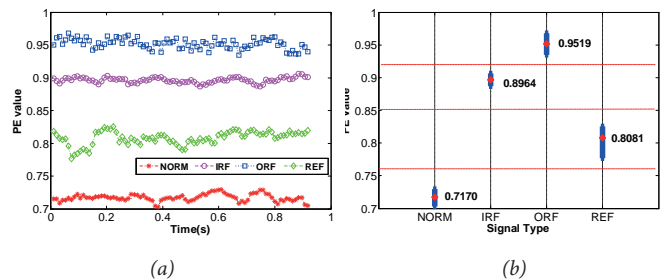


Fig. 5. The PE values of the NORM, IRF, ORF and REF signals;
(a) The PE value changes over time;
(b) The mean value and range of variation of the PE value

In Figure 5(a), it is clearly that the PE of NORM signal, IRF signal ORF signal and REF signal could be clearly separated. According to the theoretical analysis, when a localized fault occurs on the bearings, the measured bearing vibration signals will contain more internal modes and the value of PE will increase. This confirms the results in Fig.5(a). Namely, the PE values of bearing fault signals (IRF signal, ORF signal and REF signal) are higher than the PE value of normal bearing signal. The mean PE values of NORM signal, IRF signal ORF signal and REF signal are 0.7170, 0.8964, 0.9519 and 0.8081 respectively. In a word, PE is suitable to be used as a criterion for selecting the components which contain the information of the faults in rolling bearings to reconstruct the bearing fault signals.

After validating the effectiveness of the PE criterion, the analysis of the bearing fault signals (IRF signal, ORF signal

and REF signal) by our proposed method are carried out. The first process of the process method is to remove the noise from the raw bearing vibration signals by using the SK method. The results of filtered signals by SK are shown in Figs. 6–8. In Figs. 6-8, the x-axis is limited to the range of 0-500Hz so that the characteristic frequencies can be observed clearly. In Fig. 6(a), the maximum kurtosis of the IRF signal is 0.5, as shown in the red dash-line rectangle. The central frequency and band width is 3500Hz and 1000Hz, respectively. Based on the central frequency and band width, the optimal band-pass filter is designed. The filtered IRF signal and its envelope spectrum are shown in Fig. 6(b). It is clearly that the fault characteristic is well reserved in the filtered IRF signal. The same analysis process for ORF and REF signals and the results are shown in Figs. 7-8, and the fault characteristic frequencies are also well preserved in the filtered signals which obtained by the SK method.

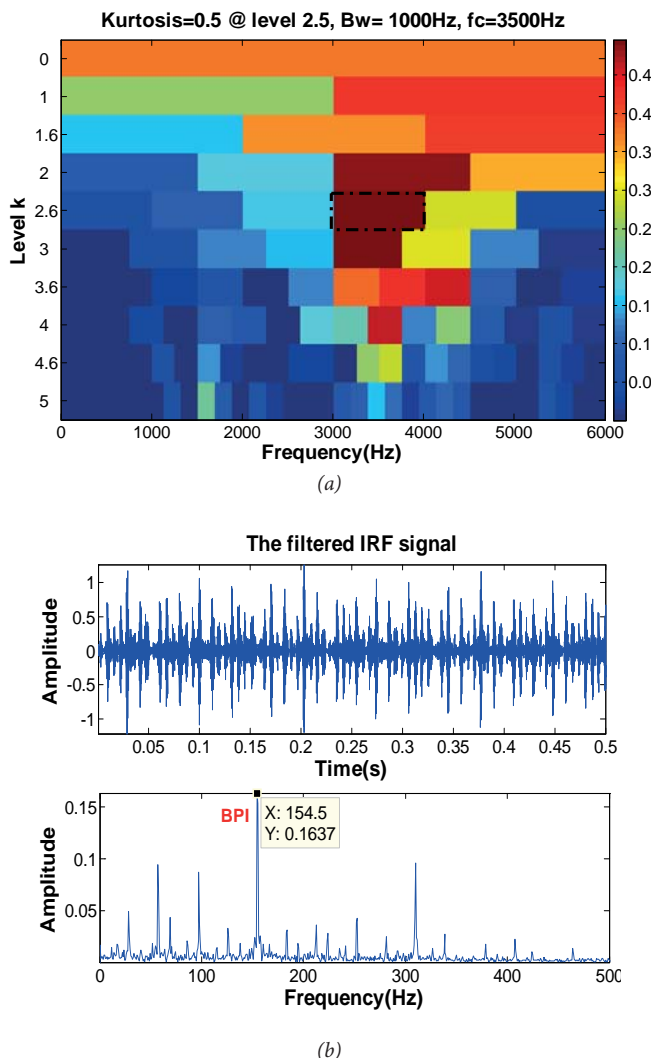


Fig. 6. The results of IRF signal by SK. (a) The 2-D SK of IRF; (b) The filtered IRF and its envelope spectrum

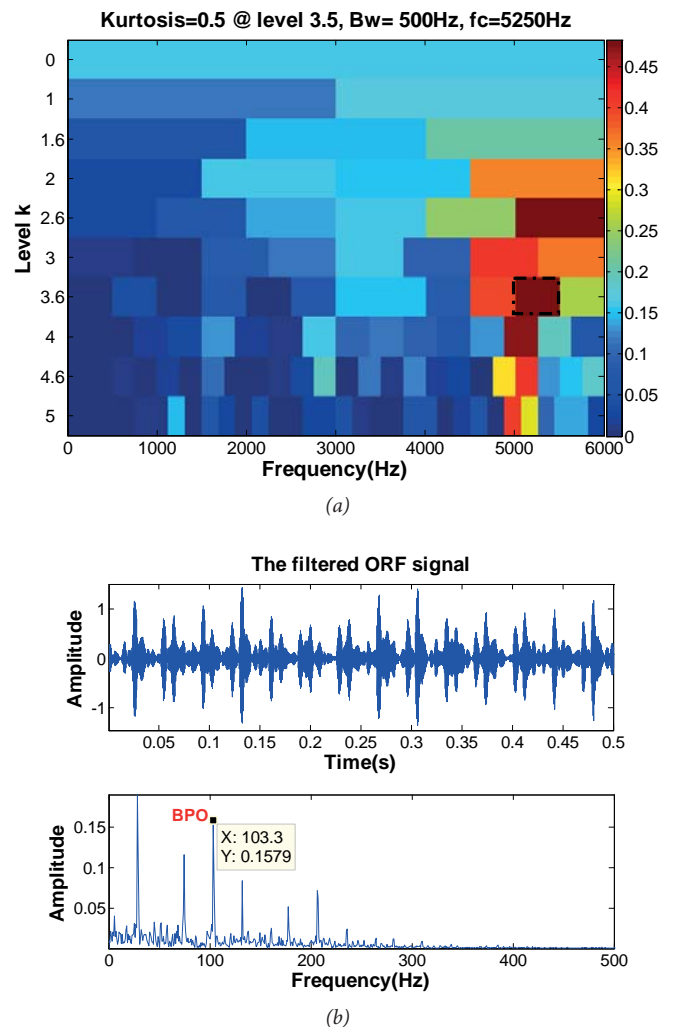


Fig. 7. The results of ORF signal by SK. (a) The 2-D SK of ORF; (b) The filtered ORF and its envelope spectrum

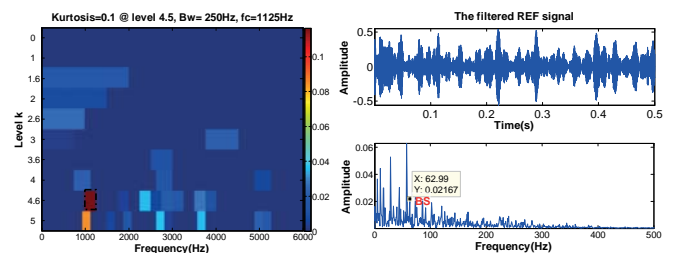


Fig. 8. The results of REF signal by SK. (a) The 2-D SK of REF; (b) The filtered REF and its envelope spectrum

After obtaining the filtered bearing fault signals through SK, MEMD and PE are further used to recover the bearing fault signals. Firstly, IMFs are obtained by decomposing the filtered bearing fault signals through MEMD. Then calculate the PE of each IMF and choose the specific IMF which contain the fault information to reconstruct the bearing fault signals by comparing the PE value of each IMF with the threshold values. Figures 9 shows the MEMD decomposition results of the filtered bearing fault vibration signals.

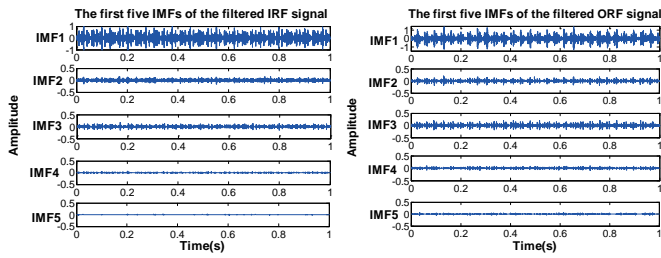


Fig. 9. The first five IMFs of the filtered IRF, ORF and REF signals; (a) The first five IMFs of filtered IRF signal; (b) The first five IMFs of filtered ORF signal; (c) The first five IMFs of filtered REF signal

The PE of the first five IMFs of filtered IRF signal, filtered ORF signal and filtered REF signal are listed in Tables 4–6. Besides, the threshold values of PE of the corresponding residual signal and NORM signal are also listed in Tables 4-6.

Tab. 4. The PE valued of the first five IMFs of filtered IRF Signal, residual IRF signal and NORM signal

PE			
	Filtered IRF signal	residual IRF signal	NORM signal
IMF1	0.798	0.826	0.717
IMF2	0.846		
IMF3	0.611		
IMF4	0.431		
IMF5	0.319		

Tab. 5. The PE values of the first five IMFs of filtered ORF signal, residual ORF signal and NORM signal

PE			
	Filtered ORF fault signal	residual ORF signal	NORM signal
IMF1	0.70	0.899	0.717
IMF2	0.91		
IMF3	0.606		
IMF4	0.479		
IMF5	0.53		

Tab. 6. The PE values of the first five IMFs of filtered REF Signal, residual REF signal and NORM signal

PE			
	Filtered REF fault signal	Residual REF signal	NORM signal
IMF1	0.876	0.801	0.717
IMF2	0.508		
IMF3	0.482		
IMF4	0.357		
IMF5	0.265		

According to the procedure of the improved feature extraction method based on MEMD and PE mentioned in Fig.1, the reconstructed bearing fault signal is composed of the specific IMF which fulfills the conditions $PE_{IMFi} > threshold_A^*$ and $|PE_{IMFi} - threshold_B^*|$ is max imum . Table 4 shows the PE value of the first five IMFs of filtered IRF signal, the residual IRF signal and the NORM signal, the $threshold_A^*$ is 0.717, $threshold_B^*$ is 0.801, and the PE values of the first IMFs

of the filtered IRF signal are 0.798, 0.8466, 0.611, 0.431 and 0.319 respectively. Therefore, the reconstructed IRF bearing fault signal is the IMF2 of the filtered IRF signal. Applying the same analysis process to the ORF signal and REF signal, so the reconstructed ORF bearing fault signal is the IMF2 of the filtered ORF signal, and the reconstructed REF bearing fault signal is the IMF1 of the filtered REF signal. Finally, the reconstructed bearing fault signals of IRF, ORF and REF and their envelope spectrums are shown in Fig.10. It is clearly that the characteristic frequencies are well reserved in the reconstructed bearing fault signals.

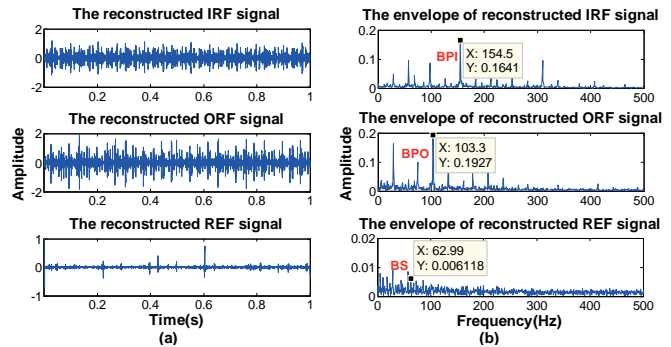


Fig. 10. The reconstructed signals and their envelope spectrums

In Table 7, the FFR of the raw bearing vibration signals, filtered bearing vibration signals and reconstructed bearing vibration signals are shown. It is obviously that, the FFR value of reconstructed signals (reconstructed IRF signal, reconstructed ORF signal and reconstructed REF signal) are higher than the FFR value of raw signals (IRF signal, ORF signal and REF signal). Therefore, it is distinct that the improved collaborative method based on MEMD and PE is effective to extract the fault characteristics of the rolling bearings.

Tab. 7. The FFR values of the raw signals, filtered signals and reconstructed signals

Fault category	FFR		
	Raw signal	Filtered signal	Reconstructed signal
Inner race fault(IRF)	0.91	1.27	1.91
Outer race fault(ORF)	1.64	1.92	2.93
Rolling element fault(REF)	0.56	2.07	7.23

According to the results in Table 8, as for the inner race fault, outer race fault and rolling element fault, the proposed method in this paper has improvement of 6.8%, 7.9% and 5.9% respectively compared with the method proposed by Guo et al, and 15.1%, 14.6% and 12.3% respectively compared with the method proposed by Wu et al. Therefore, it is distinct that, our improved collaborative method based on MEMD and PE is more effective to recover bearing fault signals from noisy raw signal, and also the fault characteristic frequencies are amplified in the reconstructed bearing fault signals.

CONCLUSION

In this paper, an improved feature extraction method for rolling bearing fault diagnosis based on MEMD and PE was proposed to extract the bearing fault features from the noisy bearing vibration signal. The proposed method solves two big problems. (1) To get rid of the irrelevant interferences of the fault frequencies by filtering the signal by optimal band-pass filter which determined by SK algorithm; (2) Combine the MEMD and PE algorithms, a novel method to get rid of the relevant interferences of the fault frequencies is put forward. Then, the proposed method is validated by the simulated signals and real bearing vibration signals. Further, some comparisons of the proposed method with the other feature extraction methods proposed in recent three years are done, and it further prove that our proposed method has better performance in the feature extraction of rolling bearing signals.

ACKNOWLEDGEMENTS

The authors wish to thank the support of the National High Technology Research and Development Program (863 Program) of China under Grant no. 2012AA040106. Add: We also thank case western university for providing the bearing data.

BIBLIOGRAPHY

1. Coiro, D.P., Troise, G., Calise, G., Bizzarrini, N.: *Wave energy conversion through a point pivoted absorber: Numerical and experimental tests on a scaled model*, Renewable Energy, Vol. 87, no. 1, pp. 317-325, 2016.
2. Martínez, M., Molina, M.G., Machado, I.R.; Mercado, P.E., Watanabe, E.H., *Modelling and simulation of wave energy hyperbaric converter (WEHC) for applications in distributed generation*, International Journal of Hydrogen Energy, Vol. 37, no. 9, pp. 14945-14950, 2012.
3. Gaspar, J.F., Calvário, M., Kamarlouei, M., Guedes Soares, C.: *Power take-off concept for wave energy converters based on oil-hydraulic transformer units*, Renewable Energy, no. 86, pp. 1232-1246, 2016.
4. Zhang, D.H., Li, W., Lin Y.G.: *Wave energy in China: current status and perspectives*, Renewable energy, Vol. 34, no. 10, pp. 2089-2092, 2009.
5. Bjarte-Larsson, T., Falnes, J.: *Laboratory experiment on heaving body with hydraulic power take-off and latching control*, Ocean Eng. Vol. 33, no. 7, pp. 847-877, 2006.
6. Hals, J., Taghipour, R., Moan, and T.: *Dynamics of a force-compensated two-body wave energy converter in heave with hydraulic power take-off subject to phase control*, In: Proceedings of the Seventh European Wave and Tidal Energy Conference, Porto, Portugal, 2007.
7. Yang, L.M., Hals, J., Moan, T.: *A wear model for assessing the reliability of wave energy converter in heave with hydraulic power take-off*, In: Proceedings of the Eighth European Wave and Tidal Energy Conference, Uppsala, Sweden, 2009.
8. Yang, L., Hals, J., Moan, T.: *Analysis of dynamic effects relevant for the wear damage in hydraulic machines for wave energy conversion*, Ocean Engineering. Vol. 37, no. 13, pp. 1089-1102, 2010.
9. Falcão, A. F. de O.: *Modelling and control of oscillating-body wave energy converters with hydraulic power take-off and gas accumulator*, Ocean Engineering, Vol. 34, no. 14-15, pp. 2021-2032, 2007.
10. Virvalo, T.: *Hydraulic systems in wave energy application*, 1st edn, World Publishing Corporation, China, pp. 56-60, 2009.
11. Lin, Y. G., and Huang, W., Zhang, D.F., Li, W., Bao, J.W.: *Application of Hydraulic System in Wave Energy Converter, Electrical, Information Engineering and Mechatronics 2011*, Lecture Notes in Electrical Engineering. Vol. 138, pp. 275-283, 2012.
12. Lopes, M.F.P., Hals, J., Gomes, R.P.F., Moan, T., Gato, L.M.C., Falcão, A.F.de O.: *Experimental and numerical investigation of non-predictive phase-control strategies for a point-absorbing wave energy converter*, Ocean Engineering, Vol. 36, no. 5, pp. 386-402, 2009.
13. Babarit, A., Guglielmi, M., Clément, A.H.: *Declutching control of a wave energy converter*, Ocean Engineering, Vol. 36, no. 12-13, pp. 1015-1024, 2009.
14. Zhan, X.Q., Zhang, Y.H., Zhao, K.D.: *Study on Mathematical Model of Hydraulic Accumulator in Secondary Regulated System*, China Mechanical Engineering, Vol. 12, no. Z1, pp. 45-46, 2001.

CONTACT WITH THE AUTHORS

Hu Zhang, Ph.D.

e-mail: zhaoleiand@sina.cn

tel.: 18807189996

School of Information Engineering

Wuhan University of Technology

Wuhan Hubei 430070

CHINA

RESEARCH ON THE MARITIME LOGISTICS PRICING MODEL OF RISK-AVERSE RETAILER-DOMINATED DUAL-CHANNEL SUPPLY CHAIN

Qing Fang^{1,2}, Ph. D.,
Zeping Tong², Associate Professor,
Liang Ren², Ph. D.,
Ao Liu, Ph. D.,

¹ School of Management, Huazhong University of Science and Technology, Wuhan 430074, China

² School of Management, Wuhan University of Science and Technology, Wuhan 430081, China

ABSTRACT

Price decision is studied in a risk-averse retailer-dominated dual-channel supply chain, which consisting of one manufacturers and one retailer with both off-line and on-line channels. Firstly, two mean-variance models in centralized and decentralized supply chain are established. Secondly, the optimal solutions under the two decision modes are compared and analyzed. The results shows that the price of dual-channel of retailer decreased with the increase of retailers' risk-aversion coefficient and the standard deviation of the fluctuation of market demand, while the wholesale price changes is on the contrary; in addition, when the market demand is greater than a certain value, the prices of dual channel are correspondingly higher in decentralized supply chain than in centralized supply chain, and vice versa. In addition, when the retailer's risk aversion is in a certain interval, the expected utility of the whole supply chain is greater in centralized supply chain than in decentralized decision, and vice versa. Finally, a numerical example is given to verify the above conclusions.

Keywords: Dual channel; Risk-averse; Retailer-dominated; Supply chain

INTRODUCTION

Internet network has created a new consumer market and a growing network of user groups, enterprises which sale products through e-commerce can quickly obtain new competitive advantage. Especially in recent years, e-commerce and online retail are rapidly growing. While under the background of slowdown of economic growth and the impact of e-commerce the traditional physical retail enterprises are facing serious challenges, for example, high operating costs, consumer loss and reduced profits, and even many of the traditional retail closed. In this case, the traditional retail enterprises began to seek changes in sales patterns and

have turned their attention to e-commerce business model. So many of the traditional retail giant enterprises, such as WAL-MART, Suning, Gome and other enterprises which in addition to continue to retain the traditional physical stores have opened a network of sales channels, namely the dual channel sales model. The implementation of dual channel will often lead to channel conflict, such as the conflict between the manufacturer and the retailer, the conflict between offline channel and online channel, and the main means to alleviate channel conflict is to determine the reasonable price of the dual channel, so the study on pricing strategy of retailer dual channel is significant.

At present, the research on pricing of dual channel supply chain mainly focuses on the manufacturer-dominated dual

channel supply chain. Such as Brynjolfsson through the empirical research on two kinds of homogeneous products, books and CDs that these two types of products in the online price cheaper than the store price of books on the Internet 9–16%, an average difference of 33% CD, the average price is 25% [1]. Chiang et al. point out that the direct selling channel is beneficial to the manufacturer and the whole supply chain, which reduces the double marginal effect of the price, while the direct selling channel is not always harmful to the retailer, because it can reduce the wholesale price of the product [2]. Hsieh et al. consider the pricing and order quantity decision making problem for multiple manufacturers and a common retailer in supply chain with uncertain demand [3]. Panda et al. discusses the pricing and replenishment decision making of a dual channel supply chain consisting of a manufacturer and a network channel Stackelberg [4]. Yao and other to build Bertrand model and Stackelberg model, the equilibrium pricing strategy [5]. Khouja et al. studies the channel choice and price strategy of the manufacturer based on the consumer preference [6].

However, at present not much research on the problem of retailers in dual channel supply chain pricing, such as Wang proposed a model of the problem of sharing in the retailer dominated option contract coordination of supply chain channels and risk [7]. Pan construct a two cycle model to study the retailer dominated multi period ordering decision problem [8]. Huang et al. studies the pricing strategy of retailer's dual channel under the condition of determining demand [9]. Zhang in a study by two manufacturers and two retailers in the supply chain, are discussed in the manufacturer Stackelberg, retailer Stackelberg and vertical Nash in three cases with alternative products in the case of deterministic demand pricing strategy [10]. Wang et al. studied the pricing strategy of a supply chain consisting of two manufacturers and a common dominant retailer [11]. Zhang mainly study the dual channel coordination problem in short life cycle [12]. With the increase of uncertainty of market demand, enterprises must consider the risk bearing capacity of enterprises in the pursuit of maximum profits.

There are fewer literatures about the risk of supply chain participants in the dual channel pricing, such as Xiao etc., and studies the influence of the retailer's risk sensitivity on the service level and price under uncertain demand [13]. Xie studied the risk aversion behavior in three different supply chain structures in the supply chain participants, results show that the structure of supply chain and supply chain risk attitude of the participants had a significant effect on the quality of investment and pricing [14]. Xu et al. studied the supply chain participants as a risk averse manufacturer's dual channel pricing strategy, and proposed a two-way profit sharing contract coordination mechanism [15]. The influence of the degree of risk aversion on the price and profit of the manufacturer's dual channel supply chain under the condition of complete information and asymmetric information by Liu and [16]. Kim et al. studied the impact of risk averse participants on the price in a decentralized dual channel supply chain [17]. Li et al. studied the effect of risk averse

retailers on Pricing in the dual channel of manufacturer under uncertain demand [18].

The reminder of this paper is organized as follows. Section 2 introduces the notations, assumptions and the model. In Section 3, we examine the optimal pricing policies for the manufacturer and the retailer in both centralized and decentralized dual-channel supply chains. The theoretical results and comparisons of these results are presented in Section 4. We illustrate some managerial insights through numerical experiments in Section 5. Section 6 gives conclusions and directions for future research.

PROBLEM DESCRIPTION

In this paper, the dual channel supply chain is composed of one manufacturer and one retailer, in which the retailer is the dominant, the manufacturer is the follower. In the dual channel supply chain, the manufacturer produces a single product at a unit cost c and distribution it through the retailer at the wholesale price w , and the retailer will resell the product through his own offline channel at price p_i and online channel at price p_e . Where $p_i > w > c$ ($i=r, e$), accordingly, the customers will migrate between two channel if they perceive the price difference. as shown in figure 1.

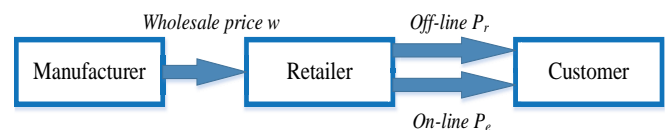


Fig.1. retailer dual-channel

Let D_r denote the consumer demand from the off-line channel and D_e denote the consumer demand from the on-line channel, respectively. we assume that the market demand is stochastic, therefore $\tilde{a}(\tilde{a} > 0)$ is assumed to be a random variable, and $\tilde{a} = a + \varepsilon$, a is a positive constant and denote the potential gross market demand, whereas ε is a random variable and $\varepsilon \sim N(0, \sigma^2)$. Let s ($0 < s < 1$) represent the degree of customer loyalty to the offline channel, Correspondingly, $1-s$ represent the degree of customer loyalty to the online channel. The parameter θ ($\theta > 0$) is the coefficient of price elasticity of D_r and D_e . The parameter b ($\theta > 0$) is the coefficient of cross-price sensitivity, $\theta > b$ means that the effect of the cross-channel price is lower than that of the self-channel price.

Given the uncertainty of market demand, participants of supply chain have different attitude on market risk. There are a lot of risk measurement methods on risk attitude, according to the Choi on the risk aversion model summary [19], this paper adopts the mean variance theory to measure risk attitude of participants of supply chain. we consider the manufacturer as risk neutral and the retailer as risk averse. We use their risk tolerance level to measure their risk aversion. A higher tolerance for risk indicates a lower degree of risk aversion in which they are less scared of uncertainty and are more adventurous. Let k_m ($k_m > 0$) and k_r ($k_r > 0$) measure

the degree of risk aversion of manufacture and retailer respectively. $k_r \geq 0$ denotes the retailer's risk tolerance (or degree of risk aversion), whereas $k_r > 0$ represents the retailer's aversion to risk. is used to signify the risk-neutral retailer. A larger implies that the retailer's degree of risk aversion is high. Similarly, $k_m (k_m \geq 0)$ refers to the manufacturer's risk tolerance or degree of risk aversion.

In model, the superscript c and d denote centralized decision and decentralized decision respectively, superscript $*$ means optimal solution; the subscript r denotes the retailer or offline channels, the subscript e represents online channels; the subscript m represents the manufacturer, the subscript sc represents the entire supply chain.

Linear demand functions have been adopted in Chiang et al. [2], Yue and Liu [20], Huang and Swaminathan [9], and many others. The corresponding demand functions to the manufacturer and the retailer are described as follows:

$$d_r = s\tilde{a} - \theta p_r + bp_e \quad (1)$$

$$d_e = (1-s)\tilde{a} - \theta p_e + bp_r \quad (2)$$

With the above assumption and notion, expected profit functions of manufacturer and retailer is as follows:

$$E(\pi_m) = (w-c)(sa - \theta p_r + bp_e) + (w-c)[(1-s)a - \theta p_e + bp_r] \quad (3)$$

$$E(\pi_r) = (p_r - w)(sa - \theta p_r + bp_e) + (p_e - w)[(1-s)a - \theta p_e + bp_r] \quad (4)$$

The variance profit of manufacturer and retailer is as follows:

$$Var(\pi_m) = E[\pi_m - E(\pi_m)]^2 = (w-c)^2 \sigma^2 \quad (1)$$

$$Var(\pi_r) = E[\pi_r - E(\pi_r)]^2 = [\Delta w_r * s + \Delta w_e * (1-s)]^2 \sigma^2 \quad (2)$$

Expected utility functions of manufacturer and retailer is as follows:

$$U_m(\pi_m) = E(\pi_m) - k_m \sqrt{Var(\pi_m)} = (w-c)[a - (\theta - b)(2w + \Delta w_r + \Delta w_e) - k_m \sigma] \quad (3)$$

$$\begin{aligned} U_r(\pi_r) &= E(\pi_r) - k_r \sqrt{Var(\pi_r)} \\ &= (p_r - w_m)(sa - \theta p_r + bp_e) \\ &\quad + (p_e - w_m)[(1-s)a - \theta p_e + bp_r] \\ &\quad - k_r [(p_r - w_m)s + (p_e - w_m)(1-s)]\sigma \end{aligned} \quad (4)$$

MODEL BUILDING AND SOLVING

In the dual channel supply chain of retailers, it is assumed that the retailer is risk averse and the leader in the supply chain. In order to analyze the influence of the retailer's risk aversion on the price and profit of the supply chain, the retailer and the manufacturer's decision making behavior are considered separately under the centralized decision-making and decentralized decision-making.

CENTRALIZED DECISION-MAKING SITUATION

According to the known conditions, the retailer is the leader in the dual channel supply chain, that is to say, the decision of the price and output of the supply chain is mainly determined by the retailer. When the dual channel supply chain is controlled or managed by a decision maker, the system will pursue the maximization of the profit of the whole supply chain. Thus, the expected profit, variance and expected utility function of the whole dual channel supply chain are respectively:

$$E(\pi_{sc}^c) = (p_r^c - c)(sa - \theta p_r^c + bp_e^c) + (p_e^c - c)[(1-s)a - \theta p_e^c + bp_r^c] \quad (5)$$

$$\begin{aligned} Var(\pi_{sc}^c) &= E[\pi_{sc}^c - E(\pi_{sc}^c)]^2 \\ &= [(p_r^c - c)s + (p_e^c - c)(1-s)]^2 \sigma^2 \end{aligned} \quad (6)$$

$$\begin{aligned} U_{sc}(\pi_{sc}^c) &= E(\pi_{sc}^c) - k_r \sqrt{Var(\pi_{sc}^c)} \\ &= (p_r^c - c)(sa - \theta p_r^c + bp_e^c) \\ &\quad + (p_e^c - c)[(1-s)a - \theta p_e^c + bp_r^c] \\ &\quad - k_r [(p_r^c - c)s + (p_e^c - c)(1-s)]\sigma \end{aligned} \quad (7)$$

Proposition 1: In a centralized retailer dual channel supply chain with a risk-averse retailer and a risk-neutral manufacturer, assuming that the demand uncertainty ε follows a normal distribution, the optimal off-line price and on-line price are

$$p_r^{c*} = \frac{(2s-1)(a - k_r \sigma)}{4(\theta + b)} + \frac{(a - k_r \sigma)}{4(\theta - b)} + \frac{c}{2} \quad (8)$$

$$p_e^{c*} = -\frac{(2s-1)(a-k_r\sigma)}{4(\theta+b)} + \frac{(a-k_r\sigma)}{4(\theta-b)} + \frac{c}{2} \quad (9)$$

Proof of Proposition 1: From Eq.(11), it is easily known that the expected utility function of the dual channel supply chain is concave function, therefore make the Eq.(11) for first-order partial derivatives on offline-price and online-price respectively. Then make them equal to 0, the above equations are solved simultaneously, proposition 1 can be obtained. From the Eq.(12) and Eq.(13), we can know:

- 1) In centralized decision model, the price of retailer dual channel decreases with the increase of the retailer risk aversion coefficient and the standard deviation of the market demand.
- 2) In centralized decision model, dual channel retailer off-line price increases with the increase of market share of off-line channels, the on-line price is on the contrary; the offline price and online price of retailer dual channel increase with the increase of potential market volume.

Proposition 2: In a centralized retailer dual channel supply chain with a risk-averse retailer and a risk-neutral manufacturer, assuming that the demand uncertainty ε follows a normal distribution, the maximum expected profit and expected utility are

$$E_{max}(\pi_{sc}^c) = \frac{(2s-1)^2[a^2 - (k_r\sigma)^2]}{8(\theta+b)} + \frac{[a^2 - (k_r\sigma)^2]}{8(\theta-b)} + \frac{(\theta-b)c^2}{2} - \frac{ac}{2} \quad (10)$$

$$\frac{\partial U_{max}(\pi_{sc}^c)}{\partial k_r} = \frac{(2s-1)^2(a-k_r\sigma)^2}{8(\theta+b)} + \frac{(a-k_r\sigma)}{8(\theta-b)} + \frac{(\theta-b)c}{2} - \frac{(a-k_r\sigma)c}{2} \quad (11)$$

Properties 1: In centralized decision scenario, the relation between expected utility $U_{max}(\pi_{sc}^c)$ and the degree of retailer risk averse k_r in the supply chain is as follow: if satisfy 1), then expected utility $U_{max}(\pi_{sc}^c)$ increase with the increase of the degree of retailer risk averse k_r ; if satisfy 2), then expected utility $U_{max}(\pi_{sc}^c)$ decrease with the increase of the degree of retailer risk averse k_r .

- 1) If $k_r \geq \frac{a}{\sigma} - \frac{2(\theta^2 - b^2)c}{[(2s-1)^2(\theta-b) + (\theta+b)]\sigma}$, then $\frac{\partial U_{max}(\pi_{sc}^c)}{\partial k_r} \geq 0$;
- 2) If $k_r < \frac{a}{\sigma} - \frac{2(\theta^2 - b^2)c}{[(2s-1)^2(\theta-b) + (\theta+b)]\sigma}$, then $\frac{\partial U_{max}(\pi_{sc}^c)}{\partial k_r} < 0$;

Proof of Properties 1: In centralized decision scenario, taking the first-order partial derivatives of expected utility $U_{max}(\pi_{sc}^c)$ with respect to k_r , we have:

$$\frac{\partial U_{max}(\pi_{sc}^c)}{\partial k_r} = -\frac{(2s-1)^2(a^2 - k_r\sigma)\sigma}{4(\theta+b)} - \frac{(a^2 - k_r\sigma)\sigma}{4(\theta-b)} + \frac{\sigma c}{2}$$

- 1) Let $\frac{\partial U_{max}(\pi_{sc}^c)}{\partial k_r} \geq 0$, then $k_r \geq \frac{a}{\sigma} - \frac{2(\theta^2 - b^2)c}{[(2s-1)^2(\theta-b) + (\theta+b)]\sigma}$;
- 2) Let $\frac{\partial U_{max}(\pi_{sc}^c)}{\partial k_r} < 0$, then $k_r < \frac{a}{\sigma} - \frac{2(\theta^2 - b^2)c}{[(2s-1)^2(\theta-b) + (\theta+b)]\sigma}$.

Properties 2: In centralized decision scenario, the relation between expected utility $U_{max}(\pi_{sc}^c)$ and the market share of off-line channels s in the supply chain is as follow: (1) if satisfy $s \in (0, 0.5)$, then expected utility $U_{max}(\pi_{sc}^c)$ decrease with the increase of the market share of off-line channels s ; (2) if satisfy $s \in [0.5, 1)$, then expected utility $U_{max}(\pi_{sc}^c)$ increase with the increase of the market share of off-line channels s .

Proof of Properties 2: In centralized decision scenario, taking the first-order partial derivatives of expected utility $U_{max}(\pi_{sc}^c)$ with respect to s and let it equal 0, we have:

$$\frac{\partial U_{sc}(\pi_{sc}^c)}{\partial s} = \frac{2(2s-1)(a-k_r\sigma)^2}{8(\theta+b)} = 0, \text{ then } s = 0.5.$$

therefore, if $s \in (0, 0.5)$, then $\frac{\partial U_{sc}(\pi_{sc}^c)}{\partial s} < 0$; if $s \in [0.5, 1)$, then $\frac{\partial U_{sc}(\pi_{sc}^c)}{\partial s} > 0$

DECENTRALIZED DECISION-MAKING SITUATION

In decentralized decision-making situation, manufacturer and retailer will make their own profit maximization as the goal of decision-making. Because of the assumption that the retailer is the leader of the supply chain and the manufacturer is the follower, the game between the manufacturer and the retailer belongs to Stackelberg. It is noted that when the retailer is the leader of the supply chain, we can't get the optimal solution when we substitute the demand function with respect to w into the profit function. Therefore, the sales price must be expressed as a function of the wholesale price, the retailer decision variables p_i are converted to the add-value of wholesale price Δw_i and expressed in the wholesale price, that is $p_i = w + \Delta w_i, i = r, e$.

In decentralized decision-making situation, according to Eq.(7), Eq.(8) and above assumption, the decision functions of manufacturer and retailer are respectively as follow:

$$U_m(\pi_m^d) = E(\pi_m^d) - k_m \sqrt{\text{Var}(\pi_m^d)} \\ = (w_m^d - c)[a - (\theta - b)(2w + \Delta w_r + \Delta w_e)] \quad (12)$$

$$U_r(\pi_r^d) = E(\pi_r^d) - k_r \sqrt{\text{Var}(\pi_r^d)} \\ = (p_r^d - w_m^d)(sa - \theta p_r^d + b p_e^d) \\ + (p_e^d - w_m^d)[(1-s)a - \theta p_e^d + b p_r^d] \\ - k_r [(p_r^d - w_m^d)s + (p_e^d - w_m^d)(1-s)]\sigma \quad (13)$$

Game between retailer and manufacturer is divided into two steps: the first step, as the leader, the retailer first determines the premium Δw_r and Δw_e of wholesale price to maximize own expected utility; the second step, as the follower, the manufacturer determines the wholesale price to maximize expected utility after observing the decisions of retailer.

Proposition 3: In a decentralized retailer dual channel supply chain with a risk-averse retailer and a risk-neutral manufacturer, assuming that the demand uncertainty ε follows a normal distribution, the optimal off-line price and on-line price are

$$p_r^{d*} = \frac{(2s-1)(a - k_r\sigma)}{4(\theta + b)} + \frac{3a - 2k_r\sigma}{8(\theta - b)} + \frac{c}{4} \quad (14)$$

$$p_e^{d*} = -\frac{(2s-1)(a - k_r\sigma)}{4(\theta + b)} + \frac{3a - 2k_r\sigma}{8(\theta - b)} + \frac{c}{4} \quad (15)$$

$$w_m^{d*} = \frac{a + 2k_r\sigma}{8(\theta - b)} + \frac{3}{4}c \quad (16)$$

Proof of Proposition 3: The proof is solved by backward induction. In the second stage of the game, the manufacturer takes its expect utility maximization as the goal, after the retailer determines the Δw_r and Δw_e , Manufacturer determines a wholesale price to maximize expected utility. The decision variable of the manufacturer is w_m^d , therefore make the Eq.(16) for first-order partial derivatives on w_m^d and make it equal to 0, then we can obtain response function w_m^d with respect to Δw_r and Δw_e .

$$w = \frac{a}{4(\theta - b)} + \frac{c}{2} - \frac{\Delta w_r + \Delta w_e}{4} \quad (17)$$

In the first stage of the game, the retailer makes decision with the goal of maximizing expected utility, his decision variable are the premium Δw_r and Δw_e of wholesale price, substitute Eq.(21) into Eq.(17), then taking the first-order partial derivatives of expected utility $U_{max}(\pi_r^d)$ with respect to Δw_r and Δw_e , and let them equal 0, we have:

$$\frac{\partial U(\pi_r^d)}{\partial \Delta w_r} = -2\theta \Delta w_r + sa - \frac{a}{4} - \frac{\theta - b}{2}c \\ + \frac{(\theta - b)(\Delta w_r + \Delta w_e)}{2} + 2b\Delta w_e - k_r s\sigma = 0 \\ \frac{\partial U(\pi_r^d)}{\partial \Delta w_e} = -2\theta \Delta w_e + (1-s)a - \frac{a}{4} - \frac{\theta - b}{2}c \\ + \frac{(\theta - b)(\Delta w_r + \Delta w_e)}{2} + 2b\Delta w_r - k_r(1-s)\sigma = 0$$

To solve the above two equations, we have:

$$\Delta w_r = \frac{(2s-1)(a - k_r\sigma)}{4(\theta + b)} + \frac{a - 2k_r\sigma}{4(\theta - b)} - \frac{c}{2} \\ \Delta w_e = -\frac{(2s-1)(a - k_r\sigma)}{4(\theta + b)} + \frac{a - 2k_r\sigma}{4(\theta - b)} - \frac{c}{2}$$

Substitute above solutions into Eq.(21), then according to $p_i = w + \Delta w_i$, we can obtain Proposition 3.

From Eq. (18-20), it is easily known:

Properties 3: In decentralized decision scenario, the p_r^{d*} and p_e^{d*} decrease with the increase of the degree of retailer risk averse k_r and standard deviation σ of market demand fluctuation; the wholesale price increase with the increase of the degree of retailer risk averse k_r and standard deviation σ of market demand fluctuation.

Properties 4: In decentralized decision scenario, the p_r^{d*} and p_e^{d*} increase with the increase of the potential market demand a . The off-line price p_r^{d*} of retailer increase with the increase of the market share of off-line channel of retailer, but The on-line price p_e^{d*} of retailer decrease with the increase of the market share of off-line channel of retailer.

Proposition 4: In a decentralized retailer dual channel supply chain with a risk-averse retailer and a risk-neutral manufacturer, assuming that the demand uncertainty ε follows a normal distribution, the maximum expect utility of retailer, manufacturer and the whole supply chain respectively are

$$U_{max}^d(\pi_r^d) = \frac{(2s-1)^2(a - k_r\sigma)^2}{8(\theta + b)} \\ + \frac{(a - 2k_r\sigma)^2}{16(\theta - b)} - \frac{(a - 2k_r\sigma)c}{4} + \frac{(\theta - b)c^2}{4} \quad (18)$$

$$U_{max}^d(\pi_m^d) = \frac{(a + 2k_r\sigma)^2}{32(\theta - b)} - \frac{(a + 2k_r\sigma)c}{8} + \frac{(\theta - b)c^2}{8} \quad (19)$$

$$U_{max}^d(\pi_{sc}^d) = \frac{(2s-1)^2(a - k_r\sigma)^2}{8(\theta + b)} + \frac{(a - 2k_r\sigma)^2}{16(\theta - b)} - \frac{(3a - 2k_r\sigma)c}{4} + \frac{(a + 2k_r\sigma)^2}{32(\theta - b)} + \frac{3(\theta - b)c^2}{8} \quad (20)$$

Properties 5: In decentralized decision scenario, the relation between expected utility $U_{max}(\pi_{sc}^d)$ and the degree of retailer risk averse k_r in the supply chain is as follow: if satisfy 1), then expected utility $U_{max}(\pi_{sc}^d)$ increase with the increase of the degree of retailer risk averse k_r ; if satisfy 2), then expected utility $U_{max}(\pi_{sc}^d)$ decrease with the increase of the degree of retailer risk averse k_r .

- 1) $k_r \geq \frac{2(2s-1)^2(\theta - b)a + (\theta + b)a - 4(\theta^2 - b^2)c}{2\sigma[(2s-1)^2(\theta - b) + 3(\theta + b)]}$;
- 2) $k_r < \frac{2(2s-1)^2(\theta - b)a + (\theta + b)a - 4(\theta^2 - b^2)c}{2\sigma[(2s-1)^2(\theta - b) + 3(\theta + b)]}$.

Proof of Properties 5: In decentralized decision scenario, taking the first-order partial derivatives of expected utility $U_{max}(\pi_{sc}^d)$ with respect to k_r , we have:

$$\frac{\partial U_{sc}(\pi_{sc}^d)}{\partial k_r} = -\frac{(2s-1)^2 a \sigma}{4(\theta + b)} - \frac{a \sigma}{8(\theta - b)} + \frac{k_r \sigma^2 (2s-1)^2}{4(\theta + b)} + \frac{3k_r \sigma^2}{4(\theta - b)} + \frac{\sigma c}{2}$$

- 1) Let $\frac{\partial U_{sc}(\pi_{sc}^d)}{\partial k_r} \geq 0$, then

$$k_r \geq \frac{2(2s-1)^2(\theta - b)a + (\theta + b)a - 4(\theta^2 - b^2)c}{2\sigma[(2s-1)^2(\theta - b) + 3(\theta + b)]}$$

- 2) Let $\frac{\partial U_{sc}(\pi_{sc}^d)}{\partial k_r} < 0$, then

$$k_r < \frac{2(2s-1)^2(\theta - b)a + (\theta + b)a - 4(\theta^2 - b^2)c}{2\sigma[(2s-1)^2(\theta - b) + 3(\theta + b)]}$$

Properties 6: In decentralized decision scenario, the relation between expected utility $U_{max}(\pi_{sc}^d)$ of the whole supply chain and the market share of off-line channels s is as follow: (1) If satisfy $s \in (0, 0.5]$, then expected utility $U_{max}(\pi_{sc}^d)$ decrease with the increase of the market share of off-line channels s ; (2) If satisfy $s \in [0.5, 1)$, then expected utility $U_{max}(\pi_{sc}^d)$ increase with the increase of the market share of off-line channel s .

Proof of Properties 6: In decentralized decision scenario, taking the first-order partial derivatives of expected utility $U_{max}(\pi_{sc}^d)$ with respect to s and let it equal 0, we have:

$$\frac{\partial U_{sc}(\pi_{sc}^d)}{\partial s} = \frac{2(2s-1)(a - k_r\sigma)^2}{8(\theta + b)} = 0, \text{ then } s = 0.5.$$

therefore, if $s \in (0, 0.5]$, then $\frac{\partial U_{sc}(\pi_{sc}^d)}{\partial s} < 0$; if $s \in [0.5, 1)$, then $\frac{\partial U_{sc}(\pi_{sc}^d)}{\partial s} > 0$.

COMPARATIVE ANALYSIS

PRICE COMPARISON UNDER TWO DECISION MODELS

- (1) Price comparison under the same decision models
According to Eq.(12-13) and Eq.(17-18), let:

$$\Delta p^c = p_r^{c*} - p_e^{c*}, \quad \Delta p^d = p_r^{d*} - p_e^{d*}, \text{ then}$$

$$\Delta p^c = p_r^{c*} - p_e^{c*} = \Delta p^d = p_r^{d*} - p_e^{d*} = \frac{(2s-1)(a - k_r\sigma)}{2(\theta + b)}$$

- (1) If $s > \frac{1}{2}$, $k_r < \frac{a}{\sigma}$, then $p_r^{c*} > p_e^{c*}$, $p_r^{d*} > p_e^{d*}$;
- (2) If $s < \frac{1}{2}$, $k_r > \frac{a}{\sigma}$, then $p_r^{c*} < p_e^{c*}$, $p_r^{d*} < p_e^{d*}$;
- (3) If $s = \frac{1}{2}$ or $k_r = \frac{a}{\sigma}$, then $p_r^{c*} = p_e^{c*}$, $p_r^{d*} = p_e^{d*}$.

From above analysis we can easily know: In the same decision mode, when the marker share of off-line channel is greater than that of the online channel, and the degree of the retailer risk aversion is less than a certain value, the price of off-line channel is higher than that of the online channel; when the marker share of off-line channel is less than that of the online channel, and the degree of the retailer risk aversion is greater than a certain value, the price of off-line channel is less than that of the online channel; when the marker share of off-line channel is equal to that of the online channel, and the degree of the retailer risk aversion is equal to a certain value, the price of off-line channel is equal to that of the online channel;

(2) Price comparison under the different decision models

According to Eq.(12-13) and Eq.(17-18), let $\Delta p_r = p_r^{d*} - p_r^{c*}$, $\Delta p_e = p_e^{d*} - p_e^{c*}$, then

$$\Delta p_r = p_r^{d*} - p_r^{c*} = \Delta p_e = p_e^{d*} - p_e^{c*} = \frac{a}{8(\theta-b)} - \frac{c}{4}$$

Further analysis:

- (1) If $a > 2(\theta-b)c$, and $\theta > b > 0$, then $p_r^{d*} > p_r^{c*}$, $p_e^{d*} > p_e^{c*}$;
 (2) If $a < 2(\theta-b)c$, then $p_r^{d*} < p_r^{c*}$, $p_e^{d*} < p_e^{c*}$.

Above analysis shows: when the market demand is greater than a certain value, the prices in decentralized dual channel are higher than that in centralized decision; when the market demand is less than a certain value, the prices in decentralized dual channel are less than that in centralized decision; when the market demand is equal to a certain value, the prices in decentralized dual channel are equal to that in centralized decision.

EXPECT UTILITY COMPARISON UNDER TWO DECISION MODELS

According to Eq.(15) and Eq.(24), let

$$\Delta U(\pi_{sc}) = U_{sc}^c(\pi_{sc}^c) - U_{sc}^d(\pi_{sc}^d), \text{ then}$$

$$\Delta U(\pi_{sc}) = U_{sc}^c(\pi_{sc}^c) - U_{sc}^d(\pi_{sc}^d) = \frac{(a - 2k_r\sigma)^2 - 12(k_r\sigma)^2}{32(\theta-b)} + \frac{(\theta-b)c^2}{8} + \frac{ac}{4}$$

It is easy to know that:

1) If $0 \leq k_r \leq \frac{-a + \sqrt{3a^2 + 8(\theta-b)^2c^2 + 16(\theta-b)ac}}{4\sigma}$,

then $U_{sc}^c(\pi_{sc}^c) \geq U_{sc}^d(\pi_{sc}^d)$;

2) If $k_r > \frac{-a + \sqrt{3a^2 + 8(\theta-b)^2c^2 + 16(\theta-b)ac}}{4\sigma}$,

then $U_{sc}^c(\pi_{sc}^c) < U_{sc}^d(\pi_{sc}^d)$.

Proof: Let $\Delta U(\pi_{sc}) \geq 0$, we can get inequality:

$$8(k_r\sigma)^2 + 4ak_r\sigma - a^2 - 4(\theta-b)^2c^2 - 8(\theta-b)ac \leq 0, \text{ and } k_r \geq 0, \text{ through solving above inequality, it is easy to obtain:}$$

$$0 \leq k_r \leq \frac{-a + \sqrt{3a^2 + 8(\theta-b)^2c^2 + 16(\theta-b)ac}}{4\sigma}$$

Similarity, let $\Delta U(\pi_{sc}) < 0$, we can obtain

$$k_r > \frac{-a + \sqrt{3a^2 + 8(\theta-b)^2c^2 + 16(\theta-b)ac}}{4\sigma}$$

Above analysis show that only when the degree of retailer risk aversion is in a range of a certain interval, the expected

utility of whole supply chain is greater in centralized decision than in decentralized decision; when the degree of retailer risk aversion exceeds a certain threshold, the expected utility of whole supply chain is less in centralized decision than in decentralized decision. This conclusion is different from that when the participants of supply chain are risk neutral.

NUMERICAL EXAMPLES

Because there are a lot of parameters in the model, the expression is more complex, to further analyze the effect of parameters on the optimal price and expected utility, the sensitivity analysis will be performed through numerical examples.

THE SENSITIVITY ANALYSIS OF PRICE

(1) The influence of k_r on the price of offline and online channel we assume that $a = 100$, $\theta = 0.6$, $b = 0.1$, $c = 2$, $s = 0.6$, $\sigma = 3$, $k_r \in [1, 30]$, drawing using Matlab software. From Fig. 2 and Fig. 3, we know that the price of offline and online channel decrease with increase of the degree of retailer risk aversion both in centralized decision and in decentralized decision.

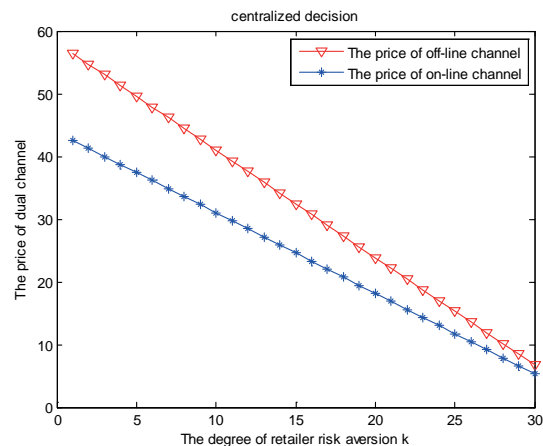


Fig.2. The influence of k_r on price in centralized decision

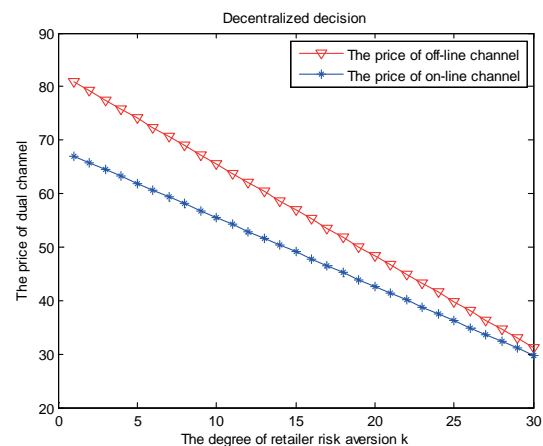


Fig.3. The influence of k_r on price in decentralized decision

(2) The influence of k_r and σ on the price of offline and online channel we assume that $a = 100$, $\theta = 0.6$, $b = 0.1$, $c = 2$, $s = 0.6$, $k_r \in [0.1, 1]$, $\sigma \in [1, 20]$, drawing using Matlab software. From Fig.4, we know that the price of offline and online channel decrease with increase of the degree of retailer risk aversion and Standard deviation of demand fluctuation both in centralized decision and in decentralized decision.

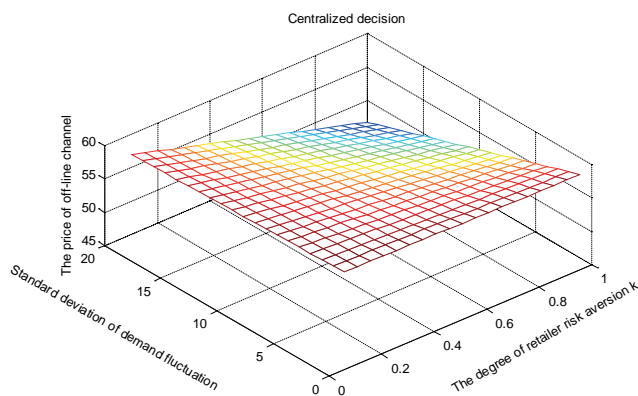


Fig.4. The influence of k_r and σ on offline price in centralized decision

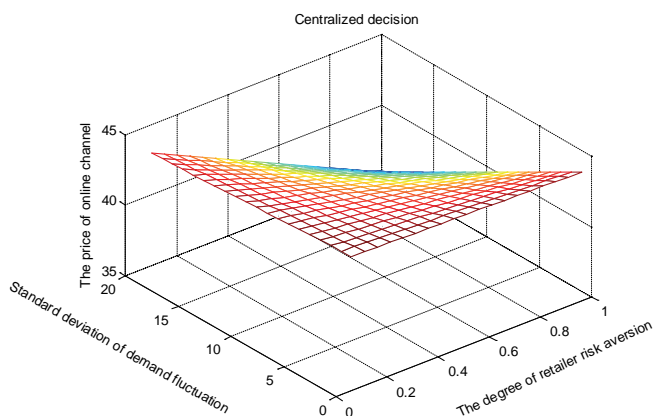


Fig.5. The influence of k_r and σ on online price in centralized decision

Similarly, in the case of the above parameters, the influence of k_r and σ on the price of offline and online channel in decentralized decision is as shown Fig.6 and Fig.7.

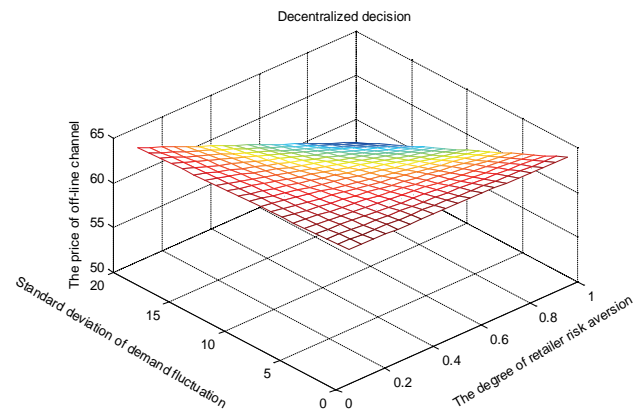


Fig.6. The influence of k_r and σ on offline price in decentralized decision

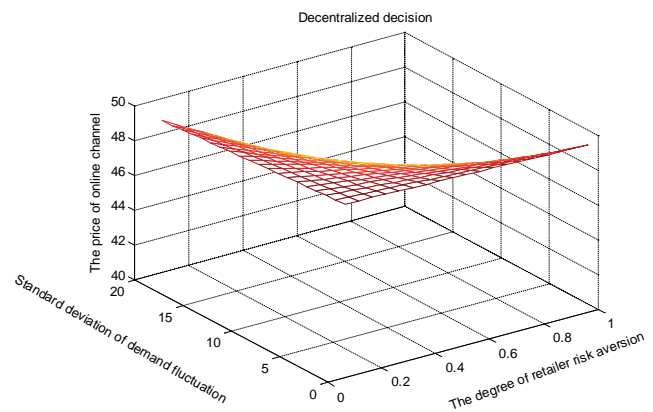


Fig.7. The influence of k_r and σ on online price in decentralized decision

THE SENSITIVITY ANALYSIS OF EXPECT UTILITY

(1) The influence of k_r on the expect utility of dual channel supply chain we assume that $a = 100$, $\theta = 0.6$, $b = 0.1$, $c = 2$, $s = 0.6$, $\sigma = 3$, $k_r \in [0, 30]$, drawing using Matlab software. From Fig.8, we know that the expect utility of supply chain in centralized decision decrease with increase of the degree of retailer risk aversion, but the expect utility of supply chain in decentralized decision increase with increase of the degree of retailer risk aversion. From Fig.9, we know that the expect utility of retailer in centralized decision first decrease and then increase with increase of the degree of retailer risk aversion, but the expect utility of manufacturer in decentralized decision increase with increase of the degree of retailer risk aversion.

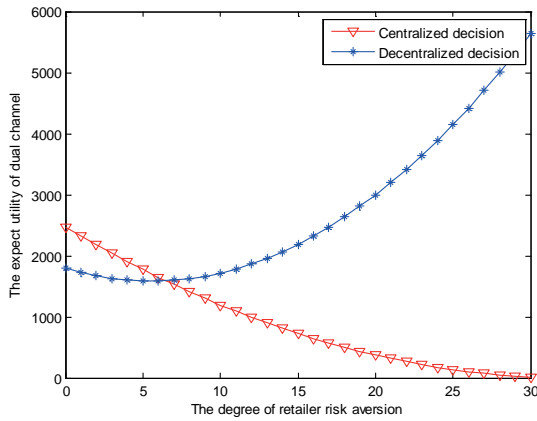


Fig.8. The influence of k_r on expect utility of supply chain in centralized and decentralized decision

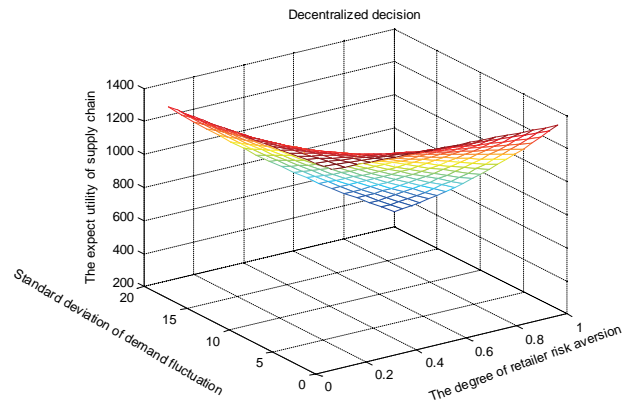


Fig.11. The influence of k_r and σ on expect utility of supply chain in decentralized decision

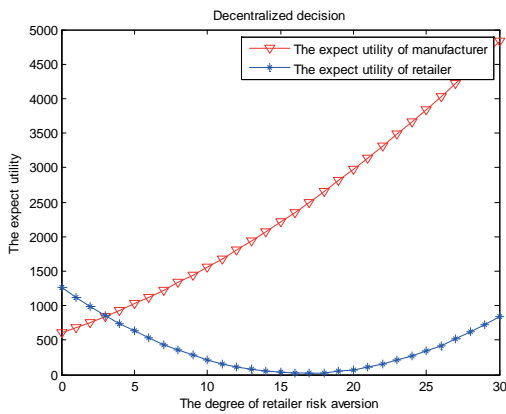


Fig.9. The influence of k_r on expect utility of retailer and manufacturer in decentralized decision

(2) The influence of k_r and σ on the expect utility of dual channel supply chain we assume that $a = 100$, $b = 0.1$, $c = 2$, $s = 0.6$, $\theta = 0.6$, $k_r \in [0.1, 1]$, $\sigma \in [1, 20]$ drawing using Matlab software. The influence of k_r and σ on the expect utility of dual channel supply chain in centralized and decentralized decision are as shown Fig. 10 and Fig. 11.

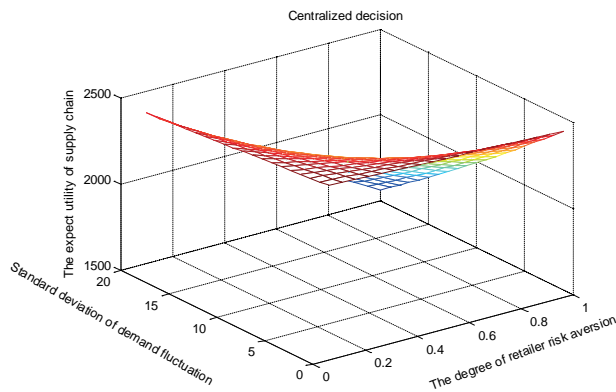


Fig.10. The influence of k_r and σ on expect utility of supply chain in centralized decision

CONCLUSION

In a dual channel supply chain which composed of one manufacturer and one retailer with both off-line and on-line channels, considering the retailer is risk averse and the manufacturer is risk neutral, two mean-variance models in centralized and decentralized supply chain are established, Secondly, the optimal solutions under the two decision modes are compared and analyzed. analysis shows that the price of dual channel decreased with the increase of the degree of retailers risk aversion and the standard deviation of the fluctuation of market demand, while the wholesale price changes on the contrary; in addition, when the market demand is greater than a certain value, the prices are higher in decentralized decision than in centralized decision, and vice versa. Moreover, when the degree of retailer risk aversion vary in a certain interval, the expected utility of the whole supply chain is greater in centralized decision than in decentralized decision, and vice versa. Further analysis found that the price of online and offline channel decreases with the increase of price elasticity coefficient, but increased with the cross price elasticity coefficient; In addition, the off-line price increases with increase of market share, but changes of on-line price on the contrary. Finally, the numerical analysis verifies the correctness of the above conclusions.

ACKNOWLEDGEMENTS

This research was supported by the National Social Science Foundation of China under Grants 16BJY160.and the National Natural Science Youth Foundation of China under Grants 71501147.

REFERENCES

1. Brynjolfsson, E., Michael, D. S.: *Frictionless Commerce? A Comparison of Internet and Conventional Retailers*, *management science*, vol. 46, no. 4, pp. 563–585, 2000.

2. Chiang, W. K., Chhajed, D., Hess, J. D.: *Direct Marketing, Indirect Profits: A Strategic Analysis of Dual-Channel Supply-Chain Design*, Management Science, vol. 49, no. 1, pp. 1-20, 2003.
3. Hsieh, C. C., Chang, Y. L., Wu, C. H.: *Competitive pricing and ordering decisions in a multiple-channel supply chain*, International Journal of Production Economics, vol. 154, no. 4, pp. 156-165, 2014.
4. Panda, S., Modak, N. M., Sana, S. S., Basu, M.: *Pricing and replenishment policies in dual-channel supply chain under continuous unit cost decrease*, Applied Mathematics and Computation, vol. 256, no. 1, pp. 913-929, 2015.
5. Yao, D. Q., Liu, J. J.: *Competitive pricing of mixed retail and e-tail distribution channels*, Omega, vol. 33, no. 3, pp. 235-247, 2005.
6. Khouja, M., Park, S., Cai, G. G.: *Channel selection and pricing in the presence of retail-captive consumers*, International Journal of Production Economics, vol. 125, no. 1, pp. 84-95, 2010.
7. Wang, X., Liu, L.: *Coordination in a retailer-led supply chain through option contract*, International Journal of Production Economics, vol. 110, no. 1, pp. 115-127, 2007.
8. Pan, K., Lai, K. K., Liang, L., Leung, S. C. H.: *Two-period pricing and ordering policy for the dominant retailer in a two-echelon supply chain with demand uncertainty*, Omega, vol. 37, no. 4, pp. 919-929, 2009.
9. Huang, W., Swaminathan, J. M.: *Introduction of a second channel: Implications for pricing and profits*, European Journal of Operational Research, vol. 194, no. 1, pp. 258-279, 2009.
10. Zhang, R., Liu, B., Wang, W.: *Pricing decisions in a dual channels system with different power structures*, Economic Modelling, vol. 29, no. 2, pp. 523-533, 2012.
11. Wang, J., Wang, A., Wang, Y.: *Markup pricing strategies between a dominant retailer and competitive manufacturers*, Computers & Industrial Engineering, vol. 64, no. 1, pp. 235-246, 2013.
12. Zhang, L., Wang, J.: *Coordination of the traditional and the online channels for a short-life-cycle product*, European Journal of Operational Research, vol. 258, no. 2, pp. 639-651, 2017.
13. Xiao, T., Yang, D.: *Price and service competition of supply chains with risk-averse retailers under demand uncertainty*, International Journal of Production Economics, vol. 114, no. 1, pp. 187-200, 2008.
14. Xie, G., Yue, W., Wang, S., Lai, K. K.: *Quality investment and price decision in a risk-averse supply chain*, European Journal of Operational Research, vol. 214, no. 2, pp. 403-410, 2011.
15. Xu, G., Dan, B., Zhang, X., Liu, C.: *Coordinating a dual-channel supply chain with risk-averse under a two-way revenue sharing contract*, International Journal of Production Economics, vol. 147, no. 1, pp. 171-179, 2014.
16. Liu, M., Cao, E., Salifou, C. K.: *Pricing strategies of a dual-channel supply chain with risk aversion*, Transportation Research Part E: Logistics and Transportation Review, vol. 90, pp. 108-120, 2016.
17. Kim, K., Park, K. S.: *Transferring and sharing exchange-rate risk in a risk-averse supply chain of a multinational firm*, European Journal of Operational Research, vol. 237, no. 2, pp. 634-648, 2014.
18. Li, B., Hou, P. W., Chen, P., Li, Q. H.: *Pricing strategy and coordination in a dual channel supply chain with a risk-averse retailer*, International Journal of Production Economics, vol. 178, pp. 154-168, 2016.
19. Choi, S.: Risk-averse newsvendor models. the degree of Doctor of Philosophy New Jersey: Newark Rutgers, 2009.
20. Yue, X., Liu, J.: *Demand forecast sharing in a dual-channel supply chain*, European Journal of Operational Research, vol. 174, no. 1, pp. 646-667, 2006.

CONTACT WITH THE AUTHORS

Qing Fang, Ph. D.

e-mail: fangqing@wust.edu.cn

tel.: 13667243266

School of Management, Wuhan University of Science
and Technology, Huang jia hu Road(West)
Hongshan District, WuHan City, Hubei province, 430065

CHINA

NUMERICAL SIMULATION OF SOLID-FLUID 2-PHASE-FLOW OF CUTTING SYSTEM FOR CUTTER SUCTION DREDGERS

Min Zhang, Ph.D.

Shidong Fan, Prof.

Hanhua Zhua, Prof.

Sen Han, Ph.D.

School of Energy and Power Engineering, Wuhan University of Technology

ABSTRACT

The study of the flow characteristics of the solid-fluid two phase flow in the cutter suction dredger is very important for exploring the slurry formation mechanism and optimizing the operational parameters. In this study, standard k-ε model and Multiple Reference Frame are applied to numerically simulate flow field in and around the cutting system, then with the steady convergent result of the simulation as the initial condition, Discrete Phase Mode is used to solve the particle motion equation by fully coupling the continuous phase and the particles. The influence of suction flow velocity and cutter's rotating speed on particles suction are analyzed, and effectively suctioned particles numbers are also quantitatively studied. The simulation result shows that the DPM model is able to simulate the movement of particles in and around the cutter suction dredger's cutting system, in the fluid flow filed velocity vector and pressure distribution on different planes show different characteristics, and under higher suction velocity and lower cutter rotating speed more particles are suctioned into the suction inlet. The results can help better understand flow characteristics of solid-fluid 2-phase-flow of cutter suction dredger's cutting system, and provide theoretical support for relative system design and operational parameters optimization.

Keywords: Numerical Simulation; Solid-Fluid, DPM; Cutting System; Cutter Suction Dredger

INTRODUCTION

Cutter suction dredger is increasingly widely used worldwide for its wide dredging depth range, good soil adaptability and high working efficiency, and it can continuously complete cutting, discharging and slurry treatment processes one time. [1] Flow characteristics of the solid-fluid 2-phase-flow in and around the cutting system of the cutter suction dredger(CSD) depend on several factors including the soil property, the dredger's structural and operational parameters composed of cutter rotational speed, swing speed and pump rotational speed and so on. Investigation on flow characteristics of this solid-fluid 2-phase-flow will be significant for slurry formation mechanism exploring and operational parameters optimization.

The cutting system and slurry transportation system cooperate to cut the soil and discharge the slurry, their respective performance and cooperation level nearly determine the working efficiency of the whole dredger. Particularly for CSD's cutting system, in most working conditions operational parameters are hard to precisely compute and adjust, so the dredger operators are most likely to rely on their experience, the dredger's working efficiency depends on the dredger operator's experience and hardly keeps stable and high. Furthermore, underwater measuring is not only difficult to carry out but also costs much time and investment. So scaled model experiment or computer simulation based on theoretical or prototype model will be more flexible, practical and economic to study the solid-fluid 2-phase-flow for the CSD.

Experimental method generally measures the velocity field with Particle Image Velocimetry (PIV) or other instrument capturing particle trajectory[2]. In computer simulation, CFD models of VOF, Mixture model or turbulence models coupling with Discrete Element Method (DEM) have been applied to handle solid-fluid 2-phase-flow. Some scholars have applied the discrete phase model (DPM) to simulate the flow characteristics of two-phase-flow for cyclone separator, centrifugal pump, complex pipeline and ballast water cyclone[3-6]. For CSD's cutting system, fluid flow simulation based on turbulence models has been studied [7, 8]. Research on simulation of 2-phase-flow of CSD's cutting system is relatively rarely focused.

In this paper, standard $k-\varepsilon$, MRF and DPM models are applied to simulate the solid-fluid 2-phase-flow of CSD's cutting system, and influence of suction velocities and cutter rotating speeds on suctioned particles is also analyzed.

GEOMETRIC AND MATHEMATICAL MODELS

GEOMETRIC MODEL AND BOUNDARY CONDITIONS

Computational domain is set with 14m in swing direction, 8.5 m in vertical and 7.5m in horizon. Ladder angle is 35 degrees as cutter's dredging position. The 3-dimensional geometry model and computational domain is shown as Fig. 2. The particle source location, where slurry particles produces, is simplified to be the inner side of 2 cutting cutter arms as shown in Fig. 1, and the slurry particles are treated as spherical.

In order to monitor the internal pressure and velocity inside the suction inlet, five sampled points marked with L1-L5, located on the plane parallel to the cutter ring and with the same radius to the cutter hub center, are taken as shown in Fig. 1.

The computational domain is meshed with structured and unstructured meshes, after simulation testing when mesh number is over 1.38 millions, the increase of mesh number has little effect on the accuracy of the calculation results. So mesh number of 1.38 millions is taken in the simulation.

The inlet of the computational domain is set velocity inlet with typical value of 0.2m/s to simulate cutting system swing movement. Suction inlet of cutting system is set to velocity type with adjustable flow rate between 1.5m/s-4m/s, which is one of the computational outlets. The bottom of the computational domain is set as wall type. In addition to the inlet and the bottom, the other sides of the whole computational domain are set pressure outflow. The rotating speed of the rotating domain can be set 15 rpm to 70 rpm with the axis of the cutter hub as rotating hub. Walls of cutter, hub, and backplate are set non-slippery boundaries. And the injected particles' diameters range from 1mm to 5mm. Boundary conditions of inlet and outlet for particles are taken as escaped or trapped. The type of collision between

the particle and the cutting system body boundaries is set as elastic rebound.

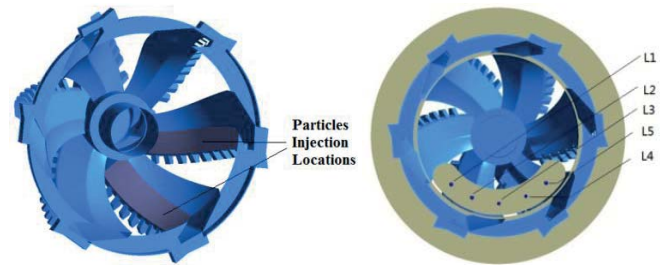


Fig. 1. Targeted Locations in Cutter Flow Field

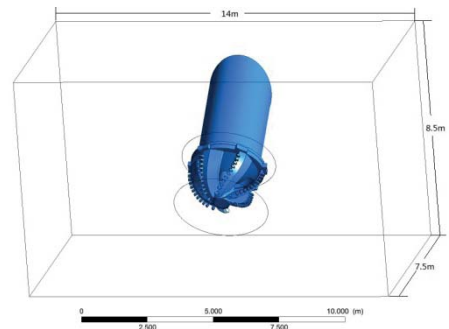


Fig. 2. Computing Domain of Cutting System Flow Field

MATHEMATICAL MODEL

In this study, water is treated as the continuous and incompressible fluid, so its governing equations are mass and momentum conservation equations. The Reynolds Averaged N-S equation is adopted to describe the fluid.

Mass conservation equation is as Eq. (1),

$$\frac{\partial \rho}{\partial t} + \frac{\partial}{\partial x_i} (\rho u_i) = 0 \quad (1)$$

Momentum conservation equation is as Eq. (2),

$$\rho \frac{\partial u_i}{\partial t} + \rho u_j \frac{\partial u_i}{\partial x_j} = p F_i - \frac{\partial p}{\partial x_i} + \frac{\partial}{\partial x_j} \left(\mu \frac{\partial u_i}{\partial x_j} - \overline{\rho u_i u_j} \right) \quad (2)$$

In Eq. (1) and Eq. (2), u_i is liquid velocity in direction x , p is liquid pressure, μ is kinetic viscosity, is fluid mass force, $\overline{\rho u_i u_j}$ is Reynolds Stress. The Reynolds equation is closed by the standard $k-\varepsilon$ mode[9,10] in which turbulent kinetic energy equation is Eq. (3) and turbulent diffusion equation is Eq. (4).

$$\frac{\partial}{\partial t} (\rho k) + \frac{\partial}{\partial x_i} (\rho k u_i) = \frac{\partial}{\partial x_j} \left[\left(\mu + \frac{\mu_t}{\sigma_k} \right) \frac{\partial k}{\partial x_j} \right] + G_k + G_b - \rho \varepsilon - Y_M + S_k \quad (3)$$

$$\frac{\partial}{\partial t}(\rho\varepsilon) + \frac{\partial}{\partial x_i}(\rho\varepsilon u_i) = \frac{\partial}{\partial x_j} \left[\left(\mu + \frac{\mu_t}{\sigma_\varepsilon} \right) \frac{\partial \varepsilon}{\partial x_j} \right] + C_{1\varepsilon} \frac{\varepsilon}{k} (G_k + C_{3\varepsilon} G_b) - C_{2\varepsilon} \rho \frac{\varepsilon^2}{k} + S_\varepsilon \quad (4)$$

$C_{1\varepsilon}, C_{2\varepsilon}, C_{3\varepsilon}$ are coefficients of constant terms of the equation,

G_k, G_b are the velocity gradient and the turbulent kinetic energy generated by the buoyancy respectively,

S_k, S_ε are user-defined functions,

G_k is the fluctuation of the pulsation expansion,

$\mu = \rho C_u \frac{k^2}{\varepsilon}$ is turbulence viscosity coefficient.

In the solid-fluid two-phase-flow field, the forces acting on a single particle are gravity, buoyancy, flow resistance, additional mass force, pressure gradient force, Basset force, Saffman lift force, Magnus force and so on [11,12]. For the particle size this study concerns, gravity, buoyancy, drag force, added mass force, pressure gradient force and forces related to rotation movement are focused. The force balance equation of the particles can be expressed as Eq. (5) in the Cartesian coordinate system,

$$m_p \frac{dU_p}{dt} = G_p + F_b + F_d + F_{VM} + F_p + F_{BA} + F_R \quad (5)$$

The particle gravity and buoyancy acting by the fluid can be described as Eq. (6),

$$G_p + F_b = m_p \cdot g \cdot \left(1 - \frac{\rho_f}{\rho_p} \right) \quad (6)$$

The drag force acting on particle is as Eq. (7),

$$F_D = \frac{18\mu}{\rho_p d_p} \cdot \frac{C_d R_{ep}}{24} (u_f - u_p) \quad (7)$$

$$F_d = m F_D = \frac{\pi \mu d_p C_d R_{ep}}{8} (u_f - u_p) \quad (8)$$

$$R_{ep} = \frac{\rho_d d_p}{\mu} |u_p - u_f| \quad (9)$$

In Eq. (7), ρ_p is particle density, F_D is the drag force of unit mass particle, d_p is particle diameter, C_d is drag coefficient, R_{ep} is particle Reynolds number, the flow velocity of particle's location, and u_p is particle velocity.

Particles will drive a certain amount of surrounding fluid to move together in fluid motion. When the particle is accelerating, the surrounding fluid will be accelerated as a result of particle driving effect, which can be equivalent to particle mass increase. The particle's virtual mass force F_{vm} is expressed by Eq. (10) and Eq. (11),

$$F_{vm} = K_m \rho_f V_p \left(\frac{du_f}{dt} - \frac{du_p}{dt} \right) \quad (10)$$

$$K_m = 1.05 - \frac{0.066}{A_c + 1.02} \quad (11)$$

A_c is particle acceleration modulus.

$$F_p = -\frac{\pi d_p^3}{6} \cdot \nabla p \quad (12)$$

F_p is the pressure difference force acting on the particles.

In the process of particle movement, the velocity is variable, fluid displacement force is acting on the particle due to the instability of surface boundary layer. For the particle with diameter between 1-5mm, the influence of Basset force can't be neglected by magnitude analysis [13].

$$F_{BA} = \frac{3d_p^2}{2} \sqrt{\pi \mu \rho_f} \int_{t_0}^{t_1} \frac{d\mu_f}{dt} - \frac{d\mu_p}{dt} \frac{dt}{\sqrt{t-t'}} \quad (13)$$

The cutter is rotating during dredging, and the particles are also acted by the centrifugal force and Coriolis force. If the cutter axis is set as the Z axis, the geometric center of cutter-ring's bottom plate is set as Cartesian coordinate origin, forces acting on the unit mass particle related to cutter rotating movement can be expressed in Cartesian coordinate system as Eq. (14),

$$\begin{cases} F_{\Omega,x} = \left(1 - \frac{\rho_f}{\rho_p} \right) \cdot \Omega^2 \cdot x + 2\Omega \left(u_{y,p} - \frac{\rho_f}{\rho_p} u_{y,p} \right) \\ F_{\Omega,y} = \left(1 - \frac{\rho_f}{\rho_p} \right) \cdot \Omega^2 \cdot y + 2\Omega \left(u_{x,p} - \frac{\rho_f}{\rho_p} u_{x,p} \right) \end{cases} \quad (14)$$

The velocity and trajectory of each position on the discrete phase can be solved by integrating the differential equation of particle force in the Laplace coordinate system.

The governing equations are converted into algebraic equations which can be solved numerically by finite volume method with pressure-based solver. In the simulation pressure equations coupling method is chosen. The pressure term is adopted in the PRESTO format, the momentum, the turbulent kinetic energy and the turbulent dissipation rate are all set as the high accuracy two order upwind scheme. The convergence judge for all variables is that the residual value is less than 10^{-3} .

MULTI-REFERENCE FRAME MODEL

In order to simulate the rotation of the cutter, Multiple Reference Frame (MRF) is adopted. The computational domain is divided into rotating domain and stationary domain. The rotating coordinate system in rotating cylindrical domain

is set as local system and the fixed coordinate system in stationary domain is regarded as absolute coordinate system. The coupling between the rotating zone and the stationary zone is realized through interface of the two domains, and finally the bidirectional continuous transfer of mass and energy between the two reference frames are realized by interfaces in MRF model[14]. Velocity and velocity gradients can be converted from reference frame to absolute inertial frame by interface between the rotor and stator defined in Fluent.

ANALYSIS OF SOLID-FLUID 2-PHASE-FLOW OF CUTTING SYSTEM

VELOCITY VECTOR AND PRESSURE ANALYSIS OF FLUID PHASE

The simulation is carried out based on the standard $k-\epsilon$ model in steady state with typical operational parameters (cutter rotating speed is 30rpm, suction velocity of the suction inlet is 2.0m/s and swing speed is 0.2m/s). 4 planes with heights of 0m, 0.45m, 0.7m, 1.6m, from the surface of cutter ring top plate and perpendicular to the cutter hub axis are sampled. The cutter radial velocity vector diagrams in rotating region (absolute velocity vector diagram, the global coordinate system as the reference) are shown in Fig. 3.

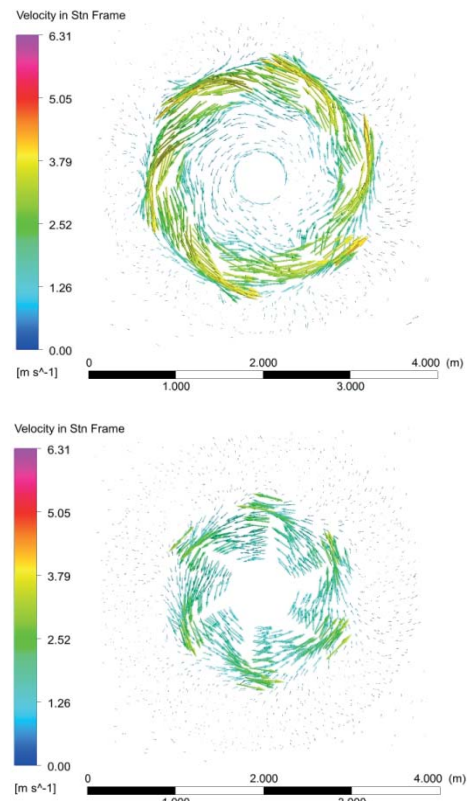
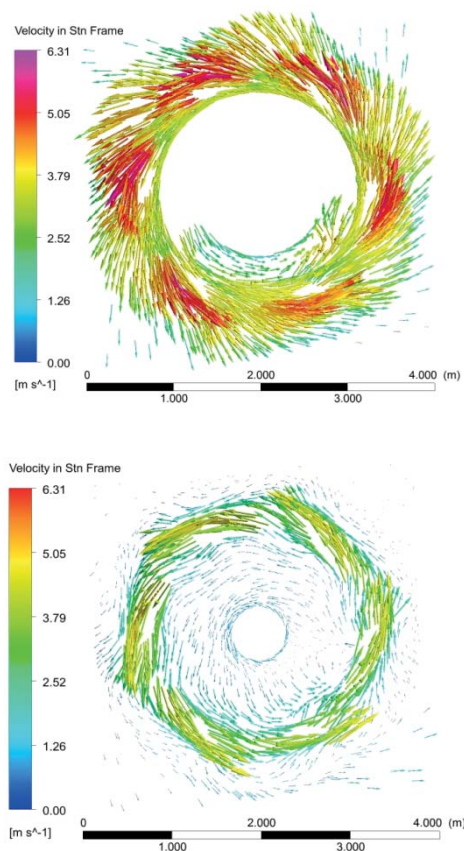


Fig. 3. Velocity Vector Diagram of Sample Planes



From Fig. 3, the rotating region full of rotating fluid forms a large vortex around cutter hub, and the vortex dominates the fluid flow in and around the cutting system, because the cutter drives the fluid in the domain in the tangential direction. On the other hand, suction effect due to suction inlet defers in different sampled planes. Near the cutter ring top ($h=0\text{m}$) rotating effect is greater than the suction effect, fluid excluding fluid inside the suction inlet is nearly unaffected by the suction effect, and a large number of fluid particles are thrown out of the cutter. On the plane of $h=0.45$, fluid particles flow across the cutter arm to the suction flow direction with high axial velocity as a result of suction inlet's suction and cutter rotating. Part fluid particles in the rotating domain flow into inner part of the cutter from opening of adjacent cutter arms, and some of those rotate with cutter hub and finally reach approach of the suction inlet, the others flow directly to the suction inlet direction. On the plane of $h=0.70\text{m}$, fluid motion characteristics are similar to those of $h=0.45\text{m}$, but the cutter radius is smaller in $h=0.70\text{m}$ so fluid tangential velocity becomes smaller. On the planes of $h=0.70\text{m}$ and $h=1.6\text{m}$, the suction effect is more weakened in turn, and affected by the hub occupation and smaller cutter opening, fluid particles have axial velocity, but the movement trend to the suction inlet is not obvious. Furthermore, with further decrease of the cutter radius, tangential velocity further decreases accordingly.

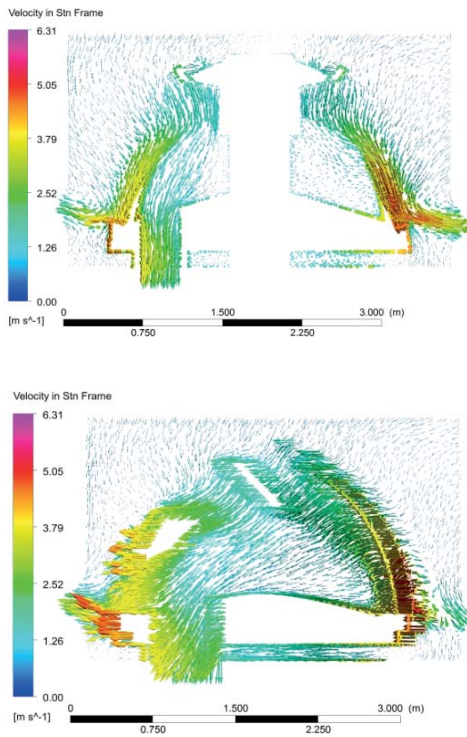


Fig. 4. Velocity Vector Diagram of Sample Planes

In order to analyze the fluid velocity vector of the planes perpendicular to the cutter ring top surface, two planes are selected which are located on the central plane ($z=0$) and the plane with distance of 0.6m from the central plane and parallel to the sampling plane of $z=0$. From velocity vector diagram of the central plane, it can be found that much fluid is approaching or entering the suction inlet due to the pump suction. With the pumping effect, macroscopic moving trend of the fluid is approaching toward the inside of the cutter through cutter arms openings, some fluid particles are rotating outside of the cutter for they are hold back by the cutter arms, and the longer the fluid particle location's radius is the higher its velocity is, most fluid particles near the cutter ring are thrown out. For fluid particles within the cutter, the velocities of fluid particles in the suction inlet side has a greater velocity component in cutter axis direction than components in cutter radial plane, most fluid particles on the opposite side of the suction inlet within the cutter keep rotating instead of approaching the suction inlet. On the plane of 0.6m from the hub, outside the cutter much fluid particles are approaching the cutter inside from openings of the cutter arms, in the cutter all fluids are trending to entering the suction inlet.

Under above cutting operating conditions, cutter radial plane's static pressure (relative pressure, the reference pressure is atmospheric pressure with 101Kp) contours are shown in Fig. 5, sampled planes are the same with velocity vector diagrams of Fig. 3..

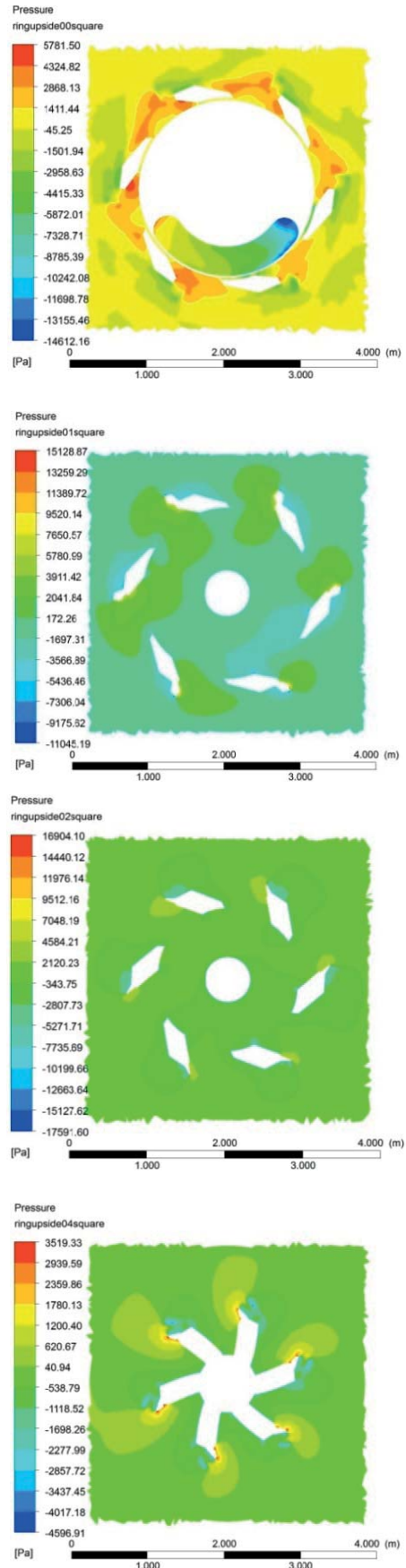


Fig. 5. Radial Pressure Contours

From the pressure contour of the plane of $h=0\text{m}$, in the suction inlet the pressure of the right region is less than that of the left, and the reason is that when the fluid particles are approaching to the suction inlet in a spiral way velocity increases and the pressure decreases, and the cutting system's geometry leads to the uneven pressure distribution, part fluid of the left is blocked and its pressure is greater than that of the right. On the pressure contours of the planes of $h=0.45\text{m}$, 0.7m , the pressure in the outer region of each cutter arm increases, this is because the fluid flows toward the suction inlet by pump suction effect and collides with cutter arm leading to velocity decrease as well as the pressure rise, so the cutter arm strength of these positions should be especially strengthened. On the planes of $h=0.45\text{m}$, 0.7m , pressure of the region near the suction inlet in the cutter is relatively lower for the velocity increases and the pressure decreases because of suction effect of suction inlet. And on the plane of $h=1.6\text{m}$ a slightly high pressure region near the outer side of the cutter can be observed, and the reason lies in that some fluid particles strike the arm leading to velocity decrease and pressure increase.

PARTICLE TRAJECTORY ANALYSIS

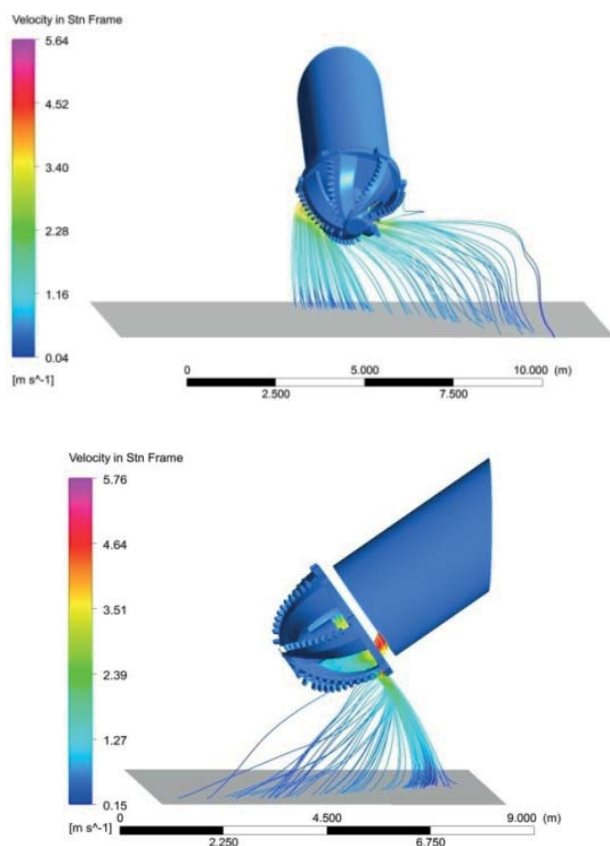


Fig.6. Particle Trajectory Colored by Velocity

Under the simulating operational conditions some of the dredged particles are approaching and entering the suction inlet, while the others are rotating outward of the cutter

and captured by the computing domain boundaries. The residential time and diameter distribution of the source particles can be tracked based on DPM model. From Fig. 6, it can be observed the number and residence time of particles depend on the cutter speeds and the inlet suction velocity. The velocities of the particles near the cutter outside and in the suction pipe are higher than those of other places.

INFLUENCE ANALYSIS OF OPERATIONAL PARAMETERS

SUCTION VELOCITY INFLUENCE ON SUCTION EFFICIENCY

With the same cutter rotation speed and swing speed the solid-fluid 2-phase-flow with suction flow velocities of 1.5m/s , 2.0m/s , 2.5m/s , 3.0m/s , 3.5m/s is simulated and compared. The variations of velocity at L1-L5 in suction inlet channel under different suction velocities are shown in Fig. 7. It demonstrates that under the same cutter rotation speed and swing speed, increasing suction flow velocity will result in nearly linear increase of the sampled locations' velocities. For suction velocity is directly determined by the pump driving power, and the pump energy consumption accounts for a large proportion of the total energy consumption during dredging, so setting a reasonable suction velocity should balance the pumping effect and the energy consumption.

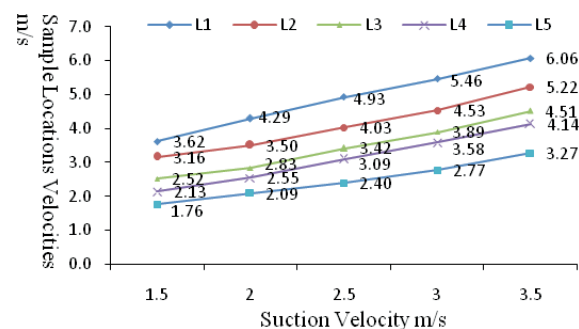


Fig. 7. Velocities of Sample Points under Different Suction Velocities

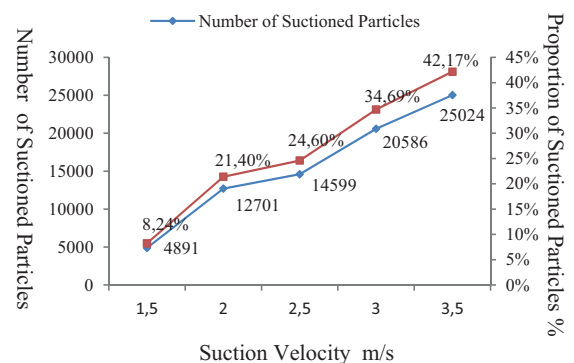


Fig. 8. Suctioned Particles Numbers with Different Suction Velocities

In this study, the number and the proportion of the suctioned particles per unit time are calculated to analyze the suction characteristics influence to the suction efficiency. Fig. 8 shows that the higher the suction flow velocity is, the more influence of the pressure difference force has and the higher the suction efficiency is.

CUTTER ROTATING SPEED INFLUENCE ON THE SUCTION EFFICIENCY

The number and the proportion of the suctioned particles per unit time are counted to analyze the cutter rotating speed influence to the suction efficiency. Fig. 8 shows that the higher the cutter rotating speed is, the greater influence of the particle's centrifugal movement is, and the lower efficiency the cutting system reaches. But when cutter rotating speed is up to 60 rpm, part particles rotate around and cross the hub and arrive the suction inlet, so the suctioned particles is 0.78% more than those of 50 rpm.

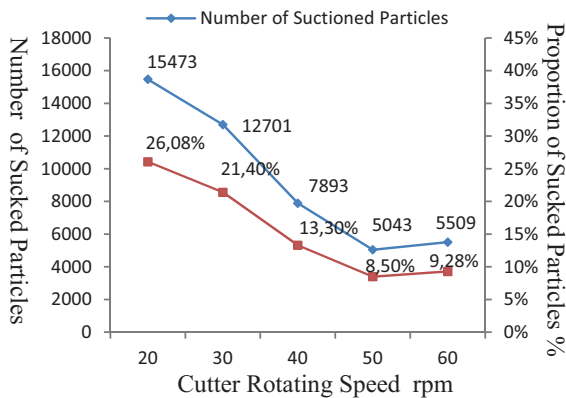


Fig. 8. Suctioned Particles Numbers with Different Cutter Rotating Speeds

CONCLUSIONS

With typical cutter rotating speeds, swing speeds and suction velocities, standard $k-\epsilon$ model and Multiple Reference Frame model are introduced to simulate the fluid flow field of the cutting system for the cutter suction dredger. Then DPM model is applied to compute the solid phase movement equation by two-way coupling interaction between particles and fluid. The main conclusions are drawn as follows:

- (1) in condition of low concentration of the solid phase, the DPM model is able to simulate the particle trajectory for cutting system of CSD.
- (2) in the fluid flow field velocity vector and pressure distribution on different planes show different characteristics.
- (3) the suction velocity of the suction inlet and the cutter rotating speeds have great influence on the flow field characteristics of cutting system of the CSD, higher suction velocity and lower cutter rotating speed will suction more particles into the suction inlet.

ACKNOWLEDGMENT

The research has been supported by the National Natural Science Foundation of China (No. 51179144 and No. 51679178).

BIBLIOGRAPHY

1. Tang Jianzhong: Research on Optimization and Control of Dredging Operations for Cutter Suction Dredgers. Hangzhou: Zhejiang University, pp.1-3, 2007
2. Yaling Li, Shouqi Yuan, Yue Tang, Ping Huang, Xiaojun Li: Discrete Phase Model Simulation of Tracer Particle Motion in Centrifugal Pump. Chinese Journal of Agricultural Machinery, Vol.143, no.11, pp.113-115, 2012
3. Li Dan, Ma Guiyang, Du Mingjun, Wang Haifeng: Numerical Simulation for Particles Track in a Cyclone Separator Based on the DPM. Journal of Liaoning Shihua University, Vol. 31, no.2, pp.37-38, 2011
4. Liu Juan, Xu Hongyuan, Tang Shu, Lu Li: Numerical Simulation of Erosion and Particle Motion Trajectory in Centrifugal Pump. Chinese Journal of Agricultural Machinery, Vol. 6, no. 2, pp.54-59, 2008
5. Zhang Tao, Li Hongwen: Simulation Optimization of DPM on Gas-Solid Two-Phase Flow in Complex Pipeline Flow Field. Journal of Tianjin University (Science and Technology). Vol.48, no. 1, pp.39-46, 2015
6. Xu Yanxia, Song Xingfu, Tang Bo, Wang Jin, Yu Jianguo: Analysis Structural Parameters of Hydrocyclone used in Ballast Water on its Performances. Chemical Industry and Engineering Progress. Vol.36, Sup. 2, pp.81-85, 2016
7. M. A. Dekker, N. P. Kruyt, M. den Burger, W. J. Vlasblom: Experimental and Numerical Investigation of Cutter Head Dredging Flow. Journal of Waterway, Port, Coastal and Ocean Engineering. Vol. 129, no 5, pp.203-209, 2003
8. Fang Yuan, Ni Fusheng: Numerical Simulation of 2-D Water Flow in and around Cutter of a Dredger. China Harbour Engineering. Vol. 173, no. 2, pp.4-5, 2011
9. Marzio Piller, Enrico Nobile, Thomas. J: DNS Study of Turbulent Transport at Low Prandtl Numbers in a Channel Flow. Journal of Fluent Mechanics, Vol.458, pp.419-441, 2002
10. Min Zhang, Shidong Fan, Haoyu Zhang: Flow Field Analysis of Cutter Head for Cutter Suction Dredgers. Proceedings of 2016 International Conference on Human-centered Computing, Sri Lanka, pp.578-579, 2016
11. Xia Mi, Li Yi, Li Fengqin: Numerical Simulation of Solid Phase Movement and Distribution in the Solid-liquid Two

Phase Flow Centrifugal Pump. Journal of Mechanical and Electrical Engineering. Vol. 32, no. 12 ,pp.1555-1557, 2015

12. Vakamalla Teja Reddy, Vadlakonda Balraju, Aketi V. Asha Kumari, Mangadoddy Narasimha: Multiphase CFD Modeling of Mineral Separators Performance: Validation Against Tomography Data. Transactions of the Indian Institute Of Met-als.Vol.70, no.2 ,pp.323-340, 2016
13. Yi Li: The Research on Numerical Simulation and Abrasion Property of Solid-liquid Two-phase-flow Centrifugal Pump. Hangzhou: Zhejiang Sci-tech University, pp.20-21, 2014
14. Zhang Tao, Yang Chenjun, Song Baowei: Investigations on the Numerical Simulation Method for the Open-water Performance of Contra-rotating Propellers based on the MRF Model. Journal of Ship Mechanics. Vol. 14, no. 8, pp.848-849, 2010

CONTACT WITH THE AUTHORS

Shidong Fan, Professor, Ph.D.

e-mail: fsd1963@263.net

Min Zhang, Ph.D.

e-mail: zhm@whut.edu.cn

School of Energy and Power Engineering
Wuhan University of Technology
Heping Avenue No 1178
Wuhan 430063, Hubei
CHINA

IDENTIFICATION OF SONAR DETECTION SIGNAL BASED ON FRACTIONAL FOURIER TRANSFORM

Wang Biao^{1,2}

Tang Jiansheng²

Yu Fujian²

Zhu Zhiyu¹

¹ School of Electronic and Information, Jiangsu University of Science and Technology, Zhenjiang, Jiangsu Prov., China

² Key Laboratory of Underwater Acoustic Warfare Technology, Beijing, China

ABSTRACT

Aiming at the source of underwater acoustic emission, in order to identify the enemy emission sonar source accurately. Using the digital watermarking technology and combining with the good time-frequency characteristics of fractional Fourier transform (FRFT), this paper proposes a sonar watermarking method based on fractional Fourier transform. The digital watermark embedding in the fractional Fourier transform domain and combined with the coefficient properties of the sonar signal in the fractional Fourier transform to select the appropriate watermark position. Using the different characteristics of the signals before and after embedding, an adaptive threshold was set for the watermark detection to realize the discrimination of sonar signals. The simulation results show the feasibility and has better resolution and large watermark capacity of this method, while the robustness of the watermark is better, and the detection precision is further improved.

Keywords: Fractional Fourier transform, Watermark, Sonar

INTRODUCTION

At present sonar is the main equipment of ocean exploration and target detection, with the increasing frequency of marine activities, underwater sources are filled with various sources of acoustic emission from unknown sources. These sonar source emit various signals, however, these signals are highly similar, resulting in the inability to identify their source, the importance of information security has become a key issue in underwater activities.

The latest method of the current sonar signal identification is based on the digital watermarking signal identification, by detecting whether the received signal contains a watermark to identify its identity. Mobasser B G and Lynch R S et al. proposed watermark embedding using short-time Fourier transform (STFT) and discrete cosine transform (DCT) for the identification of active sonar signals in 2008 and 2010 respectively. But the algorithm is more complex and does not fully consider the multiplicity, attenuation and Doppler shift of ocean channel. In 2011, the effect of channel-related

features on the performance of watermarking and the use of embedded watermarks to improve detection performance were proposed. In the identification of sonar signals has been studied in the algorithm, although channel attenuation and Doppler have been taken into account, but the influence of the pulse interference on the detection between the embedded watermark is still not improved, the robustness of the watermark in the channel is poor and also seriously affects identification accuracy. Visibility detection accuracy and robustness of watermark the improvement of these two aspects has the very important significance for the identification of sonar signal, this paper examines these two aspects. And found that the fractional Fourier transform (FRFT) has good time-frequency characteristics, based on this foundation, proposes a digital watermarking sonar identification algorithm based on FRFT.

The fractional Fourier transform can be regarded as a generalized form of the Fourier transform. In recent years, it has received extensive attention in signal processing, which combines the characteristics of the signal in the time domain

and frequency domain. Application of this method first appeared in the digital image watermarking, and has a good effect, the literature [5][6] is the application of watermark in image. In this article, the watermark is embedded into the sonar signal by fractional Fourier transform and the power of the FRFT (Frequency Fractional Fourier Transform) is taken as the degree of freedom in the watermark embedding. At the same time, it is also used as an embedded key, which not only enhances the security of the watermark but also increases the robustness of the watermark.

PRINCIPLE OF DIGITAL WATERMARK EMBEDDING BASED ON FRFT

THEORETICAL BASIS

FRFT as a generalized form of the Fourier transform, It can be interpreted as the representation of the signal in the fractional Fourier transform domain after the signal is rotated by any angle counterclockwise around the origin in the time-frequency plane. If Fourier transform of signal can be seen as a representation of counterclockwise rotation of $\pi / 2$ on the time axis to the frequency axis, then FRFT can be regarded as a representation of the signal on the time by axis counterclockwise rotation of the angle α to the μ axis (μ axis is called fractional Fourier domain), $x(t)$ of the signal the fractional Fourier transform (FRFT) is defined as:

$$X_{\alpha}(u) = \{F^{\alpha}[X(t)]\}(u) = \int_{-\infty}^{+\infty} X(t)K_{\alpha}(t, u)dt \quad (1)$$

Where FRFT transform kernel $K_{\alpha}(t, u)$ is:

$$K_{\alpha}(t, u) = \begin{cases} \sqrt{\frac{1-j\cot(\alpha)}{2\pi}} \exp(j\frac{t^2+u^2}{2} \times \cot(\alpha) - tu \csc(\alpha)) & \alpha \neq n\pi \\ \delta(t-u) & \alpha = 2n\pi \\ \delta(t+u) & \alpha = (2n+1)\pi \end{cases} \quad (2)$$

Formula: $\alpha = p, \pi / 2$ is the rotation angle of FRFT; F^{α} is the alpha Order Fractional Fourier operator symbol. The inverse transformation is:

$$x(t) = \int_{-\infty}^{+\infty} X_{\alpha}(u)K_{\alpha}(t, u)dt \quad (3)$$

When the $p=1$ ($\alpha=\pi / 2$), the FRFT degenerate to the traditional Fourier transform, when the transformation order is close to 1, the response is the frequency domain characteristic. When the transformation order is close to 0, the response is the time domain characteristic.

The so-called decomposition method is based on FRFT (Fractional Fourier transform) expression. FRFT is decomposed into the convolution form of the signal, which uses FFT to calculate FRFT. In this paper, we use the fast decomposition algorithm proposed by Bultheel A et al, which is very suitable for FRFT numerical calculation of the signal. However, the operation mechanism of this fast algorithm determines that the original signal must be normalized by dimension localization before the FRFT numerical calculation. The discrete fractional Fourier transform using dimension normalization is defined as: the time interval of the signal is $[-\Delta t / 2 \Delta t / 2]$, frequency range is $[-\Delta f / 2 \Delta f / 2]$, the time bandwidth product of the signal is $N = \Delta t \Delta f$, the scale factor of the normalized introduced dimension is S:

$$\Delta x = \sqrt{\Delta t \Delta f} \quad x = t / s \quad v = fxS \quad (4)$$

Then the interval can be normalized to $[-\Delta x / 2 \Delta x / 2]$, After normalized sampling interval $1 / \Delta x, N = \Delta x^2$.

The fractional Fourier transform can be rewritten as:

$$X_p(u) = A_{\alpha} \exp[j\pi u^2 \cot \alpha] \int_{-\infty}^{+\infty} x(t) \exp[j\pi t^2 \cot \alpha] \exp[-j2\pi ut \csc \alpha] dt \quad (5)$$

Among $0 < |\alpha| < \pi$

$$A^{\alpha} = \exp[j(P-1)\pi / 4] / \sqrt{|\sin \alpha|}, \alpha = P\pi / 2$$

By the above formula Fractional Fourier transform can be divided into:

- (1) The multiplication of the signal with the linear frequency modulation function
- (2) Fourier transform (the argument is multiplied by the scale factor $\csc \alpha$)
- (3) Multiplication with linear frequency modulation function
- (4) Multiplied by a complex factor

Finally, the normalized expression is:

$$\begin{aligned} &= \frac{A_{\alpha}}{2\Delta x} \left[\exp\left\{-\frac{j\pi \tan \frac{\alpha}{2} m^2}{(2\Delta x)^2}\right\} X \right. \\ &\times \sum_{n=-N}^{n=N} \exp\left[\frac{j\pi(\csc \alpha)(m-n)^2}{(2\Delta x)^2}\right] \\ &\times \left. \left[\exp\left\{-\frac{j\pi \tan \frac{\alpha}{2} m^2}{(2\Delta x)^2}\right\} x\left(\frac{n}{2\Delta x}\right) \right] \right. \\ X_p\left(\frac{m}{2\Delta x}\right) &= \frac{A_{\alpha}}{2\Delta x} \sum_{n=-N}^N \exp\left[\frac{j\pi(\cot \alpha)m^2}{(2\Delta x)^2} - \frac{j2\pi(\csc \alpha)mn}{(2\Delta x)^2}\right. \\ &\left. + \frac{j\pi(\cot \alpha)n^2}{(2\Delta x)^2}\right] x\left(\frac{n}{2\Delta x}\right) \quad (6) \end{aligned}$$

In the specific calculation, the signal sample is firstly interpolated twice, and after the calculation of the above

equation (6), the N sample values of the fractional Fourier transform are obtained by interpolating the result by twice times, although the value of p is 0.5 to 1.5, but using the periodic and additive of the fractional Fourier transform can be generalized to all the order of the fractional Fourier transform.

SONAR DIGITAL WATERMARK EMBEDDING SYSTEM

The FRFT coefficients are modified by embedding robust watermarks in the Fractional Fourier transform domain of the signal, the source of the robust watermark is mainly Gaussian random sequence, which combines the signal with the coefficients characteristics of the fractional Fourier transform, select the appropriate watermark position, by calculating the detection statistics to detect.

WATERMARK GENERATION

The selection of watermark sequences generally requires good autocorrelation characteristics, Gaussian sequence satisfy this requirement and its autocorrelation function has the characteristics of impulse function. The watermarking composed of random sequences of Gaussian distributions has good robustness. Gaussian noise has the characteristics of uniform energy and strong correlation. Studies have shown that the using a random sequences as a watermark for embedding does not affect the overall performance of the signal. If there is an obvious peak at a certain offset at the time of detection, and the threshold is exceeded, so indicate the watermark exists. The robustness of the watermark can be changed by changing the set threshold, this method is more prominent robustness than other watermarking methods, and detection algorithm is also relatively simple. Therefore, the use of random sequences as a watermark sequence is a better choice. In this paper, a complex random sequence is generated. The combination of two Gaussian random sequences is a complex random sequence, which produces a Gaussian sequence with mean 0 and variance of 1, the length is M , $R1$ and $R2$, which form a complex random sequence $W = R1 + jR2$. This Gaussian sequence is generated by the key control, it can be through the pseudo-noise generator, select a specific seed as a key to increase the security of the watermark, this paper uses a four-digit as a "seed".

WATERMARK EMBEDDING ALGORITHM

Preprocessing is carried out before the carrier signal is embedded in the watermark. Firstly, the sonar waveform $x(t)$ is sampled to obtain the discrete points, and the sampling points are discrete values of N to produce the discrete signal X :

$$X = \{x(n), n = 1, 2, \dots, N\} \quad (7)$$

Using the pseudo-noise generator to produce two lengths are M , respectively subject to $(0, \sigma_1)$ and $(0, \sigma_2)$ random sequences $R1$ and $R2$, to form a complex random sequence $W = R1 + jR2$. This article $\sigma_1 = \sigma_2 = 1$

The discrete signal X is decomposed by fractional discrete Fourier transform, the degree of freedom is p , and the choice of degree of freedom is based on the range of $[0, 1]$, get the fractional Fourier transform coefficients $S_i, i = 1, \dots, N$. The embedding position is selected according to the obtained fractional Fourier transform coefficient feature, and the watermark embedding selection is close to the position of the instantaneous frequency band IF (IF refers to the region of the energy distribution of the signal in the corresponding frequency domain), due to the fractional Fourier transform will occur in the rotation of the domain, so it is generally chosen to be embedded in the middle of the fractional Fourier transform. According to the additive rule, the fractional Fourier transform coefficients of the watermark can be obtained:

$$S_i^w = S_i + aW = a(R1 + jR2), i = L + 1, \dots, L + M \quad (8)$$

The embedding strength is a .

After the embedding, the fractional Fourier transform with the degree of freedom of $-p$ is used to obtain the signal after the watermark.

WATERMARK EMBEDDING CRITERION

The watermark sonar does not affect the continuity and bandwidth of the sonar signal, if the embedded watermark brings unexpected energy beyond the sonar itself is undesirable, the watermarked sonar energy is expressed by the following expression:

$$E_{sw} = \int x^2(t)dt + k^2 \int w^2(t)dt + k \int x(t)w(t)dt \quad (9)$$

The watermark strength is K .

It can be seen from the expression that the embedding watermark is attached to add energy for the non-watermarked sonar, in which the SWR (signal watermark ratio) of the embedding intensity is in the range of 15dB ~ 25dB, the SNR in the simulation environment is 10dB ~ 15dB, SWR is at least 15dB, its energy is lower than the background noise, and the watermark and the sonar are irrelevant, so the embedded watermark energy has no real effect on the sonar.

The watermark embedding is also constrained by the distribution of watermark energy, the watermark embedding is mainly to improve the accuracy of the sound source identification. Signal in the time-frequency domain, the watermark can be embedded in the instantaneous frequency domain, the distribution of the instantaneous frequency domain of the LMF signal exhibits a linear characteristic, The watermark can also be embedded outside the instantaneous frequency domain, but within the time-frequency domain, the watermark is embedded in the instantaneous frequency domain, which can be effectively hidden below the instantaneous frequency domain, but requires a smaller SWR (strong watermark) for detection, embedded outside the instantaneous frequency domain if the same test results need to achieve higher SWR, watermark is relatively weak.

WATERMARK DETECTION METHOD

The algorithm used in this paper is a fast decomposition algorithm proposed by Bultheel A et al, using this algorithm for FRFT numerical calculation will produce a certain amount of error. In order to carry out effective detection, select the appropriate detection statistics, watermark detection by calculating the detection of statistical d and with a predetermined threshold to complete. The test statistic d is calculated by the following equation:

$$\begin{aligned} d &= \sum_{i=L+1}^{i=L+M} [R1_i - jR2_i] S_i^{(a)} \\ &= \sum_{i=L+1}^{i=L+M} [R1_i - jR2_i] [S_i + a(R1_i + R2_i)] \\ &= a \sum_{i=L+1}^{i=L+M} [R1_i^2 + R2_i^2] + \sum_{i=L+1}^{i=L+M} [S_i R1_i - jS_i R2_i] \end{aligned} \quad (10)$$

$S_i^{(a)}$ indicate the FRFT coefficients of the watermarked signal may have been attacked. The attack mainly comes from the underwater noise, the simulation environment parameters can be seen in Table 1. Assuming that the watermarked signal is not attacked, since the mean values of $R1$ and $R2$ are zero and the variance respectively are σ_1, σ_2 , the mean value of the signal detection statistic d embedded in the watermark is:

$$E(d) = aM(\sigma_1^2 + \sigma_2^2) \quad (11)$$

For no embedded watermark signal, so:

$$E(d) = 0 \quad (12)$$

In both cases, the variance of d is the same, that is, the number M of FRFT coefficients of usually embedded in the watermark is very large (up to several hundred). Therefore, the value of $|d|$ will vary greatly between watermarked and non-watermarked cases, this method can detect watermarks well when the appropriate threshold is set. In view of the fact that FRFT inevitably brings some error to the coefficients, the actual value of $|d|$ is smaller than the theoretical value, and the errors caused by different transformation angles are different. According to experience, in the application, the threshold is slightly less than $|d|/2$, the simulation results also verify its effectiveness.

SIMULATION ANALYSIS

The simulation of this paper is carried out in the simulation environment as shown in Table 1, mainly through the watermark is tested primarily by the response of different watermark sequences and different transform order detectors, and the response curves under different SNR (signal noise ratio) are analyzed when the transform order is the same. This paper also analyzes the embedding strength and embedded

watermark ratio of two relevant variables of watermark capacity.

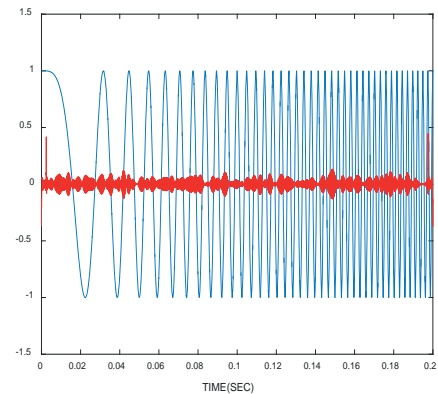
First, explain the SWR that appears in the simulation:

$$SWR = 10 \lg \frac{\text{carrier signal power}}{\text{embedding watermark power}}$$

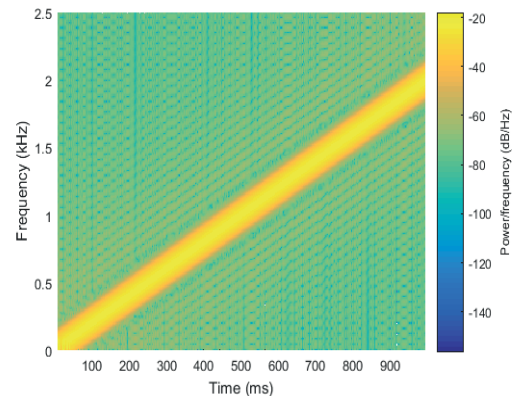
Tab. 1. Simulation parameters

Parameter name	Value
Seawater depth	200m
Transmitter / receiver depth	50m
Transmitter/ receiver horizontal distance	2000m
Channel type	Rice channel
Multi-way gain	-60dB,-65dB,-70dB
Multi-way delay	1.333(0s), 1.334(0.001s), 1.34(0.01s)
Doppler frequency shift	0Hz, 10Hz
Carrier signal waveform	Linear frequency modulation signal, time width 1s, bandwidth 2kHz

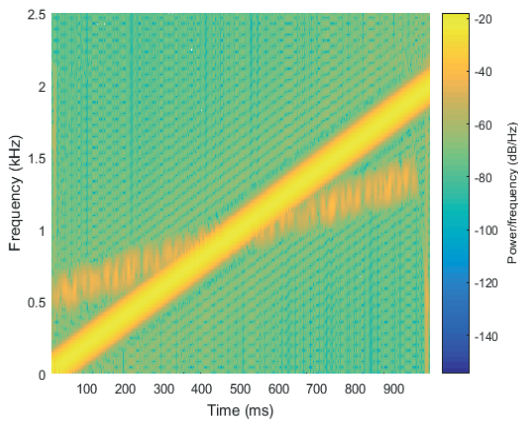
SIGNAL TIME-FREQUENCY DIAGRAM



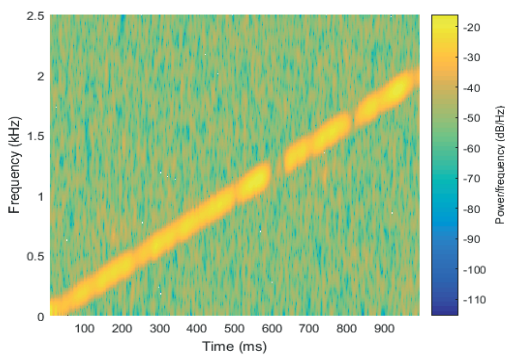
Signal plus watermark time domain diagram (a)



The original signal time-frequency diagram (b)



Embedded watermark (SWR = 15dB) time-frequency diagram (c)



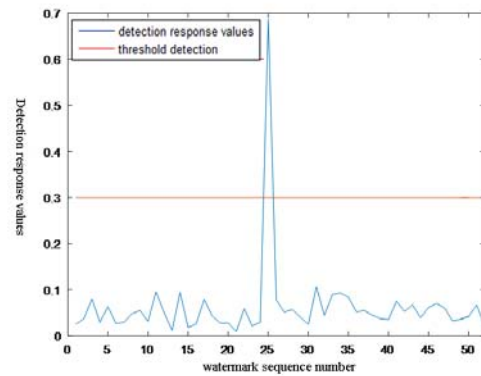
Embedded watermark plus noise (SNR = 10dB) time-frequency diagram (d)

Fig.1 Time frequency diagram

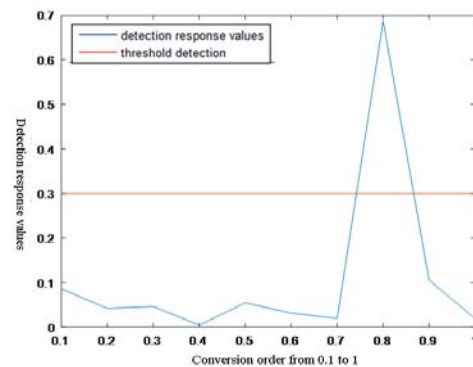
As the simulation analysis of time-frequency diagram, figure 1 (a) is a signal and watermark time-domain diagram when the number of transformations is 0.8 and the embedding intensity is 0.3. Figure 1 (b) is the original carrier time-frequency diagram, compared with Figure 1 (c) and Figure 1 (d) show that the watermark is hidden by the noise is invisible, Figure 1 (c) can be seen in the watermark embedded near Instantaneous frequency bandwidth, instantaneous frequency (IF) bandwidth is the signal exists in the time-frequency domain distribution range, through the above four graphs, it can be seen that the time-frequency characteristic of the LFM signal is not affected by the watermark.

WATERMARK CAPACITY

According to the above parameters, the detection threshold of this paper is according to the modulus of the embedded watermark detection statistic d to selected, and the detection threshold is set to 0.3. In the simulation, 51 Gaussian random sequences are used, the 25th watermark sequence is the watermark embedded in this paper. The rest of the sequence generation keys are different from the correct watermark, and the different transformation orders are also tested, the simulation results are shown in the following figures:



The response value of different watermark sequences (a)



Detector response value of different order of transformation (b)

Fig.2 Detection of different watermark sequence and order

From Figure 2 (a) and Figure 2 (b), it can be seen that the watermark is only detected when the watermark number is 25, and the watermark is detected only under the correct condition of the conversion order, the watermark sequence based on the “seed” adds another key transform order, increase the security of the watermark.

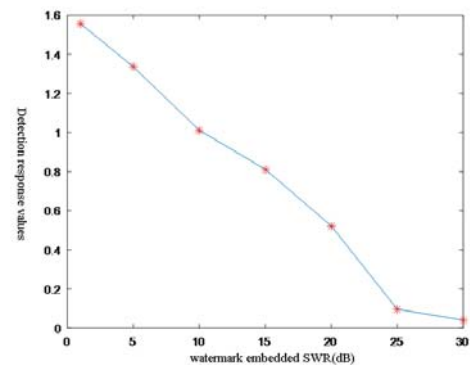


Fig.3 Detector response of different SWR

Tab. 2. Contrast data of embedding strength and swr

embedding strength K	0.07	0.1275	0.2267	0.4	0.7	1.275	2.02
SWR (dB)	30	25	20	15	10	5	1

It can be obtained from Fig. 3 that when the watermark embedding intensity is larger, through the calculation of the embedding strength is 3.03, the SWR tends to value of 0, has reached the limit value. When the watermark strength is 0.1, the SWR value reached 30, but at this time the detection response value has been lower than the detection threshold, if the embedding strength is low will appear false alarm. The above can be obtained in the SWR 10dB to 18dB is more appropriate, when the SWR is too small, as shown in Figure 1 (a) for the watermark embedded strength of 0.5 signal and watermark time domain map. The embedded watermark is Gauss sequence, it can be seen from the formula (10) that the length of the watermark sequence has a certain influence on the response value of the detector. When the length of the watermark is changed, the response value changes as follows:

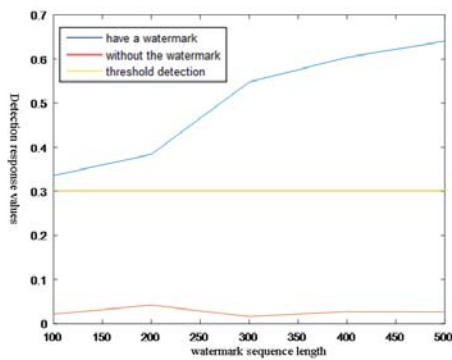
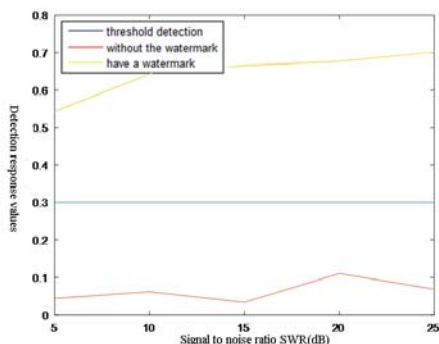


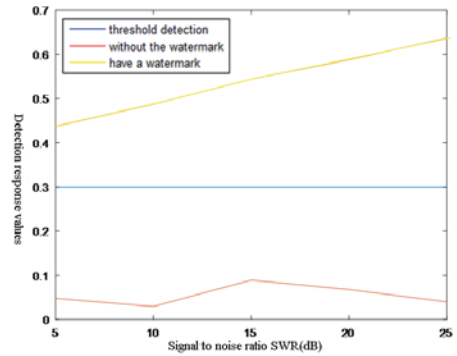
Fig.4 Detector response of different watermark length

As shown in the above figure, the results are in accordance with the theoretical results of (10), and the watermark embedding length is 400. If the length of the watermark sequence is too large, it will have an impact on the signal itself. Figure 4 and Figure 3 have the same principle, Figure 4 shows that when the transform order is fixed, the embedded strength K is constant, with the increase of the embedded sequence, the watermark SWR is decreasing, and at the same time it is consistent with Figure 3, Figure 4 is mainly used to select the appropriate sequence length.

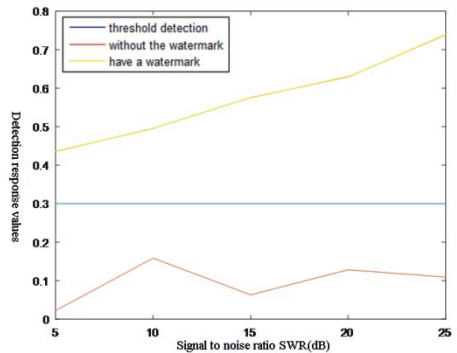
SELECTION OF P ORDER AND ANALYSIS OF WATERMARK ROBUSTNESS



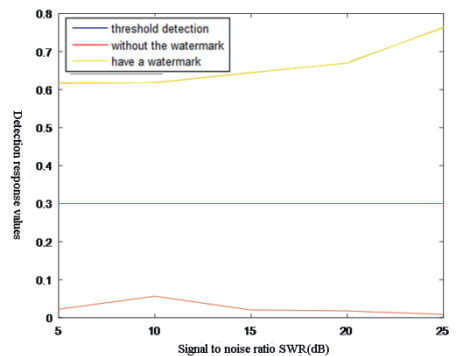
Conversion order $P = 0.2$ (a)



Conversion order $P = 0.4$ (b)



Conversion order $P = 0.6$ (c)



Conversion order $P = 0.8$ (d)

Fig.5 Response of signal to noise ratio detectors with different transform orders

In the above figures (a) to (d), the signal noise ratio varies from 5 dB to 25 dB, and the conversion order p is 0.2, 0.4, 0.6, 0.8. Figure 5, adding noise are different variance and mean of 0 Gaussian noise, can be seen from the figure with the increase of signal noise ratio, the detection response value is getting bigger and bigger, when the signal noise ratio is small, if the selected order is also relatively small, the detection response is close to the threshold as shown in Fig. 5 (a). According to the transform order, when the transform order is chosen to be 0.8, the detection response value produces a large difference, which is easily distinguishable from the watermark detection value, and the false alarm probability. The watermark in different transform orders to add Gaussian

noise, with the increase of Gaussian noise variance, the watermark detection response value is close to the detection threshold, but there is no false alarm. According to Figure 5 (a) to Figure 5 (d), even if the SNR value is 5dB, the detection response is still greater than the threshold which we set, so the probability of false alarm is very low, and the threshold selection of appropriate circumstances can strictly control the occurrence of false alarm situation. So it shows the superiority in the detection, which can be obtained in the given SNR case, in order to achieve better detection efficiency to select the appropriate threshold and the transformation order can be achieved, the detection threshold chosen by this method is high, It can be seen that the identification method can obtain high detection accuracy in the watermark with higher watermark robustness.

Through the above simulation analysis shows that when the conversion order and watermark related parameters are not known, it is basically impossible to detect whether it contains watermarks to identify the signal, strong robustness makes it difficult to destroy already embedded watermarks by setting different parameters. Therefore, the security of this method in sonar signal authentication is guaranteed, and the robustness is further improved.

CONCLUSION

This article using the fractional Fourier transform (FRFT) as a tool, utilizing all the features that gradually transform the signal from the time domain to the frequency domain as the transform order increases, and uses the good time-frequency domain characteristics of the fractional Fourier transform to design a sonar identification method based on FRFT. The watermark is embedded into the FRFT domain of the signal, the watermark embedding of different transform orders and complex random sequences improves the security and robustness of the algorithm. Through the robustness of the algorithm, the watermark capacity, and the selection of the transformation order are analyzed. The experimental results show that the sonar signal identification based on FRFT digital watermarking algorithm has better robustness and detection efficiency than other algorithms.

ACKNOWLEDGEMENTS

The authors acknowledge the National Natural Science Foundation of China (Grant: 11574120,U1636117), the Natural Science Foundation of Jiangsu province of China (Grant: BK20161359), the Open Project Program of the Key Laboratory of Underwater Acoustic Signal Processing, Ministry of Education, China (UASP1503), Six Talent Peaks project of Jiangsu Province and Foundation of Key Lab of Intelligent Ocean Information Perception and Transmission Technology.

REFERENCES

1. JinCong, Digital Watermarking Theory and Technology. [M]. Beijing Tsinghua University press, 2008
2. Mobasseri B G, Lynch R S, Carter G C. Information Embedding in Sonar for Authentication and Identification[J]. IEEE Aerospace Conference Proceedings, 2008:1-5.
3. [3] Mobasseri B G, Lynch R S. Sonar authentication performance evaluation under realistically simulated undersea channels[J]. Proceedings of SPIE - The International Society for Optical Engineering, 2010, 7678:76780R-76780R-10.
4. Mobasseri B G, Lynch R S, Chakilam N. Watermarking sonar waveforms using knowledge of channel coherence[C]// Oceans. IEEE, 2010:1-8.
5. PING Xian-jun Tao-ran ZHOU Si-yong. A new fast algorithm of fractional Fourier transform [J]. Electronic journal, 2001, 29 (3): 406-408
6. Wang Juan-feng. Research on digital watermarking algorithm based on fractional Fourier domain image features.[D] Zhengzhou University, 2007
7. Bultheel A, Sulbaran H E M. Computation of the fractional Fourier transform[J]. Applied & Computational Harmonic Analysis, 2004, 16(3):182-202.
8. Cheng Xue. Digital watermarking technology based on fractional Fourier transform [D]. Nanjing University of Science and Technology, 2009
9. Pei S C, Ding J J. Fractional Fourier transform, wigner distribution, and filter design for stationary and nonstationary random processes[J]. Signal Processing IEEE Transactions on, 2010, 58(8):4079-4092.
10. Zhu Jian-dong, Zhao Yong-jun, Tang-Jiang. Detection and estimation of linear frequency modulated continuous wave signal in periodic fractional Fourier transform [J]. Journal of electronic and information science, 2013, 35 (8): 1827-1833.

CONTACT WITH THE AUTHORS

Wang Biao, Ph.D.

e-mail: wangbiao@just.edu.cn

Faculty of School of Electronic and Information
Jiangsu University of Science and Technology
Zhenjiang, Jiangsu, 212003
CHINA

QUANTITATIVE ANALYSIS OF THE RELATIONSHIP BETWEEN SHEAR STRENGTH AND FRACTAL DIMENSION OF SOLIDIFIED DREDGER FILL WITH DIFFERENT FLY ASH CONTENT UNDER MONOTONIC SHEAR

Yang Shuai¹

Liu Wenbai²

Liu Hongwei³

¹ Master, School of Ocean Science and Engineering, Shanghai Maritime University

² Professor, School of Ocean Science and Engineering, Shanghai Maritime University

³ Master, School of Ocean Science and Engineering, Shanghai Maritime University

ABSTRACT

The dredger fill of Shanghai Hengsha Island Dongtan is solidified by curing agents with different fly ash content, and the shear strength index of solidified dredger fill is measured by the direct shear test. The microscopic images of solidified dredger fill are obtained by using SEM. The microscopic images are processed and analyzed by using IPP, and the fractal dimension including particle size fractal dimension D_{ps} , aperture fractal dimension D_{bs} and particle surface fractal dimension D_{pr} is calculated by fractal theory. The quantitative analysis of the relationship between shear strength index and fractal dimension of solidified dredger fill is done. The research results show that the internal friction angle and the cohesion are closely related to the fly ash content λ and the curing period T , and the addition of fly ash can improve the effect of curing agent; There is no obvious linear relationship between the internal friction angle and the three fractal dimensions; The smaller particle surface fractal dimension D_{pr} and particle size fractal dimension D_{ps} , the larger aperture fractal dimension D_{bs} , the greater the cohesion, and the cohesion has a good linear relationship with three fractal dimensions, and the correlation coefficient R^2 is above 0.91.

Keywords: curing agent, fly ash, shear strength, fractal dimension, SEM

INTRODUCTION

The rapid development of China's coastal economy has promoted port construction and channel dredging, resulting in a lot of dredger fill. Due to the high water content of dredger fill, the engineering properties are very poor. Mixing the curing agent in dredger fill can improve the engineering performance in a short time. The addition of fly ash can effectively improve the effect of the curing agent and reduce the cost of the curing agent, and can alleviate the pollution

of the fly ash to the environment, and play the role of waste utilization. In engineering application, the shear strength of soil is an important index. Many scholars have done a lot of research on the shear strength of solidified soil [2,3,5], and many valuable theoretical and application conclusions have been drawn. The microstructure of soil has certain self-similarity. The microstructure of solidified soil is analyzed by fractal theory [12]. Many scholars have made a lot of research on the microstructure of soil [1,4,6], including micro image processing, the extraction of microstructure parameters and the calculation method of fractal dimension, and so on.

TEST MATERIALS AND TEST METHODS

TEST MATERIALS

The dredger fill is from Hengsha Island of Shanghai. The physical indexes of the dredger fill are tested by the laboratory test and the data are shown in Tab.1. The curing agent used in the experiment is a mixture of various materials, which accounts for the main components of the material for cement and lime. The grade of fly ash used in the experiment is grade two, and its main components are shown in Tab.2.

Tab. 1. Physical indexes of the dredger fill

specific gravity	2.69
gravity kN/m ³	16.01
water content (%)	24
liquid limit	37
plastic limit	26
internal friction angle	7
cohesion (kPa)	0.826

Tab. 2. Main components of fly ash

component	content(%)
SiO ₂	90.7
Al ₂ O ₃	28.9
Fe ₂ O ₃	6.42
CaO	1.93
MgO	1.73
SO ₃	0.45
K ₂ O	0.59
Na ₂ O	0.48

TEST METHOD

In this experiment, the water content of the soil is 40%, and the sample is divided into five groups. One of the curing agent content is 4%, the other four groups of curing agent are 3%, and 0%, 2%, 4% and 8% fly ash respectively. The scheme of the proportioning in the test is shown in Tab.3. The high of cutting ring is 20 mm, the diameter of cutting ring is 61.8mm. Direct shear test and scanning electron microscope test were carried out for 14 days, 28 days, 42 days and 90 days respectively.

Tab. 3. The scheme of the proportioning in the test

test number	water content	curing agent	fly ash
1	40%	4%	0%
2	40%	3%	0%
3	40%	3%	2%
4	40%	3%	4%
5	40%	3%	8%

Scanning electron microscope test is done by field emission scanning electron microscope (ER-SEM) that made in Japan in the Analysis and Testing Center of Shanghai Jiao Tong University. The sample is dehydrated and dried by oven drying method, and then the sample is slowly cut out with a knife of 10 * 10 *20 mm, and the sample is carefully broken to reveal the fresh surface for observation.

The micro image of solidified dredger fill is processed and analyzed by using the image processing software. Main operating procedures include Image segmentation, image morphological processing, the calibration of the measuring unit, the selection of measurement parameters and data analysis and finishing. Cui Yongtao[1], Hang Li[4], Xu Riqing[10,11], Zhen Zhiheng[15] have done a detailed introduction, not tired in words here. The Microscopic image and binary image of solidified dredger fill is showed in Fig. 1.

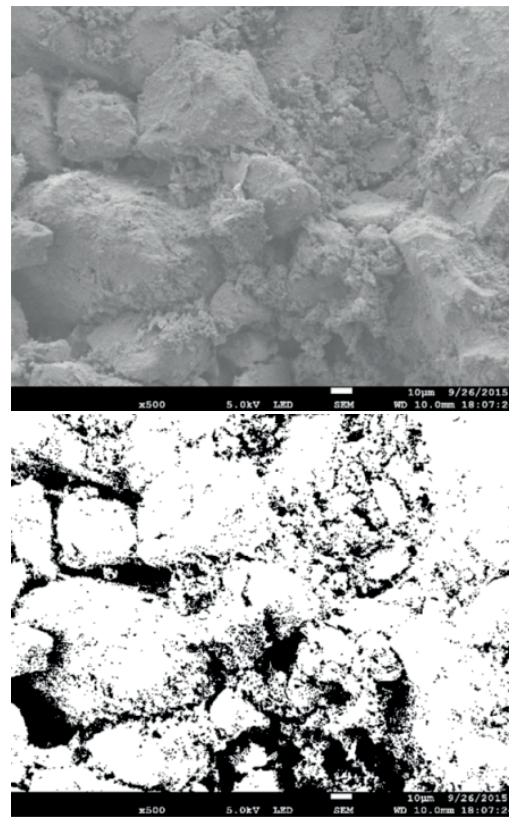


Fig. 1. Microscopic image and binary image of solidified dredger fill

FRactal THEORY

At present, fractal theory is applied to many parameters of soil microstructure, and different parameters reflect different structural characteristics. In view of the macroscopic mechanical properties of solidified dredger fill, three fractal dimensions are selected: particle surface fractal dimension D_{pr} , particle size fractal dimension D_{ps} and aperture fractal dimension D_{bs} .

PARTICLE SURFACE FRACTAL DIMENSION D_{pr}

Measuring the particle contour line of solidified dredger fill with length measuring ruler of ε , the number of required measuring ruler is $N(\varepsilon)$. By changing ε , the different $N(\varepsilon)$ can be obtained. A series of ε and $N(\varepsilon)$ as points are depicted on the double logarithmic coordinate diagram, and the negative value of the slope of the straight line fitting through these points is the particle surface fractal dimension.

$$D_{pr} = -\lim_{\varepsilon \rightarrow 0} \frac{\ln N(\varepsilon)}{\ln \varepsilon} \quad (2)$$

Where:

D_{pr} – particle surface fractal dimension
 ε – length of measuring ruler measuring the particle contour line of solidified dredger fill
 $N(\varepsilon)$ – number of measuring ruler

APERTURE FRACTAL DIMENSION D_{bs} AND PARTICLE SIZE FRACTAL DIMENSION D_{ps}

The number of aperture which is larger than r is $N(\geq r)$, r values will be changed, and a series of $N(\geq r)$ will be obtained. $N(\geq r)$ and r are depicted on the double logarithmic coordinate diagram. The negative value of the slope of the straight line fitting through these points is the aperture fractal dimension.

$$D_{bs} = \frac{-\ln N(\geq r)}{r} \quad (3)$$

Where:

D_{bs} – aperture fractal dimension
 r – aperture
 N – aperture number

Particle size fractal dimension D_{ps} is similar to the calculation principle and method of aperture fractal dimension.

TEST RESULT

DIRECT SHEAR TEST RESULT

The internal friction angle of solidified dredger fill under different curing periods and different curing agents is shown in Tab.4. The relationship between the internal friction angle and curing period is showed in Fig.2. The relationship between the internal friction angle and the type of curing agent is showed in Fig.3.

Tab. 4. The internal friction angle of solidified dredger fill

test number	curing period T/d			
	14	28	42	90
1	24.5	37.7	38.1	38.2
2	22.2	35.4	35.6	35.6

test number	curing period T/d			
	14	28	42	90
3	23	35.9	37.5	37.6
4	21.8	35.4	39	40.2
5	20	34.4	38.5	41.2

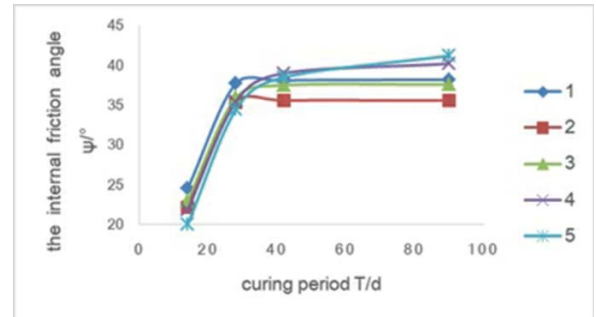


Fig. 2. Relationship between the internal friction angle and curing period

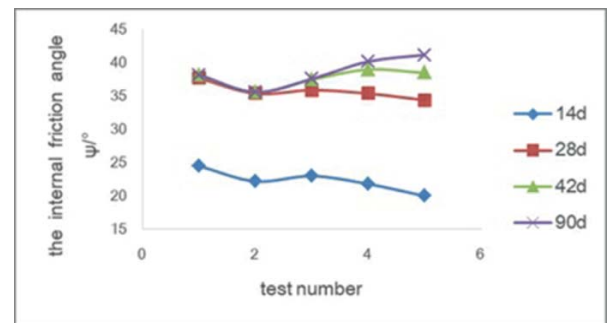


Fig. 3. Relationship between the internal friction angle and the type of curing agent

Fig. 2 shows that under the same type of curing agent, along with the curing period growth, the internal friction angle of solidified soil increases first and then tends to be stable. The internal friction angle of test 4 and test 5 had exceeded the internal friction angle of test 1 at the time of 42 days; Moreover, it can be seen that the internal friction angle between test 4 and test 5 is relatively close on the 90 day, which indicates that increasing the fly ash content will not increase the internal friction angle.

In Fig. 3, compared with 2, 3, 4 and 5 of the test, it can be seen that along with the fly ash content growth, the internal friction angle will increase first and then decrease before 42 days, and the internal friction angle will increase along with the fly ash content growth after 42 days.

The cohesion of solidified dredger fill under different curing periods and different curing agents is shown in Tab.5. The relationship between the cohesion and curing period is showed in Fig.4. The relationship between the cohesion and the type of curing agent is showed in Fig. 5.

Tab. 5. The cohesion of solidified dredger fill

test number	curing period T/d			
	14	28	42	90
1	42.4	64.4	72.4	74.7

test number	curing period T/d			
	14	28	42	90
2	31.1	51.3	59.8	59.8
3	33.1	52	77.6	77.7
4	29.5	50.4	84.5	86.5
5	20	35.6	77.2	96.9

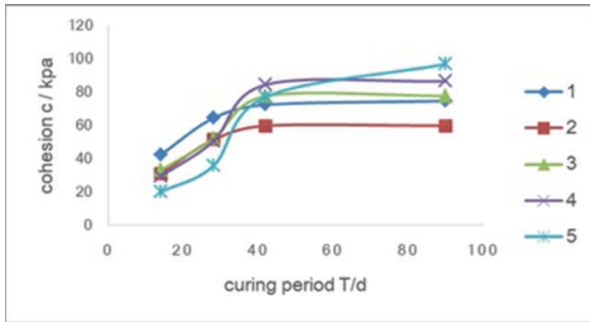


Fig. 4. Relationship between the cohesion and curing period

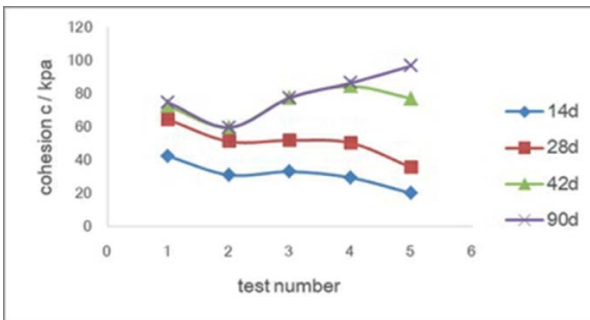


Fig. 5. Relationship between the cohesion and the type of curing agent

Fig. 4 shows that under the same type of curing agent, along with the curing period growth, the cohesion of solidified soil increases first and then tends to be stable. The cohesion of test 4 and test 5 had exceeded the cohesion of test 1 at the time of 42 days.

In Fig. 5, compared with 2, 3, 4 and 5 of the test, it can be seen that along with the fly ash content growth, the cohesion increased first and then decreased before 42 days, and the cohesion will increase along with the fly ash content growth after 42 days.

Fig. 2 and Fig.4 show that under the same type of curing agent, with the curing period growth, the hydration products with cementation increase after hydration of the curing agent, which makes the internal friction angle and the cohesion increase. When the curing agent is fully hydrated, the internal friction angle and the cohesion tend to be stable.

Fig. 3 and Fig. 5 show that fly ash played a role in filling and hindering the hydration of curing agent before 42 days, along with the fly ash content growth, the filling effect of fly ash is firstly greater than the hindrance effect, and then is less than the hindrance, which make the shear strength index increase first and then reduce; After 42 days, the fly ash will

accelerate the hydration reaction, which makes the shear strength index increase with the fly ash content growth.

The test results of the internal friction angle and the cohesion of solidified dredger fill show that the internal friction angle and the cohesion of test 4 and test 5 are much higher than those of test 1 after 42 days, which indicates that adding fly ash can enhance the effect of curing agent.

FRactal DIMENSION COMPUTING RESULT

According to the calculation method of fractal dimension of soil, the specific value of particle surface fractal dimension D_{pr} , particle size fractal dimension D_{ps} and aperture fractal dimension D_{bs} is obtained by applying the method to the solidified dredger fill with different content of fly ash.

Tab. 6 is the result of surface fractal dimension of solidified dredger fill at different curing periods and different fly ash content.

Tab. 6. The surface fractal dimension of solidified dredger fill

curing period T (d)	fly ash content $\lambda/\%$			
	0	2	4	8
14	1.142	1.143	1.144	1.143
28	1.125	1.129	1.132	1.135
42	1.123	1.12	1.12	1.122
92	1.122	1.119	1.112	1.111

Tab. 7 is the result of particle size fractal dimension of solidified dredger fill at different curing periods and different fly ash content.

Tab. 7. The particle size fractal dimension of solidified dredger fill

curing period T (d)	fly ash content $\lambda/\%$			
	0	2	4	8
14	1.436	1.462	1.458	1.457
28	1.293	1.368	1.407	1.416
42	1.288	1.295	1.325	1.335
92	1.292	1.269	1.259	1.254

Tab. 8 is the result of aperture fractal dimension of solidified dredger fill at different curing periods and different fly ash content.

Tab. 8. The aperture fractal dimension of solidified dredger fill

curing period T (d)	fly ash content $\lambda/\%$			
	0	2	4	8
14	1.483	1.478	1.504	1.489
28	1.604	1.586	1.534	1.538
42	1.613	1.633	1.648	1.638
92	1.611	1.642	1.659	1.667

QUANTITATIVE ANALYSIS OF RELATIONSHIP BETWEEN FRACTAL PARAMETERS AND MECHANICAL PARAMETERS OF SOLIDIFIED DREDGER FILL WITH DIFFERENT AMOUNTS OF FLY ASH

SURFACE FRACTAL DIMENSION D_{PS}

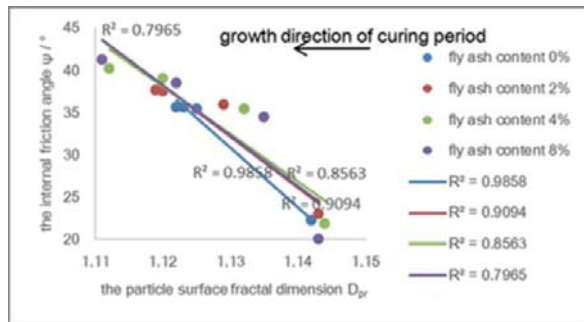


Fig. 6. Relationship between the internal friction angle and particle surface fractal dimension

The relationship between the internal friction angle and the particle surface fractal dimension is showed in Fig. 6. Fig. 6 shows that there is no obvious linear relationship between the two factors. Moreover, the point distribution in the figure is inhomogeneous, and the internal friction angle is between 35 and 40 degrees, indicating that the change between the particle fractal dimension and the internal friction angle is not obvious.

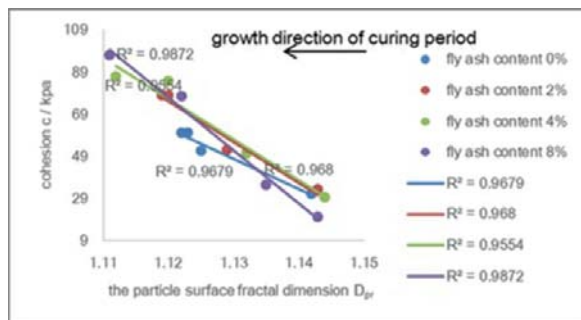


Fig. 7. Relationship between the cohesion and particle surface fractal dimension

The relationship between the cohesion and the particle surface fractal dimension is showed in Fig. 7. Fig.7 shows that along with the decrease of particle surface fractal dimension, the cohesion increases under different fly ash content, and there is a linear correlation between the two, the correlation coefficient is above 0.95.

It can also be seen that along with fly ash content growth, the inclination of fitting line increases, indicating that along with fly ash content growth, the cohesion of dredger soil is more sensitive to the particle surface fractal dimension, the influence of the degree of particle surface fluctuation on the cohesion is enhanced.

PARTICLE SIZE FRACTAL DIMENSION D_{PS}

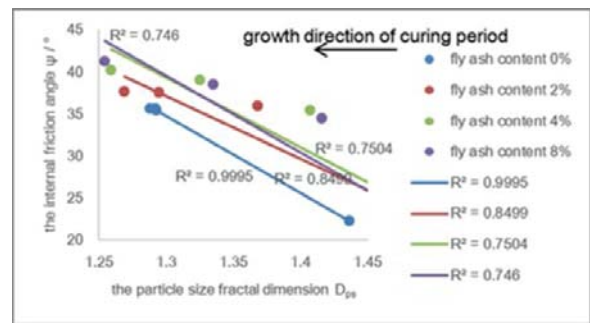


Fig. 8. Relationship between the internal friction angle and particle size fractal dimension

The relationship between the internal friction angle and the particle size fractal dimension is showed in Fig. 8. Fig. 8 shows that there is no obvious linear relationship between the two factors. Moreover, the point distribution in the figure is concentrated, and the internal friction angle is between 35 and 40 degrees, indicating that the change between the particle size fractal dimension and the internal friction angle is not obvious.

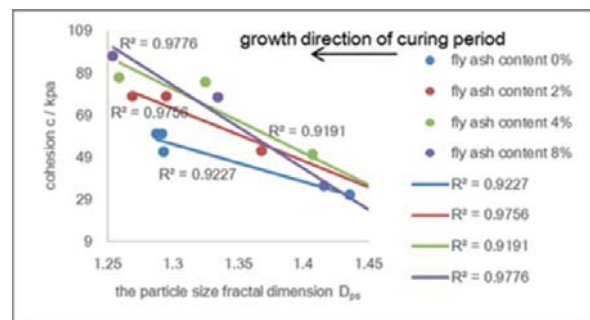


Fig. 9. Relationship between the cohesion and particle size fractal dimension

The relationship between the cohesion and the particle size fractal dimension is showed in Fig. 9. Fig. 9 shows that along with the decrease of particle size fractal dimension, the cohesion increases under different fly ash content, and there is a linear correlation between the two, the correlation coefficient is above 0.91. The particle gradation and the particle homogenization degree of solidified dredger fill will affect the cohesion.

It can also be seen that along with fly ash content growth, the inclination of fitting line increases, indicating that along with fly ash content growth, the influence of particle size fractal dimension on the cohesion of dredger fill increases, and the influence of particle homogenization degree on cohesion is enhanced.

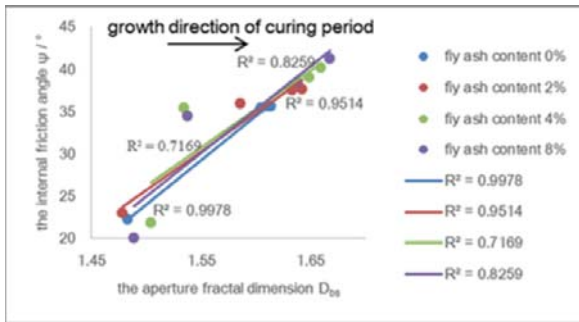


Fig. 10. Relationship between the internal friction angle and aperture fractal dimension

The relationship between the internal friction angle and the aperture fractal dimension is showed in Fig.10. Fig.10 shows that there is no obvious linear relationship between the two factors.

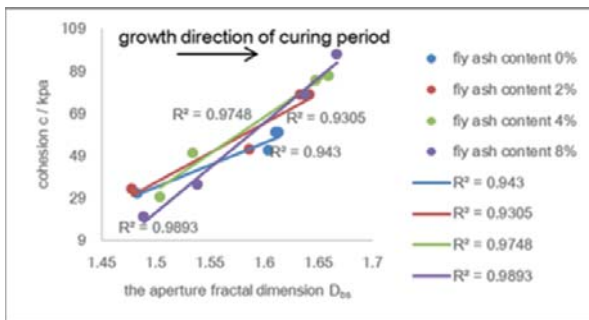


Fig. 11. Relationship between the cohesion and aperture fractal dimension

The relationship between the cohesion and the aperture fractal dimension is showed in Fig.11. Fig.11 shows that along with the aperture fractal dimension growth, the cohesion increases under different fly ash content, and there is a linear correlation between the two, the correlation coefficient is above 0.93.

It can also be seen that along with fly ash content growth, the inclination of fitting line increases, indicating that along with fly ash content growth, the influence of aperture fractal dimension on cohesion of dredger fill increases, and the influence of pore homogenization degree on cohesion is enhanced.

Fig.7, Fig.9 and Fig.11 show that with the increase of curing period, the smaller particle surface fractal dimension D_{ps} and particle size fractal dimension D_{ps} , the larger aperture fractal dimension D_{bs} , the greater the cohesion, which indicates that the change of the three fractal dimensions enhances the relationship between particles, which makes the contact area between particles increase, and the cohesion increases.

The shear strength index of solidified dredger fill is measured by the direct shear test. The microscopic images of solidified dredger fill are obtained by using Scanning Electron Microscope (SEM). The microscopic images of dredger fill are processed and analyzed by using IPP, and the fractal dimension including particle size fractal dimension D_{ps} , aperture fractal dimension D_{bs} and particle surface fractal dimension D_{pr} was calculated by fractal theory. The quantitative analysis of the relationship between shear strength index and fractal dimension of solidified dredger fill is done. The research results show that:

- 1) Under the same type of curing agent, along with the increase of curing period T, the shear strength index of solidified dredger fill increases first and then tends to be stable. This indicates that with the increase of curing period, the hydration products with cementation increase after hydration of the curing agent, which makes the internal friction angle and the cohesion increase. When the curing agent is fully hydrated, the internal friction angle and the cohesion tend to be stable.
- 2) Before 42 days of the curing period, the shear strength index increased first and then decreased with the increase of fly ash content λ , and increased with the increase of fly ash content in 42 days. This shows that, 42 days ago, fly ash plays a role in filling and hindering the hydration of the curing agent during the curing process. With the increase of fly ash, the filling effect is first greater than the hindrance effect, and then is less than the hindrance; after 42 days, fly ash plays a role in accelerating hydration.
- 3) After a period of time, fly ash will accelerate the hydration of curing agent, which indicates that adding fly ash can enhance the effect of curing agent.
- 4) The relationship between the internal friction angle of solidified dredger fill and the three fractal dimensions shows that there is no obvious linear relationship between them. Moreover, the change of fly ash content has little effect on the relationship between the internal friction angle and the three fractal dimensions.
- 5) The relationship between the cohesion of solidified dredger fill and the three fractal dimensions shows that the cohesion has a good linear relationship with the three fractal dimensions, and the correlation coefficient R^2 is above 0.91. Moreover, with the increase of curing period, the smaller particle surface fractal dimension D_{pr} and particle size fractal dimension D_{ps} , the larger aperture fractal dimension D_{bs} , the greater the cohesion, which indicates that the change of the three fractal dimensions enhances the relationship between particles, which makes the contact area between particles increase, and the cohesion increases.

ACKNOWLEDGMENTS

Financial support for this study was provided by the National Natural Science Foundation of China (51078228) and the National Marine public welfare industry research special funds of China (201105024-5).

REFERENCE

1. Cui Yongtao, Liu Wenbai, Xu Bingqin: The study of compression modulus and changes in microstructure of dredged mud before and after solidification, *Science Technology and Engineering*, Vol.16, no.15, pp.260-267, 2016.
2. Ding Jianwen, Hong Zhenshun, Liu Songyu: Triaxial shear test of flow-solidified soil of dredged clays, *Journal of Southeast University (Natural Science Edition)*, Vol.41, no.5, pp.1070-1074, 2011.
3. Fu Zhibin, Zhang Lihong, Zhang Jixing, Zhao Gang: Research on solidifying dredger fill of littoral facies with experiment, *Geotechnical Investigation & Surveying*, no.3, pp.7-11, 2012.
4. Huang Li: Quantitative Analysis of Micro-Porosity of Saturated Soft Clay and Its Fractal Description, Wuhan University of Technology, Wuhan, 2007.
5. Liu Xin, Fan Xiaoqiu, Hong Baoning: Experimental study of triaxial test of soils stabilized by cement mortar, *Rock and Soil Mechanics*, Vol.32, no.6, pp. 1676-1682, 2011.
6. Lu Peixia, Cao Ling, Xu Yongfu: Fractal Theory of Unsaturated Soil Mechanics, *Chinese Journal of Underground Space and Engineering*, Vol.11, no.2, pp. 375-381, 2015.
7. Shao Yufang, Xu Riqing, Liu Zeng-yong, Gong Xiaonan: Experimental study on new variety of cement-stabilized soil, *Journal of Zhejiang University(Engineering Science)*, Vol.40,no.7,pp.1196-1200,2006.
8. Wang Dongxing, Xu Weiya: Research on strength and durability of sediments solidified with high volume fly ash, *Rock and Soil Mechanics*, Vol.33, no.12, pp.3659-3663, 2012.
9. Wu Yuanfeng, Yi Guiyun, Liu Quanrun, Li Fenghai, Zhao Liwei, Ma Mingjie: Current situation of comprehensive utilization of fly ash, *Clean Coal Technology*, Vol.19, no.6, pp.100-104, 2013.
10. Xu Riqing, Deng Weiwen, Xubo, Lai Jianping, Zhan Xuegui, Xu Liyang, Lu Jianyang: Quantitative Analysis of Soft Clay Three-dimensional Porosity Based On SEM Image

Information, *Journal of Earth Science and Environment*, Vol.03, pp.104-110, 2015.

11. Xu Riqing, Xu Liyang, Deng Weiwen, Zhu Yihong: Experimental study on soft clay contact area based on SEM and IPP, *Journal of Zhejiang University (Engineering Science)*, Vol.08, pp.1417-1425, 2015.
12. Zhang Zhihong, Li Hongyan, Shi yumin: Experimental Study on Permeability Properties and Microstructure of Clay Contaminated by Cu²⁺, *China Civil Engineering Journal*, Vol.47,no.12,pp.122-129,2014.
13. Zhang Jiru, Hu Yong, Yu Hongling, Tao Gaoliang: Predicting soil-water characteristic curve from multi-fractal particle-size distribution of clay, *Journal of Hydraulic Engineering*, Vol.46, no.6, pp. 650-657, 2015.
14. Zhao Minghua, Dai Jie, Zhang Ling, Yin Pingbao: Fractal Theory-based Study of the Permeability of Fly Ash, *Journal of Hunan University(Natural Sciences)*, Vol.42,no.1,pp.75-80,2015.
15. Zhen Zhiheng, Gao Jianwei: The Microscopic Characteristic Analysis of Red Bed Mudstone Modified Soil Based on IPP, *Transportation Science and Technology*, Vol.08, pp.124-127, 2015.

CONTACT WITH THE AUTHORS

Yang Shuai

*e-mail:*2310746081@qq.com

School of Ocean Science and Engineering,
Shanghai Maritime University
Shanghai P. R., 201306

CHINA

Liu Wenbai

e-mail: liuwb8848@163.com

School of Ocean Science and Engineering, Shanghai
Maritime University
Shanghai P. R. 201306

CHINA

Liu Hongwei

e-mail: hwliu@shmtu.edu.cn

School of Ocean Science and Engineering, Shanghai
Maritime University
Shanghai P. R. 201306

CHINA

A FLEXIBLE CONTROL STRATEGY FOR SHORE-TO-SHIP POWER SYSTEM IN TERMS OF GRID-CONNECTED AND OFF-GRID SWITCH

Zhendong Ji

Zhihong Zhao

School of Automation, Nanjing University of Science and Technology, Nanjing, Jiangsu, China

Jianhua Wang

School of Electrical Engineering, Southeast University, Nanjing, Jiangsu, China

Zhipeng Lv

China Electric Power Research Institute, Beijing, China

ABSTRACT

There are promising application prospects for applying the shore power technology to the ships in the port for the purpose of pollution prevention. However, the grid-connection of the shore power supply to the ship power grid leads to current surges, damages the ship power consumption equipment, and results in the instability of the ship power grid system, which will seriously affect the reliability of the operation of the ship power grid system. In order to address this problem, the mathematical model of virtual synchronous generator is introduced in this paper. Then, a control method for the flexible grid-connection of the shore power supply to the ship power grid based on the virtual synchronous generator is proposed. Next, the output characteristics of the shore power supply are optimized to match the characteristics of the ship generator, which contributes to the flexible grid-connection of the shore power supply to the ship power grid system. The effectiveness and the feasibility of this method are verified by simulation and experiments.

Keywords: Shore power supply; Ship power system; Virtual synchronous generator; Flexible control

INTRODUCTION

The shore-to-ship power system in the port refers to the shore power station that powers the ship, when the ship berths at the terminal and when the operation of all the ship diesel power stations is stopped. The voltage, frequency, and power of the shore power supply should be able to meet the necessary power demand of all power facilities after the ship is docked, thus reducing the emission of pollutants at the port, which symbolizes a revolutionary advancement in the field of port and ship power supply systems [1,2].

The implementation of the shore power technology on the ships in the port for the purpose of pollution prevention has been demonstrated by experts and scholars at home and abroad. The ship grid voltage includes both low voltage

and high voltage, the former referring to 440 V/400 V while the latter referring to 6.6kV/6kV [3]. In 2000, the first high-voltage shore power system was designed and installed at the ferry terminal of Gothenburg Port, Sweden. This technology has reduced the emission of pollutants by 94%-97% during the ship docking process [2]. Subsequently, the shore power technology was successively applied in the major ports in the European Union, such as the container terminals (Rotterdam Port in Netherlands and Antwerp Port in Belgium) and ferry terminals (Zeebrugge Port and Gothenburg Port). The grid-connection of the shore power supply has significantly improved the environmental quality.

The ship power grid system generally regulates the operations through the ship energy management system and achieves the power distribution and related operating

parameters. In order to adapt to the power distribution of the ship power grid, the power electronic device generally adopts the droop control strategy on the grid-connected side [4]. The droop control simulates the droop external characteristics of the generator by sampling, feeding back, and responding to the magnitude and frequency of the grid voltage. Although this control method has achieved excellent results in the inverter operation control and power distribution during the off-grid operation, it may bring significant transient current impact to grid-connected inverters [5]. In addition, in this simulation method based on the droop external characteristics of the generator the improper design of the droop coefficients may directly lead to the instability of the grid-connected inverter system [6]. The inverter performance based on this control method obviously cannot be compared with the conventional generator. Therefore, the grid-connection of the shore power supply to the ship power grid will impact the ship's power grid and damage the ship's power equipment. Besides, there will be difficulties in designing the system parameters, which easily leads to the system instability. Consequently, it is difficult to connect the shore power supply to the ship generator.

The synchronverter technology proposed by Professor Zhong Qingchang was used to connect the synchronous generator to the power electronic device so that the power electronic device can simulate the inertia and damping characteristics of the synchronous generator, which provides new solution to the grid-connected self-synchronization issue of the distributed power supply [7]. The mechanical and electrical equations of the synchronous generator were applied to the control algorithm of the grid-connected inverter. Then, the damping coefficients and the inertia time constant were adjusted so that the inverter was equipped with the inertia and damping characteristics of the synchronous generator while performing the power conversion, which can support the voltage and frequency stability of the power grid to a certain extent [8,9]. The key part of this technology is that it can simulate the inertia characteristics of a synchronous generator and induce a certain "inertia" into the distribution network. In the shore-to-ship power system based on power electronic inverters with the power system frequency and voltage modulation control algorithm, the shore power

supply was able to simulate the frequency and voltage control characteristics of the synchronous generator. The synchronous generator can match the output characteristics of shore power supply to the characteristics of the ship generator in order to flexibly connect the shore power supply to the ship power grid, increase the stability of the shore power supply, reduce the impact on the ship power grid, and protect the ship's power consumption equipment.

This paper presents a flexible grid-connected control strategy based on the virtual synchronous generator technology. Compared with the existing shore power supply technology, the proposed method is able to realize the functions of the traditional shore power supply and optimize the output characteristics of the shore power supply by approximating them to the characteristics of the ship generator, which is beneficial for the flexible grid-connection of the shore power supply to the ship power grid. Therefore, this study is of significant theoretical and engineering value.

TOPOLOGY AND THE PRINCIPLE OF SHORE POWER SUPPLY

The shore-to-ship power system is shown in Fig. 1. The 690 V/50 Hz AC power from the land-based power grid is rectified to DC power by 12-pulse rectifier to maintain the voltage stability of the DC sides and to avoid the harmonic pollution to the power grid. The outputs of the two sets of PWM inverters are connected in parallel and then to the 440 V/60 Hz ship power grid to form a power supply system, after the ship is docked.

Under the traditional shore power supply control method, the operational process of the shore power supply when the ship is docked is as follows: the ship diesel generator is stopped (the ship load is cut off) → the shore power supply is accessed → the shore power supply is started (the ship load is restored). The virtual synchronous generator control strategy enables the shore power supply system with the output droop, electrical, and mechanical characteristics to operate similarly to those of the diesel generator sets, ensuring the stable parallel operation and realizing the same scheduling

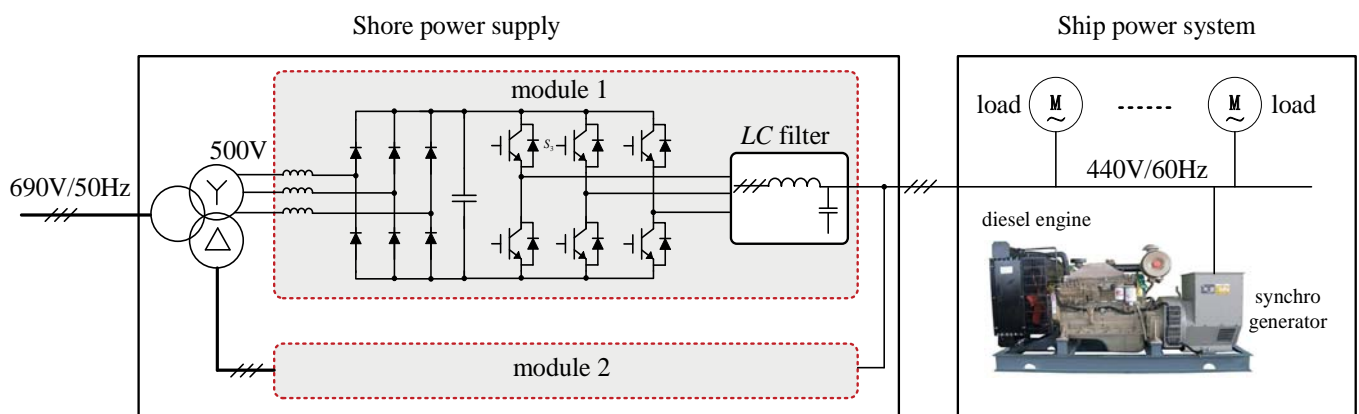


Fig. 1. Shore-to-ship power system

management of the ship's power management system (PMS) for the shore power supply and traditional diesel generator sets. The shore power supply operational process is as follows: the shore power supply is started → the shore power supply is connected to the ship power grid through the PMS scheduling control → the load is transferred → the ship diesel generators are separated from the power grid and shut down → the shore power supply provides uninterrupted power for the ship load independently. The access and withdrawal of the shore power supply do not require the cutoff of the ship load or affect the stability of the ship power system, which greatly simplifies the power supply process.

MATHEMATICAL MODEL OF SYNCHRONOUS INVERTER

MATHEMATICAL MODEL

As shown in Fig. 2, the synchronous impedance of the synchronous generator is equalized to the output filter inductance of the grid-connected inverter, while the voltage of the synchronous generator is equalized to the output voltage of the grid-connected inverter. Then, the grid-connected inverter is optimized to realize the frequency regulation and excitation control of the synchronous generator, thereby regulating the frequency and the voltage.

Based on the above analysis, the inverter can be controlled to simulate the operation of the synchronous generator with the relevant operation characteristics of the synchronous generator. Therefore, it is called the virtual synchronous generator. Firstly, the mechanical equation of the virtual synchronous generator is expressed as:

$$J \frac{d\omega}{dt} = T_m - T_e - T_d = T_m - T_e - D(\omega - \omega_0) \quad (1)$$

In Eq. (1):

J – the rotary inertia of the synchronous generator, unit: $\text{kg}\cdot\text{m}^2$;

H – the inertia time constant, unit: s;

ω – the angular speed of the synchronous generator;

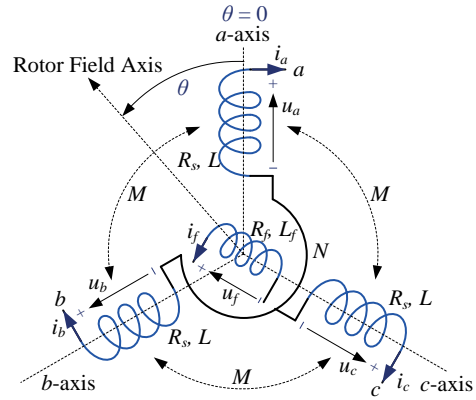
ω_0 – the synchronous angular speed of the power grid;

T_m , T_e , and T_d – the mechanical, electromagnetic, and damping torques of the synchronous generator, unit: $\text{N}\cdot\text{m}$;

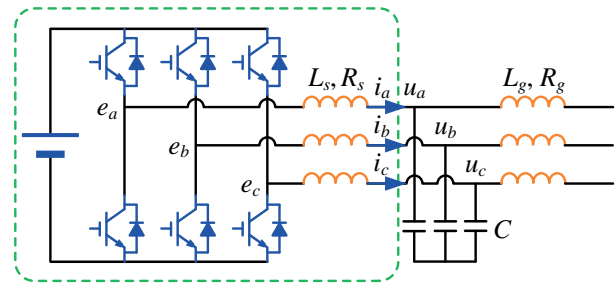
D – the damping coefficient, unit: $\text{N}\cdot\text{m}\cdot\text{s}/\text{rad}$.

Specifically, the electromagnetic torque T_e of the synchronous generator can be obtained from the potential e_{abc} and the output current i_{abc} of the virtual synchronous generator, which implies that:

$$T_e = P/\omega = (e_a i_a + e_b i_b + e_c i_c) / \omega \quad (2)$$



(a) Physical model of the synchronous generator



(b) Physical model of the grid-connected inverter

Fig. 2. Physical model of the grid-connected inverter to simulate the synchronous generator

In the control of the virtual synchronous generator, it is worth noting that the inertia time constant H provides the grid-connected inverter with the inertia characteristics similar to those of the synchronous generator, which supports the frequency stability to a certain extent. Besides, the damping coefficient D provides the grid-connected inverter with the damping characteristics similar to those of the synchronous generator, which effectively damps the fluctuation of the system output power and enables the random power supply to be smoothly connected to the grid. The above two parameters play a very important role in improving the operating performance of the grid-connected inverter [63-67].

Secondly, the electromagnetic equation of the virtual synchronous generator is obtained from Fig. 1 and is expressed as

$$L \frac{di_{abc}}{dt} = e_{abc} - u_{abc} - Ri_{abc} \quad (3)$$

In Eq. (3):

L – the synchronous reactance of the synchronous generator;

R – the synchronous resistance of the synchronous generator;

u_{abc} – the terminal voltage of the synchronous generator.

The synchronous reactance of the synchronous generator is equalized to the filter inductance of the grid-connected

inverter, while the transient voltage of the synchronous generator is equalized to the output voltage of the three-phase half-bridge inverter. It is worth noting that L and R in Eq. (3) may be different from the filter inductance of the actual grid-connected inverter. On the one hand, an increase in R can increase the system damping but lead to the control error in the system voltage and reactive power. On the other hand, an increase in L can also increase the system damping but lead to the static control error in the system, making the system output voltage and active power unable to track the given values.

(1) Electrical model

The synchronous generator parameters used in this paper are: the self-inductance and the mutual inductance of stator winding, where p pole pairs are respectively L and M ($M > 0$), as shown in Fig. 2(a).

L_f is the self-inductance of the field winding. The mutual inductance between the three-phase stator and the field core changes with the rotation angle θ , which is expressed as:

$$\begin{cases} M_{af} = M_f \cos(\theta) \\ M_{bf} = M_f \cos(\theta - 2\pi/3) \\ M_{cf} = M_f \cos(\theta - 4\pi/3) \end{cases} \quad (4)$$

The flux chain of the winding is expressed as:

$$\begin{cases} \phi_a = Li_a - Mi_b - Mi_c + M_{af}i_f \\ \phi_b = -Mi_a + Li_b - Mi_c + M_{bf}i_f \\ \phi_c = -Mi_a - Mi_b + Li_c + M_{cf}i_f \\ \phi_f = M_{af}i_a + M_{bf}i_b + M_{cf}i_c + L_fi_f \end{cases} \quad (5)$$

As $i_a + i_b + i_c = 0$, the stator flux can be expressed as:

$$\begin{cases} \phi = (L + M)i + M_f i_f \widetilde{\cos \theta} \\ \phi_f = L_f i_f + M_f \langle i, \widetilde{\cos \theta} \rangle \end{cases} \quad (6)$$

In Eq. (6):

$$\phi = \begin{bmatrix} \phi_a \\ \phi_b \\ \phi_c \end{bmatrix}, i = \begin{bmatrix} i_a \\ i_b \\ i_c \end{bmatrix};$$

$$\widetilde{\cos \theta} = \begin{bmatrix} \cos \theta \\ \cos(\theta - 2\pi/3) \\ \cos(\theta + 2\pi/3) \end{bmatrix};$$

$$\widetilde{\sin \theta} = \begin{bmatrix} \sin \theta \\ \sin(\theta - 2\pi/3) \\ \sin(\theta + 2\pi/3) \end{bmatrix}.$$

The second term in Eq. (6) is constant when the three-phase current is sinusoidal and balanced. Assuming that the stator winding is R_s and the phase voltage is $v = [v_a, v_b, v_c]^T$, the following equation can be obtained:

$$v = -R_s i - \frac{d\phi}{dt} = -R_s i - L_s \frac{di}{dt} + e \quad (7)$$

where e is the magnetic field voltage generated by the rotor rotation and is expressed as:

$$e = \dot{\theta} M_f i_f \widetilde{\sin \theta} - M_f \frac{di_f}{dt} \widetilde{\cos \theta} \quad (8)$$

(2) Mechanical model

The mechanical model of the synchronous generator is expressed as:

$$J \ddot{\theta} = T_m - T_e + D_p \dot{\theta} \quad (9)$$

In Eq. (9):

J - the rotary inertia of the synchronously rotating mechanical part in the rotor, unit: $\text{kg} \cdot \text{m}^2$;

T_m - the mechanical torque, unit: $\text{N} \cdot \text{m}$;

T_e - the electromagnetic torque, unit: $\text{N} \cdot \text{m}$;

D_p - the damping coefficient.

T_e^p - can be calculated from the total energy E of the generator, which is the sum of the magnetic energy and the kinetic energy, and is expressed as:

$$E = \frac{\langle i, L_a i \rangle}{2} + M_f i_f \langle i, \widetilde{\cos \theta} \rangle + \frac{L_f i_f^2}{2} + \frac{J \dot{\theta}^2}{2} \quad (10)$$

As the rotor mechanical angle θ_m satisfies $\theta = p\theta_m$, the following equation can be obtained:

$$T_e = p M_f i_f \langle i, \widetilde{\sin \theta} \rangle \quad (11)$$

The mechanical part of the virtual synchronous generator is modelled as above. The mechanical model and the electrical model of the virtual synchronous generator will be used in the design of the control algorithm [6].

ACTIVE POWER REGULATION

The active power regulation of traditional synchronous generators is achieved through the adjustment of mechanical torque, while the frequency regulation is achieved through adjustment of the frequency regulator. Compared with traditional synchronous generators in the virtual synchronous generator control technology, the virtual machine torque T_m can be regulated by adjusting the reference active power of the inverter. The frequency deviation feedback command ΔT and the reference mechanical torque T_0 constitute the virtual mechanical torque T_m , where $T_0 = P_{ref}/\omega$ and P_{ref} is the active power value of the grid-connected inverter controlled by the virtual synchronous generator. Therefore, the frequency is regulated by the virtual automatic frequency regulator. When the virtual automatic frequency regulator is adopted as an element of proportionality, the frequency deviation feedback command ΔT is expressed as:

$$\Delta T = k_f (f - f_0) \quad (12)$$

Where f is the frequency of the terminal voltage in the virtual synchronous generator, f_0 is the reference frequency of the power grid, and k_f is the frequency regulation coefficient.

It can be seen that contrary to the previous PQ control strategies of grid-connected inverters, the active power regulation of the virtual synchronous generator technology can track the active power and perform corresponding active power regulation in response to the frequency deviation of the power grid, thereby simulating the frequency regulation performance of the synchronous generator and effectively resolving the response of the grid-connected inverter based on power electronics technology to the frequency faults of the power grid.

REACTIVE POWER REGULATION

The traditional synchronous generator regulates the terminal voltage and reactive power through excitation regulation. The regulation of the terminal voltage and reactive power of the virtual synchronous generator can be achieved by regulating the virtual electromotive force [10-12].

The virtual electromotive force generator command of the virtual synchronous generator consists of three components. The first component is the empty-load electromotive force E_0 of the virtual synchronous generator. The second component is ΔE_Q , corresponding to the reactive power regulation, which is specifically expressed as:

$$\Delta E_Q = k_q (Q_{ref} - Q) \quad (13)$$

Where k_q is the reactive power regulation coefficient, Q_{ref} is the reference reactive power of the grid-connected inverter, and Q is the instantaneous reactive power output of the virtual synchronous generator expressed as:

$$Q = \frac{(u_a - u_b)i_c + (u_b - u_c)i_a + (u_c - u_a)i_b}{\sqrt{3}} \quad (14)$$

It is equivalent to the automatic voltage regulator or excitation regulator of the synchronous generator.

The third component is ΔE_U , corresponding to the terminal voltage regulation of the virtual synchronous generator, and is specifically expressed as:

$$\Delta E_U = \left(k_v + \frac{k_i}{s} \right) (U_{ref} - U) \quad (15)$$

Where k_v is the voltage regulation coefficient, k_i is the integral coefficient, U_{ref} is the effective terminal voltage of the virtual synchronous generator, and U is the actual measured terminal voltage of the virtual synchronous generator.

It can be seen that compared with the traditional PQ control strategies of grid-connected inverters, the reactive power regulation of the virtual synchronous generator technology can track the reactive power and contribute to the voltage regulation of the distribution network. It regulates the reactive power according to the difference between the reference output voltage of the grid-connected inverter and the actual measured voltage, adjusting the reactive power to achieve the voltage stability of power grid.

DEFINITION OF THE INERTIA CONSTANT

When the input mechanical power and the output electromagnetic power are not balanced, the synchronous generator will accelerate or decelerate, accompanied by swings in its output power, power angle, and other variables. The swing equation of the synchronous generator can be expressed as:

$$\frac{d}{dt} \left(\frac{1}{2} J \omega^2 \right) = P_m - P \quad (16)$$

Where J and ω are respectively the rotary inertia and angular velocity of the synchronous generator, P_m and P are respectively the mechanical power and the electromagnetic power of the synchronous generator.

$$\frac{d}{dt} \left(\frac{1}{2} J \omega^2 \right) = J \omega \frac{d\omega}{dt} \approx J \omega_0 \frac{d\omega}{dt} \quad (17)$$

Where ω_0 is the rated angular velocity of the synchronous generator. In addition, it should be pointed out that during the rotation of the generator's rotor, there is always mechanical friction damping, and the friction coefficient is denoted as D .

velocity of the prime mover in the generator set will decrease to a certain extent. The frequency regulator increases the output mechanical power. This process can be realized by subtracting the actual angular velocity from the rated angular velocity and by adjusting the damping control module. As shown in Fig. 3, the damping coefficient D_p is expressed as the frequency droop coefficient in the actual control process, and it is defined as the ratio of the required torque change to the angular velocity change, which is expressed as:

$$D_p = \frac{\Delta T}{\Delta \dot{\theta}} = \frac{\Delta T}{T_{mn}} \frac{\dot{\theta}_n}{\Delta \dot{\theta}} \frac{T_{mn}}{\dot{\theta}_n} \quad (20)$$

Where T_{mn} is the rated mechanical torque. As there is no delay in the frequency loop, the frequency loop time constant can be made smaller than that of the actual synchronous generator. The quotient of the reference active power P^* and the rated mechanical angular velocity is the mechanical torque T_{mn} . As shown in the upper part of Fig. 3, this control scheme achieves the closed-loop control of active power. Due to the frequency droop mechanism, the loaded active power is automatically shared by the same bus.

(2) Voltage droop and reactive power regulation

The reactive power Q can be regulated by a similar control method. The voltage droop coefficient is defined as the ratio of the reactive power change ΔQ to the voltage change Δv . The following expression is obtained:

$$D_q = \frac{\Delta Q}{\Delta v} = \frac{\Delta Q}{Q_n} \frac{v_n}{\Delta v} \frac{Q_n}{v_n} \quad (21)$$

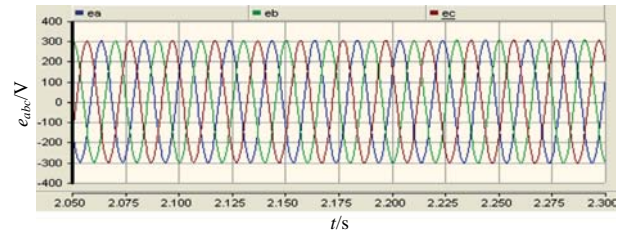
Where Q_n is the rated reactive power and u_n is the rated terminal voltage. The reactive power feedback loop is shown in the lower part of Fig. 3. Before being superimposed by the difference of real-time reactive power and the set value of the reactive power, the terminal voltage u is subtracted from the rated voltage u_n . Then, the signal M_{ij} integrator is produced from the calculation of the D_q link and the integrator with a gain of $1/K$.

SIMULATION ANALYSIS AND EXPERIMENTAL VERIFICATION

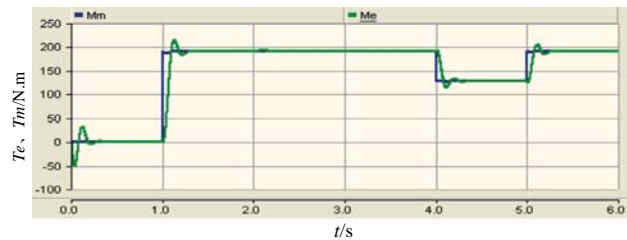
SIMULATION ANALYSIS

For the above analysis, a corresponding PSCAD simulation model was built. The voltage on the DC side was 800 V, the three-phase output line voltage was 380 V, the frequency was 50 Hz, and the switching frequency was 20 kHz. There was no load during 0~1 s. Afterwards, the load was increased to 60 kW for 1~4 s. During 4~5 s, the load was reduced to 40 kW. After 5 s, the load was restored to 60 kW. The simulation

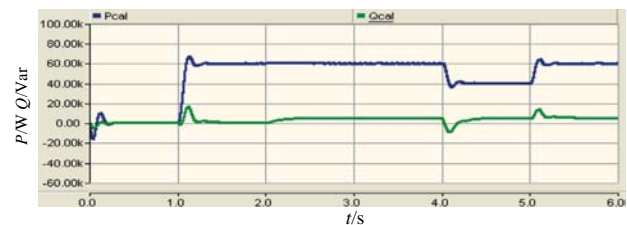
waveforms are shown in Fig. 5(a)-(d) below. It can be seen that under the control strategy based on the virtual synchronous generator, the shore power supply can automatically regulate the power according to the load fluctuations, while the frequency and the potential can be automatically regulated according to the power, which demonstrates the nature of the synchronous generator, including certain inertia and damping characteristics. Therefore, it can be utilized in the frequency and voltage regulation of the ship power grid system.



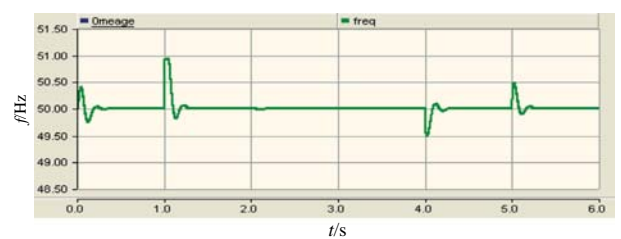
(a) Output waveform figure



(b) Torque waveform figure



(c) Power waveform figure



(d) Output frequency waveform

Figure 5. Simulation waveforms of shore power supply

EXPERIMENTAL VERIFICATION

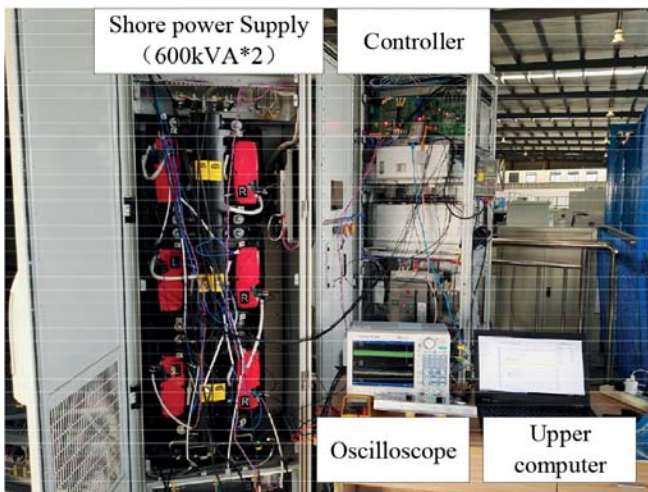
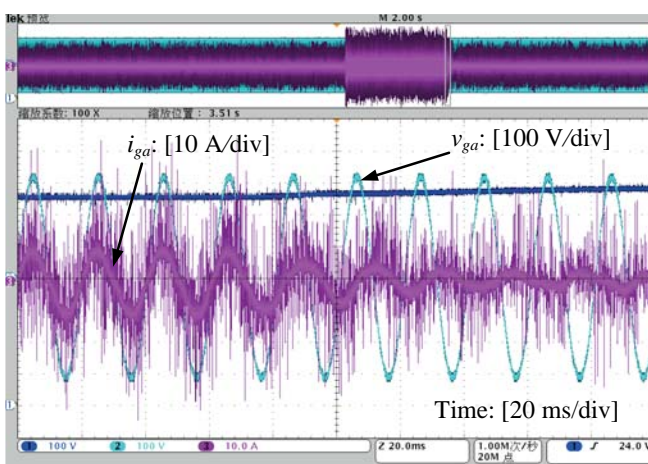


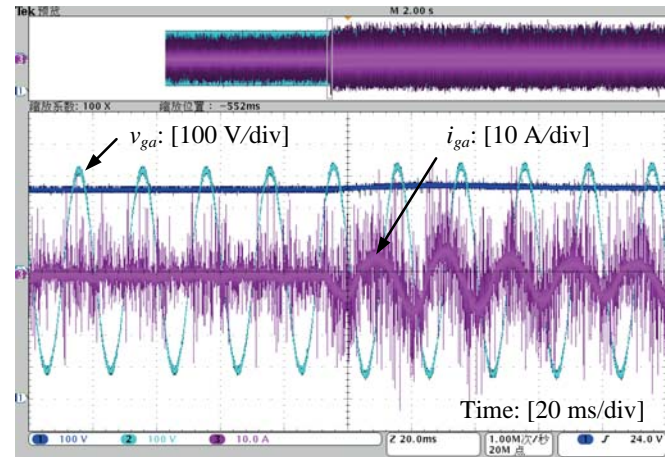
Fig. 6. 600 kVA*2 shore power supply device

Fig. 6 shows the 600 kVA*2 shore power supply device. The specific topology is shown in Fig. 1. DSP + FPGA framework is used in the controller. DSP is used to implement the control algorithm, and FPGA is used to implement logical judgment, fault handling, communication, and other functions.

Under the control method proposed in this paper, the shore power supply has the ability to automatically participate in the regulation of the ship power grid, which means that it can automatically regulate its output active power and reactive power according to the change in the grid voltage amplitude and frequency. Regarding the control parameters, the following cases are designed: the frequency of the ship grid voltage changes by 1 Hz and the active power changes by 5 kW; the amplitude of the ship grid voltage changes by 10% and the reactive power changes by 12 kVar.



(a) The frequency of the ship grid voltage reduces (increases) by 1 Hz, and the active power increases (reduces) by 5 kW



(b) The amplitude of the ship grid voltage increases (reduces) by 5%, and the reactive power reduces (increases) by 6 kVar

Fig. 7. Experimental waveforms when the shore power supply participates in the power regulation of the ship power grid

Fig. 7 shows the experimental waveforms of the following cases: (a) the frequency of the ship grid voltage reduces by 1 Hz and the active power increases by 5 kW; the frequency of the ship grid voltage increases by 1 Hz and the active power reduces by 5 kW; (b) the amplitude of the ship grid voltage decreases by 5% and the reactive power increases by 6 kVar; the amplitude of the ship grid voltage increases by 5% and the reactive power reduces by 6 kVar. It can be seen from Fig. 7 that the solid state module can automatically regulate its output active power and reactive power according to the frequency and amplitude of the grid voltage, and the power change is the same as the reference value, which meets the indicator requirement. In addition, it can be clearly seen that after the frequency or voltage jumps, it takes a certain period of time for the output active power or reactive power to stabilize, which confirms the presence of certain inertia after the integration of the virtual generator control.

Fig. 8 shows the dynamic waveforms when the shore power supply is connected to the ship power grid. At the time t_1 , the diesel generators are connected to the ship power grid, and the load is completely supplied by the diesel generators. At the time t_2 , the shore power supply is connected, and it supplies part of the load under the coordination of the PMS. Then, the output current of the diesel generators i_{dga} gradually decreases, while the output current of the shore power supply i_{ga} increases. At the time t_3 , the load is completely transferred to the shore power supply, and the diesel generators produce zero output current and can be shut down. During the entire process, the ship power grid receives uninterrupted power supply, and the flexible grid connection of the shore power supply is realized, which effectively protects the ship power grid and its power consumption equipment.

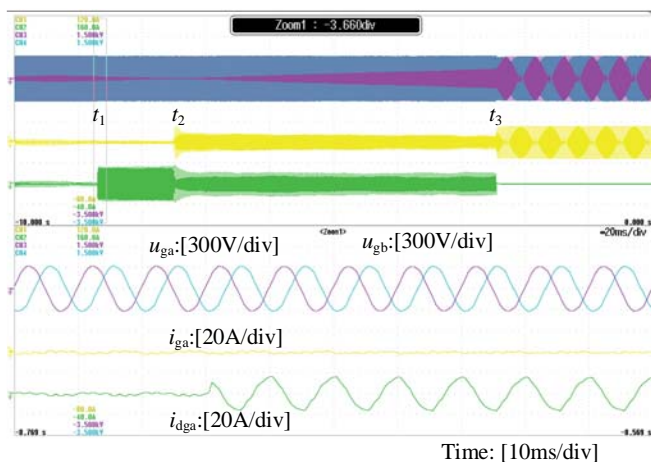


Fig. 8. Dynamic waveforms when the shore power supply is connected to ship power grid

CONCLUSION

In this paper, based on the study of the topology and the working principle of the shore power supply, a control method for the flexible grid-connection of the shore power supply to the ship power grid is proposed. The method is based on the virtual synchronous generator technology and addresses the problems of traditional control methods of the grid-connection of the shore power supply to the ship power grid: current surges, damages to the ship power consumption equipment, and the resulting instability of the ship power grid system. The proposed method can not only implement the functions of the traditional shore power supply system, but also optimize the output characteristics of the shore power supply and make them closer to those of the ship generator sets, which contributes to the flexible grid-connection of the shore power supply to the ship power grid. In order to verify the feasibility and effectiveness of the control method proposed in this paper, respective simulations and experiments are carried out. The results show that this method presents better steady-state and transient performance and has great value for its application in the shore-to-ship power system.

ACKNOWLEDGEMENTS

This project is partially supported by Natural Science Foundation of Jiangsu Province (BK20170841).

BIBLIOGRAPHY

1. K. L. Peterson, P. Chavdarian, M. Islam and C. Cayanan.: *Tackling ship pollution from the shore*, IEEE Industry Applications Magazine, vol. 15, no. 1, pp. 56-60, 2009.

2. D. Paul and V. Haddadian.: *Transient Overvoltage Protection of Shore-to-Ship Power Supply System*, IEEE Transactions on Industry Applications, vol. 47, no. 3, pp. 1193-1200, 2011..
3. M. H. Chou, C. L. Su, Y. C. Lee, H. M. Chin, G. Parise and P. Chavdarian.: *Voltage-Drop Calculations and Power Cable Designs for Harbor Electrical Distribution Systems With High Voltage Shore Connection*, IEEE Transactions on Industry Applications, vol. 53, no. 3, pp. 1807-1814, 2017.
4. M. Yu, W. Huang, N. Tai, X. Zheng, Z. Ma and Y. Wang.: *Advanced microgrid and its multi-objective regulation strategy for shore supply*, The Journal of Engineering, vol. 2017, no. 13, pp. 1590-1594, 2017.
5. EPRI.: *P124 Advanced distribution automation-program overview*, 2008.
6. J. M. Guerrero et al.: *Distributed Generation: Toward a New Energy Paradigm*, IEEE Industrial Electronics Magazine, Vol. 4, no. 1, pp. 52-64, 2010.
7. Zhong Q C, Hornik T.: *Control of power inverters in renewable energy and smart grid integration*, John Wiley & Sons, 2012.
8. Yong Chen, Hesse R, Turschner D, et al.: *Improving the Grid Power Quality Using Virtual Synchronous Machines*. *Power Engineering, Energy and Electrical Drives (POWERENG)*, pp.11-13, 2011.
9. Fang Gao, Iravani M R.: *A Control Strategy for a Distributed Generation Unit in Grid-Connected and Autonomous Modes of Operation*. IEEE Transactions on Power Delivery, Vol. 23, no. 4, pp. 850-859, 2008.
10. T. Younis, M. Ismeil, M. Orabi, E. K. Hussain.: *A single-phase self-synchronized synchronverter with bounded droop characteristics*, 2018 IEEE Applied Power Electronics Conference and Exposition (APEC), pp. 1624-1629, 2018.
11. H. Li et al.: *Single-phase synchronverter dynamic optimization and parameters design*, 43rd Annual Conference of the IEEE Industrial Electronics Society, pp. 7866-7871, 2017.
12. M. Oñate, J. Posada, J. López, J. Quintero and M. Aredes.: *Control of a back-to-back converter as a power transfer system using synchronverter approach*, IET Generation, Transmission & Distribution, vol. 12, no. 9, pp. 1998-2005, 2018.
13. D. Grider, M. Das, A. Agarwal, J. Palmour, S. Leslie, J. Ostrop, R. Raju, M. Schutten, and A. Hefner.: *10kV/120A SiC DMOSFET half-bridge power modules for 1 MVA solid state power substation*, Proc. IEEE Electr. Ship Tech. Symp, pp. 131-134, 2011.

14. K. Hatua, S. Dutta, A. Tripathi, S. Baek, G. Karimi, and S. Bhattacharya.: *Transformerless intelligent power substation design with 15 kV SiCIGBT for grid interconnection*, Proc. IEEE ECCE, pp. 4225–4232, 2011.
15. H. F. Fan and H. Li.: *High frequency transformer isolated bidirectional DC-DC converter modules with high efficiency over wide load range for 20 kVA solid state transformer*, IEEE Trans. Power Electronics, vol. 26, no. 12, pp. 3599–3608, 2011.
16. H. S. Qin and J. W. Kimball.: *AC-AC dual active bridge converter for solid state transformer*, in Proc. IEEE ECCE, pp. 3039–3044, 2009.

CONTACT WITH THE AUTHORS

Zhendong Ji, Ph.D.

e-mail: zhendong_ji@126.com

tel.: +86 18936044964

School of Automation

Nanjing University of Science and Technology

Nanjing Jiangsu 210094

CHINA

LOW TO MIDDLE VIBRO-ACOUSTIC NOISE PREDICTION IN SHIP CABIN BY USING PLATE-CAVITY COUPLING MODEL

Zhenwei Zhou

Jiaming Wu, Ph. D.

School of Civil Engineering and Transportation, South China University of Technology

ABSTRACT

A plate-cavity coupling method based on modal expansion technique in the closed sound cavity was introduced, aiming at ship cabin structural noise. Using this method, a coupled equation was established. The structural vibration acceleration of the target cabin was extracted from a ship vibration response calculation, applied to the model. Then the target cabin noise value was obtained through numerical calculation. The effectiveness and reliability of the method were validated through experiments. The coupled model predicts noise in the cabin does not require fluid finite element model of the cabin air, thus greatly reducing the calculation time compared with the pure finite element method. It was shown that the method is suitable for the calculation of noise in a single ship cabin; the method has a high calculation efficiency. Furthermore, the calculated result is a continuum. On the one hand, it can be conveniently converted to an octave or 1/3 octave according to the specification. On the other hand, the form of the continuum also provides a corresponding response to the subsequent vibration and noise control.

Keywords: low to middle frequencies; vibration; ship noise; analysis model; rapid calculation method

INTRODUCTION

The revised draft of “Rules on Ship Noise Levels” was officially approved in the 1st meeting of Maritime Safety Committee (MSC) of the International Maritime Organization (IMO), in which, the noise level requirements for ships above 10,000 GT in habitats, medical districts, restaurants and entertainment sites are lower by 5 dB as a compulsory standard[1]. With the implementation of new standards for ship noise, ship noise has become an increasingly difficult problem for shipyards. Ship noise affects ship cabin comfort, lowers workers’ work efficiency, easily causes cardiovascular diseases and damages human health[2]. For ships, it may cause acoustic vibration and fatigue damage to ship

structure, affecting normal operation of cabin instrument and equipment. To reduce ship noise, a current common practice in engineering is to achieve targeted reduction of measured ship noise after the completion of ship building, but the actual effect of this practice is unsatisfactory. According to scholar statistics, installation of acoustic equipment on built ship costs about three times more than that done in ship design and building stage[3]. Therefore, it is necessary to accurately and quickly predict cabin noise during the ship design.

The methods for noise prediction usually include engineering estimation, theoretical analysis and numerical calculation[4]. Engineering estimation method is a semi-empirical and semi-analytic method mainly characterized

by convenient use and fast estimation speed. The examples are more studied transmission path analysis[5,6] and grey forecasting methods[7,8]. Engineering estimation method makes prediction based on measured data of parent ship, which provides high prediction accuracy when the predicted ship and parent ship share similar structural characteristic parameters (ship structure, equipment type, general arrangement, etc.). The method depends more on engineering personnel experience when the predicted ship differs greatly from the parent ship and engineering accuracy requirements will not be met in case of inaccurate parameter selection. Theoretical analysis method directly establishes coupling dynamic equations on structure and air to obtain acoustic radiation values of the structure through modal expansion and integral transformation[9-11]. The method has high solving efficiency and good calculation accuracy, but only applicable to geometric structures with simple analytical solutions and thus less applied in ship noise prediction. Numerical methods include statistical energy method, finite element method, boundary method, etc. Statistical energy method can only be applied to frequencies with higher modal density, merely able to calculate the average response level of the entire modal set in the statistical sense, and unable to obtain exact response of each modal, while finite element, boundary element methods are more applied to low frequencies owing to limited computer performance.

Noise is generally categorized into low frequency, intermediate frequency and high frequency noise according to the modal density or the number of vibration modes within the bandwidth[12]. There is no clear boundary between low-frequency and intermediate-frequency and between intermediate-frequency and high-frequency noise, and the division varies for different structures and different fields. Because of its short wavelength, high-frequency noise can be easily eliminated by common passive noise control measures such as widely used cotton felt materials. Reduction of low-middle-frequency noise requires sufficient cotton felt thickness and weight, thus inapplicable to ships with narrow cabins, making low-middle-frequency noise more harmful than high-frequency noise. Given large volume and complex structure of the ship, direct calculation of low to middle frequency noise using finite element/boundary element method requires establishment of finite element models for ship structure and sound field to make coupling calculation, which has such disadvantages of large-scale calculation and low solution efficiency in view of the current complex ship structure[13]. It often takes several days to seek solution in coupling model calculation of a cabin, which is time consuming, laborious, and costly.

Ship cabin can be studied as a closed cavity. Owing to its generally regular shape, solution can be directly obtained using theoretical analysis. The ship cabin noise is affected by structural noise, air noise and electromagnetic noise. According to superposition principle of acoustics, total sound pressure can be obtained via linear superposition of values of various noise types. Air noise and electromagnetic noise are generally produced by equipment on ships, which

involves simple estimation in which ship noise is mainly solved by calculating ship structural noise. The structure is strongly coupled to the air, so structural vibration will largely affect the noise level of the cavity to which it is coupled, while sound pressure in the cavity exerts little influence on structural vibration. The study on ship noise transmission path shows that structural noise is the main source of noise for cabins without indoor air noise sources, and the impact of air noise of the main engine and propulsion system is almost negligible for the distant living cabins. Therefore, structural noise prediction of the ship is the key to ship noise prediction. It is generally difficult to determine coupling of air and structure, and the total noise can be obtained by solving structural noise and then adding it with air noise and electromagnetic noise.

In view of the impact of the ship structural noise, this paper studies rapid calculation method targeted at single ship cabin. The ship noise is divided into two types: hull structure noise and equipment noise. Air impact on structure is limited, so structural vibration noise is the main source of indoor noise when there is no noise source in the cabin. The vibration acceleration value of the target cabin is extracted from the ship's finite element calculation model. For cabin that requires noise estimation, there is no need to establish a fluid finite element model for complex fluid-structure interaction calculation, and noise value of the target cabin can be obtained by directly establishing and solving the cavity-plate coupling model.

COUPLING MODEL

PLATE-CAVITY COUPLING MODEL

The cabin was studied as a closed chamber, which was surrounded by six thin plates. The source of sound pressure in the chamber was divided into two parts: the radiation of the plate and the noise source inside the cavity. Here only the coupling equation between the cavity and the single plate needs to be deduced. According to the principle of linear superposition, the coupling of the cavity and multiple plates is a linear superposition of the coupling of the cavity and the single plate. For the cavity, the control equation is:

$$\nabla^2 p - \frac{1}{c^2} \ddot{p} = -2\rho_0 \ddot{w} \delta(z - z_0) \quad (1)$$

In Eq. (1):

- c - Sound speed in air;
- ρ_0 - The density of air;
- p - Sound pressure in cavity;
- w - Vibration displacement of the plate.

For the plate, the control equation is:

$$D\nabla^4 w + m\ddot{w} = -p|_{z=z_0} \quad (2)$$

In Eq. (2):

- D – Bending stiffness;
- E – Young's Modulus;
- h – Thickness of the plate;
- ν – Poisson's ratio;
- m – Plate mass per unit area.

The modal expansion of the vibration displacement of the plate and the sound pressure of the cavity are write respectively by:

$$p = \sum_{n=0}^{\infty} \Phi_n P_n e^{i\omega t}, \quad w = \sum_{n=1}^{\infty} \varphi_n W_n e^{i\omega t} \quad (3)$$

Each mode of acoustics and structures meets the following characteristic equations, respectively:

$$\nabla^2 \Phi_n + \frac{\alpha_n^2}{c^2} \Phi_n = 0, \quad D\nabla^4 \varphi_n - \beta_n^2 m \varphi_n = 0 \quad (4)$$

In Eq. (4):

α_n, β_n – cavity and plate n th mode angular frequencies, respectively.

Substituting Eq. (4) into Eq. (1) and using the modal orthogonality, the decoupled equation can be obtained:

$$\frac{N_j^I}{\rho_0 c^2} (\omega^2 + 2i\xi_j^C \omega \alpha_j - \alpha_j^2) P_t = \omega^2 \sum_{n=1}^{\infty} C_{jn} W_n, \quad (5)$$

$$(\omega^2 + 2i\xi_j^P \omega \beta_j - \beta_j^2) M_j W_j = \sum_{n=0}^{\infty} C_{nj} P_n. \quad (6)$$

In Eq. (6) and Eq. (5):

$$N_j^I = \iiint_{\Omega} \Phi_j^2 d\Omega, \quad M_j = m \iint_s \varphi_j^2 ds, \quad C_{jn} = \iint_s \Phi_j \varphi_n ds$$

Note that the air damping $2i\xi_j^C \omega \alpha_j$ and structural damping $2i\xi_j^P \omega \beta_j$ have been considered in equations (7) and (8), respectively, where ξ_j^C is the air damping of the n th order, and ξ_j^P is the n th order structural damping. In the calculation, the values of n need to be convergent learning to be truncated, and then the modal responses in the cavity can be obtained by the simultaneous expressions (5) and (6). The calculated result can be obtained by modal superposition to obtain the sound pressure value at any point in the cavity.

POINT SOURCE

In addition to the noise generated by the hull structure, noise sources inside the cabin, such as indoor small mechanical vibration, noise generated by rotation, and air noise generated by air conditioning and ventilation, will also have an impact on the total noise value inside the cabin, and it is related to structural noise. Superimposed to get the total noise of the cabin. The source of the sound is used to simulate the noise source inside the cabin, and the source strength of the sound source is set to Q . The control equation in the cabin is:

$$\nabla^2 p - \frac{1}{c^2} \ddot{p} = -\rho_0 \dot{q} \delta(x-x_s) \delta(y-y_s) \delta(z-z_s) \quad (7)$$

Where (x_s, y_s, z_s) is the coordinates of the sound source in the cabin, and $q=Qe^{i\omega t}$ is the intensity of the sound source. Using the modal expansion method to solve equation (7) and get the result:

$$p = -\omega \rho c Q \sum_j \frac{(x_s, y_s, z_s)}{(\omega^2 - \alpha_j^2)} \Phi_j \quad (8)$$

SYNTHETIC SOUND PRESSURE LEVEL

The sound field in a cavity is usually a combination of multiple noise sources, and the total sound pressure is a vector superposition of multiple noise sources. Assuming that there are n noise sources, and each noise source has an independently generated sound pressure of $\mathbf{p}_i, i=1, 2, \dots, n$, the expression for the total sound pressure \mathbf{p} is

$$\mathbf{p} = \sum_{i=1}^n \mathbf{p}_i \quad (9)$$

The sound pressure of each frequency under the same position can be obtained by formula (9). The formula for the total sound pressure level decibel number for all frequencies is:

$$L_p = 10 \lg \left(\frac{1}{p_0^2} \sum_{j=1}^u p_j^2 \right) = 10 \lg \left(\sum_{j=1}^u 10^{0.1L_j} \right) \quad (10)$$

In Eq. (10):

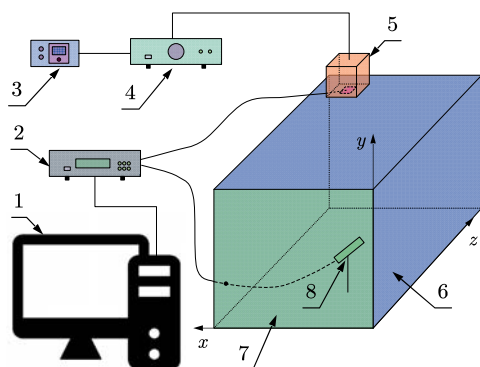
- L_p – Synthetic sound pressure level;
- p_0 – Reference sound pressure.

VALIDATION

Some simplifications have been made in the previous derivation process, and it is necessary to verify the stability and effectiveness of the procedure.

EXPERIMENTAL SETUP

Figure 1 shows a schematic of the experiment. A reverberation box made by high-density board with 25mm thick was used. The dimensions were: length(x) × height(y) × depth(z) = 0.6m × 0.8m × 1.0m. The reverberation box is open on one side and coupled to an aluminum plate. The four edges of the aluminum plate are fixed on the box by a bead. The modes are calculated according to the fixed boundary conditions. Calculations of the plate modal can use either analytical solutions[14–17] or finite element or measured results. This paper uses analytic solutions to perform the calculation[16,18,19]. The dimensions of the aluminum plate are: length (x) × width (y) = 0.6m × 0.8m, the Young's modulus of the aluminum plate is 69GPa, the Poisson's ratio is 0.3, and the plate thickness is 4mm. As shown in the coordinate system, the plane where the aluminum plate is located is the *xy* plane.



1. computer 2. dynamic signal analyzer 3. signal generator 4. amplifier
5. speaker 6. reverberation box 7. aluminum plate 8. microphone

Fig. 1. Experimental setup and related equipment connection

At the top of the box, there is a square hole 0.1m by 0.1m in the *xz* plane. The center of the square hole is [0.2, 0.8, 0.85], in meters, and a 6.5-inch speaker is installed as a sound source. There is a small cavity behind the horn to separate the horn sound from the outside world so that the horn produces only a forward plane wave. The interior of the small cavity is provided with sound-absorbing cotton, which reduces the volume of the cavity and makes the cavity not coupled with the large cavity actually tested. The actual excitation is a plane wave that enters the cavity from a square hole. Because the coupling of the plane wave and the cavity is more complicated, in the numerical simulation calculation, a point sound source is used instead of the plane wave for excitation. For the difference between the experimental model and the experimental device, corrections need to be made to ensure the accuracy of the calculation result. Cummings

gives a correction formula using a point source instead of a square hole [20]:

$$\bar{Q}(\mathbf{r}_c) = Q(\mathbf{r}_c) \prod_{i=1}^3 \sin(n_i \pi \varepsilon_i / 2l_i) / (n_i \pi \varepsilon_i / 2l_i) \quad (11)$$

Through the correction of this formula, the point source can be instead by the plane wave in the reverberation box.

MODE TRUNCATION

Since the modalities of the cavity and the plate in the formula are all extended to infinite order, the actual calculation needs to be truncated when the calculation accuracy is satisfied. In order to ensure the accuracy of the truncation, convergence learning should be performed. Choosing the fewest number of modalities involved in the coupling calculations, the whole system has higher accuracy and computational efficiency. It is a key issue for the modal expansion method to calculate. Assume that the frequency range of interest is $[f_{\min}, f_{\max}]$, f_{\min} and f_{\max} are the minimum and maximum values of the frequencies concern. The general truncation method is based on the principle of frequency truncation in modal superposition, and a certain multiple of f_{\max} is used to truncate the main mode. In the coupled system, each rectangular plate and each cavity can be regarded as a subsystem. The method of truncating the frequency of each subsystem is to adopt a certain multiple of the f_{\max} of the subsystem to perform the mode of the substructure. Truncated [21]. In general, taking 2 to 3 times of f_{\max} for truncation can achieve better accuracy [22]. In order to find the best cutoff frequency, convergence learning is performed and truncation is calculated by taking 1 to 3 times of f_{\max} respectively. In order to ensure that the calculated frequency covers all low frequencies with low modal densities, and that the comparison result has higher accuracy, the highest frequency of interest in the modal truncation calculation is taken as a slightly larger value, which is taken as 1200 Hz. Far more than the frequency of interest in actual calculations, it is used only for verifying the frequency truncation accuracy, and the smaller value actually used in the actual calculation is also guaranteed to be satisfied. See Table 1 for the order of the board and cavity.

Tab. 1. Convergence Learning mode of each structure

substructure	P_t	R	H
Plate	1	54	1202.3
	2	115	2399.7
	3	175	3592.1
Cavity	1	126	1207.6
	2	846	2399.9
	3	2671	3600

In Tab. 1:

P_t – Multiple of f_{\max} ;

R – Modal order retained;

H – The highest order modal frequency(Hz).

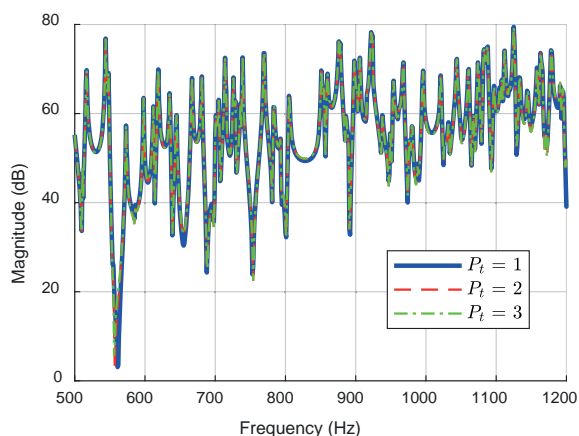


Fig. 2. Convergence Learning

Randomly select one point for the response calculation and compare the calculated results cut off at different frequencies. The coordinates of the arbitrary point taken are [0.1, 0.15, 0.05] in units of meters. In the frequency range of interest, when the error of the higher cutoff frequency calculation and the lower cutoff frequency is lower than the error, the lower cutoff frequency can be considered to meet the calculation accuracy requirement. The result of the response calculation is shown in Fig. 2. It can be seen from the figure that the response lines at Pt=2 and Pt=3 have completely coincided, which is slightly different from Pt=1. The difference between the calculations of Pt=2 and Pt=1 is a maximum of 6dB, and the average is 0.258 dB; the difference between Pt=3 and Pt=2 is a maximum of 0.87 dB, and the average value is 0.029 dB. The difference between Pt=3 and Pt=2 is very small, and the average difference of 0.029 dB is already within the calculated error range. Therefore, it can be considered that the calculation has converged when Pt=2. When Pt=2, the moduli of the plate remain the first 115 orders, and the cavities retain the first 846 orders, which can not only satisfy the calculation accuracy requirements, but also have high calculation efficiency.

VALIDATION OF SIMULATION MODEL

This section compares the measured and calculated noise. A microphone was installed inside the reverberation box to test the response of the cavity. The coordinates of the measured point is [0.12m,0.15m,0.05m]. White noise input was used for the speaker. To ensure the accuracy of the experiment, the white noise bandwidth should be more than twice the maximum frequency of interest, which is 2.5 kHz here. Since the actually used speaker is not an ideal device, the speaker's excitation of the air cavity is slightly different at each frequency. To eliminate the effect of sound source intensity, calculations and tests are performed using transfer functions instead of responses. An accelerometer was mounted on the speaker used as the excitation source, and the test data of the accelerometer and the microphone are simultaneously input to the dynamic signal analyzer to obtain the transfer function.

For the coupled model, the magnitude of the point source is Q , then the transfer function T is calculated by:

$$T = P/i\omega Q \quad (12)$$

The comparison between the calculated results of this section and the experimental results is shown in Fig. 3. It can be seen from Fig. 3 that the predicted noise value of the model agrees well with the measured value. In low frequency bands with low modal densities, formants with very high discrimination can be seen.

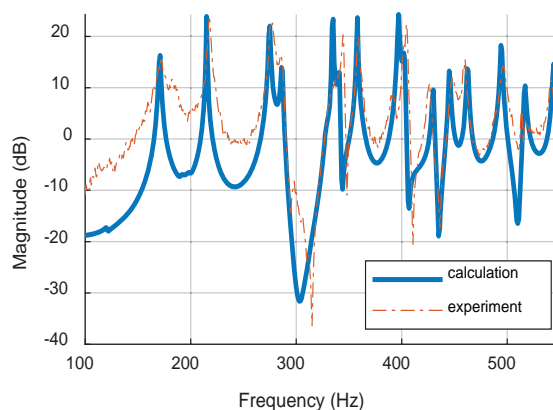


Fig. 3. Compare Experimental and Calculate Results

Tab. 2 shows the comparison of the first 10 measured peaks with the calculated peak position of the simulation. It can be seen from the table that, with the exception of the first peak occurring at 32 Hz, the other peak frequencies are all greater than 170 Hz, which is far from the 100 Hz region where the data in the experiment is not reliable. At the same time, the frequency difference between the calculation and the experiment is basically between 1 and 3 Hz and the maximum is not more than 5 Hz. From the viewpoint of the amplitude, the experimental results and the calculation results also basically coincide, and it can be considered that the results of this calculation model are reliable.

Tab. 2. Resonant Position Comparison

Peak No.	Model(Hz)	Experiment(Hz)	Error
1	170	171.5	-1.5
2	215	217	-2
3	275	277	-2
4	285	285	0
5	335	338	-3
6	359	360	-1
7	396	401	-5
8	430	426	3
9	445	447	-2
10	462	460	-2

The experimental device uses the air noise source as the excitation. In order to further understand the influence of the indoor sound source on the plate-cavity coupling model,

the six-sided rigid wall single cavity and the plate cavity coupling structure were compared, and the other settings remain unchanged. Fig. 4 is a comparison of the calculation results of the single cavity model and the plate-cavity coupling model. It can be seen from the figure that the single cavity model does not show a peak at 32 Hz. For the convenience of observation, the first 15 modes of the plate are marked with a vertical dotted line in Fig. 4 and the first 10 modes of the cavity are marked with a vertical solid line. It can be seen that in the case of the excitation source inside the cavity, the peak is mainly controlled by the cavity mode, and the first mode of the plate has the greatest influence on the cavity, and the effects of other modes on the response in the cavity are compared. Small, basically negligible. It can be seen that the coupling of air to the plate in the cavity is weakly coupled, the noise excitation inside the cavity has very little effect on the plate, and only a small resonance is excited at the first mode frequency of the plate. From Fig. 4, the resonance is located at a very low frequency, where the frequency is approximately 35 dB attenuated under the common A frequency weighting, so the total sound pressure value for the A weighting is almost negligible, in practical calculations. The influence of the coupling can be ignored directly, and it can be considered that the sound source inside the cavity and the sound source for the vibration of the plate structure can be calculated separately and independently without affecting the accuracy of the final result.

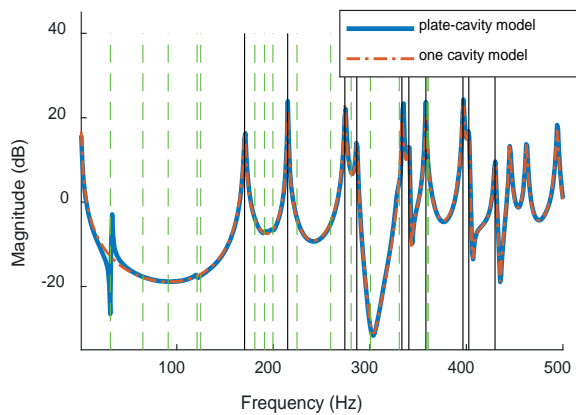


Fig. 4. Compare of Single Cavity and Cavity-Plate Model

In summary, it can be seen that it is completely feasible to divide the noise sources into cabin sound sources and structured sound sources and separate them. The method of analytical calculation is used to calculate the noise in the cavity, which has a very high calculation accuracy and can meet the requirements of ship noise prediction. The following will take a container ship as an example to calculate the noise of a ship in an upper cabin.

SHIP CABIN NOISE CALCULATION

STRUCTURAL NOISE SOURCES

The acceleration value of the structure extracted from the target cabin is used as the noise source. Fig. 5 shows the model of the target cabin. The model is part of a full-ship model for a container ship with a total length of 94.8 meters, a width of 15.4 meters and a depth of 6.9 meters. The main engine is a four-stroke inline six-cylinder diesel engine with a rated power of 1,618 kW at a speed of 600 rpm. Propeller diameter of 2.7 meters, 4 blades, speed of 200 rpm, the actual ship received power of 1522 kilowatts. According to China Ship Classification Society "Guide on Shipboard Vibration Control", ISO 6954-2000 Standard and ISO 6954-2000 (IDT) Standard, propeller excitation is considered and frequency response method is used to analyze the forced vibration response of the ship.

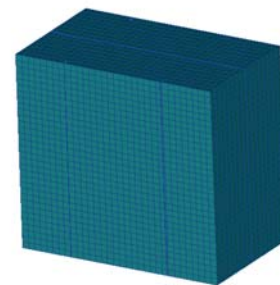


Fig. 5. Model of Target Cabin

The target cabin is located in the middle of the upper layer of the ship, with a height of 16.5m. There is no mechanical equipment that generates noise in the room. The noise source is structural vibration noise. The average acceleration curve of the extracted target cabin structure is shown in Figure 6. After obtaining the vibration acceleration of each wall of the target cabin, this acceleration is used as the excitation source of our coupling model to calculate the cabin vibration and noise.

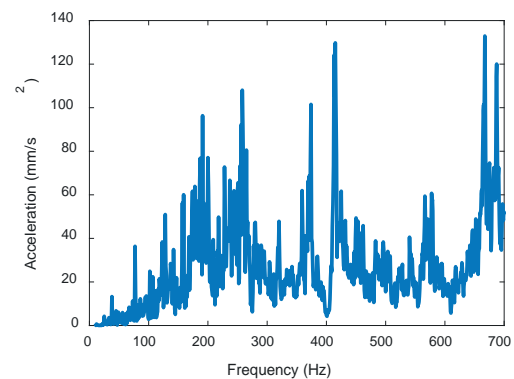


Fig. 6. Average Acceleration of the Target Cabin Structure

In order to apply the coupling model developed in the previous paragraph to the target cabin, the coordinate axes shown in Fig. 7 are established for the target cabin, where the x-axis is along the width of the ship, the y-axis is along the height of the ship, and the z-axis is along the length of the ship. The dimensions are: length (x) × height (y) × depth (z) = 2.5m × 2.3m × 1.5m. A coupled model was created and calculated for the chamber and the six plates coupled to this chamber. The boundary conditions of the six panels were all considered fixed. Using the acoustic superposition principle, the total sound pressure in the cabin is the sum of the acoustic pressure generated by the six plates coupled to the cavity.

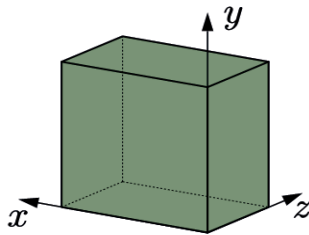


Fig. 7. Axis of Target Cabin

CALCULATION RESULTS

The result of the structural noise calculation is shown in Fig. 8. The positions of the two nodes are node 1: [1700mm, 500mm, 600mm] and node 2: [600mm, 1100mm, 300mm]. This result is the result of the continuous spectrum sound pressure level. According to the Chinese Society of Shipbuilding's "Guidelines for Control and Inspection of Ship and Product Noise Control and Detection", the method for calculation of cabin noise has a frequency interval of 1 Hz and meets the specification requirements. In order to better evaluate the impact of noise on the ship's environment and harm to the human body, according to the requirements in the guidebook, the continuum is converted into an octave and weighted by A level. The results are shown in Tab. 3.

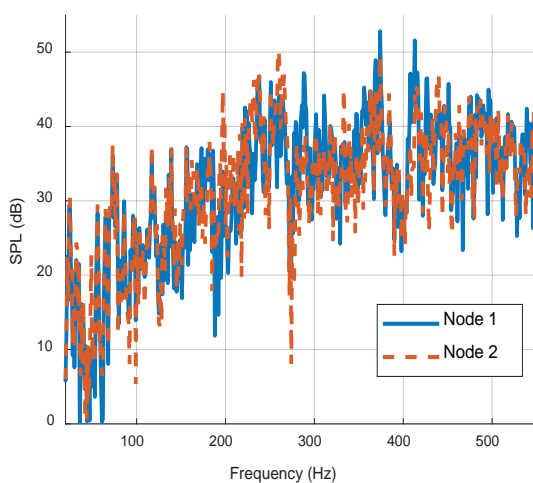


Fig. 6. Average Acceleration of the Target Cabin Structure

Tab. 3. Octave sound pressure and A – weighted total sound pressure

Octave (Hz)	Node 1 (dB)	Node 2 (dB)
31.5	32	28
63	38.5	36
125	41.4	41.7
250	49.2	50.8
500	56.9	57
total	59.2	59.6

When the ship goes straight along the design speed during the sea trial, the noise of node 1 and node 2 is measured using a sound level meter (BK 2250). The measurement frequency range was selected to be 20-550 Hz, and the total sound pressure measured was 61 dB (A) and 62 dB (A), respectively. Compared with the calculated value, the error of the two values does not exceed 3 decibels, which indicates that the calculation results using this method are more reliable and the precision required by the project is achieved.

CONCLUSIONS

In the acoustic coupling between air and structure, structural vibration generates noise in the air, and air vibration exerts very weak influence on the structure. The experiments in this paper show that when the structure encloses as a closed cavity, modal is produced in the cavity and cavity air exerts a very small effect on the vibration which is completely negligible in ship noise calculation. Therefore, in the calculation of ship cabin noise, noise falls into two categories, one is air noise, which generates noise in the cavity, and has no significant impact on structural vibration of the ship. The impact can be ignored as long as there is no such noise in and around the cabin. The other type of noise is structural noise which is generated by structural vibration of the ship. The plate-cavity coupling model developed in this paper is targeted at structural noise of the ship.

Most ship cabins are in relatively regular hexahedral shape, so it is very appropriate to apply this coupling model in cabin noise prediction. The prediction excitation derives from the calculation of the ship's finite element dynamic response. If such calculation is made for the ship in advance, direct data extraction is possible with strong adaptability. There is no need to establish finite element modeling of the fluid in the cabin. For a specific target cabin, workload of data extraction can be effectively controlled if data directly coupled to the cabin is obtained. With the finite element calculation results of ship vibration as the excitation, direct use of plate-cavity coupling model in calculation has low requirement for computer resource, and calculation only takes a few minutes if it is done on a computer with 16G memory. Nevertheless, it will take hours if air is modeled using full finite element calculation method for fluid-structure coupling calculation. The results were consistent with measurement index of real ship sailing tests when the coupling model was used to predict the cabin noise. This method is a good solution for forecast analysis of low-middle-frequency noise. Meanwhile,

continuous spectrum is obtained as the calculation result of the method. On the one hand, it can be easily converted to an octave and compared with the specification. On the other hand, the continuous spectrum also provides corresponding data basis for the subsequent vibration and noise control work.

ACKNOWLEDGEMENTS

This work was supported by a grant from the National Natural Science Foundation of China (No. 11372112).

BIBLIOGRAPHY

1. Kurt, R. E., Khalid, H., Turan, O., Houben M., Bos J., and Helvacioğlu I. H.: *Towards human-oriented norms: Considering the effects of noise exposure on board ships*, Ocean Eng., Vol. 120, pp. 101–107, Jul. 2016.
2. Kurt, R.E., McKenna, S. A., Gunbeyaz, S.A., Turan, O.: *Investigation of occupational noise exposure in a ship recycling yard*, Ocean Engineering., Vol. 137, pp. 440–449, Mar. 2017.
3. Ou, L.J., Li, D.Y., Ou, J.M., Xu, H.X.: *Prediction and Analysis of Ship Noise based on VA One*, Guangdong Shipbuilding, Vol. 143, no. 3, pp. 28–31, 2015.
4. Pang, F.Z., Yao, X.L.: *Numerical Research on Truncated Model Method of Ship Structural Borne Noise Prediction*. Harbin: Harbin Engineering University, 2012.
5. Gao, C., Yang, D.Q.: *Vibroacoustical Entropy Weighted Graph Method Transmission Path Analysis of Ship Cabin Noise*, JOURNAL OF SHANGHAI JIAO TONG UNIVERSITY, Vol. 48, no. 4, pp. 469–474, 2014.
6. Sun, Z.H., Wang, D., Yu, Y., Zhang, S.J.: *Engineering Prediction Approach for Shipboard Cabin Noise*, SHIP ENGINEERING, Vol. 36, pp. 246–251, 2014.
7. Yao, X.L., Dai, W., Tang Y.S.: *Grey Prediction of Ship Superstructure Cabins' Noise*. SHIP BUILDING OF CHINA, Vol. 47, no. 1, pp. 35–42, 2006.
8. Gui, Y.: *Prediction of Cabin Noise based on Grey System Theory and Reduction Technology Research*. SHIP ENGINEERING, Vol. 36, no. s1, pp. 243–245, 2014.
9. Zhou, J., Bhaskar A., Zhang X.: *Sound transmission through a double-panel construction lined with poroelastic material in the presence of mean flow*, J. Sound Vib., Vol. 332, no. 16, pp. 3724–3734, Aug. 2013.
10. G A. R., Sarathchandradas, M. R.: *Study and Analysis of Sound Transmission through Multilayered Structures Using Generalized Matrix Method*, Int. J. Emerg. Res. Manag. &Technology, Vol. 4, no. 11, pp. 119–125, 2015.
11. Alimonti, L., Atalla, N., Berry, A., Sgard, F.: *A hybrid finite element–transfer matrix model for vibroacoustic systems with flat and homogeneous acoustic treatments*, J. Acoust. Soc. Am., vol. 137, no. 2, pp. 976–988, Feb. 2015.
12. Yu, D.P., Zhao, D.Y., Wang Y.: *Influence of damped material and the ship model of acoustic on the ship cabin noise*, Journal of Ship Mechanics, Vol. 14, no. 5, pp. 539–548, 2010.
13. Liu X.M., Wang, X.Y., Chen, C.H.: *Numerical analysis of low and middle frequency noise in ship cabin using fluid-structure coupling*, Journal of Ship Mechanics, Vol. 12, no. 5, pp. 812–818, 2008.
14. Taylor, R.L., Govindjee, S.: *Solution of clamped rectangular plate problems*, Commun. Numer. Methods Eng., Vol. 20, no. 10, pp. 757–765, Jul. 2004.
15. LI, W.L., Daniels, M.: *A Fourier series method for the vibrations of elastically restrained plates arbitrarily loaded with springs and masses*, J. Sound Vib., Vol. 252, no. 4, pp. 768–781, May 2002.
16. Li, W.L., Zhang, X.F., Du, J.T., Liu, Z.G.: *An exact series solution for the transverse vibration of rectangular plates with general elastic boundary supports*, J. Sound Vib., Vol. 321, no. 1–2, pp. 254–269, Mar. 2009.
17. Zhong, Y., Zhang, Y.S.: *Free vibration analysis of a thin plate with completely supported by finite cosine integral transform method*, Journal of Ship Mechanics Vol. 12, no. 2, pp. 305–310, 2008.
18. Xin, F.X., Lu, T.J., Chen, C.Q.: *Vibroacoustic behavior of clamp mounted double-panel partition with enclosure air cavity*, J. Acoust. Soc. Am., Vol. 124, no. 6, pp. 3604–3612, Dec. 2008.
19. Xin, F.X., Lu, T.J.: *Analytical and experimental investigation on transmission loss of clamped double panels: Implication of boundary effects*, J. Acoust. Soc. Am., Vol. 125, no. 3, pp. 1506–1517, Mar. 2009.
20. Cummings, A.: *The effects of a resonator array on the sound field in a cavity*, J. Sound Vib., Vol. 154, no. 1, pp. 25–44, Apr. 1992.
21. Li, H., Li, G.: *Component mode synthesis approaches for quantum mechanical electrostatic analysis of nanoscale devices*, J. Comput. Electron., Vol. 10, no. 3, pp. 300–313, Sep. 2011.
22. Li, X.Q., Deng, Z.X., Li, C.B., Zhang, J.C, Li, Y.Q.: *Substructure Normal Modes Selection Method for Component Mode Synthesis*, JOURNAL OF SOUTHWEST JIAOTONG UNIVERSITY, Vol. 49, no. 1, pp. 173–178, 2014.

CONTACT WITH THE AUTHORS

Zhenwei Zhou

e-mail: zw.zhou@hotmail.com

tel.: 17098908599

School of Civil Engineering and Transportation

South China University of Technology

Guangzhou, Guangdong, 510641

CHINA

RESEARCH ON KEY PROCESS TECHNOLOGY FOR PROFILE ELECTROLYTIC FINISHING OF LARGE MARINE PROPELLER IMPELLER

Bi-Rong Ding, Ph. D.

Yuan-long Chen*, Professor

Ji Zhou, Professor

Pei-xuan Chen, Ph. D.

School of Mechanical and Automotive Engineering, Hefei University of Technology, Hefei, Anhui, China

ABSTRACT

An electrolysis process method for free-form blade surface finishing is proposed for a free-form surface impeller, and a stepwise method is used to process the inter-blade channel of the overall impeller. The forming cathode is then used to finish the blade to meet the blade processing requirements. In the design, the forming cathode structure was improved by using motion simulation software, and the flow field simulation software was used to simulate and analyze the cathode flow channel. The cathode shape and the electrolyte flow rate between the electrodes meet the processing requirements. In the process of processing experiments, the motion path of the cathode was analyzed and optimized. The effect of the feed direction on the uneven distribution of the blade machining gap was reduced through optimization, and high-frequency pulse power processing was used to reduce the machining gap and improve the machining accuracy of the blade. The experimental results show that the process scheme is feasible and the precision of the processed impeller free-form surface is significantly improved. The material is a monolithic turbine disk of high-temperature alloys, and its large twisted blade processing has always been a problem in the manufacturing industry.

Keywords: Integral impeller; Electrolysis processing; Blade

INTRODUCTION

In order to improve the precision of the overall impeller electro-chemical machining, it is planned to use the electrolytic machining method combined with numerical control and forming cathode copy forming to perform free-form surface impeller blade finishing. The combined electrolytic machining method divides the blade machining of the integral impeller into two basic steps of the inter-leaf path machining and the blade surface finishing. In the process of process design, digital manufacturing technology is used to solve the problems of cathode design, parameter selection and machining path in the process of free-form surface impeller blade [1, 2, 3]. In the design of electrolytic machining device for blade finishing, the structural forms that can be considered are open and closed. The closed structure uses a sealed chamber to form a closed electrolyte flow interval. Through the construction of the closed space to control the direction of flow of the electrolyte, so that the electrolyte flow according to the design of the path, the

pressure of the import and export is easy to control [4, 5, 6]. Due to the small space between the two blades of the impeller, the design of the sealing device is difficult. The open processing device uses a high-speed flowing electrolyte to form a machining gap flow field to meet the processing requirements. Since the open processing device does not require excessive sealing, the cathode movement is limited. Therefore, the open machining device is used to develop the overall impeller finishing process experiment [7, 8, 9].

The channel of the shaped cathode consists of an inlet, a delivery zone, a transition zone, an outlet, and a diversion zone. It also changes the flow of the electrolyte from columnar to slit-like, through the outlet of the liquid outlet, and then flows along the surface of the cathode into the processing gap under the action of the deflector. In order to grasp the flow velocity distribution in the machining gap, the flow field analysis was performed using CFX software in the design. When designing a shaped cathode shape, it must be done in the inter-blade channel space that has been machined [10, 11, 12]. Due to blade

distortion, the formation of the cathode must be considered. To prevent the occurrence of motion interference, the initial shape of the cathode is first determined according to the size of the leaves during the design, and then numerical simulation software is used to simulate the path of the cathode into the inter-leaf channel to observe the collision or interference between the cathode and the blade. In order to simulate the cathode movement during the design of the cathode design using motion simulation software, the cathode structure was modified by simulation result to avoid the interference between the cathode and the blade and the tooling. The cathode can smoothly enter the inter-leaf channel and complete the processing feed movement. In addition to considering the cathode profile, cathode profile design is also required. In the profile design, the influence of the flow field and feed motion on the blade machining accuracy is considered. In the design, the profile of the blade is used as the initial surface of the cathode. Based on this, the effects of the flow field and the feed direction on the profile are taken into consideration [13, 14, 15]. The profile is corrected and the machining requirements are achieved after multiple corrections. Figure 1 is the finished blade shape.

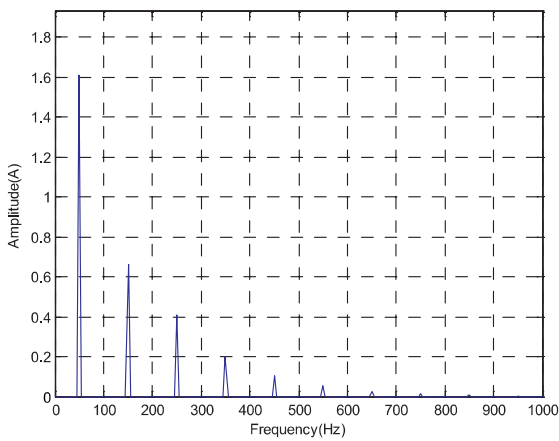


Fig. 1. Finished integral impeller

BLADE FINISHING DEVICE DESIGN

In the simulation software developed based on UG, the machining model was compared with the original blade geometry model. Sample data points are taken from the original blade surface as the analysis target of the machining error. After these points are used as normal to intersect with the machining blade geometry model, the distance between the two intersection points is obtained. This distance is the machining error. Compared with the generative method, the precision of the blade using the forming cathode machining has been greatly improved, but there is still no requirement for processing. The cathode surface correction method is used to further improve the machining accuracy. Because it is very difficult to directly measure the machining clearance of the blade, there is currently no direct method for measuring the machining gap of the formed cathode blade, but the gap distribution of the blade forming cathode machining can be indirectly calculated. Using the CAD software and its analysis tools to compare the blade geometry model with the cathode profile, the gap distribution

of the electrolytic machining of the blade can be obtained. Take some sampling points on the surface of the cathode and calculate the normal distance from the sampling point to the processing surface of the blade or set the distance in the direction of the self. The distance is the processing gap of the blade obtained through analysis and calculation. By correcting the profile of the cathode by the distribution of machining gaps, the machining accuracy of the blade is improved.

Using simple-form cathode NC machining to produce pre-channel pre-channels, and then using a shaped cathode for precision electrolytic machining can significantly improve the machining accuracy of the blade profile. This is an effective technical approach to achieve efficient and precise overall manufacturing of the free-form blade vanes. The forming cathode and special tooling design method used in the experiment can meet the flow field requirements of the overall impeller blade profile electrolytic machining, and the processing process is stable. The proposed method for determining and optimizing the forming direction of the cathode feed can significantly improve the distribution of gaps in the machining of complex profile electrolysis machining, and it is beneficial to improving the machining accuracy. They operate at high temperatures, high pressures, and high rotational speeds. Such turbines must use high-temperature heat-resistant alloy materials, and machining is very difficult. In particular, the twisted blade profile machining of integral turbine disks has always been a problem in the manufacturing industry. Develop an electro-chemical machining integrated turbine. According to the electro-technical gap and the theoretical plane of the blade to determine the generative feed trajectory, refer to the characteristics of the machine tool numerical control system, and use computer-aided programming software to generate a multi-axis linkage NC program. The cathode must be designed according to the minimum cross-section of the inter-bay channel. The one-time production process can meet the accuracy of one side of the blade, and then the channel is formed. Electrolyte leak due to no back pressure, can no longer use the same method of processing the other side, variable cross-section residual processing margin must be hand polished. Fig. 2. is the establishment of a differential equation.

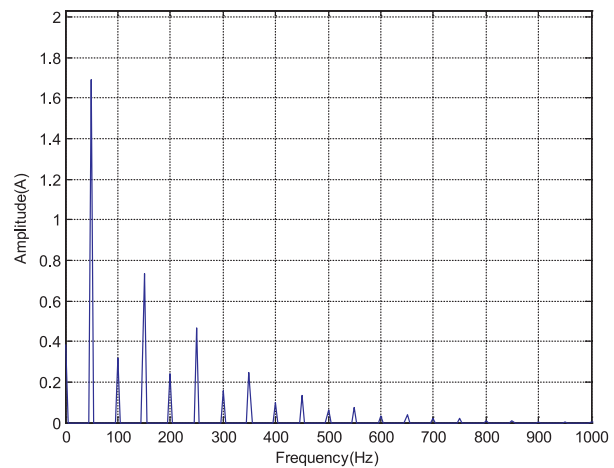


Fig. 2. Multi-axis linkage and composite plane swing development electrolysis schematic

There are many factors affecting the accuracy of CNC integral electrolysis machining of impeller blades, including cathode and fixture manufacturing errors, machine tool movement errors, machining movement trajectory, electrochemical machining cuts, and initial machining gaps. The discussion of the manufacturing error between the cathode and the fixture is not discussed here. Due to the special nature of the impeller's electrolytic processing, there is also the deviation of the processing trajectory caused by electrolytic secondary corrosion processing, processing principles and machining gap. They are the main cause of electrolytic machining errors in the overall impeller blade.

COMPOUND PLANE SWING FEED FORMING STRIPE

Multi-axis linkage NC programming is generally based on the leaf basin surface, the cathode left blade vertex is based on the programming reference of the leaf cylinder root cylinder. Due to the large distortion of the blade, the right edge of the cathode in certain area will cut into the root cylinder. Large-deflection blade profile processing, x, y, and large rotary feed, electrolyte pressure fluctuations, in the liquid-liquid shortage area or weak electrolysis of small flow rate, easy to produce surface convex. A short circuit will scrap the turbine as a whole and cause major economic losses. During the processing, the electrolyte flow field is stable and the test system is reliable. The surface of the blade after machining has no flow and metallographic defects. The leaf basin surface is used as the programming basis for multi-axis linkage feed, and additional swing feed electrolytic machining eliminates the leaf back margin. There is a principle error in the data processing of the discrete points of the blade surface; due to the distortion of the profile, the feeding speeds of the cathode and the blade along the y-axis are different, and the electrolytic gaps at the points of the same section may also be different. Changes in electrolytic parameters can also cause gaps in different cross-sections to create machining errors.

The adoption of a composite swing feed processing scheme allows one-time feed electrolysis to produce leaf and blade back profiles, shortening the auxiliary time, and effectively increasing productivity. The design of a combined cathode with a fluid flow field can effectively solve the problem of over-cutting secondary corrosion of blade backs with processed blades. The stability of electrolysis parameters is maintained, and the will have good repeatability of accuracy. The composite swing feed development and electrolytic processing is particularly suitable for batch processing of the overall turbine with large twisted blades. The use of double-sided feeding can effectively eliminate hidden faults such as electrolytic short-circuit and ensure the stability and precision of machining process. The adoption of a composite swing feed processing scheme allows one-time feed electrolysis to produce leaf and blade back profiles, shortening the auxiliary time, and effectively increasing productivity. The design of a combined cathode with a fluid flow field can effectively solve the problem of over-cutting secondary corrosion of blade backs with processed blades. The use of double-sided feeding can

effectively eliminate hidden faults such as electrolytic short-circuit and ensure the stability and precision of machining process. Figure 3 is a decryption program.

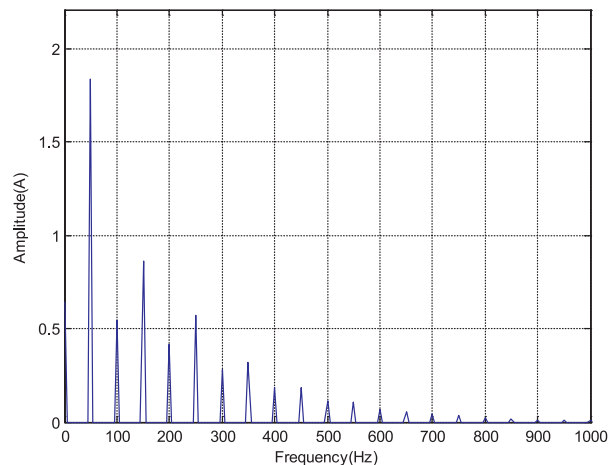


Fig. 3. Decryption program flow diagram

A cathode with a triangular cross-section has a good rigidity and a relatively large flow area, but when machining a small-sized integral impeller, the space between the leaves is limited due to the narrow passage between the leaves. The upper surface of the cathode has a large surface area facing the non-machined surface in the inter-bay channel, which can easily cause secondary corrosion of the non-machined surface. Furthermore, for cathodes of this structure, it is generally not easy to use the same cathode to process both the surface of the leaf pot and the back surface of the leaf, and it is necessary to design and fabricate cathodes for the surface of the leaf pot and the back surface of the leaf, respectively. The main parameters of the model are set up as shown in Tab. 1:

Tab. 1. DC voltage and flux of 3-phase knockdown transformer

U	I	I_a (A)	I_c (A)	M	ψ_c (Wb)
0	3.086	-0.0006	1.2732	-0.0907	1010.8835
50	4.574	0.1920	1.4134	27.6574	1010.9129
100	6.029	0.3217	1.6458	42.3184	1011.5332
200	54.250	1.9537	8.5633	74.8972	1013.0832
500	361.339	29.3409	91.7897	158.5843	1019.5658
1000	6.029	0.3217	1.6458	42.3184	1011.5332
1500	54.250	1.9537	8.5633	74.8972	1013.0832
2000	361.339	29.3409	91.7897	158.5843	1019.5658

At present, most of the researches on the overall impeller electrolytic machining are the NC development method, also known as sweeping method or envelope method. Different CNC machining methods have different machining accuracy in the leaf pot, leaf back, and root, and the applicable overall impeller type is also different. The controlled growth method is mainly applicable to the ruled surface integral impeller blade processing. If it is used to process the integral

impeller composed of non-pregnant surface, the processing error is large, especially the blade back and the blade root cannot satisfy the processing requirements of the freeform surface blade. Therefore, it is necessary to further study new processing methods in the overall impeller machining process.

VALIDATION OF SIMULATION MODEL

Generally, stainless steel is more suitable. Since the shape of the cathode is very irregular, especially the cross-section of the internal flow passage is greatly changed, and the front-end size is small, it is difficult to manufacture it by the conventional cutting processing method, so the electro-discharge molding method is used for processing. The integral blade disk is the core component of the new aero engine. It integrates the blade and the wheel disk instead of the way the hammer head and tongue groove are connected through the locking plate, which reduces the number of engine parts and reduces the weight. This can effectively improve the engine's stability and weight-to-weight ratio. Fig. 4. is the machining gap and feed depth curve.

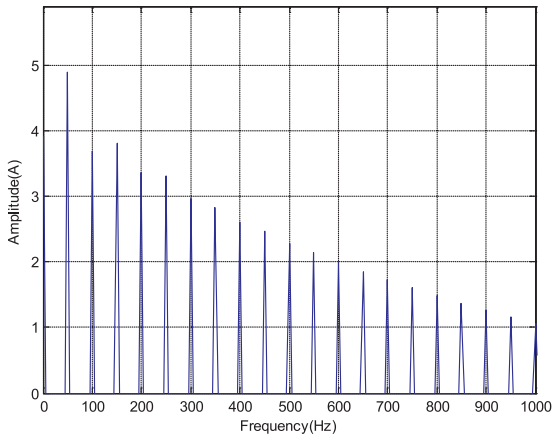


Fig. 4. Processing gap and feed distance

This paper first analyzes the genetic error theory to study the effect of genetic errors on the overall precision of leaf disk electrolysis processing. Before blade-surface electrolytic machining reaches an equilibrium state, the machining gap continuously changes with time, which belongs to the gap transition process of electroforming. Through the above-mentioned theoretical analysis, it can be known that the genetic errors and fluctuations of the blank after electrolysis rough machining of the overall blade cascade channel have little effect on the repeatability of electrolytic machining.

Therefore, the main factor causing the processing error is the fluctuation of the machining gap:

$$\begin{cases} (R_B - R_{AB}) / (R_A R_B - R_{AB}^2) = 1 / R_{AA} \\ (R_A - R_{AB}) / (R_A R_B - R_{AB}^2) = 1 / R_{BB} \\ -R_{AB} / (R_A R_B - R_{AB}^2) = -1 / M_{AB} \end{cases} \quad (1)$$

Consider the distance d between the two grounding bodies in the actual project is relatively large:

$$\begin{cases} R_{AA} = R_A \\ R_{BB} = R_B \\ M_{AB} = R_A R_B / R_{AB} \end{cases} \quad (2)$$

Equation of conductor potential and scattered current:

$$G_h \phi_N - G'_h V_M = I_M \quad (3)$$

In the process of leaf disk electrolysis, high-speed and high-pressure electrolytes flow through tiny machining gaps, making it difficult to detect them directly:

$$I_d^0 = \begin{bmatrix} I_{d(1)}^0 \\ 0 \\ M \\ 0 \end{bmatrix} = \begin{bmatrix} I_s \\ 0 \\ M \\ 0 \end{bmatrix} \quad (4)$$

According to the rule of electrolytic machining, when the feed rate of the tool electrode and the corrosion rate of the anode are basically the same, the electrolytic processing reaches an equilibrium state:

$$G_{k(i,j)} = \frac{1}{R_{g1(i,j)} + R_{g2(i,j)} + R_{l(i,j)} / 3 + R_{t1(i,j)} / 3 + R_{t2(i,j)} / 3} \quad (5)$$

According to Ohm's law and Faraday's law, the basic equation for electrolytic machining equilibrium gap is:

$$\begin{bmatrix} I_{d(1)}^1 \\ I_{d(1+n_1)}^1 \\ I_{d(1+n_1+n_2)}^1 \\ M \\ I_{d(1+n_1+n_2+\dots+n_a)}^1 \end{bmatrix} = \begin{bmatrix} I_{k(1)}^0 \\ I_{k(2)}^0 \\ I_{k(3)}^0 \\ M \\ I_{k(a)}^0 \end{bmatrix} \quad (6)$$

The relationship between the electrolysis of the current density is:

$$R = \frac{\rho}{2\pi^2 D} \ln \frac{16D^2}{hd} \quad (7)$$

It can be seen that the processing current is closely related to the machining gap. The current change leads to the fluctuation of the electrolytic machining gap, which makes the difference in blade thickness and profile after each processing, thereby affecting the consistency of the overall blade disk type surface electrolytic machining:

$$G_l \phi_N - G'_l V_M = I_d \quad (8)$$

In the past overall impeller machining test, a large-diameter integral impeller was processed using the blade back

modification method. It first processed the inter-blade channel on the basis of the leaf basin, and then finished the blade back. From the processing principle point of view, this processing scheme is feasible, and it can simultaneously improve the precision of electrolytic machining of leaf pots and leaves. From the test results, the main disadvantage is that the margin of one-pass machining in the blade back correction processing is small, and the number of cutting passes is relatively large. The processing based on the leaf pot still results in overcutting of the root. Based on the past processing technology and combined with the characteristics of the whole impeller, a new step-by-step method for impeller blade machining was proposed. The overall impeller blade electrolytic machining method divides blade processing into multiple steps.

In the alternative of blade root processing, it is difficult to design and process the profile of the shaped cathode, and a set of electrolyte sealing device is needed. The cathode needs to be rotated to enter the channel between the leaves. The cathode structure adopted in the NC generative method is simple. However, the calculation of the trajectory is relatively complex. Taking into account the above factors, the NC generative machining program is used to process the roots of the leaves. Through process simulation and other technical means, the processing area of each process is properly divided so that the shape processed by the previous process can meet the processing requirements of the next electrolytic processing process, thus achieving the continuous processing of the blade.

CONCLUSIONS

For the liquid ejecting part of the front end of the cathode, the inside should be smoothly transitioned, and the cross-sectional area of the channel should be gradually reduced to avoid drastic changes. The angle between the discharge direction of the electrolyte and its inlet direction is large. This may result in insufficient electrolyte at the end of the liquid outlet during processing, causing a short circuit in severe cases, as well as damage to the cathode and the due to burns. In order to make the electrolytic processing work smoothly and ensure the cathode has a long service life, the cathode material should have good conductivity, high strength, and strong corrosion resistance. Generally, stainless steel is more suitable. Since the shape of the cathode is very irregular, especially the cross-section of the internal flow passage is greatly changed, and the front-end size is small, it is difficult to manufacture it by the conventional cutting processing method, so the electro-discharge molding method is used for processing. There is a principle error in the data processing of the discrete points of the blade profile; due to the distortion of the profile, the feeding speeds of the cathode and the blade along the y-axis are different, and the electrolytic gaps at the points of the same section may also be different. Changes in electrolytic parameters can also cause gaps in different cross-sections to create machining errors. The feed direction of the cathode is optimized in the axial plane, and the feed direction optimization process of the axial plane is the

same as the optimization process of the radial cross section. Because the blade surface is a space curved surface and the feed direction is space vector, the three-dimensional cathode feed optimization calculation is more complex. Therefore, the three-dimensional feed direction optimization of the cathode is divided into two steps: radial in-plane optimization and axial in-plane optimization. In addition to considering the cathode profile, cathode profile design is also required. In the profile design, the influence of the flow field and feed motion on the blade machining accuracy is considered. In the design, the profile of the blade is used as the initial surface of the cathode. Based on this, the effect of the flow field and the feed direction on the profile is taken into consideration. The profile is corrected and the correction is achieved after many corrections

ACKNOWLEDGEMENTS

The study was supported by “Study on the mechanism and technology of electrochemical etching of large scale refractory metal single crystals selectivity”(Grant No.NSFC 51775161). First of all thank my tutor. He gave my guidance in the various stages of project research, such as project demonstration, research plan determination, and processing experiment, and pointed out the direction for the research of the project. Mr. Xu used his solid theory in electrolysis processing and the long-term accumulated experience in electrolysis processing to help me overcome one challenge after another at the critical moment of research. In order to make the electrolytic processing work smoothly and ensure the cathode has a long service life, the cathode material should have good conductivity, high strength, and strong corrosion resistance. In order to solve the problem of free-form surface impeller blade finishing, expand the application of electrolytic machining process in the overall impeller processing, and combine the NC development method and the forming cathode processing in the machining process to develop the integrated impeller combined electrolysis plus process research. On this basis, further study of the overall impeller blade finishing method and its forming law, using the forming cathode to achieve blade finishing.

REFERENCES

1. Wang, S.j., Yuan, P., Li, D., Jiao, Y.H.: *An overview of ocean renewable energy in China*, Renew Sustain Energy Rev, Vol. 15, no. 1, pp. 91–111, 2011.
2. Vanyashov A D, Karabanova V V, Vasenko E M.: *Influence Analysis of Flow Entry Conditions on the Centrifugal Compressor Impeller Blades to Integral Gasodynamic Characteristics in a Combine Regulation Method*. Procedia Engineering. Vol. 17, no. 1, pp. 389–394, 2016.
3. Ravi, S., Peltier, S. J., & Petersen, E. L.: *Analysis of the impact of impeller geometry on the turbulent statistics inside a fan-stirred, cylindrical flame speed vessel using piv*. Experiments in Fluids, Vol. 34, no. 6, pp. 1 16, 2013.

4. Mongeau L G, Thompson D E, Mclaughlin D K.: *Aerodynamic noise generated by a centrifugal pump impeller*. Journal of the Acoustical Society of America, Vol. 17, no. 1, pp. 87:S80 S80, 1990.
5. Seralathan S, Chowdhury D G R.: *Modification of Centrifugal Impeller and Effect of Impeller Extended Shrouds on Centrifugal Compressor Performance*. Procedia Engineering, Vol. 64, no. 2, pp. 1119–1128, 2013.
6. Rao, M. A., & Brodkey, R. S.: *Continuous flow stirred tank turbulence parameters in the impeller stream*. Chemical Engineering Science, Vol. 27, no. 1, pp. 137–156, 1972.
7. Kai U Z, Gallus H E, Niehuis R.: *A Study on Impeller-Diffuser Interaction — Part I: Influence on the Performance*. Journal of Turbomachinery, Vol. 125, no. 1, pp. 545–556, 2003.
8. Gagg C R, Lewis P R, Tsang C.: *Premature failure of a vacuum pump impeller rotor recovered from a pitch impregnation plant*. Engineering Failure Analysis, Vol. 15, no. 5, pp. 606–615, 2008.
9. Capus J.: *Industry Roadmap, update from MPIF*. Metal Powder Report, 67(4):10–11, 2012.
10. Hilton E F, Allaire P E, Baloh M J, et al.: *Magnetic suspension controls for a new continuous flow ventricular assist device*. Asaio Journal, Vol. 43, no. 5, p. 598.
11. Chatzi E G, Kiparssides C.: *Steady-state drop-size distributions in high holup fraction dispersion systems*. Aiche Journal, Vol. 43, no. 5, pp. 1640–1652, 2010.
12. Radl S, Kalvoda E, Glasser B J.: *Mixing characteristics of wet granular matter in a bladed mixer*. Powder Technology, Vol. 200, no. 3, pp. 171–189, 2010.
13. Botros K K.: *Developments in Centrifugal Compressor Surge Control-A Technology Assessment*. Journal of Turbomachinery, Vol. 116, no. 4, pp. 240–249, 2012.
14. Abu-Eishah S I, Abu-Jabal N M.: *Parametric study on the production of phosphoric acid by the dihydrate process*. Chemical Engineering Journal, Vol. 201, no. 1, pp. 231–250, 2003.
15. Trebinjac I, Claudin I.: *Results and analysis of a L2F flow field investigation within a high-speed high-pressure centrifugal compressor*. Journal of Thermal Science, Vol. 6, no. 3, pp. 155–163, 1997.
16. Darmana D, Deen N G, Kuipers J A M.: *Numerical study of homogeneous bubbly flow: Influence of the inlet conditions to the hydrodynamic behavior*. International Journal of Multiphase Flow, Vol. 35, no. 12, 1077–1099, 2009.

CONTACT WITH THE AUTHOR

Bi-Rong Ding, Graduate for Ph. D.

e-mail: dingbirong@126.com

tel: 13856007895

School of Mechanical and Automotive Engineering
Hefei University of Technology
Hefei, Anhui, 230009
CHINA

RESEARCH ON OPTIMIZATION MODEL OF MARINE INDUSTRY STRATEGIC ADJUSTMENT UNDER COMPLEX MARITIME CONDITIONS BASED ON ANT COLONY ALGORITHM

Xiao Shen, Ph. D.

School of Business, Xinyang Normal University, Xinyang, Henan , China

ABSTRACT

This article seeks to analyze the factors constraining the development of strategic marine emerging industries and the deficiencies in China's strategic marine emerging industry development policies. Learn from the successful experiences of overseas strategic marine emerging industry development policies. We will study and construct a policy framework for the development of strategic marine emerging industries in the new era, guided by the scientific concept of development and enhanced by the capacity of independent innovation. Provide policy recommendations for actively promoting the development of strategic marine emerging industries. At the same time, it provides theoretical and methodological reference for the formulation and implementation of China's strategic marine emerging industry policies. On the basis of reviewing relevant theories of industrial policy, this article first defines China's strategic emerging industries and clarifies the connotation of China's strategic marine emerging industry development policies. Then, the paper conducts detailed analysis on the development policies of strategic marine emerging industries at home and abroad, and summarizes the experience of overseas strategic development policies for marine emerging industries. Finally, combining the above-mentioned comprehensive analysis, with the guidance of the scientific concept of development, the development strategy and concrete development policy of China's strategic emerging industries in the ocean are proposed.

Keywords: Ant colony algorithm; Complex maritime; Marine industry strategy

INTRODUCTION

To judge whether an industry is strategic or not, it usually depends on whether the industry can stand at the height of the national strategy and exert an important influence on economic development. Whether it can support the current economic operation and future economic growth, whether it can promote and guide the development of national economy and industrial structure, and whether it can represent the direction of future economic development and technological progress [1,2,3]. Strategic industries are not determined based on the local interests of the industry, nor are they only related to the development of the industry itself. They are related to the division of labor status of a country in the process of globalization and to the overall national strength and

economic competitiveness of a country. To become a strategic industry must also have three basic characteristics: First, can quickly and effectively absorb innovation results, and access to new production functions associated with new technologies [4,5,6]. There is a huge market potential, is expected to obtain sustained high-speed growth. The third is that the correlation coefficient with other industries is relatively large, which can drive the development of related industries.

For a strategic emerging industry, it is necessary to possess key core technologies, have the characteristics of low resource energy consumption, large driving coefficient, multiple employment opportunities, and comprehensive benefits. Strategic marine emerging industries must be able to embody the country's marine strategic intentions, and

play a positive role in the transformation of marine economic growth patterns and the adjustment of the marine industrial structure. Therefore, in the post-financial crisis era of the 21st century, China's strategic emerging industries in the ocean mainly refer to the ability to embody the nation's strategic intentions in the ocean [7,8,9]. With the ocean and high-tech as its chief feature, it has broad market prospects and huge potential for development in marine economic development. It can lead the development direction of the marine economy, and promote the development of the marine industry witch based on the definition of strategic marine emerging industries and the connotation of industrial development policies, strategic marine emerging industry development policies refer to the needs of marine economic development as the starting point. According to the characteristics of strategic marine emerging industries, the total number of plans, plans, measures, and laws and regulations formulated in terms of resource allocation and industrial regulation for the development of strategic marine emerging industries [10,11,12].

Ant colonies can always find the shortest path from the nest to the food source, because the individual ants transfer information through a substance called Pheromone. Ants can stay on their way and perceive it in motion and use it to guide their direction of action. The ant colony's collective behavior manifests itself as a kind of positive feedback phenomenon of information: The more ants that go on a certain path, the greater the probability that the latter ant will choose this path until it finds the shortest path from the nest to the food source. This process is called the autocatalytic behavior of ants [13,14,15].

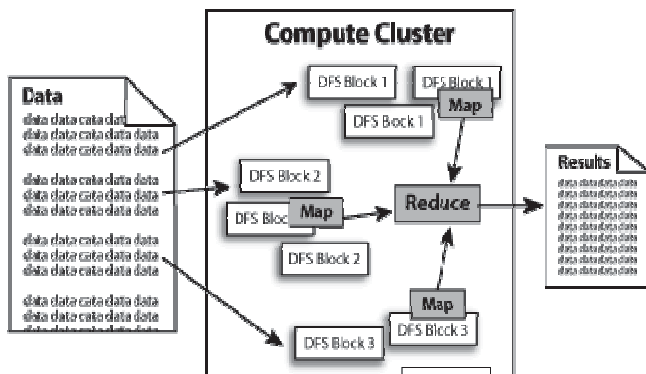


Fig. 1. Group project management resource dynamic scheduling model

ANT COLONY ALGORITHM

The scheduling of resources among group projects is one of the hot and difficult issues in project management in marine engineering and other fields. After analyzing the characteristics of this problem and subtly defining the heuristic information and scheduling model, the ant colony algorithm was introduced into the field. The example of ocean engineering project management shows that this

method can reasonably resolve the dynamic scheduling of resources, which is a more effective and practical new method for resource management of group project management. The selection of the distribution phase in the dynamic allocation in the article is based on the opinions of experts. How to determine the time in each stage is still necessary for further study. Marine industry and territorial industry are not antagonistic to each other, but are interdependent. In the early days of ocean development, many marine industries were integrated into the terrestrial industry system, but with the deepening of marine development. The marine industry groups have become increasingly sophisticated. Vertical chain relations and horizontal cross-relationships have been established between various marine development activities. Their characteristics with respect to the terrestrial economy have initially appeared, and people have begun to separate them from the terrestrial economy. However, in the study of industrial structure relations, the close relationship between land and sea economy must be considered.

How to choose a leading industry in an area is an important part of the study of regional industrial structure and industrial policy. For a region, due to the limited resources and technology, it is impossible for various industrial sectors to adopt a balanced development strategy to maximize the most effective and effective use of limited resources and technologies. It can only focus on limited resources and technologies to give priority to the development of industries that have been carefully selected to play a leading and leading role in many industrial sectors. By giving priority to the development of leading industries to a certain extent, they will promote and promote the development of other industries, and seek to achieve coordinated development of the industrial structure in non-balanced development. Only in this way can the regional economy exert its greatest advantage and form an advantageous industry with its own characteristics. Therefore, the success of leading industry choices will directly determine whether a regional economy can develop rapidly and in a coordinated manner.

Aiming at the hot issues of marine engineering project management—the difficulties in the management of group projects, namely the rational and dynamic scheduling of resources such as manpower, funds, equipment and materials, a resource scheduling method based on ant colony algorithm (ACO) is proposed. This method utilizes the similarity between the resource scheduling problem and the traveling salesman problem (TSP) of group projects, combines the characteristics of the ACO algorithm, and compares the time that the resource needs to be used in each subproject with the urgent need of the resource as the information in the algorithm. The example of resource scheduling in marine project group project management shows that this method realizes the rational and dynamic scheduling of resources, and provides a more effective resource scheduling algorithm for marine project group project management, which can improve the project management of marine engineering and other fields in China.

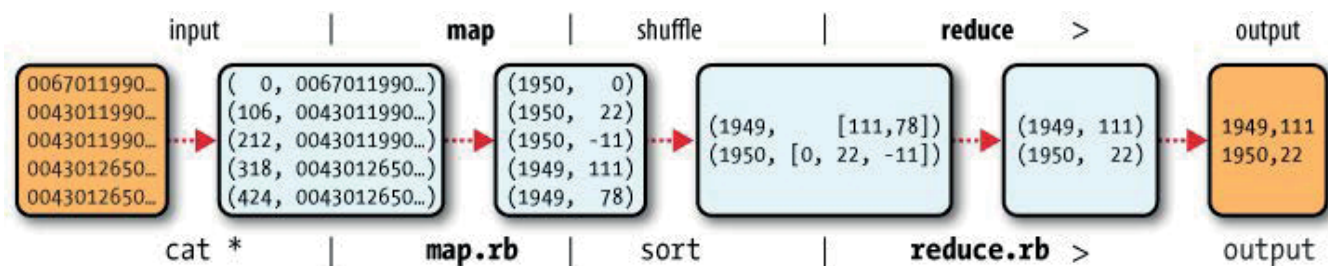


Fig. 2. The number of published papers on domestic marine industries in key journals

Child industry classification is the foundation for establishing the structure of the marine industry. It is the basis for analyzing the economic activities of various marine industry sectors and the relationship between them and their proportional relationship. It is also an important basis for the management of marine economy. Due to the diversity of research objectives, the diversity of marine industry classification is also formed. According to the history and trend of marine industry development and development, using technology, resources and time as three parallel standards, the marine industry can be divided into traditional marine industry, emerging marine industry and future marine industry. Industrial structure refers to the relationship between the production technology economic relations and the quantitative ratio between the various industries of the national economy in the process of social reproduction. The internationally accepted concept of industrial structure includes two aspects: First, the proportional relationship between industries in terms of production scale, the coordination and balanced development among industries.

MARINE INDUSTRIAL STRUCTURE

The theory of industrial structure optimization is based on the theory of industrial structure adjustment. Optimization of industrial structure refers to the process of industrial adjustment, the coordinated development of the industry, and meeting the growing needs of the society. Industrial structure optimization is a relative concept. It does not mean the absolute level of the industrial structure. It means that under the objective of the best national economic benefits, according to the characteristics of the country's geographical environment, resources, and economic development stage, through the adjustment of the industrial structure, it can achieve the state of coordinated development of various industries adapted to the above conditions. According to the selection of optimization criteria, the industrial structure optimization theory mainly includes the industrial structure rationalization theory and the industrial structure advanced theory. At present, the theoretical and industrial realms of the rationalization of industrial structure are inconsistent, and the research on the rationalization of industrial structure is mainly focused on the rationalization of benchmarks, the selection of strategic industries, and the maintenance of the coordinated development of the three industries, as well as

mechanisms and motivation. As a constantly developing new field of human beings, the geography community has become increasingly interested in the relationship between marine economy and the development of marine resources and coastal planning. At present, the world's major maritime powers generally attach great importance to the development of the marine economy, and the marine industry has developed into a growth area that goes beyond the traditional industries. In the same way, the marine economy has rapidly become a new area for China's coastal provinces and cities to enhance their international competitiveness, participate in the economic cycle, and develop the national economy.

Coastline ocean economic density analysis is to obtain the relationship between marine industry development and marine space by analyzing and comparing the relationship between the total output value of marine economy and the coastline. From the comparison of the contribution of the marine industry output of the coastal line length of the coastal units of each province and city, it can be relatively intuitive to reflect the important position of Tianjin in the development of the marine economy in the country. The optimization of the marine industry structure refers to the rational allocation and coordinated development of the production factors of the marine industry. It is embodied in the full and effective use of marine natural resources, environment and human resources. In addition to the United States, other oceanic economic powers also actively take measures to promote the development of strategic marine emerging industries. The Japanese government has always attached great importance to the research and development of marine science and technology and proposed the integration of the ocean into the national strategy and global perspective. Focusing on the development of marine key technologies such as deep ocean submarine technology and deep-sea resource development technology, Japan has achieved remarkable achievements in the fields of marine biology, seawater desalination and comprehensive utilization.

This paper uses the basic principles of industrial economics, based on an analysis of the status quo of the development of China's strategic emerging industries in the ocean, and carefully scrutinizes the existing policies of China's strategic marine emerging industries. Based on the successful experience of foreign strategic development policies for marine emerging industries, China's strategic marine emerging industry development policy system has been constructed. First of all, China's strategic emerging

industries in the ocean have related policies and regulations that are not perfect and lack corresponding management and coordination agencies. The shortage of high-level talent and the need for strengthening international cooperation. The emergence of these problems is attributed to the stage of industrial development and the constraints of technology, funds, and talents, which is precisely the starting point for solving these problems from the policy level.

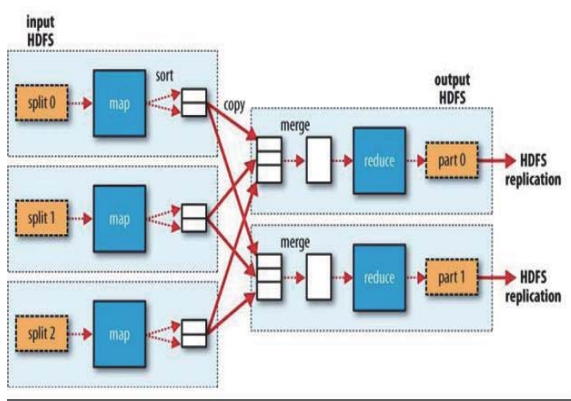


Fig. 3. Author collaboration network of marine industries

Combining the specific characteristics of China's strategic marine emerging industries and drawing on their common successes and models to formulate China's strategic marine emerging industry development policies, it is of positive significance for promoting the leap-forward development of China's strategic marine emerging industries. Thirdly, through the analysis of the characteristics, lacks, and policy needs of the existing development policies of China's strategic marine emerging industries, China's strategic marine emerging industry development policy system is constructed.

Tab. 1. Project team available resources

Year	Import and export		Import	
	Amount	Growth rate	Amount	Growth rate
1980	378.2	28.9	182.7	33.8
1981	440.1	16.4	220.1	20.4
1982	416.1	-5.5	223.2	1.4
1983	436.2	4.8	222.3	-0.4
1984	535.5	22.8	261.4	17.6
1985	696.0	30.0	273.5	4.6
1986	738.5	6.1	309.4	13.1
1987	826.5	11.9	394.4	27.5
1988	1027.8	24.4	475.2	20.5
1989	1116.8	8.7	525.4	10.6
1990	1154.4	3.4	620.9	18.2
1991	1357.0	17.6	719.1	15.8
1992	1655.3	22.0	849.4	18.1
1993	1957.0	18.2	917.4	8.0

VALIDATION OF SIMULATION MODEL

The strategic marine emerging industries have not developed to a complete marketization stage and require the guidance and regulation of the government. Therefore, how to establish a policy evaluation system from a macro perspective, establish a measure of the validity of policies, and grasp the effectiveness of policies must also be studied in depth. The development of strategic marine emerging industries that use ocean high technology as the main feature is to use advanced technology and equipment as the material basis. However, China's current marine technology equipment lags far behind the developed countries in the ocean. Development of offshore oil and gas resources and exploration of deep-sea mineral resources require a large number of imported technological equipment. Many advanced instruments and test equipment required by the Marine Science Research Institute also need to be imported from abroad. There are fewer technologies or equipment with independent intellectual property rights. This strong dependency has restricted the vigorous development of strategic marine emerging industries. In addition to relying on the strong support of ocean science and technology, the development of strategic marine emerging industries also needs sustained substantial funds to support its sustainable development. For a long time, the source of funds for the development of China's marine economy has mainly relied on government funding, with a single source channel and limited funds. For strategic marine emerging industries that require large amounts of funds to be injected, there is an urgent need to establish a diversified source of funds for the conflict between limited government funding and large capital requirements.

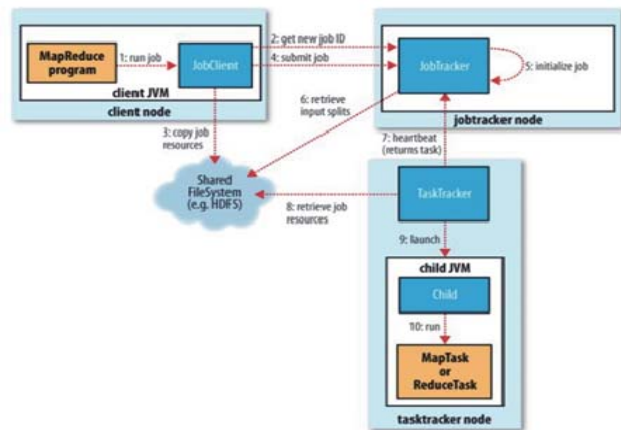


Fig. 4. The main research organizations network of marine industries

In recent years, venture capital and securities markets in Western countries have gradually replaced government investment and become an important source of technological development. China's strategic emerging industries in the ocean have also gradually adopted venture capital to finance the funds. However, the main source of China's venture capital is still the government's funding technology grants and bank's science and technology development loans.

At a certain level of marine economic development, there will inevitably be a corresponding marine industrial structure. With the development of marine economy, the marine industrial structure will also undergo corresponding changes. The level of marine economic development is in line with the state of marine industrial structure:

$$(\mathbf{F}_N \cdot \mathbf{Y}(:, m+1)) = (\mathbf{F}_N \cdot \mathbf{Y}(:, m)) \ominus \mathbf{P} + \begin{bmatrix} 1 \\ \vdots \\ 1 \end{bmatrix}_{N \times 1} \cdot (y_{k-s+N_c-(m-1)} - y_{k-s-(m-1)}) \quad (1)$$

$$\mathbf{P} = [\alpha^0, \alpha^1, \dots, \alpha^{N-1}]^T, \alpha = e^{-j2\pi(1/N)}$$

The evolution of marine industrial structure can also measure the development process of marine economy. Different marine industrial structures have different economic benefits:

$$z_i(k) = D_i \cdot \text{row}_i(\mathbf{F}_N) \cdot (\mathbf{Y} \cdot \mathbf{w}) = \text{row}_i(\underbrace{\mathbf{F}_N \cdot \mathbf{Y}}_{T \text{ FFTs}}) \cdot \underbrace{\mathbf{w} \cdot D_i}_{\mathbf{w}_i} \quad (2)$$

The marine economy includes all economic activities derived wholly or partly from the ocean or the Great Lakes basin:

$$C_{Nz} = C_{N_x} \cdot \sum_t s_i^N(t) \quad (3)$$

Scheduling problems are generally divided into dynamic scheduling problems. The scheduling problem of resource within the project group is to determine the dispatch and execution sequence of the resources according to the appropriate allocation strategy in a dynamic and real-time manner on the premise of satisfying certain resource constraints and priority constraint relationships:

$$\begin{bmatrix} z_1(k) \\ \vdots \\ z_N(k) \end{bmatrix} = \begin{bmatrix} D_1 & 0 & \dots \\ 0 & \ddots & 0 \\ 0 & \dots & D_N \end{bmatrix} \cdot \mathbf{F}_N \cdot (\mathbf{Y} \cdot \mathbf{w}) \quad (4)$$

In addition, the static pre-distribution is performed first, and then dynamic allocation is performed by real-time calculation of the resource usage and the degree of demand, so that the organic combination of dynamic scheduling and static scheduling can be realized:

$$\mathbf{P} = \begin{bmatrix} \mathbf{O} & \mathbf{I}_{N_c} \\ \mathbf{I}_N & \end{bmatrix} \quad (5)$$

In the initial stage, China's marine industry was in its initial stage of development. The marine primary industry accounted for a large proportion, and the layout of the marine industry structure was prominent.

$$\mathbf{Y} = \begin{bmatrix} y_{k-s+N_c+1} & y_{k-s+N_c} & \dots & y_{k-s+N_c-T+2} \\ y_{k-s+N_c+2} & y_{k-s+N_c+1} & \dots & y_{k-s+N_c-T+3} \\ \vdots & \vdots & \ddots & \vdots \\ y_{(k+1)-s} & y_{(k+1)-s-1} & \dots & y_{(k+1)-s-T+1} \end{bmatrix} \quad (6)$$

Therefore, the study of the marine industry during this period focused on the rational distribution of marine industrial structure and the development of marine resources:

$$K_x(M, N) = \frac{C_{M_x}}{[C_{N_x}]^{M/N}} \quad (7)$$

In the stage of steady growth, China's marine industry has developed rapidly and the marine industry has become an important growth point for regional economic growth:

$$P_r(d) = \frac{P_t G_t G_r \lambda^2}{(4\pi)^2 d^2 L} \quad (8)$$

The optimization and upgrading of marine industrial structure is the core area of marine industry research. Under the background of the optimization and upgrading of China's industrial structure, the connotation of marine industrial structure has a strong quantitative color. Therefore, most studies have defined the marine industrial structure from the perspective of quantity, focusing on the quantitative relationship of the industrial structure, and lacking a qualitative perspective to explore the connotation of the marine industry structure.

CONCLUSIONS

The most common view is that the marine industrial structure refers to the proportional composition of the various marine industries and their interdependence and mutual restraint. In the crucial period of the restructuring and upgrading of the marine industry, we should further expand the connotation of the marine industry structure in terms of improving the quality of marine industry structure. The structural optimization of the marine industry focused on the current status of the marine industrial structure of the coastal provinces and key coastal cities in China, the selection and optimization of the leading industries, and the evolution of the marine industrial structure. According to the research scale, the study can be divided into two levels: the coastal provinces and cities and the coastal provinces and cities. In general, most of the existing studies on the optimization of the marine industry structure are based on the problems existing in the regional oceanic industry. Through empirical methods, the practical problems in the development of the regional ocean economy are analyzed and solved, which are characterized by timeliness and strong policies. However, as far as the theory itself is concerned, research on marine

industrial structure mainly relies on the reference to other industrial development theories. It has not formed a set of industrial structure theory with the characteristics of marine economy and marine industry.

ACKNOWLEDGEMENTS

This work is supported by Nanhu Scholars Program for Young Scholars of XYNU with Grant No. 2017B52.

BIBLIOGRAPHY

1. Semenov I.: *The multidimensional approach to marine industry development: Part I. Obstacles and willingness to the EU marine industry reengineering*, Polish Maritime Research, Vol.15, no.3, pp. 77-85, 2008.
2. Lazakis D.: *Establishing an innovative and integrated reliability and criticality based maintenance strategy for the maritime industry*, Cell, Vol.41, no.6, pp. 24-26, 2011.
3. Ludgate J J.: *The Economic and Technical Impact of TBT Legislation on the USA Marine Industry*, Applied and environmental microbiology, Vol.57, no.4, pp. 1194-1201, 1987.
4. Sanderson J.: *Target identification in a complex maritime scene[C]// Motion Analysis and Tracking*, Xplore, Vol.15, no.2, pp.1-4, 1999.
5. Zaidi F.: *Maritime constellations: a complex network approach to shipping and ports*, Maritime Policy & Management, Vol.39, no.2, pp. 151-168, 2012.
6. Sanderson J G, Teal T J.: *Target identification in complex maritime scenes*, Vol.21, no.2, pp. 463 - 467, 1997.
7. Sanderson J G, Teal M K.: *Characterisation of a complex maritime scene using Fourier space analysis to identify small craft[C]// Image Processing and ITS Applications*, Seventh International Conference on, Vol.17, no.2, pp. 803-807, 1999.
8. Bukhari A C, Kim Y G.: *A research on an intelligent multipurpose fuzzy semantic enhanced 3D virtual reality simulator for complex maritime missions*, Kluwer Academic Publishers, Vol.23, no.12, pp. 156-169, 2013.
9. Caschili S, Medda F R.: *A Review of the Maritime Container Shipping Industry as a Complex Adaptive System*, Interdisciplinary Description of Complex Systems, Vol.10, no.1, pp. 1-15, 2012.
10. Bukhari, Kim F A.: *A research on an intelligent multipurpose fuzzy semantic enhanced 3D virtual reality simulator for complex maritime missions*, Applied Intelligence, Vol.38, no.2, pp. 193-209, 2013
11. Rub M G, Toksubayeva G P, Chernov B S.: *Composition and origin of a tungsten-bearing magmatic complex in an area of Soviet Maritime Province*, International Geology Review, Vol.12, no.3, pp. 313-326, 1970.
12. Engineer F G, Furman K C, Nemhauser G L.: *A Branch-Price-and-Cut Algorithm for Single-Product Maritime Inventory Routing*, Operations Research, Vol.60, no.1, pp. 106-122, 2012.
13. Rajendran C, Ziegler H.: *Ant-colony algorithms for permutation flowshop scheduling to minimize makespan/ total flowtime of jobs*, European Journal of Operational Research, Vol.155, no.2, pp. 426-438, 2004.
14. Shelokar P S, Jayaraman V K, Kulkarni B D.: *An ant colony approach for clustering*, Analytica Chimica Acta, Vol.509, no.2, pp. 187-195, 2004.
15. Liang Y C, Smith C E.: *An ant colony optimization algorithm for the redundancy allocation problem*, Transactions on Reliability, Vol.53, no.3, pp. 417-4233, 2004.

CONTACT WITH THE AUTHOR

Xiao Shen, Ph. D.,
e-mail: 2012101050017@whu.edu.cn

School of Business,
Xinyang Normal University,
Xinyang, Henan, 464000
CHINA

STUDY ON THE OPTIMIZATION AND PERFORMANCE OF TDMA ALLOCATION ALGORITHM IN SHIPS' AD HOC NETWORKS

Xiaofeng Han, Ph. D.¹

Yan Li, Ph. D.²

Guodong Liu, Ph. D.³

¹ College of Mathematics and Systems Science, Shandong University of Science and Technology, Qingdao 266590, China

² College of Electrical Engineering and Automation, Shandong University of Science and Technology, Qingdao 266590, China

³ Jinan Branch, Shandong University of Science and Technology, Jinan 250031, China

ABSTRACT

This paper analyzes the requirements of the information transmission network of ship integrated condition monitoring system, and proposes a design scheme of ship condition monitoring system based on wireless ad hoc network. The wireless ad hoc network protocol was designed, its networking process was analyzed in detail, and the network transmission performance of the monitoring system was tested. The results proved the feasibility of the system. The above solution can be used for the transmission of ship state information that satisfies the requirements of wireless transmission, and has important theoretical and practical significance. The slot allocation algorithm has been receiving extensive attention as an important part of the TDMA system research. This paper analyzes the summarization and summarization of TDMA time slot assignment algorithms from several aspects such as slot synchronization, existing slot allocation algorithm, and slot assignment model, laying an important foundation for researchers to do further research. In the TDMA system, time is divided into non-overlapping time frames, and the time frames are divided into non-overlapping time slots. Each node in the network performs corresponding operations in each time slot.

Keywords: Timeslot allocation algorithm; Ships; Ad hoc network

INTRODUCTION

The number and types of ships in China have also been continuously developed. Therefore, the application of modern technologies to enhance the ship's own safety management has always been an important research field for shipping safety. The ship navigation safety state real-time monitoring system is a combination of sensing technology, network technology, and computer technology to realize the safety status of the hull structure, the ship loading status, the cabin and the cab environment. Provides the analysis and control basis for the safe operation of the ship, as well as the early danger alarm and damage assessment, thus greatly enhancing the overall monitoring system for the survivability of the ship [1,2,3]. For a long time, all kinds of state signal transmission networks

have been based on fieldbus technology. Due to the limited space on the ship, the cables on the ship were laid too much, which caused difficulties in troubleshooting and overhauling. How to reduce the laying of cable networks and improve the transmission capacity of ship status information is a hot topic in recent years. Because it does not require wiring, it can be dynamically networked, so since its debut, it has been favored by all walks of life. If the wireless sensor network can be applied to the collection of state of ships and the transmission of some state signals of ships suitable for wireless transmission, the wiring of the ship's wired network will be effectively reduced, and the dynamic joining or withdrawal capabilities of its monitoring objects will be improved. In this way, a more scientific and reasonable form of shipbuilding

networking can be achieved, providing a more convenient way for the condition monitoring and network maintenance of ships [4,5,6]. Based on the above ideas, this paper proposes a ship integrated condition monitoring system based on wireless ad hoc networks. The self-organizing principle of the networking and the networking process are analyzed in detail, and the performance of the networking is tested specifically. This provides a new solution for the development of the ship status monitoring system [7,8,9].

In actual operation, the sensor node is mainly responsible for collecting various status data of the ship monitoring area, and after parsing and encoding the collected data, it is transmitted to the upper routing node through the ad hoc network. The routing node is responsible for forwarding the received data and managing the sensor nodes, and then transmitting the vessel status data to the upper routing node or aggregation node. The aggregation node transmits the status data of the ship to the ship comprehensive condition monitoring and management platform through the serial port. The ship status monitoring and management platform is responsible for analyzing, storing and displaying these data, and is also responsible for managing the nodes in the network. In addition, the platform also provides mobile terminal services to facilitate the management personnel to view the status information of the ship in real time through the Android client anytime anywhere [10,11,12]. The above hierarchical structure can greatly reduce the complexity of the network and can also reduce the power consumption of the terminal nodes. The sink node and the routing node do not have the requirement of low power consumption, and are set to remain in the information receiving state during their idle time. The sensor node works in the dormant state most of the time, and periodically sends wake-up information and heartbeat information.

In addition, the sink node does not directly communicate with the sensor node. The sensor node and the sensor node do not need to communicate with each other, which reduces the complexity of the network and reduces the power consumption. All nodes in the sensor network have unique physical addresses. Common channels and general physical addresses are used for broadcast and private physical addresses are used for unicast. The design of the system's routing protocol relates to the performance and quality of the network. Therefore, the network topology of this system adopts the form of hierarchical clustering. In this paper, the sensor nodes are roughly distributed in the nacelle, compartment and so on [13,14,15]. According to the regional distribution of sensor nodes, sensor nodes located in the same area form a cluster. If the sensor nodes in the same area are distributed more, they are divided into multiple groups. After receiving the networking command from the vessel condition monitoring and management platform, the sink node starts listening to the requesting network access information in the network. After receiving the network access request information of the routing node, if the address space of the child node of the convergence node is not full, it is allowed to access the network, the network address of the

corresponding routing node is allocated, and the routing node is returned. After a successful network access, the routing node is listening and receives information from other nodes. Then, after the sensor node is powered on, it starts sending network requests. The routing node checks its address space after receiving the information. When the address space is not full, the child node information is returned and its network address is assigned to allow access. When the address space is full, its access to the network is denied.

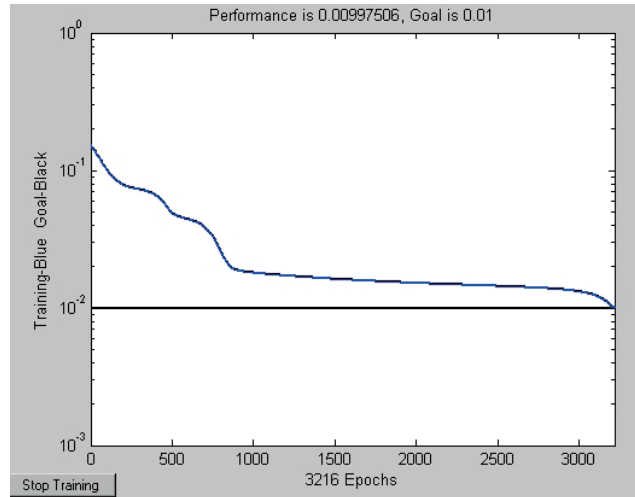


Fig. 1. TDMA-based fixed slot allocation algorithm frame structure

HOC NETWORK PROTOCOL DESIGN

Before the routing node accesses the network, the communication process sends a network request to the routing node in broadcast mode. After receiving the request, the aggregation node processes the message format and determines whether the node address is full. If the address space of the child node is not full, the incoming network information is immediately restored. The information includes the network address assigned to this routing node by the parent node. After receiving the reply message from the sink node, the routing node replies with an ACK and sets the network address of this routing node as the network address allocated by the sink node. If the address space of the sub-node in the sink node is full, the sub-node is denied access to the network. After the routing node successfully enters the network, the aggregation node and the routing node use the network address to communicate, that is, complete the communication process in the form of private signaling. The current family of wireless ad hoc network routing protocols is very large, but none of them are specifically designed for ship ad hoc networks. However, because there is a commonality between the ad hoc network and the wireless ad hoc network, the latter's routing protocols can also be applied directly to the former or can be applied to the former in the light of specific marine scenarios. This chapter begins with the analysis of the requirements of the ship's ad hoc network, studies and compares the advantages and disadvantages of the current routing protocol applied to it, and selects a more suitable

routing protocol; Then, based on the requirements, the best route for the current routing metrics cannot be selected, and it is difficult to deal with the insufficiencies of the complex and ever-changing marine transmission environment, and a route improvement scheme is proposed.

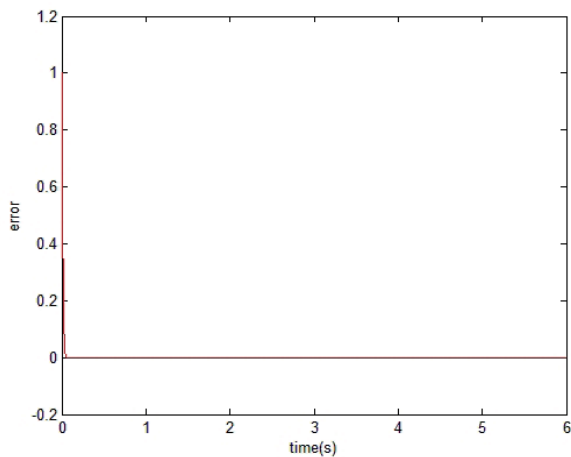


Fig. 2. Allocation based on MAC protocol performance

As an improved version of the OLSR routing protocol, MP-OLSR inherits its advantages of establishing a convenient and rapid route. It also made full use of network resources by adopting multiplexing, and it also added route repair and loop detection mechanisms, which improved the stability of the transmission and effectively reduced the delay. We believe that MP-OLSR can also play its own advantages in marine ad hoc networks with ocean backgrounds, and have better performance than OLSR. Therefore, it is the basis of the agreement. With the increasing demand for maritime Internet access, Ocean Internet has emerged, but it is still in its infancy. In order to meet the needs of marine safety, marine information, and the needs of offshore operators, the development of the Ocean Internet is of strategic importance. However, the traditional idea of land-based Internet construction is not suitable for promotion to the sea because of its vast sea area and the lack or even the inability to lay down infrastructure. At this time, using a ship's device to easily form a ship ad hoc network in a sea area is an idea for the development of the maritime Internet, among which, routing protocols are one of the key technologies.

SHIP INTEGRATED CONDITION MONITORING SYSTEM

In actual operation, the sensor node is mainly responsible for collecting various status data of the ship monitoring area, and after parsing and encoding the collected data, it is transmitted to the upper routing node through the ad hoc network. The routing node is responsible for forwarding the received data and managing the sensor nodes, and then transmitting the vessel status data to the upper routing node or aggregation node. The aggregation node transmits the

status data of the ship to the ship comprehensive condition monitoring and management platform through the serial port. The ship status monitoring and management platform is responsible for analyzing, storing and displaying these data, and is also responsible for managing the nodes in the network. In addition, the platform also provides mobile terminal services to facilitate the management personnel to view the status information of the ship in real time through the Android client anytime anywhere. The above hierarchical structure can greatly reduce the complexity of the network and can also reduce the power consumption of the terminal nodes. The sink node and the routing node do not have the requirement of low power consumption, and are set to remain in the information receiving state during their idle time. The sensor node works in the dormant state most of the time, and periodically sends wake-up information and heartbeat information. In addition, the sink node does not directly communicate with the sensor node. The sensor node and the sensor node do not need to communicate with each other, which reduces the complexity of the network and reduces the power consumption.

All nodes in the sensor network have unique physical addresses. Common channels and general physical addresses are used for broadcast and private physical addresses are used for unicast. Before the routing node accesses the network, the communication process sends a network request to the routing node in broadcast mode. After receiving the request, the aggregation node processes the message format and determines whether the node address is full. After receiving the reply message from the sink node, the routing node replies with an ACK and sets the network address of this routing node as the network address allocated by the sink node. If the address space of the sub-node in the sink node is full, the sub-node is denied access to the network. After the routing node is successfully connected to the network, the aggregation node and the routing node communicate using the network address. The design of the system's routing protocol relates to the performance and quality of the network. Therefore, the network topology of this system adopts the form of hierarchical clustering. In this paper, the sensor nodes are roughly distributed in the nacelle, engine compartment and so on. According to the regional distribution of sensor nodes, sensor nodes located in the same area form a cluster. If the sensor nodes in the same area are distributed more, they are divided into multiple groups.

Based on the characteristics of actual tasks, the analysis of the data network requirements of the network clearly identifies the type and number of NPG members, the frequency of messages sent by members, throughput estimation during system operation, message update rate, and relay opening sequence. This results in the requirement of time slots for the members, and then estimates the size of the time slot blocks required by each NPG, and allocates them accordingly. Although the research of the ship's ad hoc network has just started, the research of the wireless ad hoc network has been very in-depth. As one of them, the ship self-organizing network can learn from the latter's research results and combine its own characteristics to develop a

theoretical system with its own characteristics. The same is true for ship ad hoc routing protocols. This chapter will introduce the characteristics of the ad hoc network from the aspects of the characteristics of wireless ad hoc networks, the characteristics of marine scenes, the characteristics of ships, and the architecture of ship ad hoc networks. Subsequently, the ship ad-hoc network routing protocol was introduced, including its main categories and routing metrics. Finally, two protocols, OLSR and MP-OLSR, were highlighted.

Vessel ad hoc network is a kind of wireless ad hoc network, which has all the characteristics of the latter. Due to its dependence on the marine background, the ship is a mobile node. Compared with the wireless ad hoc network in the general sense, it has other special properties. The status of each node in the wireless ad hoc network is equal, and each node is a receiving and sending terminal as well as a relay route. Due to their mobility, they enter or leave the network frequently and do not need to inform others in the network in advance. Their entry or departure will not affect the communication between other members. Nodes collaborate through wireless links to exchange and transfer data. Due to the limited transmit power, the source node and the destination node may not be able to directly communicate with each other, and it is necessary to rely on multiple relays of other nodes of the network to transfer data packets. Accordingly, a routing protocol is also required for packet forwarding decision.

Tab. 1. Classroom activity process

Name	good	commonly	Not so good
Design ideas	16	2	0
	41	5	0
progress	18	6	0
	45	15	0
Incentive	13	17	0
	32.5	42.5	0
Applicability	3	11	1
	7.5	27.5	2.5

Analyze and calculate the number of time slots allocated by the members of each NPG and the operational satisfaction requirements of the time slot occupation method. For example, analyze the calculation of the collision probability or the system response time of different priority messages. If the requirements are met, the designed time slot allocation scheme passes, and based on the main evaluation indicators such as data volume, message update rate, and relay requirements, the overall performance of the protocol is given. Otherwise, the time slot allocation scheme will be re-evaluated.

VALIDATION OF SIMULATION MODEL

Comparison of commonly used time slot allocation strategies. At present, many of MANET's theories and technologies are still in the exploratory stage, but their enormous potential will receive more and more attention from people. Based on the fixed time slot allocation algorithm based on TDMA, this paper proposes an improved dynamic TDMA time slot allocation algorithm, which adopts a dynamic hierarchical classification of nodes and a two-tier topology structure. Under the premise of guaranteeing the basic service quality, according to the increase of the number of nodes, the communication demands of a large number of users are met to the maximum extent.

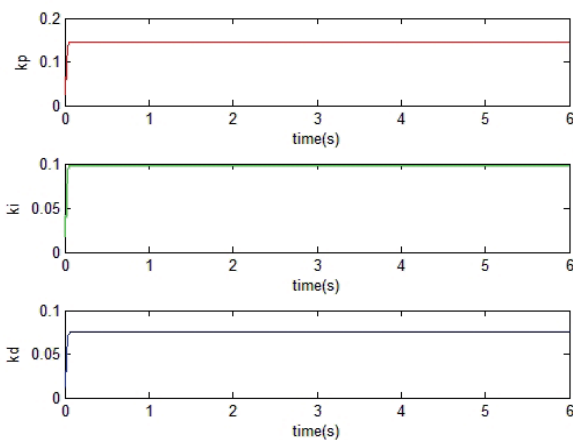


Fig. 3. NS2 mobile node structure diagram

This routing protocol requires each node to maintain the link state of each member of the network at any time. It is a distributed routing protocol, so there is no requirement for a control center to reliably transmit routing control information. The information available in the marine communications environment is not limited to the quality of the link, including the location of the vessel. Subsequent protocols can use the position information of the vessel as a reference condition for routing and optimize the performance of the routing protocol.

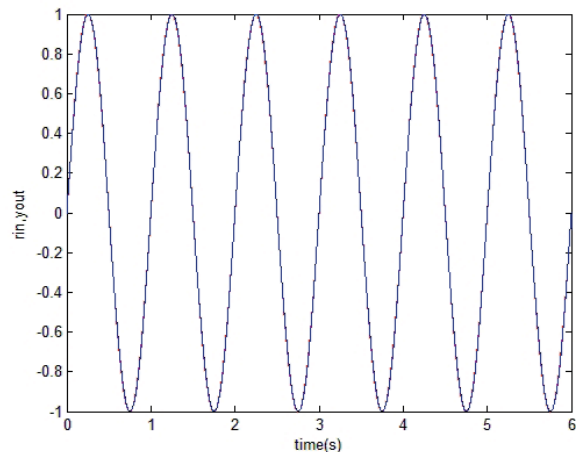


Fig. 4. CBR data flow diagram

To study the TDMA protocol, the most important thing is to study the slot allocation algorithm. This paper analyzes, sums up and summarizes the TDMA time slot allocation algorithms from the connotation, status quo, and theoretical support, so that researchers can review the research situation in the field and lay an important foundation for further in-depth research. In the contention-based MAC protocol, when a node has a transmission task, it usually occupies the channel by means of free competition. When the number of nodes competing for the same channel at the same time is equal to or greater than two, a collision occurs:

$$\Delta w_{jk} = -\alpha \frac{\partial E}{\partial w_{ij}} = -\alpha \frac{\partial E}{\partial net_k} \cdot \frac{\partial net_k}{\partial w_{ij}} \quad (1)$$

In the fixed time slot allocation algorithm based on TDMA, each node will allocate time slots evenly under normal operating conditions, so that the system has the lowest delay guarantee, ensuring the stability and timeliness of data transmission:

$$\Delta v_{ij} = -\beta \frac{\partial E}{\partial v_{ij}} = -\beta \frac{\partial E}{\partial net_j} \cdot \frac{\partial net_j}{\partial v_{ij}} \quad (2)$$

$$\Delta w_{jk} = \alpha \delta_k^o \cdot y_j = \alpha (d_k - o_k) o_k (1 - o_k) y_j \quad (3)$$

In the fixed time slot assignment algorithm based on TDMA, each node can averagely obtain the time slot. This has good performance in delay performance and node anti-collision performance when the transmission efficiency is not high:

$$\Delta v_{ij} = \beta \delta_j^y x_i = \beta \left(\sum_{k=1}^n (\delta_k^o w_{jk}) \right) \cdot y_i (1 - y_i) x_i \quad (4)$$

However, when the number of nodes gradually increases and the network transmission efficiency is required to be higher, the fixed time slot allocation algorithm based on TDMA does not adapt well to such a dynamic scenario:

$$\hat{L} = \frac{L - L_{\min}}{L_{\max} - L_{\min}} \quad (5)$$

Therefore, it is necessary to propose a new TDMA time slot allocation protocol that can dynamically adjust these parameters according to the number of nodes:

$$\left. \begin{aligned} O_1^{(3)} &= K_p \\ O_2^{(3)} &= K_I \\ O_3^{(3)} &= K_D \end{aligned} \right\} \quad (6)$$

Especially in areas where marine disasters and meteorological environment are unstable, major monitoring is needed:

$$\left. \begin{aligned} \frac{\partial u(k)}{\partial O_1^{(3)}} &= e(k) - e(k-1) \\ \frac{\partial u(k)}{\partial O_2^{(3)}} &= e(k) \\ \frac{\partial u(k)}{\partial O_3^{(3)}} &= e(k) - 2e(k-1) + e(k-2) \end{aligned} \right\} \quad (7)$$

The frequency of periodic detection is dynamically adjusted according to the number of secondary nodes in its neighbors:

$$\frac{\partial E(k)}{\partial net_1^{(3)}} = \frac{\partial E(k)}{\partial y(k+1)} * \frac{\partial y(k+1)}{\partial u(k)} * \frac{\partial u(k)}{\partial O_1^{(3)}} * \frac{\partial O_1^{(3)}}{\partial net_1^{(3)}} \quad (8)$$

The hierarchical division of mobile nodes follows a fundamental principle that each secondary node has at least one primary node within one hop. Two kinds of algorithms are compared and simulated. The simulation results show that the improved dynamic TDMA slot allocation algorithm can adapt to the changing number of nodes. MANET is usually composed of a group of mobile terminals with wireless transceivers. It is a dynamic network that does not require infrastructure support. The TDMA protocol based on the dynamic allocation algorithm allocates the required time slot to the node when it needs to send data. After the data is sent, it no longer allocates the time slot to the node.

CONCLUSIONS

The slot allocation algorithm has been receiving extensive attention as an important part of the TDMA system research. This paper analyzes the summarization and summarization of TDMA time slot assignment algorithms from several aspects such as slot synchronization, existing slot allocation algorithm, and slot assignment model, laying an important foundation for researchers to do further research. In the TDMA system, time is divided into non-overlapping time frames, and the time frames are divided into non-overlapping time slots. Each node in the network performs corresponding operations in each time slot. The system uses TDMA access, which requires designing how to allocate time slots. That is, how to allocate time slots to each node in the network so that collisions occur when packets are transferred between adjacent nodes, and the throughput and spatial reusability of the system are as high as possible. The centralized dynamic TDMA protocol generally has a central control node that knows the information of the entire network node, and the central node allocates timeslots for the nodes in the entire network. The distributed dynamic TDMA protocol does not exist in the control node. The nodes in the network reserve the respective transmission time slots through mutual information. The TDMA protocol based on the hybrid allocation algorithm fixedly allocates time slots to the corresponding nodes, while allowing other nodes to compete for the time slots without disturbing the use of the transmission of the nodes. The slot allocation model is an important mathematical theoretical basis for the slot allocation algorithm. Different slot allocation schemes have different slot allocation models. The fixed time slot assignment model and distributed dynamic time slot assignment model are respectively introduced below.

BIBLIOGRAPHY

1. Sakhaee E., Jamalipour A.: *Stable Clustering and Communications in Pseudolinear Highly Mobile Ad Hoc Networks*. Transactions on Vehicular Technology, Vol. 57, no. 6, pp. 3769-3777.
2. Folio R., Cain J B., Kota S.: *Challenges in the Verification of Mobile Ad Hoc, Networking Systems*. International Journal of Wireless Information Networks, Vol. 14, no. 2, pp. 107-120, 2007.
3. Akyildiz I F., Pompili D., Melodia T.: *Underwater acoustic sensor networks: research challenges*. Ad Hoc Networks, Vol. 3, no.3, pp. 257-279, 2005.
4. Sagduyu Y E., Ephremides A.: *On Joint MAC and Network Coding in Wireless, Ad Hoc, Networks*. Transactions on Information Theory, Vol. 53, no. 10, pp. 3697-37131, 07.
5. Little P E., Hutchison B L.: *RO/RO safety after the Estonia - a report on the activities of the ad hoc panel on RO/RO safety*. Marine Technology, Vol. 32, no. 3, pp. 159-1631, 1995.
6. Guha D., Goswami V., Banik A D.: *Equilibrium balking strategies in renewal input batch arrival queues with multiple and single working vacation*. Performance Evaluation, Vol. 94, no. 1, pp. 1-24, 2015.
7. Toh C K.: *Maximum battery life routing to support ubiquitous mobile computing in wireless ad hoc networks*. Communications Magazine, Vol. 39, no. 6, pp. 138-147, 2011.
8. Gavin Holland., Nitin Vaidya.: *Analysis of TCP Performance over Mobile Ad Hoc Networks*. Wireless Networks, Vol. 8, no.3, pp. 275-28, 2002.
9. Conti M., Maselli G., Turi G.: *ross-Layering in Mobile Ad Hoc Network Design*. Computer, Vol. 37, no. 2, pp. 48-5, 2006.
10. Alzoubi, Khaled, Li: *Geometric Spanners for Wireless Ad Hoc Networks*. Transactions on Parallel and Distributed Systems, Vol. 14, no. 4, pp. 408-421, 2003.
11. Feeney L M.: *An Energy Consumption Model for Performance Analysis of Routing Protocols for Mobile Ad Hoc Networks*. Mobile Networks and Applications, Vol. 6, no. 3, pp. 239-249, 2001.
12. Niculescu D S., Nath B.: *Localized Positioning in Ad Hoc Networks*. Ad Hoc Networks, Vol. 1, no. 2, pp. 247-259, 2003.
13. Andrew M., Hunter, Jeffrey G.: *Transmission capacity of ad hoc networks with spatial diversity*. Transactions on Wireless Communications, Vol. 7 no. 12, pp. 5058-5071, 2007.
14. Boban M., Vinhoza T T V., Ferreira M.: *Impact of Vehicles as Obstacles in Vehicular Ad Hoc Networks*. Journal on Selected Areas in Communications, Vol. 29, no. 1, pp. 15-28, 2011.
15. Hara T., Madria S K.: *Data Replication for Improving Data Accessibility in Ad Hoc Networks*. Transactions on Mobile Computing, Vol. 5, no. 11, pp. 1515-1532, 2006

CONTACT WITH THE AUTHOR

Xiaofeng Han, Ph.D.
e-mail: hanxiaofeng@sdust.edu.cn

College of Mathematics and Systems Science
Shandong University of Science and Technology
Qingdao Shandong, 266590
CHINA

APPLICATION OF SOLAR PHOTOVOLTAIC POWER GENERATION SYSTEM IN MARITIME VESSELS AND DEVELOPMENT OF MARITIME TOURISM

Yaqi Shi¹

Wei Luo, M.S.²

¹ Wuhan Technical College of Communications, Wuhan 430074, Hubei, China

² Hubei Urban Construction Vocational and Technological College, Wuhan 430074, Hubei, China

ABSTRACT

The use of new energy generation technologies such as solar energy and electric propulsion technologies to form integrated power propulsion technology for ships has become one of the most concerned green technologies on ships. Based on the introduction of the principles and usage patterns of solar photovoltaic systems, the application characteristics of solar photovoltaic systems and their components in ships are analyzed. The important characteristics of the marine power grid based on solar photovoltaic systems are explored and summarized, providing a basis for future system design and application. Photovoltaic solar cells are made using semiconductor effects that convert solar radiation directly into electrical energy. Several such battery devices are packaged into photovoltaic solar cell modules, and several components are combined into a certain power photovoltaic array according to actual needs, and are matched with devices such as energy storage, measurement, and control to form a photovoltaic power generation system. This article refers to the basic principle and composition of the land-use solar photovoltaic system, and analyzes the difference between the operational mode and the land use of the large-scale ocean-going ship solar photovoltaic system. Specific analysis of large-scale ocean-going ship solar photovoltaic system complete set of technical route, for the construction of marine solar photovoltaic system to provide design ideas.

Keywords: Solar photovoltaic system; Ship; Photovoltaic control system

INTRODUCTION

As the core part of the system, solar panels function to directly convert solar energy into direct-current form of electrical energy, and generally only output energy during the day when there is sunlight. According to the needs of the load, the system generally uses lead-acid batteries as the energy storage link. When the power generation is greater than the load, the solar battery charges the battery through the charger. When the power generation is insufficient, the solar battery and the battery simultaneously supply power to the load. Currently used grid-connected photovoltaic power generation systems have two structural forms. The battery-storage energy link is called schedulable grid-connected photovoltaic power generation system; the non-battery link is

called grid-connected photovoltaic power generation system. For large-scale ocean-going vessels, a comprehensive analysis of the energy utilization optimization, program feasibility, system reliability, and economic efficiency, etc., the feasible photovoltaic energy utilization mode is the grid connection mode and off-grid mode [1,2,3]. Considering that a ship is a limited space body, the links among them, equipment and systems are very relevant, and the design process can refer to the design of land-use photovoltaic systems. But at the same time, we must also fully consider the differences between the land-use and marine-use PV systems. As a maritime mobile platform, large-scale ocean-going vessels must be equipped with any equipment to ensure the safety of vessels [4,5].

Building a solar photovoltaic system on a large-scale ocean-going vessel involves not only the ship power system, but also aspects such as the hull structure, safe operation of the ship, and economical analysis. Therefore, the installation and use of photovoltaic systems on large ocean-going vessels needs to be completed in stages according to actual conditions. Due to the differences in the structure, functions and applicable routes of different ship types, when a large-scale ocean-going ship is to build a high-power solar photovoltaic system, it is not possible to arbitrarily select a ship as a loading platform [6,7,8]. We must consider the arrangement of photovoltaic solar arrays in large areas, the level of safety protection, and the solar radiation resources of shipping lines. We can only select the target ship type through evaluation and analysis. When solar panels are installed on ships, they must meet safety regulations, maximize area, and aesthetic principles. At the same time, the stability, maneuverability and aerodynamic characteristics of the ship should not be excessively affected. It is necessary to evaluate whether the installation of solar arrays is reasonable by calculating the stability of ships and local strength. Analyze the photovoltaic cell conversion efficiency, anti-corrosion problems, and vibration impacts and safety guarantees when solar panels are used in marine environments, and verify the reliability of marine solar photovoltaic systems designed and installed. The application of solar photovoltaic technology in ships has been developed in recent years, and in particular, there have been preliminary successful application cases in small vessels and yachts on rivers [9,10,11]. However, in the area of ocean-going vessels, the application of solar photovoltaic technology is not yet mature, and many countries are committed to the development and improvement of this technology.

This article through analysis, plans to establish a set of solar photovoltaic power generation system in the conventional ship, to provide some power support for the ship, to achieve the purpose of energy conservation and emission reduction. The basic working principle of solar photovoltaic power generation is that under the sunlight, the energy generated by the solar cell module is charged by the controller to the battery or directly to the load when the load demand is satisfied. If the sun is insufficient or at night, the battery supplies power to the DC load under the control of the controller. For the AC load, an inverter must be added to convert the DC power into AC power [12,13,14,15]. The most significant feature of grid-connected photovoltaic systems is the direct current generated by solar cell components. The use of new energy generation technologies such as solar energy and electric propulsion technologies to form integrated power propulsion technology for ships has become one of the most concerned green technologies on ships. For the application of solar photovoltaic system in ships, based on the introduction of the principle of solar photovoltaic systems and the use of models, the application characteristics of solar photovoltaic systems and their components in ships are analyzed. The important characteristics of the ship-based power grid based on solar

photovoltaic systems are discussed and summarized, which provides a basis for future system design and application.

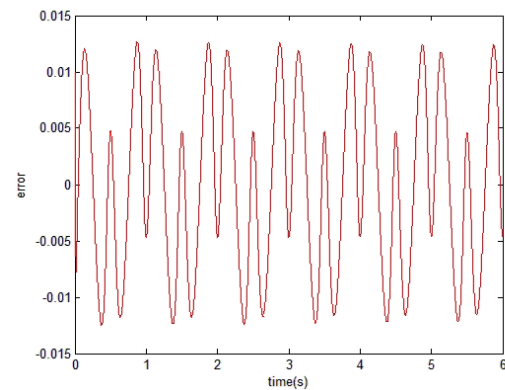


Fig. 1. The photovoltaic characteristics of solar photovoltaic arrays

PV SYSTEM INTRODUCTION

With the development of tourism and the development of tourism resources such as lakes and scenic spots, cruise ships, as a carrier of nature, have gradually become an entertainment way for people to travel and vacation. However, the problem of water, air and noise pollution caused by oil, water, and noise emitted from the cruise ship's power system has become increasingly serious, making the development of green ships more practical. Solar energy is a kind of renewable energy source, easy to get, and inexhaustible, inexhaustible, the application of solar energy on the cruise ship, its pollution problems will be solved. Therefore, there are more and more applications of solar photovoltaic systems on ships, and the application technology of solar energy has become one of the most important green technologies for ships. Because of the performance characteristics of the solar photovoltaic power supply system itself, it has its unique advantages and related constraints in its application.

Especially applied to the ship power grid, in order to obtain continuous, stable solar energy, and ultimately become an alternative energy source that can compete with conventional energy sources, it is necessary to solve the problem of energy storage. In other words, the solar energy in sunny days is stored to meet the needs of use at night or on rainy days. At the same time, efforts should be made to prevent hot spot, islanding, and grid stability. At present, these problems are the weakest links in the application of solar energy in ships, and have also become the key issues that we must consider in the design of marine solar applications in the future. The analysis made in this paper provides a design reference for solar photovoltaic systems in marine applications. The simulation results show that the model can correctly reflect the characteristics of the transformer ground fault, and protect the transformer in time. It has good quickness and stability. The differential protection model can provide an important basis for observation and analysis of transformer

faults, and has a certain guiding role in the research and design of ship transformer protection devices in the future.

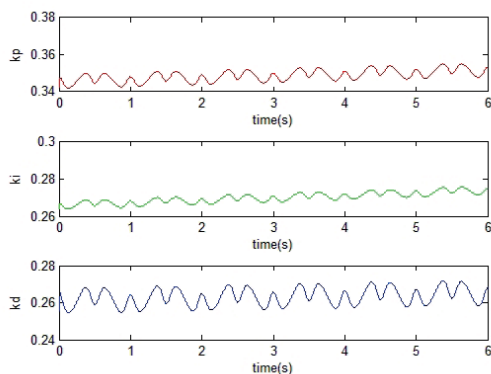


Fig. 2. Electricity boosting method program flow

OCEAN SHIP SOLAR PHOTOVOLTAIC SYSTEM OPERATION

The direct current generated by solar cells enters the battery first, and the characteristics of the battery affect the efficiency and characteristics of the system. The battery technology is very mature, but its capacity is affected by the amount of electricity at the end of the day and the duration of the sun (power generation time). Therefore, the battery watt-hour capacity and ampere-hour capacity are determined by the scheduled continuous sunshine-free time. The research on the reliability of photovoltaic systems in this paper is an important support to ensure the rational design, reliable operation, fault prevention and maintenance of photovoltaic power generation systems. After reviewing related application examples and domestic and foreign scholars' research on photovoltaic power generation system and reliability theory, a comprehensive analysis of the factors affecting the reliability of photovoltaic power generation systems was conducted. Summarized the evaluation of reliability indicators for photovoltaic power generation systems and proposed suggestions for improving the reliability of photovoltaic power generation systems. Photovoltaic power generation is based on the principle of photovoltaic effect, using solar cells to convert solar energy directly into electrical energy. Regardless of whether it is used independently or connected to the grid, the photovoltaic system is mainly composed of solar panels (components), controllers and inverters. The primary solution for photovoltaic applications is how to convert solar energy into electricity. Photovoltaic solar cells are made using semiconductor effects, which convert solar radiation directly into electrical energy. Several of these devices are packaged into photovoltaic solar cell modules, and then several components are combined into a certain power photovoltaic array according to actual needs, and are matched with energy storage, measurement, and control devices to form a photovoltaic power generation system.

The controller is a device that controls and manages the solar photovoltaic power generation system. "Because the controller can adopt a variety of technical implementation methods, the actual application of the controller to the controller is not consistent. Therefore, the functions performed by the controller are also different. The photovoltaic system operates under the control of the controller. The controller can use a variety of technical means to achieve its control function. More common logic control and computer control two ways. In harsh marine environment conditions, in addition to taking into account extreme weather issues such as hail, photovoltaic power generation system components in particular should consider the use of weather protection and salt spray protection devices in the marine climate environment. Although most glass covers for solar panels are made of toughened glass with high light transmittance, they are prone to a series of problems such as contamination in long-term environments with large temperature differences, large salt, and high humidity.

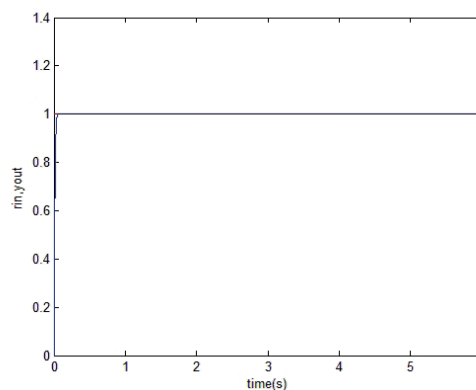


Fig. 3. Solar cell characteristics simulation model

To install and use solar photovoltaic systems on large-scale ocean-going vessels, in order to fully utilize the advantages of photovoltaic energy, it is necessary to conduct in-depth research on the power output characteristics of installed solar panels in the marine environment. In order to complete the optimal design of the photovoltaic system installation and power conversion control based on the characteristic parameters obtained in the specific environment. At present, solar photovoltaic technology has been applied on land on a large scale, and applications and innovations on ships have also been continuously improved. However, it can be seen from the existing solar ship cases that the application of PV technology to ships has fundamentally obvious constraints. Ships are a kind of transportation tools that work in marine complex environmental conditions. Its own power system is a network structure that is relatively independent and requires high reliability and stability.

By comparing the implementation mode and operational characteristics of land-use solar photovoltaic conversion and utilization technologies, the current status and trends of solar-powered ships are analyzed. Based on the selection of the target ship type, the analysis of the power system and the assessment of economic performance, the research direction

for the application of solar photovoltaic technology to large-scale ocean-going vessels as an auxiliary energy source is identified. Completed the overall framework design process for marine solar photovoltaic power generation systems. From the point of view of green shipping and sustainable development, solar photovoltaic conversion does not produce secondary pollution to the environment because it generates non-chemical reactions. The effective use of photovoltaic energy will correspondingly reduce the work load of the ship generator set, which will inevitably be accompanied by a reduction in the amount of fuel consumed by the ship, the greenhouse gas emissions of the ship and harmful gas emissions. The research and design of solar photovoltaic technology and its application in large-scale ocean-going vessels have been conducted from both technical feasibility and economic feasibility. Completely discusses the power matching method, the system optimization analysis process and the consideration of related issues, and provides detailed analysis ideas, calculation methods, and data references for the evaluation of the early implementation process of the project.

Tab. 1. Indications of echocardiography

Codon	Hexadecimal	Codon	Hexadecimal
CUU	100	AUU	200
CUC	101	AUC	201
CUA	102	AUA	202
CUG	103	AUG	203
CCU	110	ACU	210
CCC	111	ACC	211
CCA	112	ACA	212
CCG	113	ACG	213
CAU	120	AAU	220
CAC	121	AAC	221
CAA	122	AAA	222

The solar cell's power output characteristics change in the marine environment, especially under water fog erosion and hull vibration conditions. Considering the idea: the former is mainly aimed at analyzing the change of physical and chemical characteristics of the light-receiving material on the surface of the battery under water fog corrosion, and determining the influence of the material change on the solar light transmission; The latter mainly analyzes the influence of the vibration of the battery substrate on the reflection and transmission of sunlight on the light-receiving surface, the dynamic change of energy. Based on the simplification of the solar cell in the simulation process of this test system, in the next step of research, the changes in the power output at different temperatures and different radiation intensities must be incorporated into the influencing factors of the entire grid-connected system to be considered. Harmonic waves in the solar PV inverter pollution and impact on the ship's power grid, hazards of islanding effects and remote monitoring of the PV system of the ship. The third major objective is to give

an assessment of the working status of the PV system and provide technical support to the crew.

OPTIMIZATION AND ANALYSIS OF OFFSHORE VESSEL PV SYSTEM

The research and design of solar photovoltaic systems for large-scale ocean-going vessels is a relatively large system project. It involves not only the ship power system, but also the structure of the hull, the safe operation of ships. Therefore, how to select the right target ship to carry out optimization design and evaluation analysis of the entire system is the first problem to be solved. When transplanting the PV system to the ship, it is necessary to consider that the arrangement and installation of solar panels are easily affected by the placement and safe work of the deck machinery equipment such as pipelines, passages and cranes on the deck of the ship. Therefore, it is necessary to select the target ship type in a targeted manner and make some explanations for the rationality of the installation method of the photovoltaic system. Currently, crystalline silicon high-efficiency solar cells and various types of thin-film solar cells are the focus of research and development of new global solar cells.

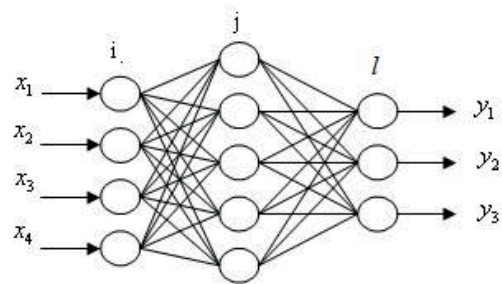


Fig. 4. Solar cell characteristics simplify simulation algorithm flow

The system can also act as a power regulator to stabilize the grid voltage! Harmonic components can be cancelled to improve power quality. In this system, the grid-connected inverter converts the DC power generated by the solar panel into AC power with the same frequency and phase as the grid voltage. When the main grid is powered off, the system automatically stops supplying power to the grid. When there is sunlight exposure and the AC power generated by the PV system exceeds the load, the excess will be sent to the grid.

$$y(k) = \frac{a(k)y(k-1)}{1 + y^2(k-1)} + u(k-1) \quad (1)$$

Comprehensive analysis, the application of solar energy should consider its instability, mutation and low confidence characteristics, so the use of the ship, the following two types of situations are recommended:

$$X_m = [e(k), e(k-1), e(k-2), 1]^T \quad (2)$$

$$\left. \begin{aligned}
 \frac{\partial E(k)}{\partial x(k+1)} &= -(r(k+1) - y(k+1)) = -e(k+1) \\
 \frac{\partial u(k)}{\partial O_1^{(3)}} &= e(k) - e(k-1) \\
 \frac{\partial u(k)}{\partial O_2^{(3)}} &= e(k) \\
 \frac{\partial u(k)}{\partial O_3^{(3)}} &= e(k) - 2e(k-1) + e(k-2) \\
 \frac{\partial O_1^{(3)}}{\partial net_1^{(3)}} &= g[net_1^{(3)}] \\
 \frac{\partial net_1^{(3)}}{\partial \omega_{ji}^{(3)}} &= O_j^{(2)}(k)
 \end{aligned} \right\} \quad (3)$$

As solar energy is affected by climate and light conditions, there is a fluctuation phenomenon in power generation. Therefore, when an off-grid PV system supplies power to a load, auxiliary energy storage batteries are usually provided:

$$\frac{\partial E(k)}{\partial net_1^{(3)}} = \frac{\partial E(k)}{\partial x(k+1)} * \frac{\partial x(k+1)}{\partial u(k)} * \frac{\partial u(k)}{\partial O_1^{(3)}} * \frac{\partial O_1^{(3)}}{\partial net_1^{(3)}} \quad (4)$$

The capacity of the battery shall be determined according to the requirements of the effective time and proportion in the photovoltaic power generation throughout the day, and at the same time, a certain number of days of self-sufficiency shall be taken into consideration, so that the photovoltaic power generation system can meet the load requirements of the entire day:

$$E(k) = \frac{1}{2} (r(k) - y(k))^2 \quad (5)$$

As the proportion of power generation capacity of photovoltaic power generation system increases, it will directly affect the voltage stability of the power grid:

$$X_{in} = [e(k), e(k-1), e(k-2), 1]^T \quad (6)$$

Inrush current caused by unsynchronized voltage phases caused when power is restored may cause tripping again or damage to photovoltaic system, load and power supply system:

$$\frac{\partial O_j^{(2)}}{\partial net_j^{(2)}(k)} = f'[net_j^{(2)}(k)] \quad (7)$$

The solar controller is an automatic control device for controlling the solar cell array to charge the battery and the battery to supply the solar inverter load in the solar power system:

$$\frac{\partial net_j^{(2)}}{\partial \omega_{ij}^{(2)}(k)} = O_i^{(1)}(k) \quad (8)$$

Considering the installation and orientation, occlusion issues should also be considered, such as crystalline silicon

solar cells, where very little shielding will cause a large power loss; However, the effect of shielding on the thin film battery will be much smaller. In addition, the ventilation conditions are very important for the cooling of solar modules. As the temperature increases, the power generation will decrease; and the module temperature will also have a certain influence on the installation method.

CONCLUSIONS

With the development of tourism and the development of tourism resources such as lakes and scenic spots, cruise ships, as a carrier of nature, have gradually become an entertainment way for people to travel and vacation. However, the problem of water, air and noise pollution caused by oil, water, and noise emitted from the cruise ship's power system has become increasingly serious, making the development of green ships more practical. Solar energy is a kind of renewable energy source, easy to get, and inexhaustible, inexhaustible, the application of solar energy on the cruise ship, its pollution problems will be solved. Therefore, there are more and more applications of solar photovoltaic systems on ships, and the application technology of solar energy has become one of the most important green technologies for ships. The grid-connected photovoltaic power generation system directly connects the direct current generated by the solar module to the public power grid after the grid-connected inverter is converted into an alternating current that meets the requirements of the mains grid. The grid-connected photovoltaic power generation system has centralized large-scale grid-connected photovoltaic power stations, which are generally state-level power stations. The main feature is that the generated power can be directly transferred to the grid, and the grid can be uniformly deployed to supply power to users. However, this kind of power station has a large investment, a long construction period, and a large area, and it is difficult to develop. The decentralized small-scale grid-connected photovoltaic system, especially the photovoltaic building integrated power generation system, is the mainstream of grid-connected photovoltaic power generation due to its advantages of small investment, quick construction, small land occupation, and strong policy support.

BIBLIOGRAPHY

1. Sukamongkol Y., Chungpaibulpatana S., Ongsakul W.: *A simulation model for predicting the performance of a solar photovoltaic system with alternating current loads*. Renewable Energy, Vol. 27, no. 2, pp.237-258, 2002.
2. Kolhe M., Kolhe S., Joshi J C.: *Economic viability of stand-alone solar photovoltaic system in comparison with diesel-powered system for India*. Energy Economics, Vol. 24, no. 2, pp. 155-165, 2002.

3. Dubey S., Tiwari G N.: *Thermal modeling of a combined system of photovoltaic thermal (PV/T) solar water heater*. Solar Energy, Vol. 82, no. 7, pp. 602-612, 2008.
4. Kolhe M.: *Techno-Economic Optimum Sizing of a Stand-Alone Solar Photovoltaic System*. Transactions on Energy Conversion, Vol. 24, no. 2, pp. 511-519, 2009.
5. Kolhe M.: *Techno-Economic Optimum Sizing of a Stand-Alone Solar Photovoltaic System*. Transactions on Energy Conversion, Vol. 24, no. 2, pp. 511-519, 2009.
6. Quaschnig V.: *Technical system comparison of photovoltaic and concentrating solar thermal power systems depending on annual global irradiation*. Solar Energy, Vol. 77, no. 2, pp. 171-178., 2004.
7. Kelly N A., Gibson T L.: *Improved photovoltaic energy output for cloudy conditions with a solar tracking system*. Solar Energy, Vol.83, no. 11, pp. 2092-2102, 2009.
8. Ravindra M., Moharil, Prakash S.: *Kulkarni. Reliability analysis of solar photovoltaic system using hourly mean solar radiation data*. Solar Energy, Vol. 84, no. 4, pp. 691-702, 2010.
9. Hoppmann J., Huenteler J., Girod B.: *Compulsive policy-making—the evolution of the German feed-in tariff system for solar photovoltaic power*. Research Policy, Vol. 43, no.8, pp. 1422-1441, 2014.
10. Mandal P., Madhira S T S., Haque A U.: *Forecasting Power Output of Solar Photovoltaic System Using Wavelet Transform and Artificial Intelligence Techniques*. Procedia Computer Science, Vol. 12, no. 1, pp. 332-337, 2012.
11. Mbewe D J., Card H C., Card D C.: *A model of silicon solar cells for concentrator photovoltaic and photovoltaic/thermal system design*. Solar Energy, Vol. 35, no. 3, pp. 247-258, 1985.
12. Ilango G S., Rao P S., Karthikeyan A.: *Single-stage sine-wave inverter for an autonomous operation of solar photovoltaic energy conversion system*. Renewable Energy, Vol. 35, no. 1, pp. 275-282, 2010.
13. Richards B S., Conibeer G J.: *A comparison of hydrogen storage technologies for solar-powered stand-alone power supplies: A photovoltaic system sizing approach*. International Journal of Hydrogen Energy, Vol. 32, no. 14, pp. 2712-2718, 2007.
14. Patterson M., Macia N F., Kannan A M.: *Hybrid Microgrid Model Based on Solar Photovoltaic Battery Fuel Cell System for Intermittent Load Applications*. Transactions on Energy Conversion, Vol. 30, no. 1, pp. 359-366, 2015.
15. Natarajan S K., Mallick T K.: *Numerical investigations of solar cell temperature for photovoltaic concentrator system with and without passive cooling arrangements*. International Journal of Thermal Sciences, Vol. 50, no. 12, pp. 2514-252, 2011.

CONTACT WITH THE AUTHOR

Yaqi Shi, B. S.
e-mail:13026183800@163.com

Department of Electronics and Information Technology
Wuhan Technical College of Communications
6 Baishazhou Road
Hongshan District
Wuhan Hubei
430065
CHINA